Exploring the Application of Ultrasonic Phased Arrays for Industrial Process Analysis

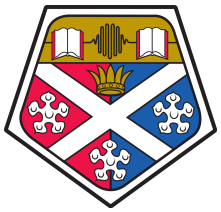

Marcus Ingram

Department of Electronic and Electrical Engineering

University of Strathclyde

A thesis submitted for the degree of

Doctor of Philosophy

2019

Copyright Declaration

All data supporting this Thesis will be available from the University of Strathclyde PURE repository, here, following the cessation of an embargo period. Further details relating to the data and the embargo can be requested using the contact details available on the portal landing page.

Signed:

Date:

In dedication to my late grandfather

Dr Alasdair C. F. Kenmure

Acknowledgements

I would like to express my sincere gratitude to my supervisor Anthony Gachagan for guiding me through this PhD programme. My gratitude extends to everyone in our team namely Alison Nordon, Anthony Mulholland and Martin Hegarty whose support has been highly valuable throughout this PhD programme.

I would also like to thank my colleagues in the Centre for Ultrasonic Engineering for making this an enjoyable experience, namely Jerzy Dziewierz, Tim Lardner and Carmelo Mineo for their patience while helping me through the learning process.

This project would not have been possible without the Engineering and Physical Sciences Research Council as well as BP Chemicals Limited who funded and provided the industrial drive for this research.

Last but not least, I would like to express my heartfelt thanks to my family; they have been dedicated to ensuring my education throughout my life and it is greatly appreciated.

Abstract

Typical industrial process analysis techniques require an optical path to exist between the measurement sensor and the process to acquire data used to optimise and control an industrial process. Ultrasonic sensing is a well-established method to measure into optically opaque structures and highly focussed images can be generated using multiple element transducer arrays. In this Thesis, such arrays are explored as a real-time imaging tool for industrial process analysis.

A novel methodology is proposed to characterise the variation between consecutive ultrasonic data sets deriving from the ultrasonic hardware. The pulse-echo response corresponding to a planar back wall acoustic interface is used to infer the bandwidth, pulse length and sensitivity of each array element. This led to the development of a calibration methodology to enhance the accuracy of experimentally generated ultrasonic images.

An algorithm enabling non-invasive through-steel imaging of an industrial process is demonstrated using a simulated data set. Using principal component analysis, signals corresponding to reverberations in the steel vessel wall are identified and deselected from the ultrasonic data set prior to image construction. This facilitates the quantification of process information from the image.

An image processing and object tracking algorithm are presented to quantify the bubble size distribution (BSD) and bubble velocity from

ultrasonic images. When tested under controlled dynamic conditions, the mean value of the BSD was predicted within 50% at 100 mms^{-1} and the velocity could be predicted within 30% at 100 mms^{-1}. However, these algorithms were sensitive to the quality of the input image to represent the true bubble shape.

The consolidation of these techniques demonstrates successful application of ultrasonic phased array imaging, both invasively and non-invasively, to a dynamic process stream. Key to industrial uptake of the technology are data throughput and processing, which currently limit its applicability to real-time process analysis, and low sensitivity for some non-invasive applications.

Contents

Abbreviations

ADC - Analogue-to-Digital Converter

AE - Acoustic Emission

BSD - Bubble Size Distribution

CUE - Centre for Ultrasonic Engineering

DLL - Dynamic link library

FMC - Full Matrix Capture

FRD - Full Raw Data

GC - Gas Chromatography

GPU - Graphics Processing Unit

GUI - Graphical User Interface

ID - Identity

LSM - Linear Systems Model

LUT - Look-Up Table

NDE - Non-Destructive Evaluation

PAC - Phased Array Controller

PC - Personal Computer

PCA - Principal Component Analysis

PCF - Phase Coherence Factor

PCI - Phase Coherence Imaging

PDF - Probability Density Function

PIV - Particle Image Velocimetry

PRF - Pulse Repetition Frequency

PSD - Particle Size Distribution

ROI - Region of Interest

RP-GCM - Reverberation Pattern Gain Correction Method

SCF - Sign Coherence Factor

SDH - Side-Drilled Hole

SNR - Signal to Noise Ratio

TGC - Time Gain Compensation

TFM - Total Focusing Method

TOF - Time of Flight

UK - United Kingdom

Symbols

A - Active aperture [-]

$b(t)$ - Sign bit as a function of time [-]

C_{Y_e} - Covariance of the full raw data [-]

d - Piezoelectric charge constant [NC^{-1}]

dP - Pixel dimension [m]

D - Electric displacement [Cm^{-2}]

e - Element width [m]

E - Electric field strength [Vm^{-1}]

f_0 - Centre frequency [Hz]

F_s - Sampling frequency [Hz]

g - Piezoelectric voltage constant [CN^{-1}]

h - Inter-element spacing [m]

I_{ij} - Intensity of pixel at coordinate (i,j) [-]

K - Number of elements in active aperture [-]

L - Straight line path length to back wall [m]

l_1 - Object width [pixels]

l_2 - Distance from object mid-point to key-point 3 [pixels]

m - Gradient of straight line [-]

M - Number of A-Scan lines in full raw data [-]

N - Number of time samples [-]

$n(t)$ - Noise signal [-]

p - Element pitch [m]

P_i - Incident pressure [Pa]

P_r - Reflected pressure [Pa]

P_t - Transmitted pressure [Pa]

$r(n)$ - Ray path length [m]

$r(t)$ - Reverberation signal [-]

r^2 - Pearson correlation coefficient [-]

R_p - Reflection coefficient [-]

R_x - Receiving element index [-]

S - Mechanical strain [-]

$s_f(t)$ - Signal of interest [-]

$\hat{s}_f$ - Modified full raw data [-]

S_i - Imaginary component of Hilbert transform [-]

S_r - Real component of Hilbert transform [-]

t - Time [s]

t_0 - A-Scan start time [s]

t_{em} - Empirical time-of-flight [s]

t_{err} - Time-of-flight error [s]

t_{ob} - Observed time-of-flight [s]

t_{reverb} - Time between first and second back wall reflections [s]

T_p - Transmission coefficient [-]

T_x - Transmitting element index [-]

$\mathbf{u}_m$ - Eigenvector [-]

U_r - Clutter subspace [-]

V_i - Input voltage [V]

V_o - Output voltage [V]

W - Passive aperture [m]

Y - Young's Modulus [-]

Y_e - Full raw data [-]

$y(t)$ - Time domain A-Scan signal [-]

Z - Acoustic impedance [MRayl]

Z_a - Acoustic impedance of active element [MRayl]

Z_m - Acoustic impedance of matching layer [MRayl]

Z_l - Acoustic impedance of load [MRayl]

z_{st} - Steel thickness in z dimension [m]

η - Number of eigenvectors corresponding to void and noise subspace [-]

ϵ - Absolute permittivity [Fm^{-1}]

θ - Reflector angle [degrees]

Γ Mechanical stress [Pa]

λ - Wavelength [m]

λ_m - Eigenvalue [-]

μ - Mean [-]

ν - Acoustic velocity [ms^{-1}]

ρ - Denisty [Kgm^{-3}]

σ - Standard deviation [-]

ϕ - Object curvature ratio [-]

$\psi(t)$ - Instantaneous phase as a function of time [radians]

Ω - Envelope response [-]

Chapter 1

Introduction

1.1 Graphical Abstract

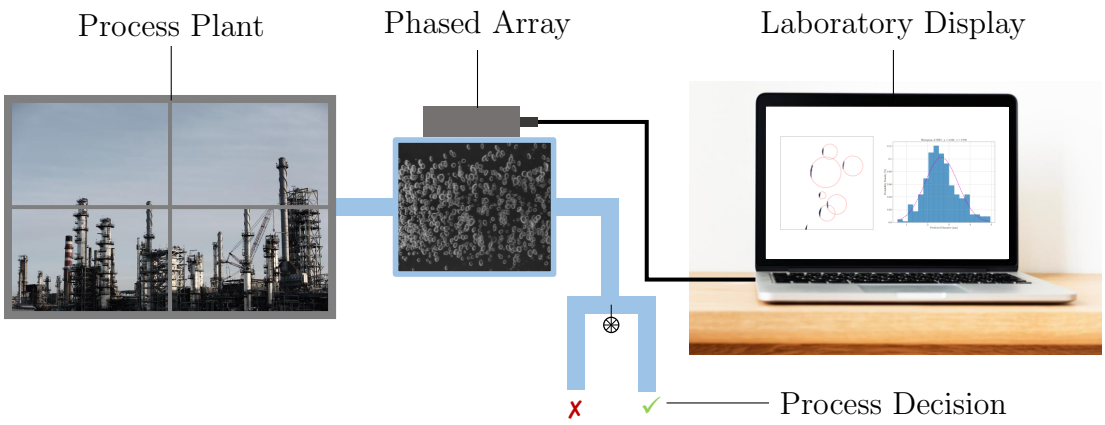

Figure 1.1: *Schematic of ultrasonic phased array imaging system for industrial process analysis.*

1.2 Background

Currently more than half of the United Kingdom's (UK) exports come from manufacturing [1] and its industries account for around 8% of UK jobs [2]. To support this sector, the UK government has identified the development of sensing and measurement technologies as a key driver to fuel the UK economy, particularly in the field of autonomous manufacturing [3]. For example, sensor technologies are deployed for the characterisation of industrial processes during chemical manufacture.

Industrial process analysis provides data that is used to control and/or optimise industrial processes such as those utilised during chemical manufacture [4]. Robust industrial process control increases workplace safety by moving the analyser instrument away from the process, improves consistency of product quality and improves environmental impact by reducing waste [5].

Chemical manufacturing typically involves the flow of heterogeneous material within solid vessels, both of which may be optically opaque [5, 6]. This means spatial information about the process cannot be acquired using standard optical techniques without modification of the process and/or vessel material [7]. Ultrasonic sensing is a well-established technology that provides a safe methodology for imaging into optically opaque materials because it utilises mechanical rather than electromagnetic waves [8].

Ultrasonic images can be generated by manually scanning the node of interest through a linear path with a single transducer element [9] or by using a multiple-element phased array transducer [10]. An ultrasonic phased array transducer is

a sensing device comprising a number of individually addressable active piezoelectric elements, each capable of transmitting and receiving ultrasound into and from the load medium [8]. These actuating and sensing devices can provide highly focussed images due to the precise positioning of their transmitting and receiving elements [10].

Such arrays are typically used for sonar, medical diagnosis and non-destructive evaluation (NDE), however, they have not yet been applied in the field of industrial process analysis. In this Thesis, ultrasonic phased arrays are explored as an imaging tool for industrial process analysis.

1.3 Motivation for this Work

This PhD project originates from the output of a post-doctoral research project completed between 2012 and 2014, investigating the feasibility of using ultrasonic phased arrays for imaging of industrial processes [11]. Given that at the time, ultrasonic phased array technology had not been investigated within the context of industrial process analysis, the primary research questions behind this work were:

i. Can ultrasonic phased arrays be deployed to image dynamic processes?

ii. If so, how can these images provide novel information about the process?

As a result of the phased array controller (PAC) hardware available at the time of this work, a significant challenge identified was the low resolution of ultrasonic images that were constructed. This limited the quality of the images that were

generated and the accuracy of information extracted from these images.

A key challenge to monitor dynamic systems, such as industrial processes, is the ability to capture and process information fast enough to provide real-time feedback about the system. For a measurement system to provide real-time feedback about a process depends on the time scale of the overall process. For example, fermentation may take several days to reach its end-point [12], so a 15 minute delay between process measurement and the result can be said to provide real-time process analysis.

Extracting quantitative information about industrial processes using ultrasonic phased array imaging requires a multiple-stage process. After the ultrasonic data has been acquired, pre-processing techniques can be deployed to manipulate this ultrasonic data set prior to image construction. Following this, additional signal processing techniques can be deployed to post-process these images to remove noise artefacts. Finally, these images can be processed to extract information relating to the image target. It is the aim of this Thesis to address the optimisation of each of these individual stages in this chronological order presented.

Recent technological advances in multiple-channel PACs and graphics processing units (GPU) have accelerated data acquisition and ultrasonic image construction algorithms. This has provided the opportunity to apply ultrasonic phased array imaging to dynamic processes. In light of this, an aim of this research is to optimise the ultrasonic data throughput to minimise the delay of feedback to the analyst within the current technological constraints.

This Thesis aims to build upon the previous work and take advantage of current technological advances by considering:

i. What alternative data acquisition methodologies and image construction algorithms should be deployed?

ii. How can acoustic imaging overcome challenges in process analysis specifically associated with optical imaging techniques?

iii. What challenges exist to deploy this technology towards real-time process analysis and how can these be overcome?

1.4 Aims and Objectives of the Research

The overall aim of the research is to explore the application of ultrasonic phased arrays for industrial process analysis. In particular, it is the aim to deploy ultrasonic phased arrays for imaging of a dynamic process stream and to use these ultrasonic images to obtain quantitative information about the process. It is the aim to image the process both intrusively, whereby the array is positioned in direct contact with the process material, and non-invasively, whereby the ultrasound must transmit through the wall of the process vessel to be detected.

To achieve these aims the ultrasonic imaging system outlined in Figure 1.2 was created. A linear array is mounted to the outside wall of a process vessel that is used to transmit ultrasound into the process material via the vessel wall. The ultrasound is reflected at the surface of the bubbles and returns to the linear array to be detected. The objective of the research is to develop a signal and image processing procedure to determine the bubble size distribution (BSD) and velocity of these bubble reflectors from the ultrasonic images generated.

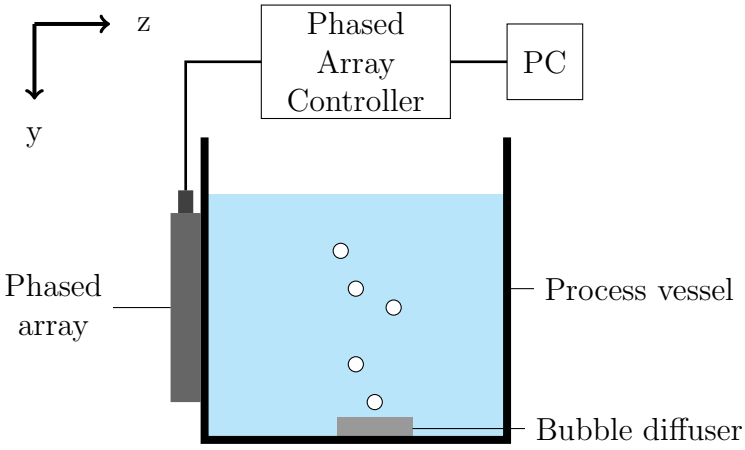

Figure 1.2: *Schematic representing target application; ultrasonic phased array imaging of a dynamic target via process vessel wall.*

Note, the phased array is coupled to a PAC that enables the analyst to manipulate the pressure field transmitted from the phased array. This is coupled to a personal computer (PC) to run the software to construct the ultrasonic images.

It is standard practice, when performing ultrasonic spectroscopy for particle sizing, to remove bubble reflectors from the process fluid [13]. This is because ultrasound is strongly reflected at the gas-fluid interface, creating scattering interference during ultrasonic spectroscopy. Therefore, since bubbles suspended in water generate strong ultrasound reflections measurement of gas bubbles poses a well suited application for ultrasonic process imaging when performed in pulse-echo mode.

Gas-liquid two-phase systems are found in a wide variety of industrial processes. For example, solvent sublation is a process used in waste water treatment whereby hydrophobic organic compounds adsorb at the bubble-fluid interface removing organic pollutants [14]. In the petrochemical industry the Fischer-Tropsch

process is used to convert natural gas into commercial products like fuels [15]. During this process syngas bubbles are contacted with liquid slurries containing catalyst particles, where these bubbles can be on the millimetre length scale and travel at low superficial gas velocities within the fluid [15]. Another example from the petrochemical industry is the coal liquefaction process whereby hydrogenation of the hydrocarbon is performed by supplying hydrogen bubbles to a coal slurry [16]. Bubbles within a fluid are used in separation processes, whereby suspended particles attach to bubbles rising to the surface of a fluid, for example, in flotation cells [17]. Here, the froth characterisation provides an indication of the drainage and coalescence behaviour inside the flotation cell [18].

The rate of mass transfer between the fluid and gas phases is highly dependent on the interfacial area between the dispersed and continuous phase in bubbly flows [19]. The mass transfer of a dispersed phase is defined by its size, velocity and concentration [20]. For these processes, it is important to measure the BSD as this is directly related to the interfacial area of the bubble phase [17, 19]. This in turn provides an understanding of the mass transfer capability and reactivity of these processes.

1.5 Contributions to Knowledge

i. The uncertainty in measured ultrasonic data has been investigated using an experimental characterisation and calibration technique. The novel aspect of this process has been the ability to decouple the time domain error associated with transmission and reception at each element index. Incor-

porating these errors into an image construction algorithm had the impact of refocussing the ultrasonic time domain signals relative to uncertainty introduced from the hardware.

ii. An algorithm has been developed to generate non-invasive through steel ultrasonic images corresponding to a typical industrial process. The algorithm was influenced by literature published in the NDE and medical communities that have been typically used to remove coherent noise artefacts from ultrasonic signals containing reverberations. The novel aspect of this work is the application of the algorithm to the full matrix of ultrasonic data available from an ultrasonic array. This extended the applicability of the technique to more advanced image construction methodologies.

iii. An image processing algorithm has been developed to extract quantitative information from ultrasonic images relating to an industrial process. This algorithm was calibrated and tested under dynamic conditions where a novel aspect of this work relates to the use of a six-axis robotic arm to acquire ultrasonic data of a controlled dynamic system. Application of this image processing algorithm to experimental data resulted in a novel methodology for the determination of bubble size distribution (BSD) in industrial flows.

iv. An object tracking algorithm has been created to extract the velocity of individual objects in a sequence of image frames relating to a dynamic process. When this was applied to experimental data, this presented a novel methodology for bubble velocimetry of industrial flows.

1.6 Dissemination of Results

Paper Output

[1] M. Ingram, A. Gachagan, A. J. Mulholland, A. Nordon, M. Hegarty and E. Becker "Calibration of Ultrasonic Phased Arrays for Industrial Applications," in *IEEE Sensors*, pp.1518–1520, Nov. 2017.

[2] M. Ingram, A. Gachagan, A. J. Mulholland, A. Nordon, J. Dziewierz and M. Hegarty, "Enhanced Phased Array Imaging Through Reverberating Interfaces," in *Review of Progress in Quantitative Non-Destructive Evaluation*, Jul. 2018.

[3] M. Ingram, A. Gachagan, A. J. Mulholland, A. Nordon and M. Hegarty, "Ultrasonic Array Imaging through Reverberating Layers for Industrial Process Analysis," in *IEEE International Ultrasonics Symposium (IUS)*, Oct. 2018.

[4] C. Avila, A. Gachagan, E. Becker, A. Nordon, A. J. Mulholland, M. Ingram, "Design and Calibration of a Phased Array Ultrasound Imaging System for Bubble Size Characterization," in preparation.

Presentation Only

[5] M. Ingram, A. Gachagan, A. J. Mulholland, A. Nordon and E. Becker "Ultrasonic Process Analysis through Metallic Interfaces," at *EuroPACT*, Potsdam, Germany, May. 2017.

[6] M. Ingram, A. Gachagan, A. J. Mulholland, A. Nordon, J. Dziewierz and M. Hegarty "Calibration of Ultrasonic Phased Arrays for Industrial Applications," at *RCNDE Early Stage Researchers Conference*, Bristol, UK, Jun. 2017.

[7] M. Ingram, C. Mineo, A. Gachagan, A. Nordon, A. J. Mulholland and M. Hegarty "Real-time 2D Ultrasonic Imaging of Dynamic Process Streams," at *CPACT Research Day*, Glasgow, UK, Oct. 2017.

[8] M. Ingram, A. Gachagan, A. Nordon, A. J. Mulholland, C. Mineo and M. Hegarty "In-situ Ultrasonic Imaging of Dynamic Process Streams: System Calibration and Image Processing," at *SciX*, Reno, NV, USA, Oct. 2017.

[9] M. Ingram, J. Dziewierz, A. Gachagan, A. Nordon, A. J. Mulholland and M. Hegarty "Non-Invasive Ultrasonic Imaging of Dynamic Process Streams," at *Spring SciX*, Glasgow, UK, Apr. 2018.

[10] M. Ingram, J. Dziewierz, A. Gachagan, A. Nordon, A. J. Mulholland and M. Hegarty "Towards Non-Invasive Imaging of Dynamic Processes through Metallic Interfaces," at *ULTRASONICS*, Caparica, Portugal, Jun. 2018.

[11] M. Ingram, A. Gachagan, A. Nordon, A. J. Mulholland, J. Dziewierz and M. Hegarty, "Calibration of Ultrasonic Hardware for Enhanced TFM Performance," at *Review of Progress in Quantitative Non-Destructive Evaluation*, Jul. 2018.

[12] M. Ingram, A. J. Mulholland, A. Gachagan, A. Nordon, J. Dziewierz and M. Hegarty, "Calibration of Ultrasonic Hardware for Total Focusing Method

Imaging," at *57th Annual British Conference on Non-Destructive Testing*, Sep. 2018.

1.7 Structure of the Thesis

The main content of the work is presented over seven chapters. This Chapter introduces the commercial niche where the relevance of this technical work lies. The motivation behind this research is provided within the context of an associated research project and the current technological constraints. Finally, an overview is provided of the novel aspects of the work presented in this Thesis.

Chapter 2 provides a review of industrial process analysis and establishes the gap in the literature this work aims to fill. This review begins with an overview of process analysis and ultrasonic systems. The context of the research problem is described and current techniques to overcome this technical problem are discussed. An in-depth critique of the current state of the knowledge is provided within the specific context of the work presented in this Thesis.

Chapter 3 gives insight into the experimental variation associated with the ultrasonic hardware. When acquiring multiple data frames of a dynamic process it is important to understand the variation between individual data sets. This Chapter presents a methodology to capture this variation and an algorithm to characterise the ultrasonic hardware. Following this, a methodology is established to incorporate this measurement uncertainty into the ultrasonic image construction process.

Chapter 4 presents the challenge of performing ultrasonic imaging through vessel walls. Several methodologies are proposed to overcome the reverberation pattern exhibited when imaging through steel vessel walls. An approach that does not require any *a priori* information about the non-invasive system is found to be most effective at reverberation suppression and this is demonstrated using a simulated ultrasonic data set.

Chapter 5 serves as an introduction to the image processing algorithm developed to extract the BSD of an industrial flow from ultrasonic images. The algorithm is tested using simulated and experimental data sets of stationary reflectors to provide certainty in its functionality.

Chapter 6 expands the application of this image processing algorithm to controlled dynamic systems. Using a six-axis programmable robotic arm, the phased array has been used to scan a solid sample containing bubble-like reflectors at set speeds. This provides ground truth that ultrasonic phased array imaging can be used to extract quantitative information about a dynamic system. This Chapter also presents an object tracking algorithm used to group the size distribution of objects present in multiple image frames and to extract the velocity of these tracked objects.

Chapter 7 brings together all these concepts into a single experimental set-up of an uncontrolled process. Here, non-invasive ultrasonic imaging is presented as a robust analytical tool for industrial process analysis. It is demonstrated that typical process parameters used in process monitoring and control can be extracted using ultrasonic phased array imaging.

The Thesis concludes with an overview of the key findings presented through-

out the research. The implication of the research findings are discussed in the context of the applicability of ultrasonic phased arrays for industrial process analysis. Finally, an overview of the future potential of this technology in terms of the practical limitations of the experimental work, ultrasonic hardware design and computer processing power is presented.

Chapter 2

Review of Process Analysis and Ultrasonic Applications

2.1 Introduction

This Chapter presents a review of the current state of the knowledge of industrial process analysis and ultrasonic hardware used to generate ultrasonic images. The structure of the Chapter is split into four key areas. Firstly, an overview of industrial process analysis and ultrasonic systems provides a broad understanding of the scope for ultrasonic measurement in process analysis. In doing so, the advantages of using phased array imaging for process analysis are outlined. Next, the context of the work is discussed to provide an understanding of the motivation behind specific aspects of the literature review. This is followed by an in-depth critique of the current state of the art in the field. Finally, the ideas presented are collated in terms of the gap in the literature that this research aims to fill.

2.2 Overview of Industrial Process Analysis

2.2.1 Background

Industrial process analysis is the measurement of data that can be used to control a chemical process [4]. The benefits of understanding the current status of a chemical process include increased process safety, enhanced product consistency and reduced environmental impact by reducing waste [5]. Industrial process analysis uses a control feedback loop containing three key aspects; the measurement sensor to acquire information about the system, the analyst to interpret this information and the actuator that carries out any decision made by the analyst. This is illustrated in Figure 2.1 where external disturbances to a process are monitored by sensors that acquire point or spatial measurements, feeding information to the analyst.

Process measurement sensors can be positioned intrusively in direct contact with the process material or non-invasively without direct contact with the process. The latter requires information about the process to be transmitted through the vessel wall before reaching the sensor. These measurement methodologies are considered to be in-situ if the sensor measures the bulk process without undertaking extractive sampling of the process stream [5].

Extractive sampling, whereby a portion of the process stream is removed and sent to the sensor via a sampling line, is typically used for mass spectrometry and gas chromatography (GC) measurements [4]. Using a sampling line increases the cost of measurement and creates a time delay between the sample extraction

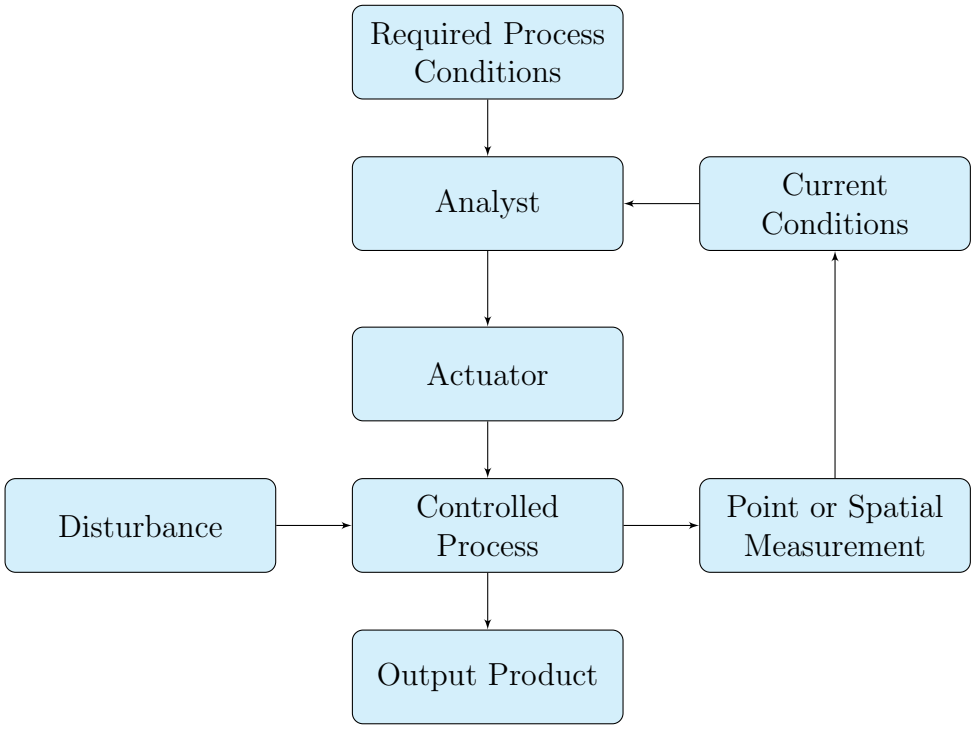

Figure 2.1: *Flow chart illustrating an industrial process control procedure.*

and its analysis. In addition, careful consideration of the process conditions such as temperature must be taken to ensure the sample does not undergo modification during transit through the sample line. Therefore, extractive sampling may not generate real-time information about the process. Acoustic-based techniques are not typically deployed this way because they require measurements to be made on the bulk process [21]. Therefore, acoustic measurements are typically more characteristic of the overall process than measurements relating to extracted samples.

Where the sensor is positioned in-situ and intrusively within the process, this positioning can lead to disturbances within the process and fouling of the sensor due to flow restriction. This can reduce the accuracy of information gathered

about the bulk process. Therefore, if the sensor is positioned in-situ and non-invasive to the process this has the ultimate desirability [5]. This is typically achieved by inserting a *sampling window* [5] into the process because optical techniques, for example, Raman, infra-red, ultraviolet-visible spectroscopies and digital image capture, require an optically transparent path between the sensor and the process. The introduction of a *sampling window* also requires modification of the vessel structure prior to implementation of the sensor. If this is retrofitted to the vessel rather than being incorporated in the initial plant design, this incurs additional measurement costs as well as requiring the process to be switched off to be installed.

Non-invasive measurement has several advantages over both extractive and intrusive measurement as summarised below:

i. It does not interfere with the process or induce flow vortices, so reduces fouling and disturbances to the process;

ii. It provides increased measurement flexibility because hardware can be easily maintained or replaced without disruption to the process;

iii. It reduces the measurement and build cost as it does not require the installation of a sampling line and

iv. It creates a safer measurement environment and overall system integrity because there is no direct contact with the process.

A key challenge to industrial process analysis is that the sample to be measured is typically dynamic in nature. Therefore, measurements must be interpreted in the context of both spatial and temporal resolution. Quantification of the size

distribution of particles, crystals or bubbles in a process stream presents such a challenge. The size distribution of these components, by definition, provides information on the spread of the process behaviour, however its representativeness at a given point in time depends on the sampling period between measurements. For dynamic processes, there is a need to capture the variation within the process by taking multiple measurements, however as the measurement frequency and the quantity of information about the process increases, processing of this information in real-time becomes challenging [22]. For example, bubble sizing in bubbly flows is highly dependent on the coalescence and break-up of bubbles, which introduces sizing errors in flows with high superficial velocities [19]. Therefore, measurements of dynamic systems are only relevant to the region local to the sensor and at the timestamp of the measurement [23].

2.2.2 Standard Measurement Techniques

Industrial process analysis typically involves the measurement of qualitative and quantitative information relating to the current state of a process in terms of its chemical composition, concentration or mass transfer efficiency [4]. In addition, these factors are dependent on the physical conditions of the process, for example, temperature, pressure and flow rate [4]. These parameters can also influence the measurement hardware, for example, piezoelectric transducers will lose their piezoelectric effect above the Curie temperature ($\approx$ 200 °C) [24]. Given the multivariate nature of process analysis there is no all-encompassing process analytical measurement tool. Process control and optimisation is based on information from a range of complementary measurement tools to maximise understanding of the

process [5].

The development of process analysis was pioneered by the petrochemical industry prior to the pharmaceutical industry or the process analytical technology initiative that was driven by the need for greater safety standards [5]. The two main process analytical techniques deployed by the petrochemical industry are GC and mass spectrometry. These are used for automated on-line analysis of gaseous volatile liquid samples and are typically used as complementary techniques [25].

Sample separation using GC can be easily automated to perform on-line analysis, however, it requires extractive sampling of the bulk process [5]. This creates a time delay between sample extraction and its analysis and there is a high cost to create the extraction line. Liquid chromatography is not as well established in process analysis because the large volume of liquid mobile phase required to perform on-line analysis means regular recalibration and maintenance is required, which a time consuming process [4]. In addition, the main challenge with deploying liquid chromatography in a process environment is sample preparation, whereby sample dilution can be difficult to automate and maintain consistency across sample replicates [4]. Both forms of chromatography operate in similar ways, whereby the sample is eluted through a separation column relative to physical or chemical properties of the sample [25].

Upon injection of a liquid sample into the GC instrument, the sample undergoes instantaneous vaporisation and is mixed with a neutral carrier gas, for example, helium [25]. This gas is carried through the separation column, where the order of elution is dependent on the relative boiling point of each molecule

in the sample. The chromatogram generated relates to the retention time and intensity of each molecule, represented by individual peaks under well resolved conditions. The retention time corresponds to molecular weight and the peak area to its concentration. Using linear regression, the concentration in an unknown sample can be determined from the relative peak area to an internal standard [26].

Another well established technique for determination of the molecular composition of low volatile compounds is mass spectrometry [27]. The instrument begins by ionising and fragmenting the injected sample using an electron beam from a heated filament [4]. Following this, the fragmented sample is passed through a magnetic field where the fragments are separated relative to their mass to charge ratios [4]. The key limitation of mass spectrometry is sample introduction, which is why it is limited to gases and volatile liquids [28]. However, for a similar maintenance cost to GC it provides greater dynamic range of concentration detection [27].

One of the key practical implications of process analysis is the ability to transfer information from the process to the analyst. To do this as safely as possible it is important for the analyst to be remote from the process [5]. For GC and mass spectrometry, extractive sampling means the instrumentation is not necessarily located at the process. However, for vibrational spectroscopy techniques, in-situ measurement on the bulk process is made possible through the use of optical fibres [29].

The most widely used optical technique used in process analysis is infra-red spectroscopy [30]. This corresponds to the region in the electromagnetic spectrum

with wavelengths just below that of visible light. Near infra-red, that closest in wavelength to visible light, can be transferred by optical fibres up to one kilometre in length [31]. This makes it very suitable for in-situ measurement, whereby the analyser can be remote from the process, increasing the system integrity. Infra-red spectroscopy can be deployed to measure the chemical composition of a process and also the physical state of a process, for example, particle size distribution (PSD) [30].

Raman spectroscopy is a form of vibrational spectroscopy often used for molecular composition determination in process analysis. For process analysis applications, it uses a laser with a wavelength, λ, of typically 785 nm to excite the vibrational state of the sample [32]. As the vibrational state of the sample reaches its first excited vibrational state it scatters the incident energy at frequencies depending on its composition [32]. This measurement technique can be performed in-situ and non-invasive to the process making it a highly desirable tool for on-line analysis. However, this requires an optically transparent *sampling window* to be installed at the measurement point, reducing the flexibility of the measurement [32]. As the sample reaches its excited state only a small fraction of the scattered energy reaches the detector, reducing the sensitivity of the tool. This has led to the development of surface enhanced Raman spectroscopy [33] to increase the degree of scattering, however, this requires direct access to the sample for treatment so cannot be performed in-situ.

Quantification of the PSD is fundamental to processes involving crystallisation, flocculation and gelation [34, 35]. Laser diffraction techniques, such as focussed beam reflectance measurement, are commonly used for this measurement [36].

This measures the chord distribution of particles ranging from nanometres to millimetres in length by measuring the diffracted path length of a laser as it passes through the load medium. Unfortunately, it does not translate well to in-situ measurement. This is because it requires very dilute samples and sample preparation can be difficult to automate for large scale processes [37].

2.2.3 Ultrasonic Measurement Techniques

Ultrasonic measurement is also a well established technique in process analysis for particle sizing [13]. Ultrasound is typically the term that describes sound or mechanical waves with frequencies above that of typical human hearing, approximately 20 kHz. Ultrasound is redcommonly generated and detected using ultrasonic transducers containing piezoelectric ceramic that converts the electrical pulse to a mechanical displacement and vice versa [24]. The phenomenon of generating an electrical charge by compression is known as the direct piezoelectric effect, with the reverse process being the indirect piezoelectric effect [38].

There are two distinct ultrasonic measurement techniques typically used in process analysis, namely passive and active measurement [39]. Passive measurement refers to the detection of sound generated from within the process, for example, acoustic emission (AE) [40]. Active measurement refers to the detection of sound that has been injected into the process [41].

Active measurements can be performed in through-transmission or pulse-echo modes. The former, illustrated in Figure 2.2(a), requires two ultrasonic transducers to be positioned on opposite sides of the vessel. One transducer is used

to transmit ultrasound into the process, the ultrasonic wave then interacts with the process and is received by a second transducer. The latter, illustrated in Figure 2.2(b), uses a single transducer that operates as both a transmitter and receiver. In pulse-echo mode the transducer is switched to receive shortly after transmission of the ultrasonic pulse [39], this time delay between the ultrasound transmission and the start of the recorded signal is called the start time, t_0 (s).

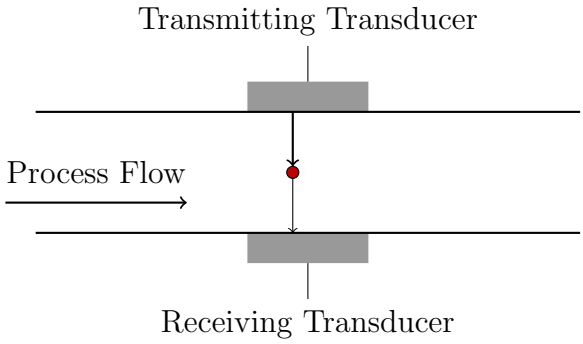

(a) *Through-transmission ultrasonic measurement.*

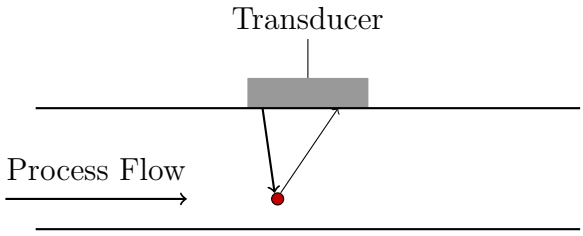

(b) *Pulse-echo ultrasonic measurement.*

Figure 2.2: *Active acoustic measurement methods.*

Ultrasonic spectroscopy is an active measurement technique used for particle sizing in process analysis [13]. This involves determination of the frequency dependent attenuation that contains contributions from scattering and non-scattering events within the process [13]. The contributions from non-scattering events can be determined by measuring the pure component or the dispersed

phase spectrum [13]. This can then be subtracted from the original response to determine the contribution from scattering events, relating to the PSD in the process [13]. This is then used to predict the PSD by fitting the subtracted spectrum to an analytically or numerically modelled response [42].

To create these modelled solutions requires a strong understanding of scattering theory of ultrasound waves. The solution for a single spherical scattering object was first proposed by Rayleigh in 1896 [43]. This was extended to model the of compressibility, thermal and viscosity effects by Epstein and Carhart [44] for liquid-solid systems and by Allegra and Hawley [45] for solid-solid systems. This model was found to be ill-conditioned under numerical analysis, so was simplified by establishing conditions whereby the contribution from thermal effects was constrained [46].

Ultrasonic spectroscopy provides a means for particle sizing across a wide dynamic range, however, there are some drawbacks for practical deployment in process analysis. The technique requires a good understanding of the physical constants relating to the measured system, for example, its thermal conductivity, density and elastic modulus [13]. These are needed to fit the measured attenuation spectrum to a modelled system response, which could change depending on the dynamic nature of the process to be measured. In addition, the technique requires a background response to be measured to remove effects from non-scattering signals. In a process analysis environment this background response may not always be available.

On the other hand, there are several advantages to using ultrasonic spectroscopy and ultrasound measurement in general. Due to the wide frequency

range feasible, from 20 kHz to 200 MHz, particle sizing between 10 nm and 1 mm is possible [47]. This makes ultrasonic measurement highly suited to typical colloidal and emulsion processes [6]. A significant advantage of using ultrasound measurement is that it is not limited to optically transparent materials, so is well-suited to non-invasive measurement [13]. This means it can be readily deployed in-situ on the bulk process and can be used without extractive sampling or sample treatment. This makes ultrasound measurement an attractive tool for practical industrial process analysis, alongside the spectroscopic and chromatographic techniques mentioned previously.

2.3 Overview of Ultrasonic Systems

2.3.1 Ultrasonic Transduction

Ultrasound exhibits similar wave behaviour properties to electromagnetic radiation, for example, reflection and refraction [39]. An ultrasonic wave can undergo these phenomena when it reaches an acoustic boundary or interface in the propagating medium. An acoustic boundary occurs where two media have different acoustic impedances, as shown in Figure 2.3.

The acoustic impedance, Z (Rayl) of a material is

$$Z = \nu\rho, \tag{2.1}$$

where ν (ms^{-1}) is the acoustic velocity and ρ (kgm^{-3}) is the density.

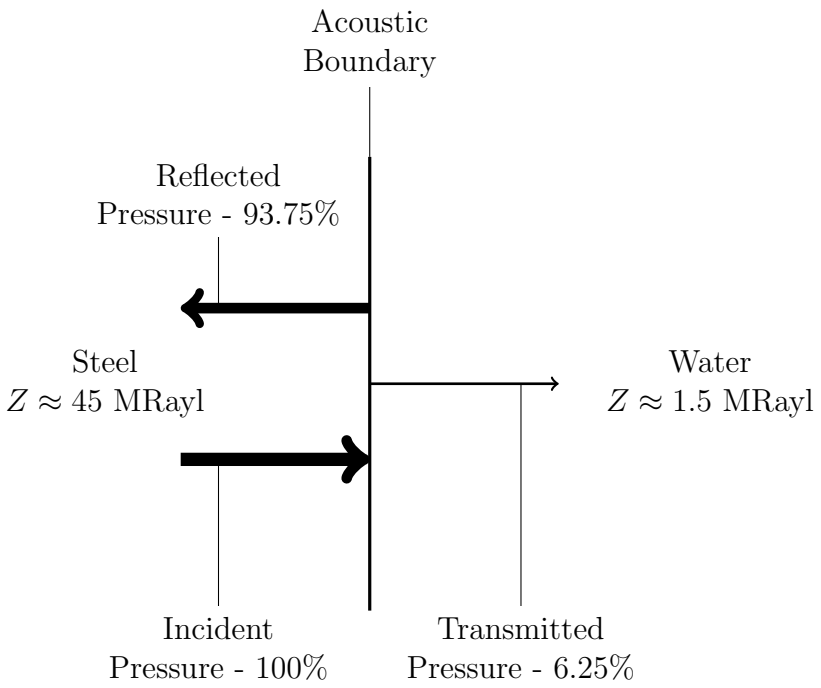

Figure 2.3: *Ultrasonic wave interaction with an acoustic boundary.*

At an acoustic boundary the total incident pressure, P_i (Pa), is either transmitted across the boundary or reflected from the boundary

$$P_i = P_r + P_t, \tag{2.2}$$

where P_r (Pa) is the reflected pressure, P_t (Pa) is the transmitted pressure. Relative to the incident pressure, the transmission, T_p, and reflection, R_p, coefficients can be determined by

$$\frac{P_i}{P_i} = \frac{P_t}{P_i} + \frac{P_r}{P_i} \tag{2.3}$$

$$1 = T_p + R_p. \tag{2.4}$$

Ultrasonic transduction at an acoustic interface depends on the relative acoustic impedance of the material either side of the acoustic interface [39]. For example, when ultrasound propagates from steel, $Z = 45.0$ MRayl, to water, $Z = 1.5$ MRayl, as shown in Figure 2.3, the transmission coefficient is

$$T_p = \frac{2Z_2}{Z_1 + Z_2}. \tag{2.5}$$

Therefore, 93.75% of the incident pressure is reflected as the ultrasonic wave reaches this acoustic boundary.

2.3.2 Modelling Ultrasonic Systems

2.3.2.1 Analytical Models

The key components of an ultrasonic system are the transducer, the connected circuitry and the field of wave propagation or load [39]. The first attempt to analytically model an ultrasonic system was performed by Mason [48] using an equivalent circuit to represent both the mechanical and electrical components of the system that were coupled by an ideally performing transformer [49]. The underlying mathematics of Mason's one-dimensional transduction model were based on the analytical solution to the direct and indirect piezoelectric equations.

The direct piezoelectric effect is described by

$$D = \epsilon E - gS, \tag{2.6}$$

where D (Cm^{-2}) is the electric displacement within the material, ϵ (Fm^{-1}) is

the absolute permittivity, g (CN^{-1}) is the piezoelectric voltage constant and S (dimensionless) is the mechanical strain [50]. The indirect piezoelectric effect is described by

$$\Gamma = YS - dE, \tag{2.7}$$

where Γ (Pa) is the mechanical stress, Y is the Young's Modulus, d (NC^{-1}) is the piezoelectric charge constant and E (Vm^{-1}) is the electric field strength [50].

It is important to recognise that both piezoelectric effects are modelled by two components: the intrinsic polarisation of the material and piezoelectric transfer. The former is a dielectric material property, defined by the permittivity of the material and the latter is the electrical polarisation within the material generated by a strain [39]. When considered in a single dimension as above, the piezoelectric equations correspond to an ideally operating transducer that vibrates in thickness mode [39]. This means vibrations only occur in the axial direction and there are no transverse vibrations.

Although Mason's model generated an analytical solution to the piezoelectric equations, it required an imaginary capacitance component to exist [49]. This issue was removed by Krimholtz et al [51] in the form of the KLM equivalent circuit model. Cochran and Démoré [52] also highlighted drawbacks of Mason's model in terms of its complexity when, for example, it is extended to model a phased array.

The linear systems model (LSM), developed by Hayward et al [50], provides

an analytical solution to the piezoelectric equations by assuming linearity of all variables. The LSM directly relates a force incident on the front face of the transducer to an output voltage and vice versa, via a linear transfer function. This is achieved by deriving a solution in the Laplace domain, which also lends itself to facile interpretation of feedback loops and modelling of reverberations [50]. However, the one-dimensional models have a distinct disadvantage in that they cannot model lateral mode vibrations within the piezoceramic. In particular, a disadvantage of both the equivalent circuit models and the LSM is that they only describe the macro-structure of the device. For example, piezocomposite transducers that contain both active piezoelectric material and passive polymer material, would require material interactions to be taken into account. This was achieved by Smith and Auld [53], who modelled an equivalent set of material parameters for piezocomposite materials as a function of piezoceramic volume fraction.

Longitudinal or bulk wave propagation in a solid or fluid is characterised by its compressibility and density [54]. As a pressure is exerted upon the material, its compressibility will return the material to its original state and its density will resist this compression. These properties enable ultrasonic waves to be transmitted through such materials [54]. Assuming the material is lossless and homogeneous the ultrasonic wave propagation is described by the linear second order partial differential equation *ie.* the wave equation

$$\nabla^2 p(\mathbf{r}, t) - \frac{1}{c^2} \frac{\delta^2 p(\mathbf{r}, t)}{\delta t^2} = 0, \tag{2.8}$$

where $p(\mathbf{r}, t)$ is the pressure field deriving from a longitudinal pressure wave at

the measurement position, $\mathbf{r} = (x, y, z)$, c is the speed of sound in the medium and t is time [54].

2.3.2.2 Finite Element Analysis

As the number of variables influencing the ultrasonic wave propagation increases, the ability to analytically solve these ultrasonic systems becomes increasingly difficult. This is where numerical modelling becomes important, for example, Finite Element (FE) analysis that provides a quick method for approximating the solution to the piezoelectric equations.

One example of an FE software program is PZFlex (OnScale, USA) [55]. PZFlex uses an explicit transient solver to find an approximate solution to Equation (2.8). In PZFlex the mesh size is set by the slowest velocity or the highest frequency of interest to capture all ultrasonic effects [56]. When determining the mesh size, the minimum number of elements required to adequately describe a single wavelength is 15 [56]. As the number of elements per wavelength increases beyond this value, the FE model better approximates the solution to the piezoelectric equations but this is at the cost of additional computation time. Given that the wavelength depends on the frequency of the ultrasonic pulse

$$\lambda = \frac{\nu}{f}, \tag{2.9}$$

where f is the frequency (Hz); the greater the value of the frequency the smaller the size of the wavelength. Therefore, increasing the model frequency requires more elements to adequately capture a given propagation distance, which in turn

increases the computation time required to run the model.

Uncertainty in the solution to the piezoelectric equations derives from the material properties, for example, the density or stiffness supplied to the FE model [56]. However, providing the material properties are accurate, the FE model will be representative of the ultrasonic system.

An additional challenge associated with FE analysis is numerical dispersion. Discrete time steps are used to approximate the solution to the piezoelectric equations and as the size of this time step approaches zero the model becomes closer to continuous in nature. As a result, the FE solution is only an approximation of the exact solution, which would require a continuous time domain function to be achieved. The minute error associated with this approximation is amplified when the number of time steps is increased, known as numerical dispersion. In terms of an ultrasonic wave propagation system, these truncating errors begin to occur approximately 250 wavelengths from the ultrasonic source [56].

2.3.3 Transducer Design

There are two key functionalities to consider when designing an ultrasonic transducer, namely the transmitted signal bandwidth and its reception sensitivity. The signal bandwidth corresponds to the range of frequencies transmitted from the device, increasing its resolving power [24]. The transducer sensitivity is influenced by the efficiency of the signal generation and reception [24]. Both can be controlled by the design of the active element, matching layer and backing layer, illustrated in Figure 2.4.

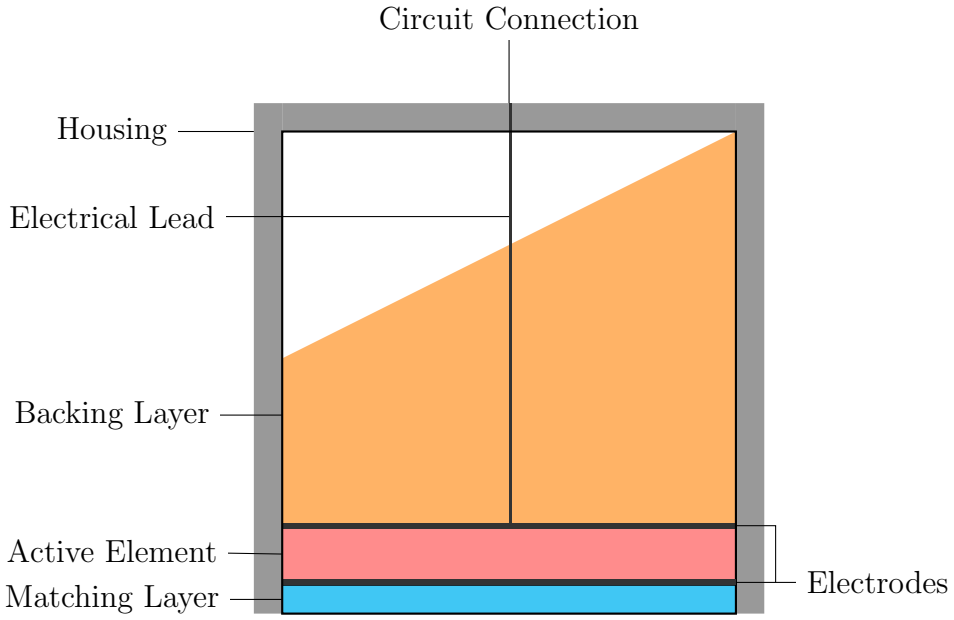

Figure 2.4: *Main design components of an ultrasonic transducer [24].*

The active element contains the piezoelectric ceramic that undergoes the piezoelectric effect when exposed to an electrical or mechanical signal. Most transducers designed for medical and sonar applications require the sound to be propagated into a water load. However, the acoustic impedance of typical piezoelectric ceramics, such as PZT-5H ($Z = 34$ MRayl), is much higher than that of water ($Z = 1.5$ MRayl). This creates an acoustic boundary between the active element and the load material. To reduce the acoustic impedance of the active element, it is designed as a composite using a passive polymer material. Typically, this is arranged as pillars aligned parallel to the longitudinal axis of the active element, known as 1-3 connectivity [53]. This has the additional impact of reducing lateral wave modes that generate interference across the device.

The resonance frequency of the active element corresponds to its thickness, where it is typically designed as a half-wavelength resonator [24]. For example, if

the centre frequency of the device is designed to operate at 5 MHz, the thickness of the active element would be

$$\frac{\nu}{2f} = 0.46 \text{ mm}, \tag{2.10}$$

where ν corresponds to the longitudinal velocity of a 1-3 connectivity piezocomposite containing PZT-5H and hard setting epoxy for example, $\nu = 4600$ ms^{-1} [24].

The backing or damping layer is designed to be highly attenuating. As the active element transmits ultrasound, it transmits energy from its front and rear faces. To prevent this energy being trapped within the active element, the acoustic impedance of the backing layer must be well matched to the active element. The backing layer is designed to prevent ultrasound energy returning to the active element, where it would be detected as a signal corresponding to the load. For this purpose, it is often designed with a sloped edge to increase the path length of the ultrasound as it travels through the attenuating backing layer [24].

On the other hand, the matching layer is designed to facilitate the propagation of ultrasound energy from the active element to the load. Under ideal conditions, the acoustic impedance of the matching layer, Z_m, is set to the geometric mean of the active element and the load medium.

$$Z_m = \sqrt{Z_a Z_l}, \tag{2.11}$$

where Z_a and Z_l are the acoustic impedances of the active element and load material respectively. Also, if the thickness of this matching layer is set to exactly

one quarter of its ultrasonic wavelength at the designed centre frequency, then perfect transmission, $T_p = 1$, is theoretically possible [24].

2.3.4 Phased Array Design

A phased array transducer is a single device containing a number of individually addressable elements, each capable of transmitting and receiving ultrasound [8]. Due to the precise positioning of these elements within the transducer, highly accurate imaging is possible. The simplest array configuration is a linear array, where the main design components are illustrated in Figure 2.5. By applying time delays to the excitation of individual elements, mechanical beam steering and focussing is possible in the lateral dimension. By extending the array to a two-dimensional configuration it is possible to generate volumetric images, however, this greatly increases the complexity of transducer manufacture [8].

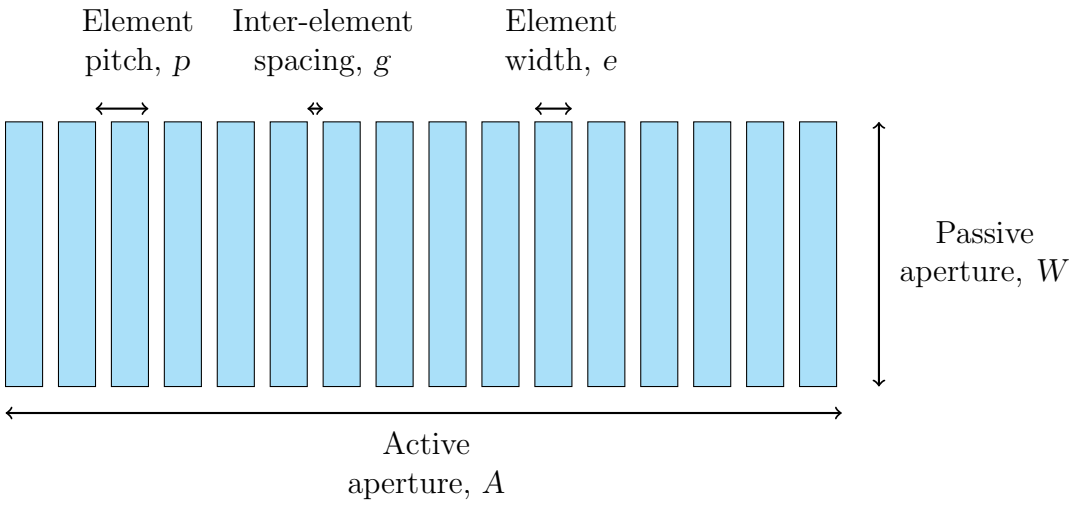

Figure 2.5: *Design components of a $K = 16$ element linear array [8].*

The element width is typically designed as half a wavelength, relative to the

acoustic velocity of the load and the designed centre frequency of the transducer [57]. This creates a wide transmitting beam, increasing the angular sensitivity of the array [24]. Note, the total spatial information acquired by the array is dependent on the number of elements in the active aperture, K, and not the element width [24].

In the interest of reducing the transducer size relative to the element width, the inter-element spacing is minimised whenever practically possible. In a linear array the individual elements are modelled as line sources in order to simplify the beam directivity interpretation [58], which is achieved by having a passive aperture much greater in size relative to the element width.

2.3.5 Application of Phased Arrays

When ultrasonic energy interacts with the active element in the transducer, the direct piezoelectric effect converts this mechanical energy into electrical energy. The analogue voltage response is converted to a discrete digital signal using an analogue-to-digital converter (ADC), by sampling the continuous signal at a set sampling frequency, F_s (Hz). The amplitude of the resulting digital signal is then compressed to an unsigned 16-bit integer. This individual time-voltage response associated with a specific transmit and receive element index is known as an A-Scan.

An example of an A-Scan signal is shown in Figure 2.6. The time axis begins at $t_0 = 2$ μs, which includes the time between the array transmitting the ultrasonic signal and switching to receive mode and an additional delay to remove

interference from the high amplitude transmitted pulse. This high amplitude *bang* would offset the amplitude of the weaker received signal. Figure 2.6 shows the time domain response, whereby there is a delay before the recorded signal begins at 2 μs, following this there is a time delay before the pulse-echo response is received around 14 μs, which relates to the signal of interest here. The smaller peak around 16 μs could relate to a transducer effect *i.e.* ultrasound trapped and reverberating within the transducer device. In the medical community time-gain compensation (TGC) is often applied to A-Scan signals because the load medium, typically tissue or water, is highly attenuating. However, for the purpose of this work, TGC has not been applied to the A-Scan signals because the image depth was small.

When the array is used to receive A-Scan signals from multiple element locations, the ultrasonic data is output in the form of full raw data (FRD). This is a single data set with rows relating to the A-Scan index of the transmitting and receiving elements and columns relating to the time sample number. There are several methods to deploy the array to acquire an FRD data set, for example, linear stepping of a sub-aperture of elements or full matrix capture (FMC) [10].

In linear stepped acquisition mode, delay laws are applied to a sub-aperture, for example 16 out of 128 elements, to focus the ultrasonic beam using element indices 1 to 16. These elements are used to record 16 individual A-Scans, then the sub-aperture is stepped to transmit and receive on element indices 2 to 17. This is repeated for the full aperture and the A-Scans are collated into a single FRD sample. This FRD can then be restructured into a brightness mode or B-Scan

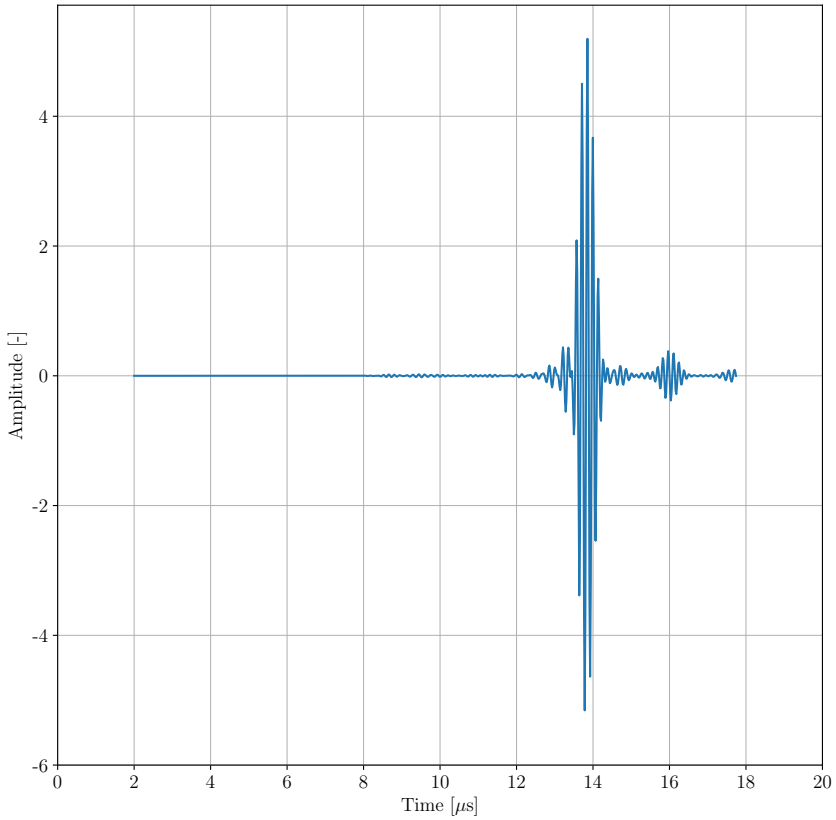

Figure 2.6: *Example of A-Scan signal of a back wall reflection.*

image using the row indices in the FRD to translate the position of the elements into the image scene. B-Scan images are not well resolved as the number of pixels in the z-axis, corresponding to the image depth, is dependent on the number of time samples, N, in the A-Scan and cannot be enhanced further.

In recent years FMC has become more common, especially within the NDE community. This is the acquisition mode whereby the sub-aperture corresponds to one element and all available receiving elements are used to record time domain

signals. The transmitting element is then sequentially moved across all available transmitting elements in the full aperture. This results in an FRD data set containing the maximum quantity of information about the image scene, however, the signals are weaker than larger aperture acquisition modes because only one element is transmitting during a transmit event. So, if $K = 128$ elements, FMC would result in an FRD containing 128^2 individual A-Scans. Using the FMC acquisition mode, highly focused ultrasonic images can be generated using the total focusing method (TFM) algorithm [10]. The TFM is considered to be the gold standard imaging methodology in the NDE community [59] because it focusses the ultrasonic data set at every pixel in the image scene.

For an FMC data set acquired using $K = 128$ elements the FRD has dimensions of $M = K^2$ A-Scan time domain signals, $y_m(t)$, by N time samples. The TFM algorithm first requires the image scene to be set in terms of the axes dimensions and the grid size relating to the number of pixels in each dimension. This image scene has i pixels in the y or lateral dimension and j pixels in the z or axial dimension. The TFM algorithm uses a delay and sum approach to determine the intensity value at a given pixel, I_{ij} from

$$I_{ij} = \sum_{m=1}^{M} y_m(t) \tag{2.12}$$

$$= \sum_{m=1}^{M} y_m(\tau_{ij} - t_0), \tag{2.13}$$

where τ_{ij} is the time-of-flight (TOF) between the transmitting element (T_x) and the receiving element (R_x) via the pixel of interest [10]. So, for each pixel in the image scene there are M TOF calculations required.

The TFM algorithm assumes that all reflectors are point-like in nature and maps this assumption onto the image pixels. This results in the phenomenon whereby signals reflected from two different points in space can incorrectly combine and contribute to the value of a pixel where no real reflector exists. This is known as signal aliasing, demonstrated in Figure 2.7 where the path length between one pair of elements and two different spatial positions is the same. In this scenario, the signal amplitude from the position of the real reflector will contribute to the value of a pixel where no real reflector exists. In Figure 2.7 the TOF from the transmitting element, T_x, to the receiving element R_x, via the pixel position I shown in red is identical to that of the pixel position II shown in grey. However, there is only a reflector present at pixel position I. This means in the final TFM image, the value of pixel position II will have amplitude contributions corresponding to pixel position I. It is due to this signal aliasing that planar surfaces, which only specularly reflect ultrasound, are mapped as poorly defined clouds instead of well-defined lines.

Note, all images and schematics displayed in this Thesis have been orientated whereby the z-axis represents the depth into the image from left to right and the y-axis represents the distance from the centre of the array.

Given that the TFM imaging algorithm is currently at the forefront of NDE research, there are many pre and post processing tools available that are directly relevant to the TFM algorithm. This means typical technical challenges likely to be encountered during the research have often been previously considered by the NDE community. For example, a key challenge associated with deployment of the TFM in industry has been the computation time. The wavenumber al-

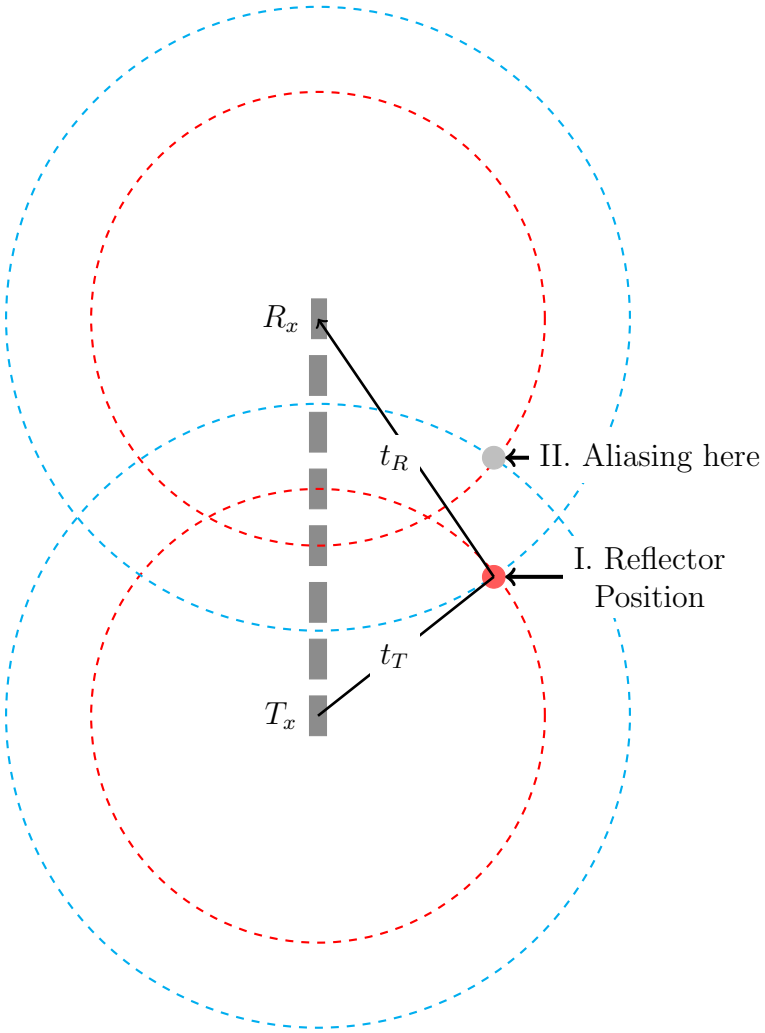

Figure 2.7: *Schematic showing the localisation of signal aliasing using the TFM algorithm.*

gorithm is considered the frequency domain partner algorithm to the TFM [60]. By inspecting the FMC data set in the frequency domain the computation time is accelerated by several orders of magnitude, however, it was observed that this compromised the flexibility of the algorithm to specific array and image geometries [60]. An alternative approach for accelerating the image construction time in the time domain is using GPU technology to run the image construction process

of each pixel value in parallel [61].

To enhance the image construction time for the work conducted in this Thesis, a CUE proprietary TFM script was deployed that uses GPU technology (GeForce GTX 750 Ti, NVIDIA, USA) to enable faster image construction [62]. An important feature of this algorithm is its ability to incorporate refraction at an acoustic boundary by specifying the acoustic velocity in the two media.

2.4 Context of the Proposed Research

2.4.1 Current Methods for Bubble Sizing

Typical methodologies to measure BSD involve taking physical measurements of the system, for example, using pressure gauges to monitor pressure differentials throughout the process, which can be used to monitor flow regime behaviour [63]. Another pressure monitoring method is dynamic gas disengagement whereby the supply of the gaseous phase is prevented from flowing through the pipe and the resulting pressure drop is used to indicate the gas phase hold-up [64]. The latter methodology requires disturbing the process so is akin to an intrusive measurement.

A highly intrusive technique to monitor BSD has been developed using a wire mesh arranged as a grid or array within the cross-section of a pipe [65]. The wires measure the local electrical conductivity of the two-phase flow at two discrete and perpendicular positions within the pipe. This led to measurement of the instantaneous gas cross-section, where the smaller the mesh pitch the higher

accuracy of local bubble sizing [66]. However, this was at the cost of increased disturbance to the flow. Using this technique, the bubble sizing accuracy was within 20% for bubbles greater than 4 mm in diameter and within 10% for bubbles greater than 8 mm in diameter [67]. However, given the intrusive nature of the methodology, disturbance to the flow was such that the measured BSD was no longer valid after the measurement position [68].

Each of the bubble sizing techniques described above have been deployed in-situ, however modification of the vessel or intrusive measurement has been required that perturb the flow. In addition, these techniques require the construction of multivariate calibration models to predict the BSD. This is a time consuming process and must be repeated for individual processes. These techniques only provide a single point or chord measurement of the process and therefore do not provide spatial information. It is for these reasons that imaging techniques have gained prominence in the field of bubble sizing and shape detection [69] and this will be discussed in further detail in Section 2.6. Imaging techniques can be applied non-invasively, typical using an optically transparent window, and do not require the construction of a multivariate calibration model to extract information about the process. In addition, image processing techniques are well established in the literature thus enabling quantitative information about the process to be readily obtained from a wide range of imaging technologies.

2.4.2 Current Methods for Bubble Velocimetry

Determination of flow velocity of industrial processes by ultrasound has been largely dominated by two ultrasonic techniques. These are ultrasound Doppler

flowmeters [70, 71] and echo particle image velocimetry (PIV) [72]. Both techniques were initially developed for measurement of blood flow velocity for medical applications but have more recently been applied to industrial process analysis.

Ultrasound Doppler velocimetry measures the frequency shift of a transmitted pulse due to the Doppler effect. The technique can be deployed using pulse-echo [71] or through-transmission modes [73]. When applied to bubble flows it has shown to be effective at extracting the flow velocity up to 732 ± 60 mms^{-1} [71] and has more recently been demonstrated at flow velocities up to 3200 mms^{-1} [74]. Where this technique breaks down is measurement at slower velocities, approximately less than 150 mms^{-1} because the frequency shift becomes too small to be accurately detected [75].

Echo PIV uses cross-correlation between individual B-Scan images to determine the vector field of ultrasound contrast agents, for example, microbubbles in water [76]. Typical frequency ranges reported are between 5 MHz [77] to 10 MHz [78], where higher frequencies are used to image smaller particles. Echo PIV for medical applications uses contrast agents on a length scale of 12 μm [79], which is much smaller than the ultrasonic wavelength in water. Therefore, a high concentration of this contrast agent is used to create a dense distribution of reflective particles. Therefore, this technique cannot be used to image individual particle or bubbles.

2.5 Calibration of Ultrasonic Hardware

2.5.1 Background

To quantify the BSD and velocity of a dynamic process requires the acquisition of multiple image frames. The temporal resolution between image frames depends on the bubble movement, discussed in Section 6.2.3, and the consistency of ultrasonic measurements across individual data sets. In order to understand the experimental variation within and between individual ultrasonic data sets a calibration methodology has been proposed in Chapter 3. In light of this, current methodologies of ultrasonic hardware calibration in the context of medical and NDE applications are discussed in this Section.

2.5.2 Established Calibration Methodologies

Calibration of ultrasonic hardware has typically focused on beam integrity rather than array integrity [80]. Given that beam steering and focussing are the most common methods of phased array deployment in both medical and NDE applications, this is understandable. However, this means there are few examples in the literature pertaining to array calibration using FMC. Indeed, the lack of calibration methods relevant to FMC has even been identified as a hindrance to its uptake by industry [81]. The nature of FMC means that no beamforming takes place during data acquisition, so inconsistencies between measured signals can be associated with individual element locations. As FMC becomes more widely used in industry, array calibration methods are likely to shift towards the investigation

of array integrity and its impact on image quality.

In NDE, element performance checking is synonymous to array calibration. Here, the performance of an array is regarded as the efficiency of the array to steer and focus the ultrasonic beam [80]. Therefore, in this context, an under-performing device would exhibit beam artefacts such as increased frequency domain side lobe activity, increased main beam width or reduction in the main beam energy level. These beam artefacts lead to spurious signals being detected, increasing the uncertainty in the localisation of reflectors.

The impact of inter-element amplitude and phase variations on beam directivity has been discussed by Lancée et al [82, 83]. It was their aim to develop a quantitative criterion whereby array performance could be declared adequate or insufficient for medical applications. To simulate the beam directivity, they created a 32 element, 3.1 MHz FE array model based on Mason's equivalent circuit model [48]. In doing so, they have removed variations due to PAC circuitry and assumed errors only derive from the individual element performance. In terms of beamforming ability, it was concluded that amplitude variations had minimal impact on the beam integrity when they were randomly distributed. However, phase variations were determined to be more significant and so a quantitative criterion, corresponding to the variance of element phase, was established where for a given angle and focal depth, this variance can be minimised.

In terms of beam integrity, a criterion for the tolerable number of inactive elements in an array was investigated by Nageswaran [84]. The impact on beam directivity, from both randomly distributed and contiguous blocks of inactive elements, was discussed. The threshold between the frequency domian side lobe and

main beam amplitudes was selected to be -20 dB because this indicates a 100% difference in signal strength. The work concluded that the threshold would be reached when 10% of elements became inactive and were distributed randomly across the aperture. However, for the same number of elements arranged as a contiguous block, the threshold would not be reached because it would increase the width of the main beam instead of increasing the side lobe activity in the frequency domain. It should be noted that in practice it is far more likely for inactive elements to be randomly distributed within the array. Indeed, if the array were to be deployed using FMC and a contiguous group of inactive elements did exist (preferably at the edge of the total available aperture), the operator could still perform FMC using a sub-aperture of active elements. In addition, this highlights the impact of array geometry on the main beam width due to a contiguous block of inactive elements. The presence of inactive elements with a larger element pitch led to greater amplification of the main beam width, as expected. Therefore, higher frequency arrays, with smaller pitch dimensions should be less adversely affected by the presence of a contiguous block of inactive elements.

2.5.3 Novel Calibration Methodologies

The first example in the literature linking the application of FMC to phased array performance was presented by Zhang et al [85]. They constructed a 64 element FE model coupled to a defect-free NDE calibration block and extracted information about the array from the back-wall reflection. Similar to Lancée et al [82, 83] and Nageswaran [84] they established a single measurement of the overall

array sensitivity rather than investigating individual element performance. This sensitivity statistic was then related to the TFM image performance. To estimate the peak time and amplitude, they windowed the time domain reflection, transformed this signal into the Fourier domain then performed a back-propagation methodology before applying the inverse Fourier transform to obtain a time domain peak. From this peak they estimated the peak time and sensitivity from the position of the peak maximum. One of the key findings of their work was the suggestion that, despite the robustness of the TFM algorithm for inter-element variation, peak time error was considered the most significant factor leading to the distortion of TFM images.

In the papers mentioned above, the elements were switched off to simulate them being inactive. In practice this does not necessarily model the true cause of an element to appear inactive. For example, due to a limited number of channels available in a PAC, a multiplexor is often required to record an FMC data set. This could mean that the channel on the PAC used to transmit could be different to that used to receive a signal for a given array element. In the event that one PAC channel is compromised, an element might be connected to an active channel in transmit mode but connected to an inactive channel in receive mode. Given the nature of FMC, reflected signals would be received at neighbouring elements connected to active channels, so upon manual inspection of the data set this anomaly could go unnoticed. Therefore, modelling an inactive element by switching off both its transmit and receive functionalities risks oversimplifying the ultrasonic system and potential problems resulting from the PAC.

A comprehensive study of inter-element performance variation was performed

by Duxbury et al [80]. Previous work by Lancée et al [82, 83] and Nageswaran [84] used a single quantifier to model the overall array performance, whereas here, individual element performance was considered. An FE model was built to investigate the individual element sensitivity and the impact this had on the beam directivity. This work investigated the impact of array integrity rather than beam integrity on the beamforming performance. As a result, this work can be more readily applied to FMC than previous calibration methods because it characterises the individual element performance. In close agreement to Nageswaran [84], they suggested an acceptance criterion of less than 10% of inactive elements before deterioration in the beam artefacts was observed. However, although they were successful in decoupling the array integrity from the beam integrity, they have assumed that individual element variation contributes equally in both transmit and receive modes. This means that variation due to the PAC circuitry has not been included in their FE model.

Subsequently, a calibration methodology designed specifically for FMC applications has been developed by Mosey et al [81]. Similar to standard NDE calibration methods, a solid calibration sample with side-drilled holes (SDH) of known diameter and position is required. The array is manually scanned over the surface of the calibration sample while acquiring multiple FMC data sets. These are used to generate multiple TFM images of the NDE sample that are then transformed into a 'persistence image'. For a given image scene, this is generated by adding the maximum pixel values from the previous TFM image to the next in the sequence of TFM images and then interpolating pixel amplitudes between the pixels corresponding to the SDHs. Therefore, this method assumes

no aliasing has occurred between pixel values and that the persistence image is representative of the TFM image scene. Then the amplitude of a test TFM image matrix is normalised relative to this interpolated persistence image, resulting in a calibrated TFM image. However, given that the operator must manually scan the array over the surface of a solid calibration block, the methodology is prone to experimental error. In addition, the flexibility of the methodology is limited to specific TFM image scenes and therefore must be repeated depending on the image scene. Moreover, the methodology does not calibrate the hardware integrity but rather the integrity of individual TFM images for NDE applications.

2.5.4 Element Acceptance Criteria

Performance criteria for individual array elements are typically arbitrarily defined thresholds relative to the performance of the array at the time of measurement. For example, according to the International Organisation for Standardisation the centre frequency of *'each element shall be within* ± 10 % *of the average centre frequency'* [86]. Alternatively, Mosey et al [81] stated that the amplitude of each element response should be within -3 dB relative to the average element amplitude. These methods do not account for a global deterioration of the array over time and make assertions about the current hardware performance without referencing historical performance values. In addition, these acceptance criteria are only valid for ultrasonic transducers manufactured in batches greater than 10, where a degree of consistency across the product is expected [86].

An acceptance criterion for the minimum number of operational elements in an array has not been previously established for FMC applications. This is because

investigations into the impact of inactive elements, for example by Zhang et al [85], have used a single quantifier for the overall array performance rather than discretising the elements.

2.6 Imaging in Process Analysis

2.6.1 Established Imaging Methods in Process Analysis

Imaging of dynamic processes has recently become an established measurement tool for industrial process analysis. This trend has correlated with the increased computer processing power available to researchers that is required for real-time image processing [19]. Images provide spatial information about a process that cannot be acquired from a point measurement, therefore images are often exploited for the measurement of crystal morphology [87], PSD [88] and bubble hydrodynamics [89]. The broad range of potential process applications complements the wide range of imaging techniques available. For example, hyperspectral imaging can be used to capture the chemistry of a substance within an image [90]. Each pixel pertains to an individual frequency spectrum, therefore these images are spatially and chemically resolved. Recent advances in this technology have seen the acquisition time increase from one hour per image frame, when using a raster scan [91], to over one hundred image frames per second using a push-broom technique [92].

Imaging of industrial processes has been typically performed using optical waves in the visible frequency range. For example, bubble sizing has been per-

formed using a digital camera coupled with a microscope [93, 94]. The reason for using the visible frequency range compared to x-ray imaging, for example, is the overall hardware cost of a digital camera is much less than x-ray instrumentation, not to mention the increased safety risk associated with using x-rays in a process environment.

Non-invasive image acquisition using visible light requires the vessel material to be optically transparent. This has been typically achieved using Perspex [7, 19, 89] or glass [95]. The accuracy of images acquired via Perspex or glass is sensitive to the optical path length between the process and the camera. For example, fouling on the inside vessel wall led to one team incorporating a lid into their process apparatus to provide cleaning access for the inside vessel wall [7]. This dependency on a clear optical path limits the flexibility of the overall measurement system because the camera can only be positioned where the optical window has been fitted to the vessel and there is a risk of measurement uncertainty due to fouling.

Extractive sampling has been proposed as a methodology to capture bubbles for imaging in order to reduce the impact of bubble dynamics on image accuracy. For example, a 10 mm diameter sample line, positioned 45° relative to the bulk flow direction has been deployed for a microbubble flow system [95]. The diameter of the inlet was much larger than the mean bubble diameter, minimising the impact of bubble coalescence at the sample line entry point. However, when a 1 mm diameter capillary was used for bubble capture it was found that the capillary line perturbed the bubbles as they entered the sample line [7]. Here, for example, a 4.5 mm volume-equivalent diameter bubble was observed dividing into

two parts such that the equivalent diameter of the bubble from the image analysis was 3.3 mm. This corresponded to the upper limit of the measurement system and made the system biased towards smaller bubbles leading to underestimation of the true BSD and a reduction of the representativeness of the imaging system. This demonstrates why imaging should be performed in-situ on the bulk process rather than via a sampling line.

It is important to understand that determination of accurate quantitative information about the process from images requires the image to be representative of the process. The information gathered about the process is only as accurate as the information contained within the image [17]. For example, fluorescence dye has been dissolved in the continuous phase of a bubble flow to enhance the image contrast [96]. A bandpass filter was then positioned in front of the camera lens such that the spatial resolution of the bubble objects was enhanced. This shows how hardware optimisation, which includes the sensor, vessel material and image target is a key aspect of the overall imaging system for industrial process analysis.

2.6.2 Image Processing Techniques

Once an image has been captured of an industrial process and it is deemed representative of the process, image processing is used to extract quantitative information from an image. Examples of image processing in industrial process analysis include the quantification of droplet size distribution, velocity and acceleration [20] and BSD [7]. It has been argued that manual image processing can provide accurate sizing of bubbles [97], albeit at the cost of increased measure-

ment time [98]. However, to deploy this for real-time process monitoring requires immediate processing of these images. This is a particular advantage of digital image processing as it can be easily automated on a PC enabling real-time process measurement.

To extract spatial information from these process images, it is necessary to convert the dimensions of identified objects from units of pixels to millimetres. For optical images acquired with a digital camera, the image construction process is intrinsic to the camera device. This means the end-user does not define the image construction parameters such as the pixel dimension and this must be determined experimentally [99]. For example, a calibration grid can be positioned in the test cell and images acquired under identical experimental conditions are used to determine the pixel dimension [19]. This has been specifically highlighted as a drawback to using optical images for industrial process analysis [20]. On the contrary, ultrasonic image construction is not limited in this sense as the pixel dimension can be arbitrarily selected prior to image construction. For example, it is possible to control the pixel dimension in both the y and z directions of ultrasonic images generated using the TFM [10]. Therefore, square pixels can be used, greatly reducing experimental uncertainty associated with the conversion of object sizes from pixels to millimetres.

A key technical challenge associated with optical images is that objects of interest can be out-of-focus. This reduces the accuracy of object edge detection that can lead to inaccurate bubble sizing [98]. One attempt to overcome this issue was to categorise different regions of optical images of bubbles depending on whether they were in or out-of-focus and to apply different image processing

methods to these two categories [19]. However, in this example, this added to the computation time required to process the images because the algorithm cannot treat all regions of the image the same. This presents another advantage of using ultrasonic image construction as images generated using the TFM are, by definition, focussed at every pixel.

A common problem associated with both optical and ultrasonic images is that larger objects have a greater pixel density, so image processing methods to quantify bubbles become biased towards larger objects [98]. This manifests itself in a different way for optical and ultrasonic images depending on the image construction approach deployed. For ultrasonic images, only the front face of a bubble reflector is imaged because ultrasound cannot be transmitted through the bubble object. This means smaller objects in the ultrasonic shadow of larger objects are masked. However, in optical images, where the incident beam can penetrate through bubble objects, overlapping of reflectors in the same plane can lead to two objects being quantified as a single larger object. Therefore, it is important that image processing takes this source of bias into account by incorporating this information into the overall measurement process.

Image illumination can be considered as the intensity of the incident beam at each pixel in the image. The greater the illumination, the greater the sensitivity of the overall image scene, therefore increasing the validity of comparisons between different regions in the same image. For example, in ultrasonic images the incident beam attenuates as it travels through the load medium. Regions further from the transducer experience a lower illumination than regions close to the transducer. This is particularly true when measuring systems with high bubble densities,

where bubbles near the transducer shadow objects deeper into the load medium. One method to enhance the illumination of ultrasonic images is to apply TGC, however, this does not account for ultrasonic scattering effects [100]. For optical images where a single light source is used, adequate illumination is achieved by passing the incident beam through a translucent medium to diffuse the flash through the image scene [19, 98]. The impact of variable illumination throughout the image scene is that image processing methods, for example thresholding via Otsu's method [101], often rely on the assumption that the image is equally illuminated at every position.

Image thresholding is a well-established image processing technique used to create simplified binary depictions of the image scene. This can be achieved using a global threshold value, where the same threshold value is applied across the entire image or an adaptive or local threshold value, which is different depending on local variations within the image. Although local thresholding can achieve greater binary resolution it requires a much longer computational time than global thresholding, limiting its application to real-time process analysis [102].

Background subtraction is another well-established image processing technique, which is used to separate background noise from signals of interest. This assumes that objects of interest are only located within the foreground, relative to a pre-determined background response. For example, background-foreground separation has been used for microbubble imaging [103]. The background was identified using a training set of image frames, the number of which was selected based on minimisation of the computation time. This background signal was then subtracted from the remaining image frames to determine the microbubble flow

velocity between frames. However, it has been argued that background subtraction, although able to compensate for temporal non-uniformity, is not stable when the illumination intensity varies spatially and temporally [19]. This means that using background subtraction on ultrasonic or optic images relating to bubbly flows could result in the loss of information relating to the bubbles [19].

One key advantage that ultrasonic imaging has over optical-based techniques is that it can be used to image into optically opaque structures [8]. This means the process medium does not need to be optically transparent, enabling quantification of BSD in cloudy bubble flows or slurries. In addition, ultrasound imaging presents greater flexibility to the end-user as there is a variety of image construction algorithms available [10]. Therefore, ultrasonic imaging has become a strong candidate for the next generation of process imaging techniques.

2.6.3 Phased Arrays for Process Imaging

Ultrasonic phased arrays have been widely used to image dynamic systems in the medical community such as cardiovascular movement in adults [104] and foetuses [105]. However, there are few examples in the literature relating to their deployment for imaging of industrial processes. The potential of ultrasonic phased array imaging for real-time industrial process analysis was first identified in 1998 using B-Scan images to indicate the state of mixing in a particle-fluid two-phase system [106]. A 64 element, 3 MHz linear phased array was positioned intrusively in the process, where the particle reflectors were approximately 5 mm in diameter facilitating strong ultrasonic reflections back to the transducer. It was not clear why this research was not pursued further, however, a key technical challenge at

the time was the data acquisition rate that was limited by the electronics of the PACs available.

Typically phased arrays have been used to steer and focus the ultrasonic beam towards the target load in medical and NDE applications. The same is true for their deployment to industrial process analysis. For example, a two-dimensional, 16 element flexural phased array has been designed to steer an ultrasonic beam through a process stream towards a single element receiver [107]. Both the transmitter array and single element receiver were positioned intrusively within the process at opposite sides of a pipe. By steering the ultrasonic path through the dynamic process the velocity measurement of the process was made more accurate and the measurement flexibility to different processes was enhanced. However, as this was performed intrusively it required modification of the pipe material.

Velocimetry measurement of dynamic systems has been achieved using ultrasonic phased arrays deployed in a variety of different ways. For example, B-Scan imaging of microbubble contrast agents has been used in the medical domain to determine the blood flow velocity in blood vessels [108]. In terms of industrial process analysis, bubble flow velocity has been estimated using A-Scans acquired using a 128 element, 8 MHz phased array transducer [109]. A-Scans were used because the active aperture was limited to three elements due to channel restrictions on the PAC. Therefore, imaging of the flow was not possible in this example and the temporal resolution was limited by the acquisition time (> 6 ms) required to switch between channels on the PAC.

An ultrasonic array has also been used to map the velocity flow profile of high temperature melts [110]. To prevent damage to the piezoelectric elements

a waveguide was deployed between the array and the process and a virtual array was conceptualised using the time-reversal technique. The increased path length between the ultrasonic transducer and the process decreased the data acquisition rate available. Therefore, the images were not well focussed, reducing the quality of the images and the quantity of process information contained within the images.

A Multiple-Input Multiple-Output array of 300 kHz single element transducers has been shown to provide accurate monitoring of liquid level detection [111]. Sixteen transducers were arranged as a linear array of four transmitters either side of eight receiver elements. By using single element transducers the sensitivity of the ultrasonic system was increased, however the array was not used to generate images of the liquid level. It was explicitly stated in this paper that the next stage of the research was to deploy the experimental apparatus with a 3.5 MHz linear phased array for imaging of the dynamic liquid level, however, at the time of writing, this has not been published.

Ultrasonic phased arrays have been used to generate images of slow-moving but dynamic bubbles during the resin transfer moulding process [112, 113, 114]. A 128 element, 10 MHz linear phased array was mounted to a Perspex vessel containing viscous silicone oil. The Perspex vessel was well-matched to the acoustic impedance of the silicone oil providing a high degree of ultrasonic transmission into the oil layer. The ultrasonic beam was focussed onto the back of the oil layer using a 32 element sub-aperture. The bubbles were individually passed through the silicone oil at velocities ranging 5 - 15 mms^{-1} and B-Scan images were generated to show the cross-section of the bubble movement. The image frame rate

was limited to 0.1 Hz, which resulted in blurred images depicting the full bubble movement path.

2.7 Non-Invasive Process Measurement

2.7.1 Background

Non-invasive process analysis involves the transmission of process information through the process vessel wall. For ultrasonic measurement through steel, the acoustic boundary at the steel-fluid interface introduces noise artefacts into the measured data. At this interface most energy is reflected back towards the transducer, making signals reflected from within the process relatively weak. The energy that is reflected at this acoustic boundary, as illustrated in Figure 2.3 on page 26, then becomes trapped within the steel layer, creating reverberations that further complicate the ultrasonic system. These reverberations cannot be mechanically removed from the ultrasonic system and so this creates the key technical challenge to be overcome.

2.7.2 Current Techniques

Ultrasound can be used to measure into optically opaque structures. Therefore, ultrasound presents an advantage over optical-based techniques used in industrial process analysis such as Raman spectroscopy because it enables the transfer of information through optically opaque materials, for example, steel or aluminium. In theory, ultrasound-based techniques do not require modification of the vessel

material to create a *sampling window* into the process and can be deployed as a *clamp-on* style measurement system. An example of a such a product is the Flow Pulse ® [115]. This has been developed to exploit the Doppler effect for particle sizing through steel vessel walls. The product cannot be used for process imaging but is an example of a higher Technology Readiness Level archetype for the work discussed in this Thesis.

An example of a steel-coupled ultrasonic measurement system has been proposed by Bamberger and Greenwood [116]. The attenuation of the reverberation pattern in a steel vessel wall was quantified to estimate the transmission coefficient at the steel-fluid interface. This was used to determine the fluid density inside the pipe. To do so required the construction of a linear regression model, which is a time consuming process, to calibrate each process to be monitored. Since the fluid density was inferred from measurements of the reverberation pattern within the steel vessel, the methodology does not directly measure the process. However, this demonstrates the quantity of information about the process that is contained within the reverberation pattern alone.

Non-invasive acoustic monitoring of dynamic processes has been achieved through glass by Nordon et al [40] and Tramontana et al [117]. Single element transducers were mounted to the outside wall of a glass reactor vessel and AE deriving from the process itself was used to characterise the processes. Although the AE intensity is low the ultrasound only needs to cross the acoustic boundary once, increasing the amplitude of ultrasonic signals relative to pulse-echo or through-transmission measurement. In addition, the signal of interest relates to the integration of various AE sources over time, therefore reverberations do not

interfere with the TOF measurement.

To acquire direct measurements beyond a reverberating layer, there have been several solutions proposed in the literature. The typical approach has been to reduce or eliminate the acoustic boundary generating the reverberation pattern. For example, in the medical domain a similar problem arises when performing procedures on tissue through a bone interface. To overcome the acoustic impedance mismatch between bone and tissue, shear wave mode conversion has been used to steer an ultrasonic beam through an *ex vivo* human skull [118]. Using shear waves instead of longitudinal waves, the acoustic velocity in the skull was reduced. In doing so, this reduced the acoustic impedance of the incident ultrasound relative to the brain tissue and enhanced the transmission of ultrasound across this acoustic boundary. However, the target application of this investigation was not to receive reflections from the brain tissue but to focus the energy beyond the reverberating interface. Therefore, the reverberation pattern within the skull was not completely removed.

In the context of industrial process analysis, signals reflected or deriving from within the load medium need to be received. In light of this, the acoustic impedance mismatch has been typically overcome by modification of the vessel material. Examples have typically used poly(methyl methacrylate) [119], commonly referred to as acrylic, Plexiglas, Rexolite or Perspex. This has a lower density and speed of sound than steel and therefore has an acoustic impedance value that is more closely matched to water relative to steel. The benefit of this is two-fold, it promotes the transmission of ultrasonic energy across the vessel-fluid interface and it reduces the amplitude of the reverberations within the vessel

wall. For example, pulse-echo measurements have been successfully used to estimate the void fraction [120] and phase velocities [121] of gas-liquid two-phase flows. These examples, using Perspex pipe material, demonstrate the capability for ultrasound to be a useful non-invasive measurement tool for industrial process analysis.

An additional problem to be overcome when performing through-steel ultrasonic measurement is signal attenuation within the steel vessel. The degree of attenuation is a function of the vessel wall thickness, therefore it has been recommended to use pre-amplifiers to increase the signal-to-noise ratio (SNR) [40] when measuring through steel. If vessel wall thickness presents a measurement hindrance, a solid waveguide is typically deployed between the process and the transducer [119]. Ultrasonic waveguides are designed to provide a wave propagation path between the process and the sensor that does not distort or attenuate the signal of interest, therefore mitigating interference from reverberations.

Sikorska and Pan have investigated the impact of different waveguide materials on the signal amplitude and frequency that reaches the detector for AE applications [122, 123]. The materials inspected were: carbon steel, mild steel, aluminium, alumina ceramic and Delrin resin. They noted that mild steel led to the lowest degree of attenuation, however, both mild and carbon steel generated frequency artefacts not observed in the input signal [122]. Therefore, signals received via a steel conduit contained spurious artefacts corresponding to the waveguide rather than the region of interest.

A disadvantage of using waveguides is that they reduce the flexibility of the measurement system. The ultrasonic transducer can only be positioned at the

specific point in the process where the waveguide is situated and cannot be used as a *clamp-on* style measurement system. On the other hand, they can be used to mitigate heat-transfer from within the process. This is particularly important in process environments where vessel surfaces can be higher than the Curie Temperature for piezoelectric elements. For example, as mentioned in Section 2.6.3, an ultrasonic waveguide has been conceptualised using a virtual array for imaging of a high temperature melt system [110].

Wada et al investigated the transmission of ultrasound through steel and Perspex for pulse-echo measurement of two-phase flows [124]. Using a single element transducer immersed in water, A-Scans were recorded, through a 5 mm thick carbon steel plate, of a bubble flow in water. The impact of incident beam angle on the intensity of the ultrasonic beam beyond the steel layer was investigated. It was determined that the maximum incident beam amplitude was observed when the transducer front face was 19° from the normal of the steel layer. This was due to shear wave mode conversion at the initial water-steel interface that reduced the acoustic impedance mismatch between the steel and the water, enhancing the amplitude of the received signal.

2.7.3 Novel Methods for Non-Invasive Ultrasonic Measurement

Throughout the literature relating to non-invasive ultrasonic measurement, the idea that the reverberation pattern cannot be mechanically removed from the measurement system has not been challenged. That is true except for one idea

proposed by Shen et al [125] to construct an anisotropic metamaterial positioned between the transducer and the reverberating layer. This enables sound to pass through the reverberating interface unhindered, as if the reverberating layer did not exist. The proposed metamaterial is a composite material designed to have properties such as negative density and compressibility, which would otherwise not be possible but is achieved through the specific structural design of the material.

The feasibility of the structural design has been demonstrated using an FE model to represent the physical composite structure rather than using materials with effective parameters. The FE model was designed as a 50 kHz phased array where the material design was dependent on its ultrasonic wavelength. Therefore, to increase the driving frequency to the MHz range requires the construction of a metamaterial with a unit cell on the micrometre length scale, which is beyond the scope of typical mechanical workshops.

An additional setback to practical implementation of these metamaterials was their dependency on the dimensions of the reverberating layer [125]. The thickness of the bulk metamaterial was dependent on the thickness of the reverberating layer, such that a different metamaterial would need to be designed for different vessel wall thicknesses. Due to surface roughness or corrosion, the vessel thickness in a typical process plant is not well defined. In light of this and given that the metamaterial thickness design is required to be reasonably accurate [125], it was not expected that these materials could provide a solution to the problem addressed in this work at the time of writing.

2.7.4 Non-invasive Ultrasonic Imaging Methods

Non-invasive ultrasonic imaging of industrial process streams has been limited to ultrasonic tomography. This has been demonstrated using an array of up to forty-two individual transducers mounted on the perimeter of a pipe to generate cross-sectional images inside the pipe [126]. Typically the data acquisition rate is low relative to pulse-echo phased array transducers because the ultrasonic path length must cross the entire diameter of the pipe [127]. Indeed, for process analysis of dynamic systems, the limited data acquisition rate inherent to ultrasonic tomography reduces the capacity to use this technique to measure in real-time. To increase the sensitivity of the ultrasonic system, single element transducers are used but this restricts the space available to mount transducers around the pipe. These individual transducers are sometimes manually mounted around the pipe perimeter, introducing further uncertainty in the path length measurement used to construct the tomographic images.

Early examples of ultrasonic tomography have highlighted the challenge associated with propagating ultrasound through the vessel walls [127]. This was initially overcome by Xu and Xu [126] who used a Perspex pipe in their experiments and this was repeated in subsequent ultrasonic tomography papers [128, 129]. More recently, steel pipe systems have been considered [130] for pipe thicknesses less than 20 mm. However, to minimise attenuation within the vessel walls and the process, low frequency transducers were used, ranging between 40 - 50 kHz.

Therefore, due to the low frequency range available and low data acquisi-

tion rate, the images generated using ultrasonic tomography are typically low resolution binary depictions of two-phase flow. In light of this, using a single ultrasonic transducer array provides higher frequency inspection and therefore enables higher resolution images to be created, along with reduced set-up time and measurement uncertainty. However, introducing higher frequencies means compromising the image depth possible as signal attenuation is greater. This compromise must be taken into consideration when deploying high frequency phased arrays towards process analysis. For example, if the target image region is a bubble column in the centre of a reactor vessel but the array is positioned non-invasive to the process, the acquisition time and signal strength will be compromised using phased array imaging.

2.8 Gap in the Literature

i. To date, characterisation of hardware integrity has only been performed using simulated data sets, where conclusions have been assumed to be representative of experimentally measured data. However in practice, variation in element performance can be attributed to error in the element sensitivity and different PACs. Therefore, to calibrate the performance of ultrasonic hardware requires an experimental procedure to be established. In light of this, an experimental hardware characterisation procedure is presented that incorporates variation introduced from the PAC as well as the phased array itself.

ii. To the author's knowledge, there are no examples in the literature relating

to ultrasonic hardware characterisation describing variation between individual FRD data sets. Therefore, there is a need to assess the spread in measured ultrasonic data due to experimental error. This is addressed in this Thesis by expressing the measured response at each array element index with a single standard deviation error bar to represent the spread across FRD data sets.

iii. Zhang et al identified the sensitivity of the TFM imaging algorithm to peak time error [85]. However, they did not propose a correction method for this offset and they suggested this should be the next stage in enhancing TFM image performance. Therefore, a gap exists to create a methodology to calibrate FMC data that is directly relevant to the TFM imaging algorithm. This is tackled by establishing a methodology to decouple time delay errors associated with transmission and reception and introducing these into the TFM algorithm.

iv. The ability to capture detailed images relating to industrial processes has been more or less confined to optical imaging using digital cameras. Imaging using this technology restricts the analyst's ability to adapt the image construction process to specific applications. Also, optical imaging can only be deployed on processes that are optically transparent, including a clear optical path between the camera and the process. This reduces the applicability of the overall measurement tool to specific industrial processes. Ultrasonic phased arrays have been successfully demonstrated for imaging of highly controlled dynamic processes but have yet to be used for imaging of complex industrial flows. Here, there exists a gap in the literature to

develop the capability for imaging without the dependency on an optically transparent process. Ultrasound imaging can fill this gap as it is specifically deployed to image into optically opaque vessel materials.

v. Velocimetry of bubble flows has been achieved using ultrasonic Doppler flow meters and echo PIV, however, these techniques are restricted in their applicability to process analysis. Ultrasonic Doppler flow meters require a minimum velocity profile of more than 150 mms^{-1}, which reduces its applicability below this value. For example, superficial gas velocity during the coal liquefaction process is typically less than 100 mms^{-1} [16]. Echo PIV has not been performed on millimetre length scale reflectors, which are typically found in water treatment processes and flotation cells. Therefore, there is a gap in the literature for bubble flow velocimetry of flows moving less than 150 mms^{-1}. This is addressed in this Thesis through the development of an object tracking algorithm that is deployed to bubbles moving within this velocity range outlined above.

vi. There have been several methodologies proposed in the literature to combat the acoustic impedance mismatch encountered in typical process analysis environments. These methodologies typically fall into two categories:

   - Modification of the acoustic properties of the system, including the vessel material and

   - Inference of information about the process from the reflections at the acoustic boundary.

Except for the design of acoustic metamaterials, every approach has consid-

ered the ultrasonic reverberation pattern to be intrinsic to the non-invasive system. Indeed, the physics of this ultrasonic system cannot be mitigated and there will be a low sensitivity for signals from beyond a steel interface. Current methodologies assume that signals reflected from beyond a strongly reflecting interface are undetectable. Therefore, to overcome attenuation effects, kilohertz frequency ultrasound has been typically deployed for through-steel measurement. However, if the receiving transducer has adequate sensitivity, the signals of interest would only appear weak relative to those signals corresponding to the reverberations. This has created a gap in the literature to investigate signal processing methodologies to identify and minimise the reverberation signals thus enabling direct measurement of the process. When deployed with phased arrays, this gap can be narrowed to investigate non-invasive through-steel imaging of industrial process streams.

Chapter 3

Calibration of Ultrasonic Hardware

3.1 Introduction

Calibration is employed to remove one source of uncertainty in measured data. This process is regularly undertaken in industries where confidence in ultrasonic beam integrity is fundamental to measured data, for example, in medical diagnosis [131] and NDE [80]. In the context of ultrasonic hardware, the calibration process aims to identify how the transmitted and received signals vary from their designed specification, and in doing so, provide information that can then subsequently be used to remove this source of uncertainty.

One source of ultrasonic measurement uncertainty typically manifests itself as inter-element inconsistency or variation in the signals corresponding to different

element positions [85]. The source of this variation can derive from individual elements on the array or from inter-channel variation on the PAC when the array and PAC are deployed together. Under ideal conditions, for the lifespan of an array, all array elements would exhibit an identical impulse response function, directivity pattern and time delay [85]. Likewise, under ideal conditions for the PAC, all channels should operate with the same sensitivity, which is particularly crucial when multiplexing array elements across multiple channels.

The impact of not detecting an under-performing array can be critical. If deterioration of an array's performance significantly influences the beam artefacts then the accuracy of ultrasonic images generated from these data is compromised. This could lead to a misdiagnosis or incorrect sizing of a flaw [84]. Therefore, it is important to understand how ultrasonic hardware behaves, which can be achieved through adequate and regular calibration, to increase certainty of measured data.

Phased array elements are typically labelled sequentially from one up to the number of elements across the array aperture, which is often 128 elements. It is common practice in the literature to directly relate the individual element performance to the received signal at these element locations [8]. This assumes that variation in received signals is derived purely from the element performance and is independent of the overall hardware performance, for example, due to inconsistencies on the PAC. Therefore, to distinguish the potential sources of hardware variation in this Chapter, element numbers shall only pertain to the location of that element. When referring to the signal transmitted or received from an individual element this will be stated explicitly. Also, comparisons are

drawn between individual data sets, each of which was acquired in the FRD format. Therefore, when referencing an individual FRD data set, this is referred to as an FRD sample and comparisons are drawn between samples of FRD.

In this Chapter a robust, easy-to-use and efficient calibration methodology is presented. The aim is to establish an understanding of variation between elements and between FRD samples and to illustrate how this relates to the certainty of measured ultrasonic data for industrial process analysis.

3.2 Methodology

3.2.1 Ultrasonic Hardware

There were several linear phased arrays and PACs available for this research. In this Thesis, the term 'Hardware System' refers to the ultrasonic phased array coupled to the PAC, where the three Hardware Systems used are outlined in Table 3.1. Hardware System 1 belongs to BP Chemicals Ltd whereas Hardware Systems 2 and 3 are property of the Centre for Ultrasonic Engineering (CUE) at the University of Strathclyde.

Two linear phased arrays (Vermon S.A., France) have been used during this project. Both arrays have a designed centre frequency of 5 MHz, a 128 element aperture and are acoustically matched to Perspex. The phased array in Hardware System 1 could only be coupled to the PAC in Hardware System 1 as it had a different adapter to the other PACs available in CUE. Three PACs have been deployed, each comprising 32 transmit and receive channels. Hardware Systems

1 and 2 both use an FIToolbox (Diagnostic Sonar Ltd., UK) PAC while Hardware System 3 uses a Dynaray (Zetec Inc., Canada) PAC.

Table 3.1: *Ultrasonic hardware systems.*

Hardware System	Phased Array	PAC Model	PAC Manufacturer
1	1674J001	FIToolbox	Diagnostic Sonar Ltd.
2	1279E001	FIToolbox	Diagnostic Sonar Ltd.
3	1279E001	Dynaray 256/256PR	Zetec

The key aspect in the selection process of the acquisition mode was the data acquisition rate. Using the FIToolbox PAC it is possible to acquire and export multiple FMC data sets in quick succession. This PAC has been designed to maximise the throughput of ultrasonic data, therefore, since FMC provides the maximum quantity of information about the image scene it was selected as the data acquisition mode for this research. Using FMC also overcomes the challenge of low image resolution identified by Avila et al [11] as TFM images can be created from these FMC data.

3.2.2 Overview

A calibration procedure has been designed to extract information about the ultrasonic hardware from an FMC data set using a reflection from a planar interface. By acquiring an FMC data set, the maximum quantity of data is obtained for the hardware. The methodology is designed for linear array calibration, however, it is transferable to alternative array geometries if the appropriate signals are extracted. The algorithm requires the following:

- List of FMC data sets;
- Acoustic velocity in calibration sample;
- Straight line path length from array surface to the back wall;
- Element pitch;
- Hardware gain;
- Hardware voltage and
- Upper and lower bandpass frequencies of the filter design.

Through signal processing of these back wall reflections, the bandwidth, centre frequency, pulse length, sensitivity and peak time error, referred to as the hardware performance characteristics, are extracted for each element. In addition, the spread between each FRD sample is measured for each element, providing insight into the degree of experimental error. The methodology established is similar to that presented by Zhang et al [85], whereby information from a planar back wall reflection was used to infer the hardware performance.

3.2.3 Data Acquisition

The array was mounted onto a crown glass calibration block with a straight line path length, L, of 50 mm to the back wall, as shown in Figure 3.1. There is a high degree of certainty in L because the calibration block was manufactured in bulk to its specific dimensions. A crown glass sample was chosen because it permits visual inspection, reducing the uncertainty from flaw reflections. Water was used to couple the ultrasonic path between the array and the sample and the

array was clamped to the calibration sample. The glass block was placed on two blocks so that the back wall had an air load, creating a high acoustic impedance mismatch, leading to a large reflection coefficient.

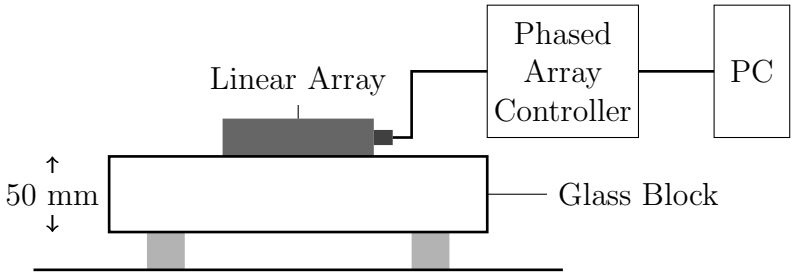

Figure 3.1: *Apparatus for ultrasonic hardware calibration.*

Using all available elements, FMC data of the back wall reflection were acquired five times in quick succession as this represents the typical deployment of the array. The array was not uncoupled from the PAC between FRD sample measurements. Rapid FMC acquisition was made possible by using the FIToolbox PAC; all FMC samples were recorded in less than one second. Including the apparatus set-up time, the data acquisition process can be completed in under five minutes per array. These data are then saved into Pickle [132] binary format, *.bin*, for off-line processing and to extract the hardware performance characteristics. Pickle was chosen because it provides efficient and robust serialisation of the raw data to binary format. An advantage of this methodology, apart from its efficiency, is that the FRD can be uploaded to a repository, permitting inspection of hardware deterioration over time.

3.2.4 Signal Processing

3.2.4.1 Signal Preparation

Signal processing of the FMC data was performed using the Python 3.6 programming language [133], where the full calibration program can be found at the University of Strathclyde PURE repository, here, or the full link can be found in Appendix A.

The hardware calibration process begins by creating an instance of the *Calibration* class. The program has been designed such that a call to determine any one of the hardware performance characteristics invokes a call to unpack or extract the relevant *calib_signals* from the FMC data sets and to filter and normalise these only once. To reduce the uncertainty in the measured data, only the signals corresponding to the two most reliable path lengths were unpacked. That is, the direct path to the back wall when the transmitting and receiving element indices are the same and the path when transmitting on one element and receiving on the adjacent element index. The signals to be extracted are demonstrated in Figure 3.2 for an FMC data set acquired with a 16 element aperture. The darker shaded squares represent the direct path to the back wall and the lighter shaded squares represent the adjacent element path. The unpacking process is performed for each FMC data set, where two sets of signals are extracted:

i. The diagonal of the FMC matrix, corresponding to signals with same transmit and receive indices and the vertical ray path for the propagating wave and

ii. The A-Scans with an index one greater than the diagonal, corresponding

to transmission on element n and reception on element $n+1$. Note, for T_n this signal is not recorded as it does not exist, where n is the number of elements in the array.

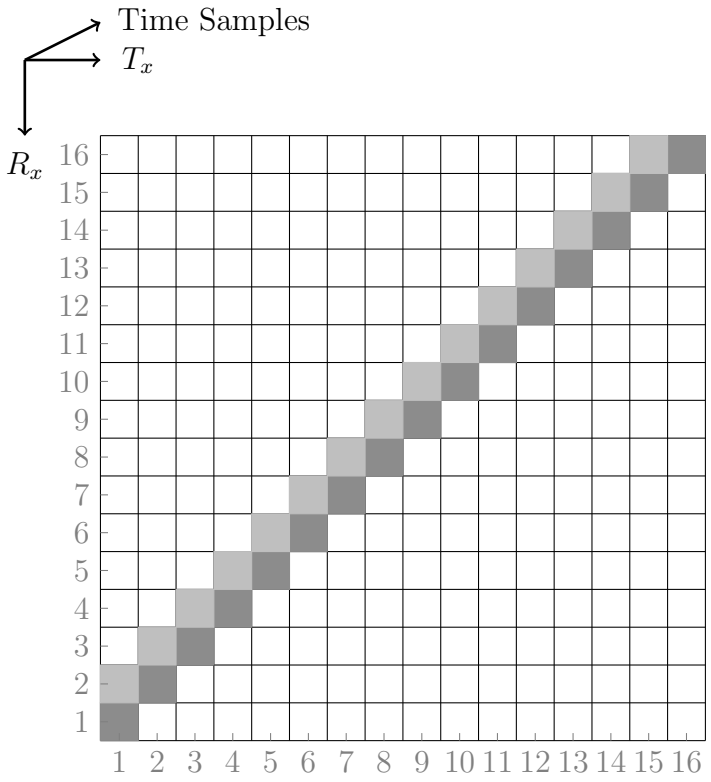

Figure 3.2: *Schematic of FMC data set for a 16 element aperture, where each square represents an individual A-Scan and the shaded squares represent signals extracted for the calibration process.*

Next, the unpacked calibration signals were normalised relative to the driving *voltage*, *gain* and integer *precision*. This translated the unit of the signal amplitudes into received volts per input volt. The signals were then mean-centred to remove any baseline offset that could be introduced by inter-channel variation. Next the artefact corresponding to the back wall reflection was windowed using a rectangular function with a value of zero everywhere except the time samples

corresponding to the back wall echo where it has a value of one.

After unpacking the calibration signals, they were sent through a zero-phase Butterworth band-pass filter. The reason for doing so is that there were several spikes observed around the designed centre frequency of the arrays in frequency domain response. Therefore to reduce the error of identifying the wrong frequency peak the frequency band around the designed centre frequency was filtered. The end-user can arbitrarily define the lower and upper limits of the bandpass, however, for this investigation these were set to ± 1 MHz of the array's designed centre frequency. Note the value of the sampling frequency, F_s, was set to 40 MHz which was greater than the Nyquist sampling rate. The filter design achieves a zero-phase shift by applying the filter once, flipping the signal, applying the same filter again and flipping the signal back to recover the original signal phase with filtered amplitudes. Once the calibration signals were extracted and filtered, the next stage of the calibration process was the detection of the back wall peak in both time and frequency domains.

3.2.4.2 Time Domain Parameter Extraction

For the time domain analysis the peak detection methodology employed was that developed by Namas et al [134]. For each A-Scan in the unpacked time domain calibration signals, the Hilbert transform was computed to establish the in-phase, S_r and quadrature, S_i terms of the time domain signal. From these, the envelope response, Ω of the time domain signal was computed

$$\Omega = \sqrt{S_r^2 + S_i^2}. \tag{3.1}$$

An example of the original A-Scan (post-filtering) and the envelope response is shown in Figure 3.3. The peak time was extracted from Ω at the time sample corresponding to the maximum of the envelope. An advantage of this method over using the maximum amplitude of the raw time domain response proposed by Zhang et al [85] is that it results in a single clear peak of the back wall reflection, without spikes in the amplitude. This means more accurate estimation of the pulse length can be achieved as there is less uncertainty in the start and end times of the peak.

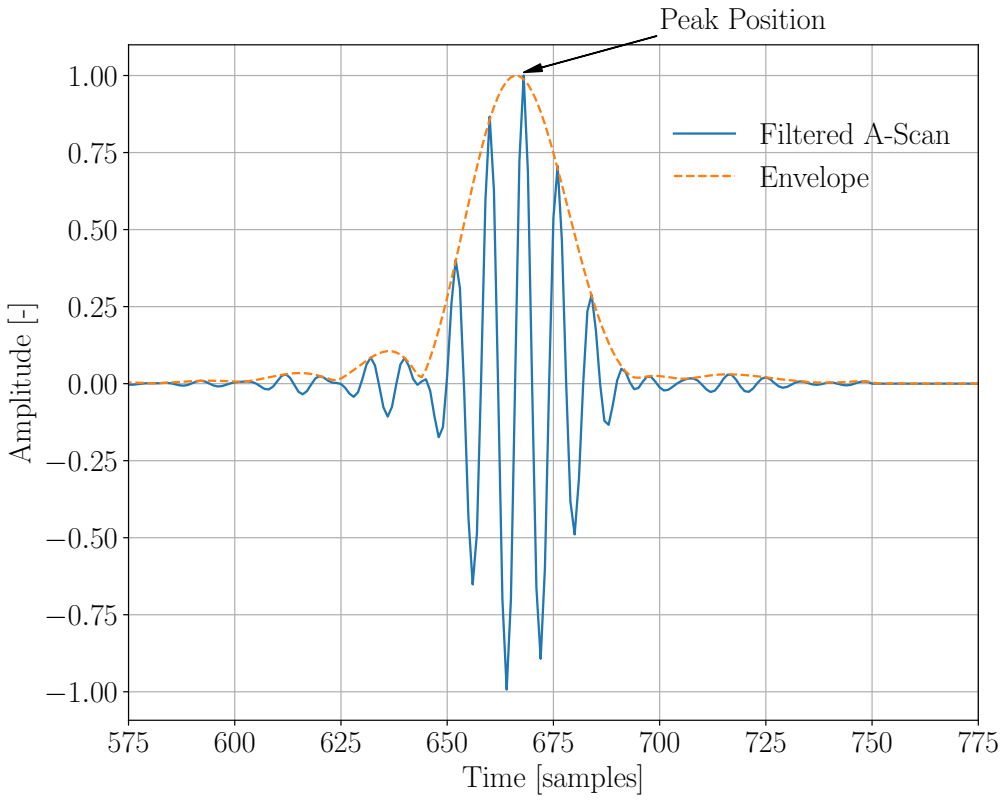

Figure 3.3: *Time domain peak detection from envelope response.*

To determine the speed of sound, ν, in the calibration sample it was important

to decouple variation due to the ultrasonic hardware from the calculation. This was achieved by measuring the TOF between the first and second back wall reflections, t_{reverb}, for A-Scans corresponding to the direct path to the back wall. If the time delay resulting from the PAC switching between transmit and receive modes is considered as a single event that is independent of the A-Scan length, the time difference between two subsequent reflections must be independent of ultrasonic hardware variation. Given that the distance travelled between the first two reflections is known, ν can be determined

$$\nu = \frac{2L}{t_{reverb}}. \tag{3.2}$$

The time difference between the first two peak reflections was determined for the A-Scans corresponding to the FMC diagonal in each FMC sample, demonstrated in Figure 3.4. This was performed using the peak maximum of the Hilbert transformed envelope response to identify the time sample of the first and second reflections. From these values, the mean and standard deviation of ν were calculated to be 5973 $\pm$ 85 ms^{-1} and these were assumed to be homogeneous throughout the sample. Note, the surface roughness of back wall could introduce error in the speed of sound calculation due to the uncertainty in the path length to the back wall. This would have the impact of elongating the envelope response but was not considered to introduce a significant degree of error here as the calibration sample was made from glass.

Determination of the pulse length begins with identification of the peak maximum of the first back wall reflection. Then samples either side of the peak are iterated until the sample index of the last sample above -6 dB is reached. The

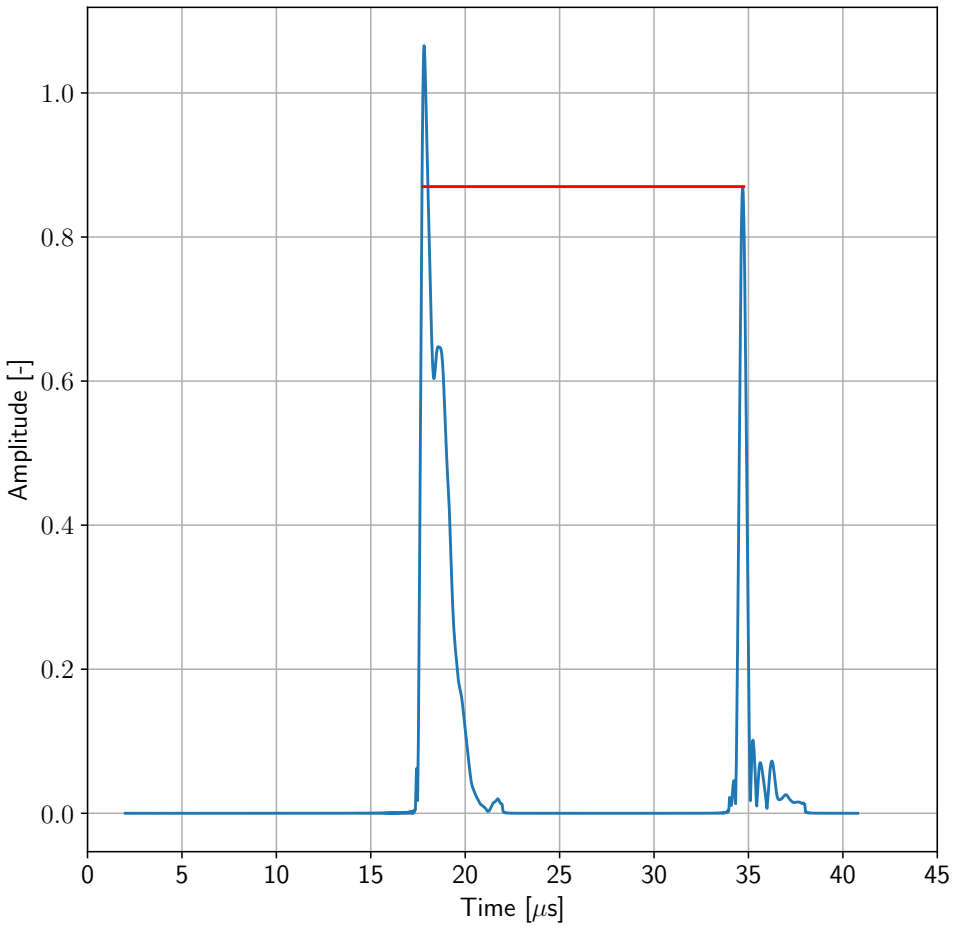

Figure 3.4: *Determination of t_{reverb} using the TOF between the first two back wall reflections corresponding to the red line.*

time difference between these two sample indices was recorded as the pulse length. The estimated pulse length was demonstrated in Figure 3.5 as the red line, where the algorithm has selected only samples greater than -6 dB relative to the peak maximum. Note, the red line does not extend to the blue curve because the blue curve has interpolated between individual data points.

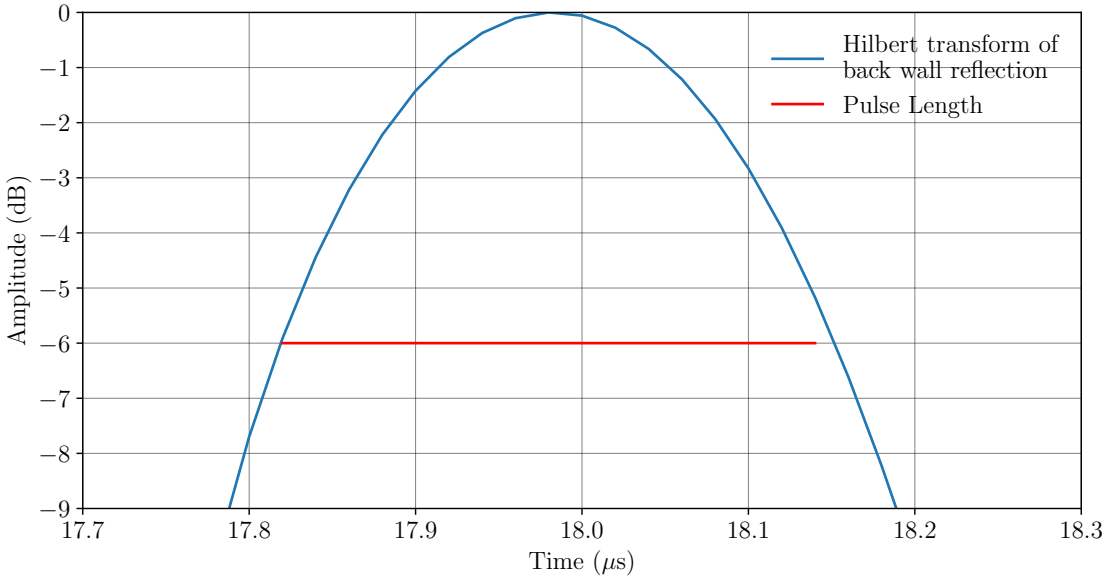

Figure 3.5: *Time domain back wall peak detection showing -6 dB signal cut-off limit in red to estimate the pulse length.*

From the peak position the sensitivity can be extracted. The element sensitivity (V_o/V_i) corresponds to the ratio between the the detected signal voltage (V_o) at the peak maximum and the input signal voltage (V_i). From this same peak position the observed peak time, t_{ob}, can be extracted, which is the time corresponding to this peak maximum. Following this, the peak time error, $t^{(n)}$ was calculated as:

$$t^{(n)} = t_{em} - t_{ob}, \tag{3.3}$$

where the empirical TOF, t_{em}, is equal to t_{reverb} for A-Scans from the FMC diagonal. However, for the A-Scans with a receiving element index one greater

than the diagonal, t_{em} was calculated using the element pitch

$$t_{em} = \frac{2}{\nu}\sqrt{L^2 + \left(\frac{p}{2}\right)^2}. \tag{3.4}$$

It was highlighted by Zhang et al [85] that peak time error contributed significantly to degradation of TFM images. For pulse-echo measurements, the total error associated with the peak time is due to error in both transmission and reception. Decoupling the error associated with these two processes was considered not possible by Duxbury et al [80], where they assumed a 50% error contribution from each process. In light of these two conclusions, it was proposed that the error associated with transmission and reception could be experimentally approximated using variations of Equation (3.3) and incorporated into the TFM imaging algorithm. To do this required the assumption that error in the peak time was purely due to hardware variation and was independent of sample heterogeneity. This was considered a valid assumption because variation in acoustic velocity is not typically considered during NDE or medical measurements. In addition, it was assumed that the total error was the sum of the error from the transmission and reception processes.

Using the known distance to the back wall and the element pitch of the array, the path length between two adjacent elements can be estimated using Pythagoras' Theorem. From this, two equations can be established that relate to the peak time error for each individual element:

i) $t_1^{(n)}$ - the peak time error associated with a direct path to the back wall for a given element, n, so transmitting on element $T_x = n$ and receiving on

element $R_x = n$;

ii) $t_2^{(n)}$ - the peak time error associated with a direct path to the back wall between two adjacent elements, so transmitting on element $T_x = n$ and receiving on element $R_x = n + 1$.

Note, T_x is the number of the element that is transmitting whereas T_{x_n} is the time delay associated with the transmitting element number n. There are two unknowns for each element, the peak time error associated with transmission, T_{x_n} and reception, R_{x_n}. The peak time error is a function of both the transmission and reception processes and so the following two equations can be derived

$$t_1^{(n)} = T_{x_n} + R_{x_n} \tag{3.5}$$

$$t_2^{(n)} = T_{x_n} + R_{x_{n+1}}. \tag{3.6}$$

To solve for these parameters, the delay in transmission for the first element was assumed to be zero, $T_{x_1} = 0$. This has the impact of normalising all time delays relative to a new start time, t_0. In practice there will be a time delay between the PAC sending the instruction for element 1 to fire and the element actually transmitting. However, in FMC all subsequent element transmission events are dependent on the previous element having already fired. Therefore, any delay in transmission of the first element is not dependent on a prior transmission delay so is irrelevant in the context of the timing of the overall data acquisition process. For the first transmitting element, Equations (3.5) and (3.6) can be rewritten

as

$$t_1^{(n)} = 0 + R_{x_1} \tag{3.7}$$

$$t_2^{(n)} = 0 + R_{x_2} \tag{3.8}$$

and so

$$R_{x_1} = t_1^{(1)} \tag{3.9}$$

$$R_{x_2} = t_2^{(1)}. \tag{3.10}$$

Then the transmission delay for the subsequent element, can be determined by redefining Equations (3.5) and (3.6) in the context of $T_{x_{n+1}}$,

$$t_1^{(2)} = T_{x_2} + R_{x_2} = T_{x_2} + t_2^{(1)} \tag{3.11}$$

$$t_2^{(2)} = T_{x_2} + R_{x_3} \tag{3.12}$$

where R_{x_2} has already been determined in Equation (3.10). Therefore, Equation (3.11) can be rearranged to solve for T_{x_2} and following this, Equation (3.12) can be solved for R_{x_3}, so

$$T_{x_2} = t_1^{(2)} - t_2^{(1)} \tag{3.13}$$

$$R_{x_3} = t_2^{(2)} + t_2^{(1)} - t_1^{(2)} \tag{3.14}$$

This process is repeated for each transmitting element in the aperture and for each FRD sample, resulting in an average peak time error for each element in

both transmission and reception. So

$$T_{x_n} = \sum_{m=2}^{n} t_1^m - \sum_{m=1}^{n-1} t_2^m \tag{3.15}$$

$$R_{x_n} = \sum_{m=1}^{n-1} t_2^m - \sum_{m=2}^{n-1} t_1^m \tag{3.16}$$

These values can then be incorporated into the TFM algorithm by adding them to the TOF calculation for each pixel depending on which element is transmitting and/or receiving.

3.2.4.3 Frequency Domain Parameter Extraction

To extract the frequency domain hardware performance characteristics the unpacked time domain calibration signals were transformed into the frequency domain using the fast Fourier transform. To increase the speed of the Fourier transform operation, the time domain signals were zero-padded. This involves adding zero value samples at the end of the time domain signal such that the length of the signal is 2 raised to the power of the number of samples in the signal. The centre frequency was measured as the frequency corresponding to the peak maximum. The element bandwidth was determined using the same technique used for the pulse length, shown in Section 3.2.4.3. From the frequency peak maximum, samples either side of the peak are iterated until the sample indices of the last sample above -6 dB are reached. The bandwidth was then determined as the frequency difference between these two samples.

Note, the glass block frequency-dependent attenuation was ignored for this

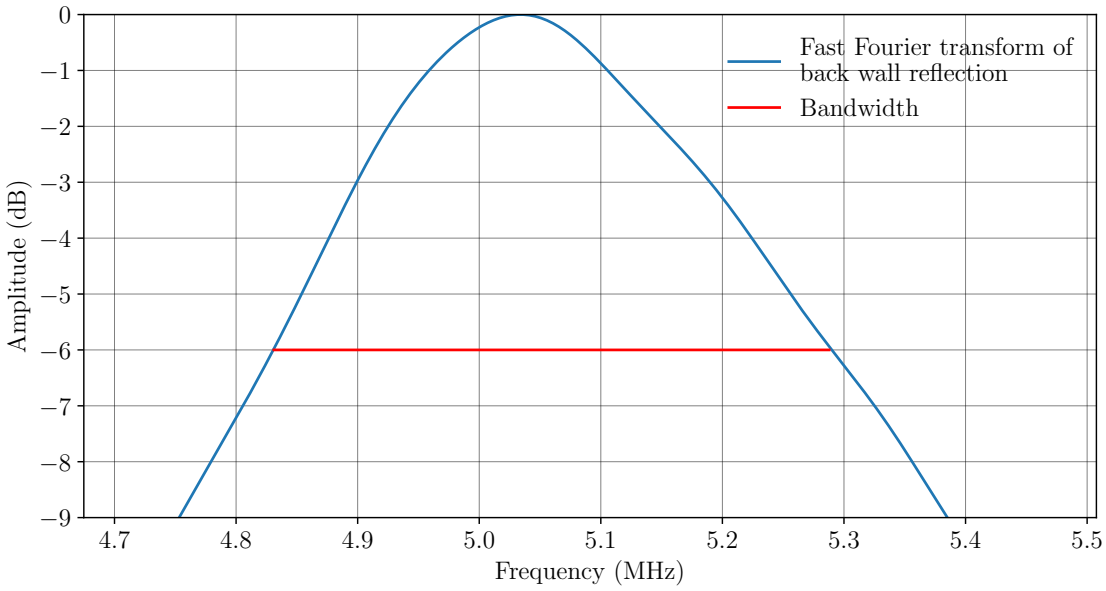

Figure 3.6: *Frequency domain back wall peak detection showing -6 dB signal cut-off limit in red to estimate the bandwidth.*

procedure; this assumption could be verified by executing the data acquisition over two different path lengths however this was not possible due to the geometry of the crown glass block.

3.2.5 Graphical User Interface

Interpretation and visualisation of the results was assisted by the development of a graphical user interface (GUI), which is demonstrated in Figure 3.7. There are three key outputs provided by the GUI:

- variation of hardware performance characteristics across the FRD samples;
- variation of hardware performance characteristics between elements and
- individual A-Scan response inspection in both time and frequency domains.

This enables the end-user to identify variation between FRD samples and individual elements and to then inspect the cause of this variation more closely. The GUI is interactive so the user can select which element and FRD sample to inspect and the plots will automatically update. The code to generate this GUI can be found at the University of Strathclyde PURE repository, here, or the full link can be found in Appendix A.

(a) *Data acquisition and upload tab.*

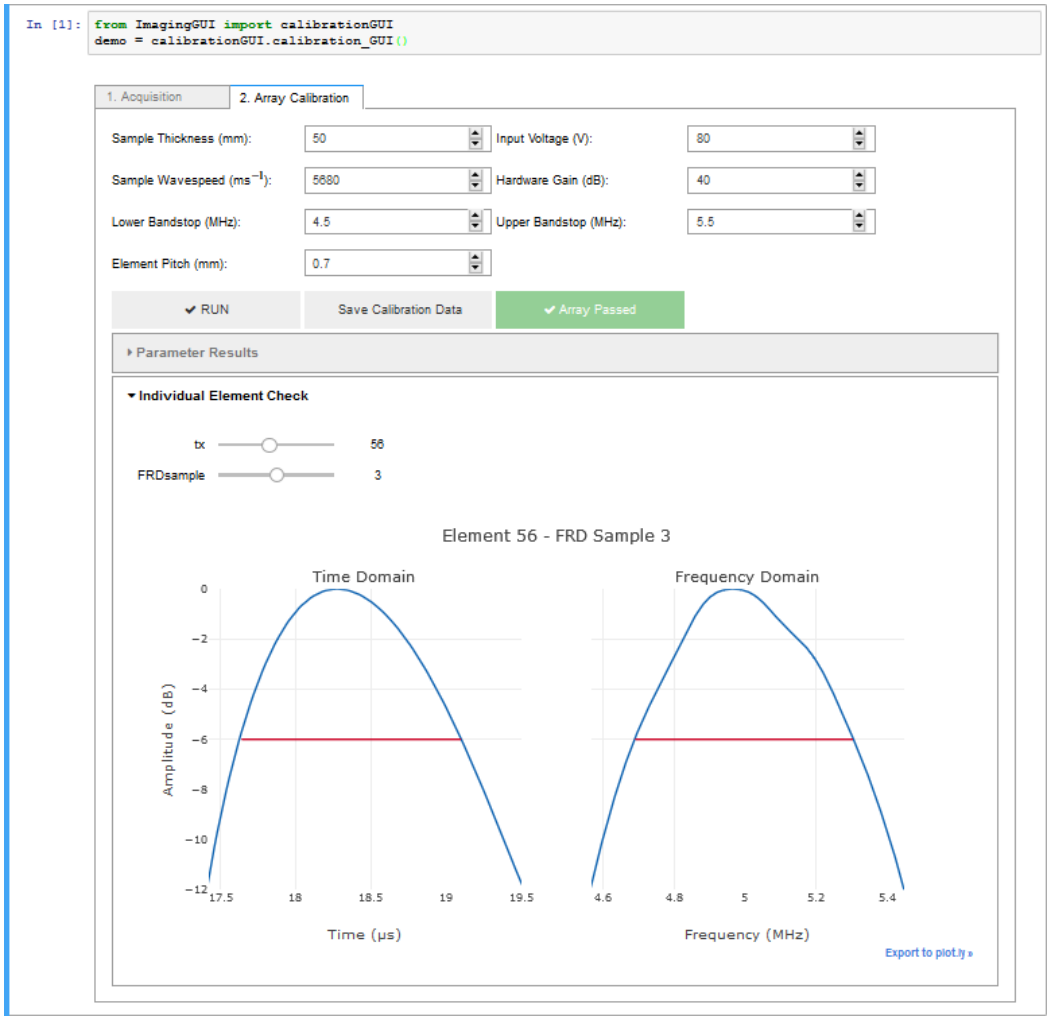

(b) *Data processing and analysis tab.*

Figure 3.7: *Demonstration of graphical user interface.*

3.3 Results and Discussion

3.3.1 Overview

In this Section the results for Hardware System 1 in Table 3.1 are presented in detail to provide an overview of typical results obtained from the new ultrasonic hardware calibration methodology. In addition, Hardware Systems 2 and 3 in Table 3.1 will be used to demonstrate how the results differ between PACs. Following this, the impact of incorporating these calibration data into the TFM imaging algorithm is demonstrated.

3.3.2 Inter-element and Inter-FRD Variation

Each ultrasonic hardware performance characteristic is represented by an individual error bar plot. The x-axis represents the individual element indices and the y-axis represents the amplitude of the relevant performance characteristic. Therefore positional variation between element indices is represented as trends on the x-axis of the error plot. The information pertaining to average and spread through FRD samples is represented as a single point at each element index with y-axis error bars corresponding to one standard deviation. For a given element index the mean and spread were calculated from the five individual values corresponding to each FRD data set. The individual data points in Figure 3.8 onwards represent the mean value of each element across the five FRD samples, where the colour of the data point represents whether the element is an outlier relative to the other element indices for the given hardware characteristic. Those elements out-

side the upper and lower 3σ control limits are coloured red to highlight that those points are outliers, whereas data points inside the 3σ control limits are coloured in green. This plotting method was also incorporated into the GUI, enabling the end-user to evaluate the spatial relationship of element performance.

Using data obtained with Hardware System 1, the frequency domain A-Scans were initially inspected to ensure adequate filtering of the back wall reflection. Given that the designed centre frequency of the array was 5 MHz, the signals were filtered using a bandpass between 4-6 MHz and with a filter order of 4. The results presented in Figure 3.8(a) show approximately a 20% variation across array elements 1 to 116 and approximately a 35% variation across all 128 array elements. These values are relatively large given that it is typically assumed that the frequency response from the array is consistent. The presence of this variation highlights the importance of the application of ultrasonic hardware calibration. In addition, there is a low degree of variation between the FRD samples, shown by the small error bars in Figure 3.8(a). Indeed, the one-sigma error bars in Figure 3.8(a) are almost not visible except for element index 6. For this element index, the frequency domain peak was mis-identified in one sample replicate, introducing the variance recorded in the plot. The array element indices greater than 117 exhibited a discontinuity in the centre frequency response. The reason is that these elements have a dual-peak response, indicated in Figure 3.8(b) as peaks either side of the designed centre. The peak around 4.1 MHz in Figure 3.8(b) has a higher amplitude peak maximum than the peak around 5.7 MHz, therefore the left-hand peak is selected by the algorithm to represent the frequency domain response from that element index. For comparison the frequency response from

element index 64 was also plotted in Figure 3.8(b), showing a single peak.

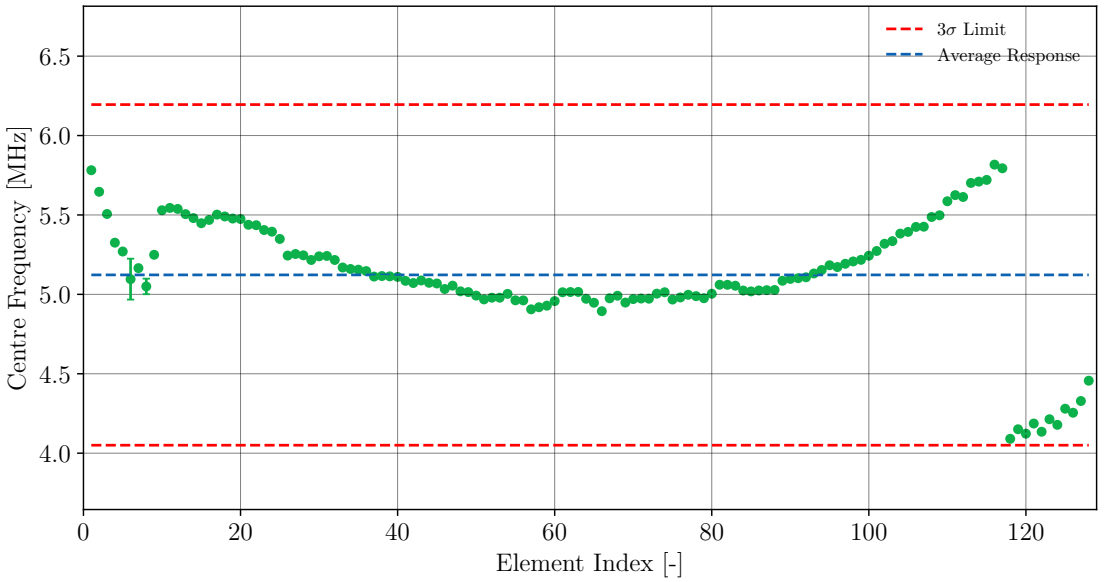

(a) *Mean and spread of centre frequency response for each element index.*

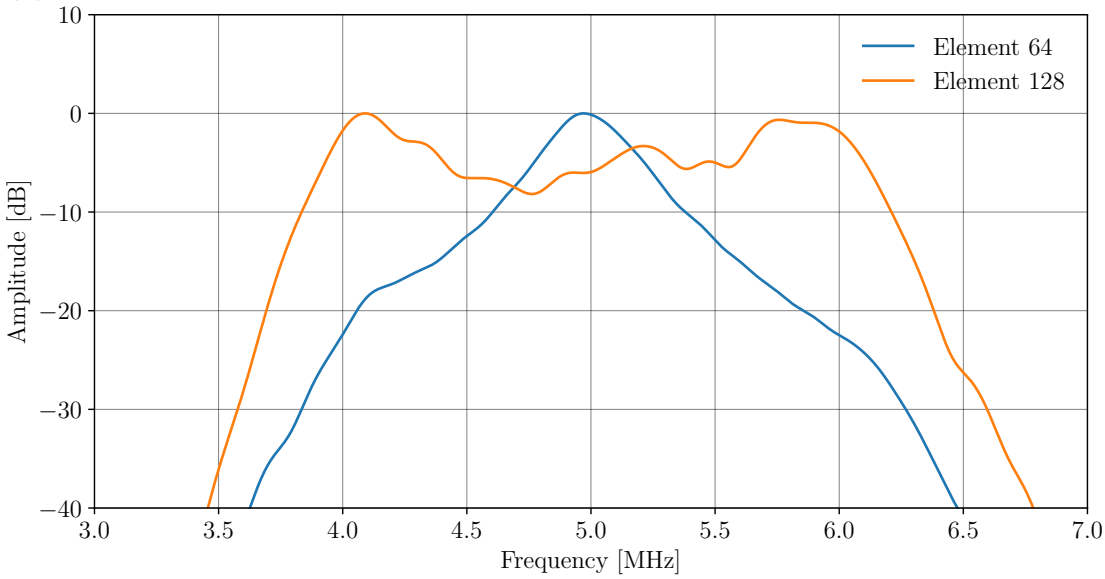

(b) *Frequency domain A-Scan for element indices 64 and 128.*

Figure 3.8: *Frequency response with a filter design of order 4 and bandpass between 4 - 6 MHz.*

Therefore to capture the frequency domain response by a single clear peak, it

was necessary to reduce the width of the bandpass. The filter design was narrowed by 500 kHz either side of the designed centre frequency, therefore reducing the filter order to 3. Following the application of this modified filter design the frequency response across the FRD samples for each element index was plotted again in Figure 3.9(a). The modified filter reduced the amplitude of the two peaks in Figure 3.9(b), thus enhancing the region around the designed centre frequency. This removed the discontinuity for element indices greater than 117 but risked compromising the quality of information contained within the calibration signals. This modified filter design was used to obtain the remainder of the results presented in this Chapter.

The results presented in Figure 3.10 show the mean and standard deviation across the five FRD samples for the remaining four hardware characteristics acquired using Hardware System 1. For all performance characteristics there is a good degree of consistency between the FRD samples, shown by the small error bars in Figure 3.10. This suggests there is a good degree of certainty between measured FRD data sets. However, across the array element indices there were variations in each performance characteristic. To determine if these variations were randomly distributed across the element indices or whether there was a spatial relationship between them, control limits were determined for each of the hardware performance characteristics.

For a data set that follows a normal distribution, 99.7% of the data points will lie within three standard deviations (3σ) relative to the mean of the data set. Therefore, if a data point lies out-with this 3σ control limit, it can be said to be statistically significant. This is a more valid assumption than using an arbitrary

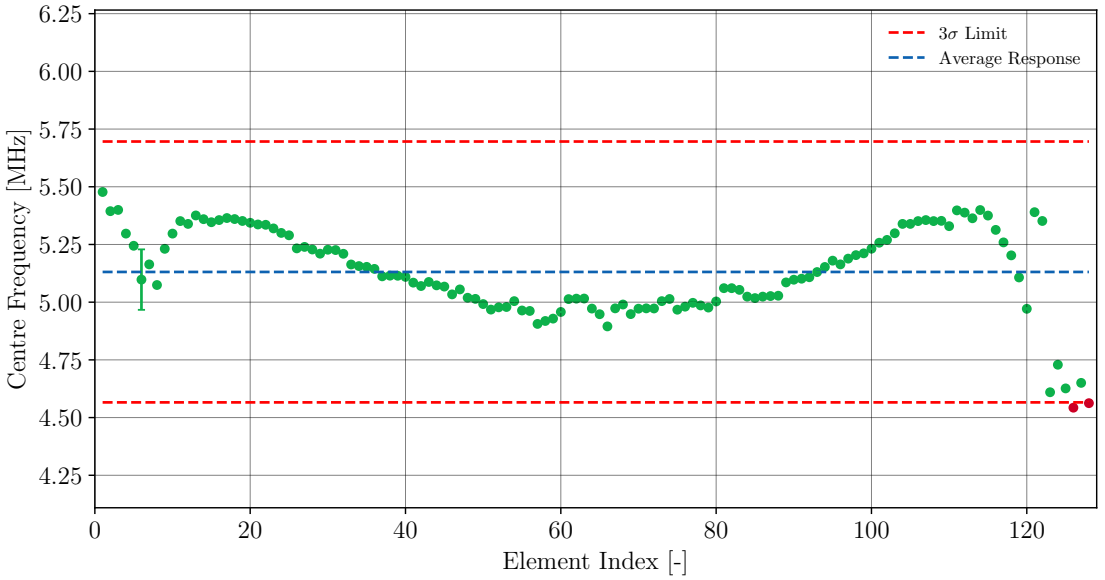

(a) *Mean and spread of centre frequency response for each element index.*

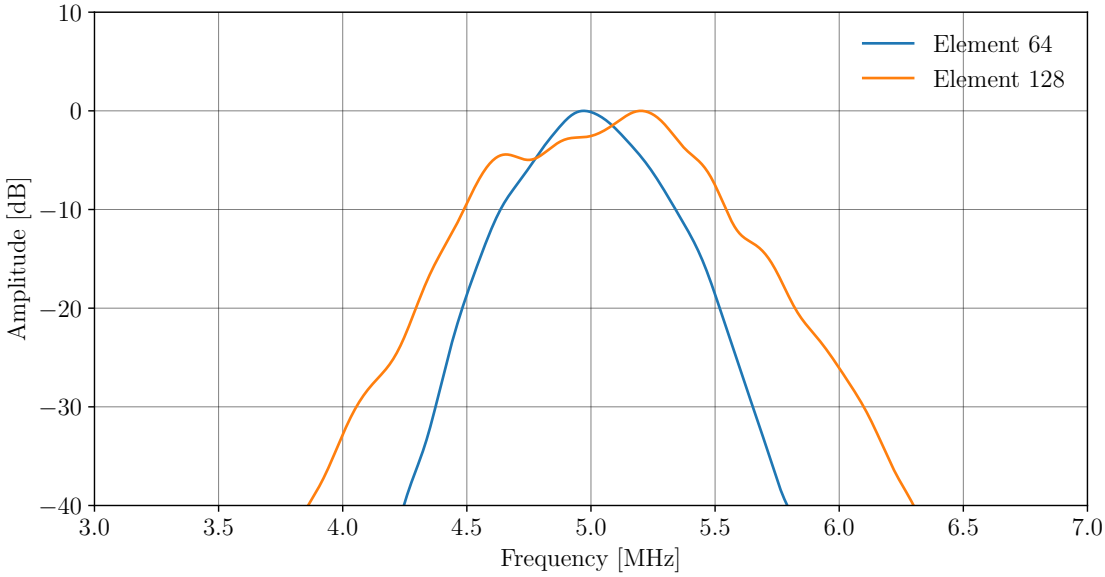

(b) *Frequency domain A-Scan for element indices 64 and 128.*

Figure 3.9: *Frequency response with a filter design of order 3 and bandpass between 4.5 - 5.5 MHz.*

-6 dB limit, so was used to determine if an individual element was an outlier for a given performance characteristic. The mean values and 3σ control limits were plotted for each hardware characteristic in Figure 3.10 as the blue and red

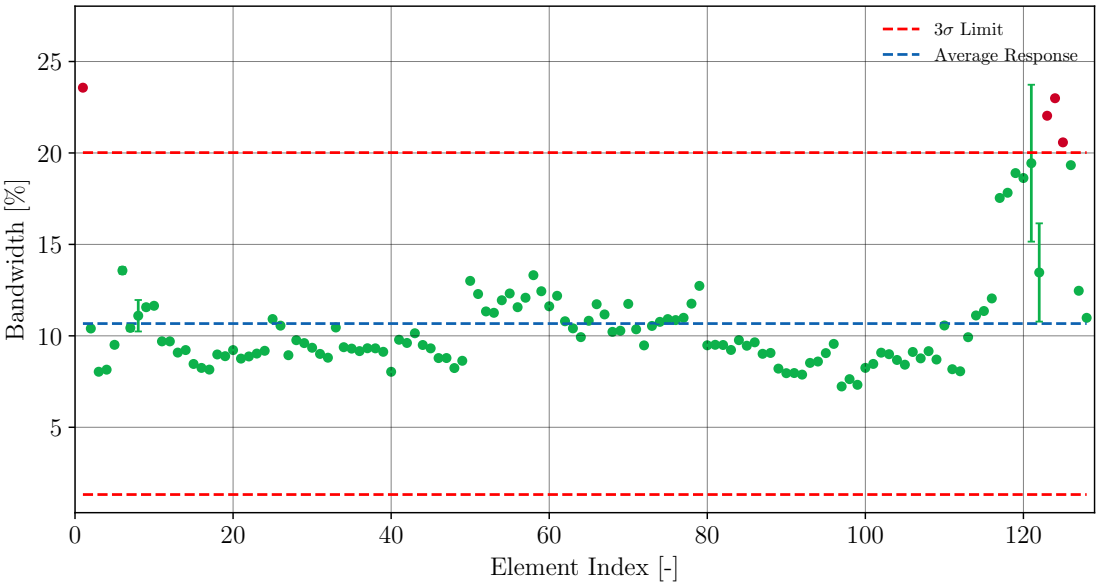

(a) *Bandwidth for each element index.*

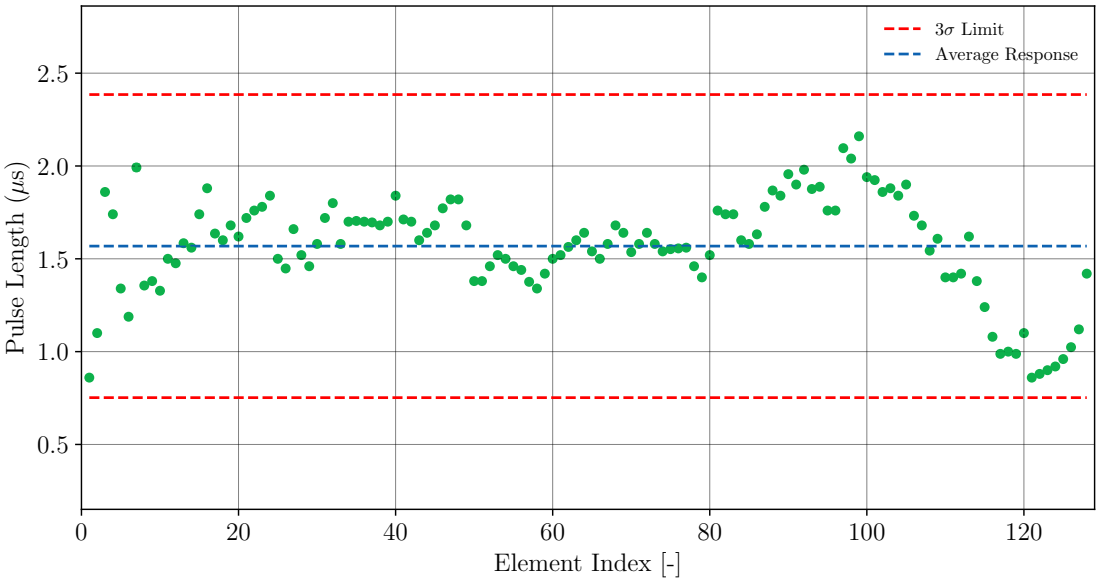

(b) *Pulse length for each element index.*

Figure 3.10: *Ultrasonic hardware performance characteristics at each element index shown relative to 3σ control limits.*

lines respectively. Note, the data were not tested for normality these values were determined from the empirical data.

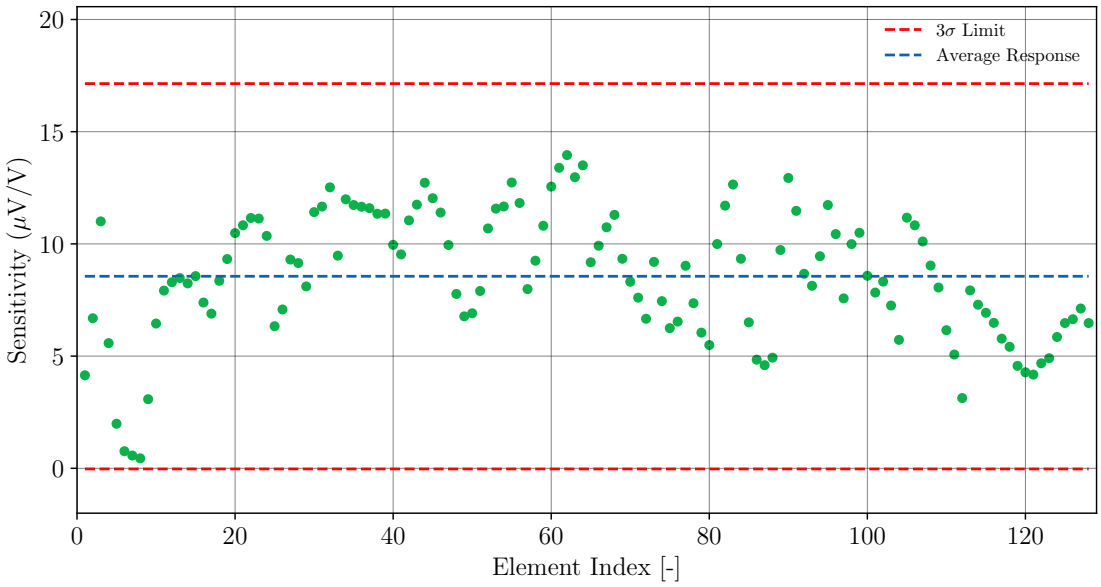

(c) *Sensitivity for each element index.*

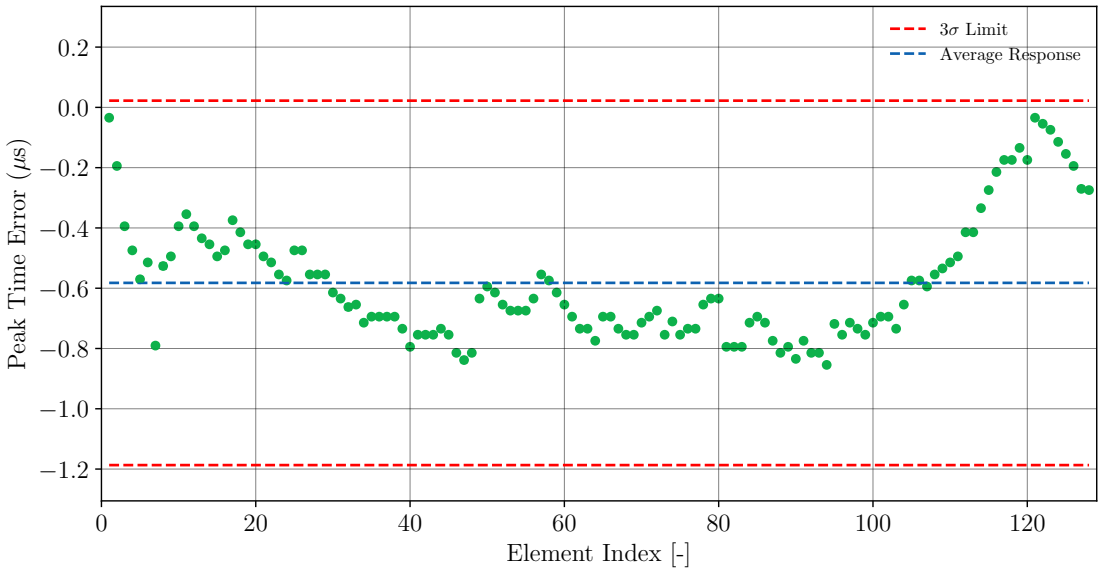

(d) *Peak time error for each element index.*

Figure 3.10: *Ultrasonic hardware performance characteristics at each element index shown relative to 3σ control limits.*

From Figure 3.10(a), the mean bandwidth response was 544 kHz and four elements were outliers, namely elements 1, 123, 124 and 125. The bandwidth response from element indices 121 and 122 was recorded with a greater spread than all other indices. Upon inspection of the frequency domain A-Scan responses it was observed that there was a shoulder peak that had a trough very close to the -6 dB level. For 3 of the FRD samples, the trough did not dip below -6 dB, so the algorithm did not accept this as the last time sample to estimate the bandwidth. The mean centre frequency was 5.14 MHz, in Figure 3.9(a), which was within 10% of the nominal centre frequency (5.0 MHz) stated in the array data sheet, therefore passing the acceptance criterion set out in [86]. However, two elements namely elements 126 and 128 were outliers. The mean pulse length was 1.58 μs in Figure 3.10(b) and there were no outliers. The mean element sensitivity was 8.70 μV/V in Figure 3.10(c) and no elements were outliers. Finally, the mean value of the peak time error was -0.56 μs and again there were no outlying element indices. Note, for the peak time error, all element indices show a negative value that suggests the observed peak time is longer than the empirical time of flight to the back wall. Across the performance characteristics the average number of outliers was 3. This corresponds to 2.34% of the total aperture which is below the 9.94% threshold adopted by Duxbury et al [80], therefore it would have been accepted as performing adequately under their protocol. However, this does not consider the absolute values of the performance characteristics and only the values relative to the mean result.

Note, except for element index 1 for the bandwidth response, all other outliers were in the element index region greater than 123, which suggests there is a

spatial relationship in terms of the error recorded for Hardware System 1. An implication of this could be to reduce the active aperture of future work by not including these elements as there is a lower degree of certainty that these element indices will perform as desired.

There is also potential to monitor the hardware deterioration over time using these control charts. Given that the data correspond to the first instance of this calibration methodology it is not possible to incorporate historical data. However, it is recommended that the control limits from this calibration data set are incorporated into future calibrations to monitor the hardware deterioration over time.

3.3.3 Variation between Phased Array Controllers

In this Section, Hardware Systems 2 and 3 are investigated. The reason for this is that it was not possible to couple the phased array used in Hardware System 1 to either of the PACs in Hardware Systems 2 and 3 because it had a different connector. Therefore experimental variation associated with the PAC in Hardware System 1 could not be captured. A key difference between Hardware Systems 2 and 3, apart from their manufacturer, is their age, where Hardware System 2 is approximately ten years younger than Hardware System 3. To demonstrate any variation deriving from the PAC rather than the phased array itself, the centre frequency and peak time for Hardware Systems 2 and 3 were plotted in Figures 3.11 and 3.12.

In Figure 3.11(a), which corresponds to the frequency domain response for

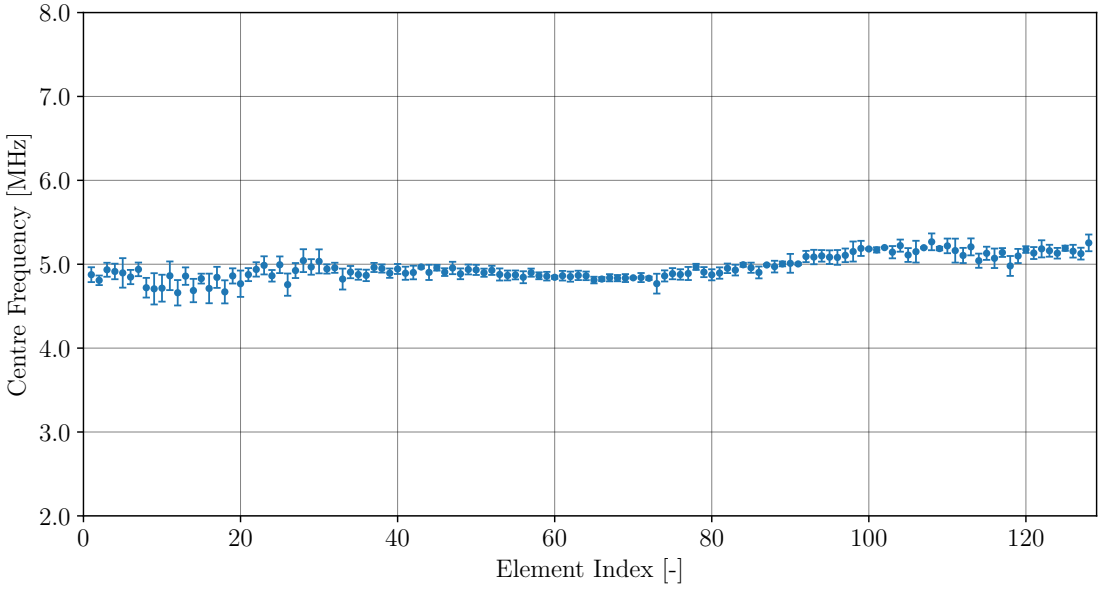

(a) *Centre frequency per element index for Hardware System 2.*

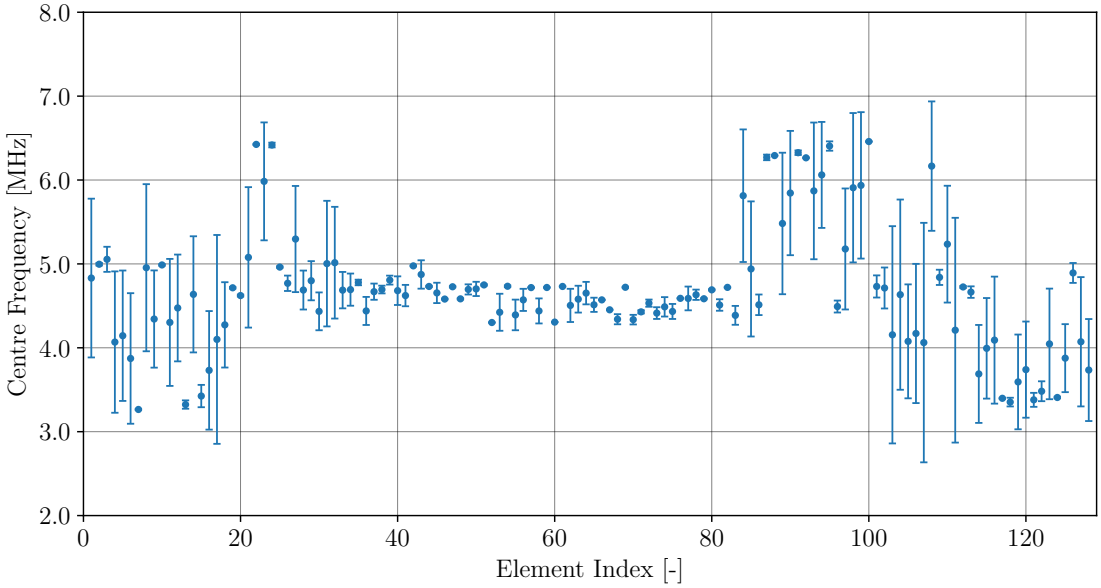

(b) *Centre frequency per element index for Hardware System 3.*

Figure 3.11: *Centre frequency represented as the mean and spread between FRD samples for each element index for Hardware Systems 2 and 3.*

Hardware System 2, there is a good consistency between FRD samples and between element indices. However, when the same data acquisition method and

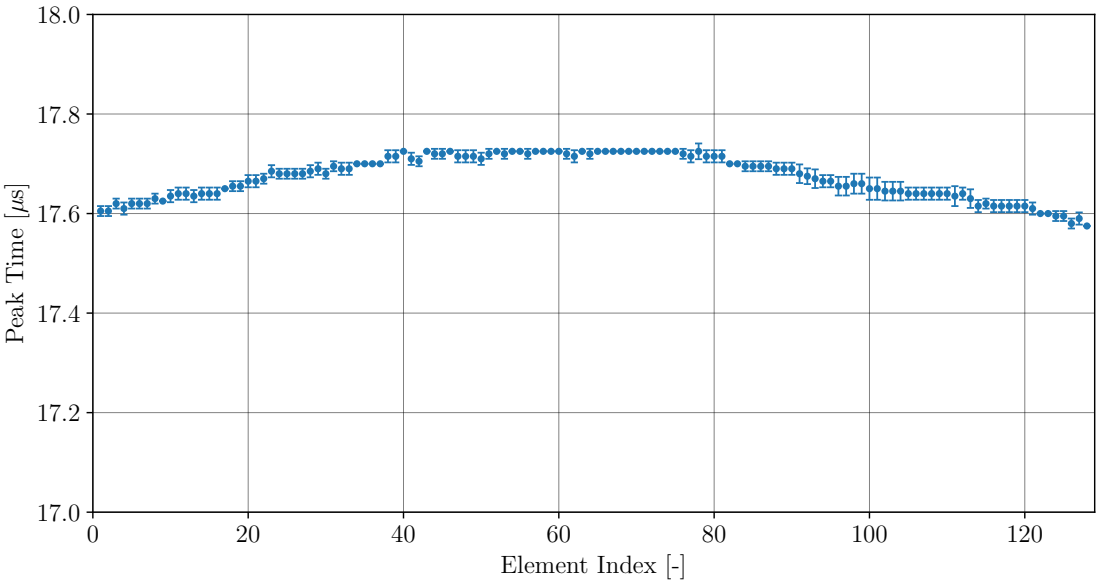

(a) *Peak time error per element index for Hardware System 2.*

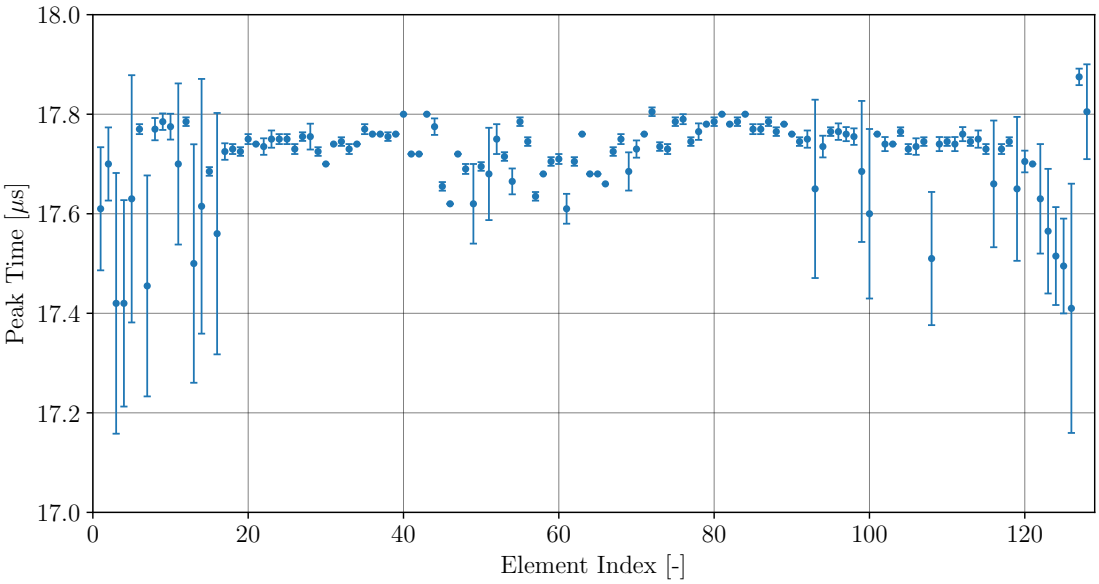

(b) *Peak time error per element index for Hardware System 3.*

Figure 3.12: *Peak time error represented as the mean and spread between FRD samples for each element index for Hardware Systems 2 and 3.*

same signal processing is applied to data acquired with Hardware System 3 in Figure 3.11(b), a large degree of variation was observed. This variation was observed both as an increase in variation between FRD samples and across the

array element indices. The peak time response, plotted in Figure 3.12, showed a similar degree of inconsistency. These results suggested that the elements were experiencing different driving conditions from each PAC that could be a result of the hardware ageing over time.

Overall, this shows that Hardware System 2 generated less spread across the hardware performance characteristics. Given that the FIToolbox is a more modern instrument relative to the older Dynaray, this result can demonstrate how ultrasonic hardware technology has advanced over time or how it has deteriorated over time, for example, due to being dropped. However, without a comparative data set from a previous point in time, it is not possible to determine either case with certainty.

This finding demonstrated the necessity of undertaking this calibration investigation because it is typically assumed that the PAC behaves as expected and does not significantly influence the recorded signal response. Given that the time and frequency domain responses are both dependent on the overall Hardware System and not just the array itself, any images generated from received data will be impacted by the quality of the PAC. This could have several implications in the NDE or medical fields where the lifespan of a PAC could impact on the ability to identify flaws or provide accurate medical diagnosis. It is recommended that calibration of ultrasonic hardware should pertain to a specific phased array-PAC coupled system and results from this calibration procedure should not be used to infer uncertainty in measured data relating to a different Hardware System. Although this increases the time required to perform calibration, this approach greatly benefits the understanding of the overall ultrasonic system, so is a cost

worth paying.

There was one constraint in terms of the application of this calibration methodology to the TFM. To accurately decouple the error associated with transmission and reception, a precise understanding of the overall peak time error is required. Therefore, the spread between FRD replicates exhibited by Hardware System 3 resulted in the methodology being unable to adequately remove the measurement uncertainty due to the ultrasonic hardware from the TFM images.

3.3.4 Contiguous Block of Element Indices

The maximum number of transmit-receive channels available on the FIToolbox was 32. As will be discussed in Chapter 6, the number of elements used to acquire FMC data was set to 32 in order to maximise the FMC acquisition rate. Therefore to determine which contiguous block of 32 elements presented the lowest degree of uncertainty for Hardware System 1, the variation in element sensitivity across every combination of 32-element contiguous block was determined. Using the method outlined in Section 3.2.4.2 the sensitivity was determined at each element index and repeated for the relevant signals from each FRD replicate. These sensitivity values were then averaged across the FRD replicates at each element index. Following this the standard deviation was determined for element indices 1 to 32 and then 2 to 33 and so on. The results were plotted in Figure 3.13 and show that the lowest spread was exhibited from elements 11 to 42 and the maximum spread from elements 2 to 33, recorded in Table 3.2.

However, upon application of elements 11 to 42, it was discovered through

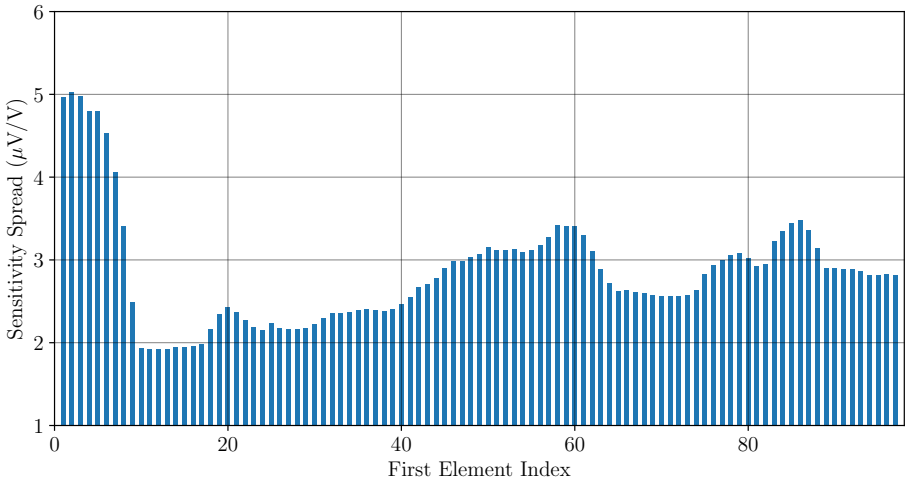

Figure 3.13: *Spread in sensitivity for each contiguous block of 32 elements, where the x-axis value represents to first element index in the block.*

Table 3.2: *Sensitivity spread for contiguous blocks of elements.*

Element Range	Sensitivity Spread ($\mu V/V$)
11 - 42	1.92
2 - 33	5.02
1 - 32	4.97

visual inspection of the FMC data set that the order of A-Scans indices were incorrect. This was a bug associated with the software used to control the PAC and is described in detail in Appendix B. After performing this investigation, it was found that the A-Scan indices were in the correct order when transmitting from elements 1 to 32, so wherever possible, these elements were used in the remainder of the Thesis despite exhibiting a sensitivity spread close to the maximum.

3.3.5 Impact of Peak Time Error

Zhang et al [85] proposed that an average peak time error greater than 0.5 μs resulted in severely distorted TFM images and for Hardware System 1 the mean peak time error was -0.59 μs. Therefore, TFM images generated from these data would be compromised if not calibrated for this error. The peak time error associated with transmission and reception was decoupled from the overall peak time error using Equations (3.15) and (3.16). The results were then plotted in Figure 3.14 for both transmission and reception.

The error associated with transmission, shown in Figure 3.14, is close to zero across the array element indices. However, the transmission peak time error is not always negative, for example, element index 8, which suggests that some error is due to the PAC firing the element slightly early. The error associated with reception, shown in Figure 3.14, is much larger in amplitude and is always negative, which suggests there is an additional time delay associated with the phased array controller switching from transmit to receive mode.

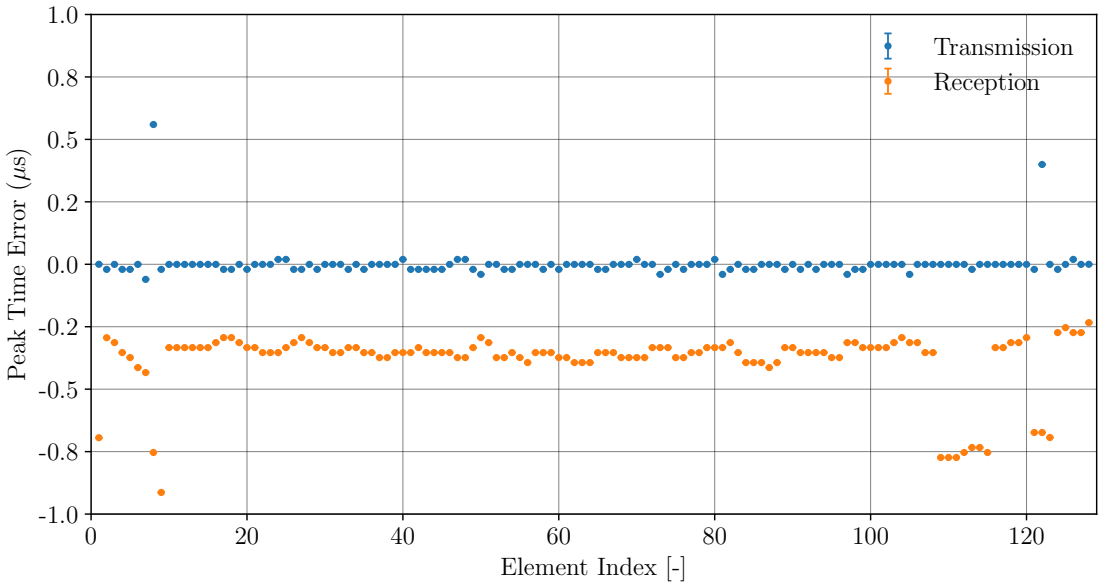

Figure 3.14: *Transmission and reception peak time error represented as the mean and spread between FRD samples for each element index for Hardware System 1.*

3.3.5.1 Finite Element Model Design

To illustrate the impact of peak time error on the TFM image algorithm, an FMC data set was simulated in PZFlex. An overview of the FE model is illustrated in Figure 3.15, where a 3 mm diameter void reflector has been suspended in water. The water was modelled at 25 °C with a density of 1000 kgm^{-3} and speed of sound of 1496 ms^{-1}. The mesh size was set to 15 elements per wavelength relative to a 5 MHz input function and the speed of water. The centroid of the void reflector was positioned 15 mm from the array and at the mid-point perpendicular to the array. Each element of the 128 element array applied a pressure load that incorporated these experimentally measured delays so that the impact of the peak time error could be assessed and to provide certainty that any impact on image quality was due to peak time error only.

A 5 MHz, Blackman-Harris wavelet was used as the driving function to ensure a Gaussian spread of the frequency was produced from the elements. Given that the data set was simulated there was no time between the elements firing and the measurement of the received signal and each element exhibited identical behaviour. The element width was designed to be coupled to water, so this was set to a value of 0.15 mm corresponding to half a wavelength of the 5 MHz driving function.

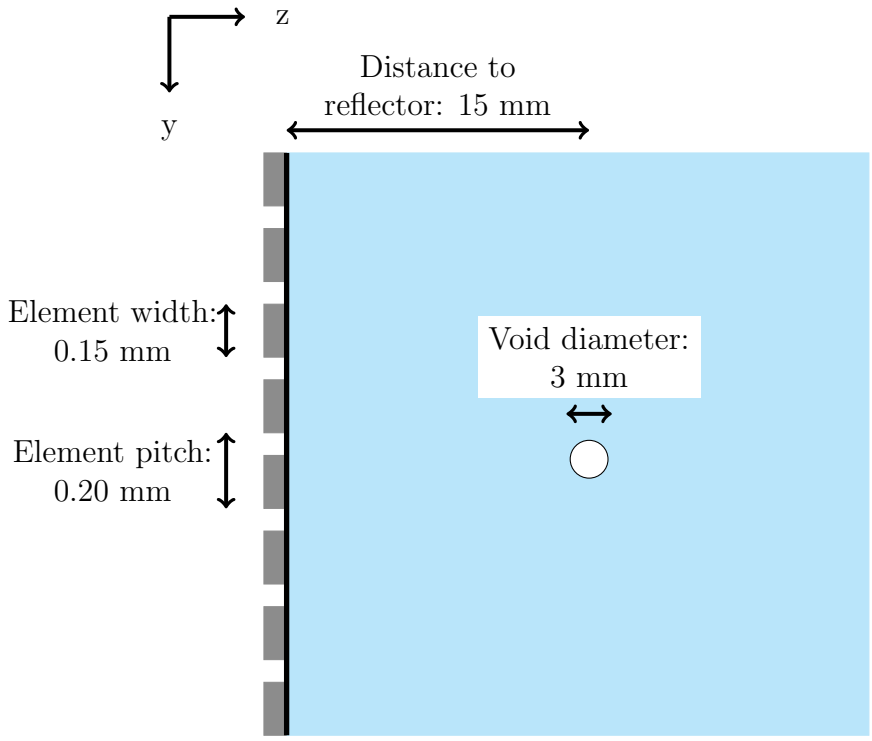

Figure 3.15: *Schematic of FE model of void reflector suspended in water.*

3.3.5.2 Application of Peak Time Errors to TFM

TFM images were generated from the simulated FMC data set output from the FE model. In the simulated data, T_{x_n} and R_{x_n} do not exist because each of

the element indices were identical in nature. Therefore, T_{x_n} and R_{x_n} needed to be introduced to the FMC data to observe the same phenomenon observed with experimental data. When the peak time error recorded from Hardware System 1 was introduced to the simulated FMC data set, the image generated is shown in Figure 3.16(a). The black circle represents the true location of the void reflector. When the peak time errors were not introduced to the simulated FMC data, in Figure 3.16(b), the TFM image was restored to its correct state, showing the reflector shape and position align with that of the black circle. The difference between Figures 3.16(a) and 3.16(b) highlights the potential to improve the TFM image quality through calibration of the ultrasonic hardware.

To emphasise this observed enhancement of the TFM image accuracy and to validate the method experimentally, the method was applied to an experimental FMC data set of a 3 mm diameter SDH in Perspex. This experimental arrangement was identical to the FE model, except the element width was approximately 0.6 mm increasing its sensitivity. The SDH was located 15 mm from the surface of the sample and the array was centred over the SDH. Using all 128 elements, FMC data were acquired using Hardware System 1 and the TFM images generated without the peak time correction method is shown in Figure 3.17(a) and that obtained with the peak time error incorporated into the TFM algorithm is shown in Figure 3.17(b). These results show the typical degree of image enhancement observed when using Hardware System 1 for reflectors with an acoustic impedance mismatch typically found in process analysis. In addition, since the acoustic properties of Perspex are very different to those of the glass calibration medium, this highlights the robustness of this TFM calibration procedure to dif-

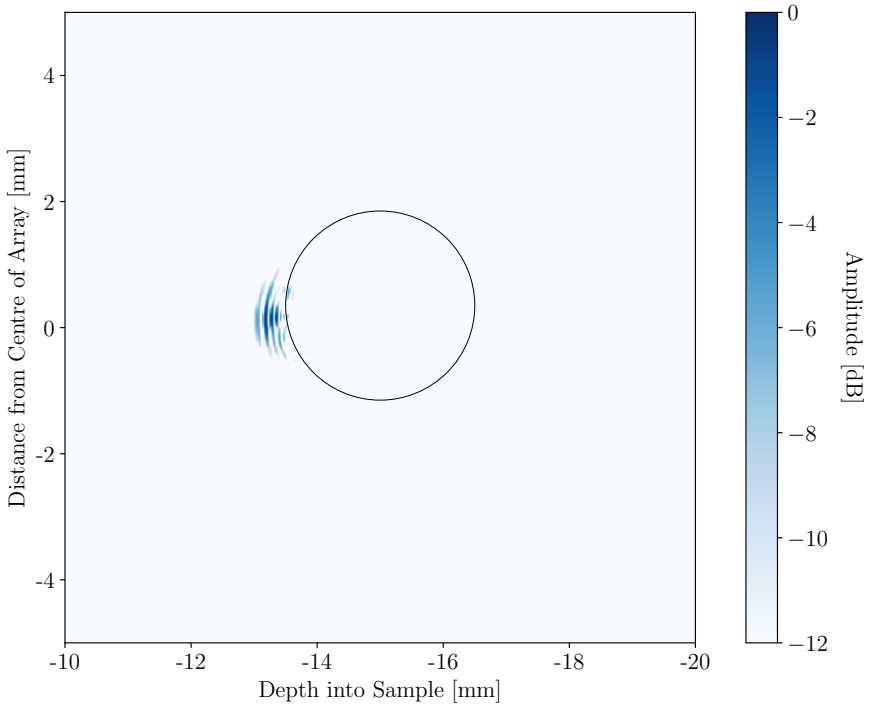

(a) *TFM image of simulated 3 mm diameter void reflector in water with measured peak time error incorporated into TFM algorithm.*

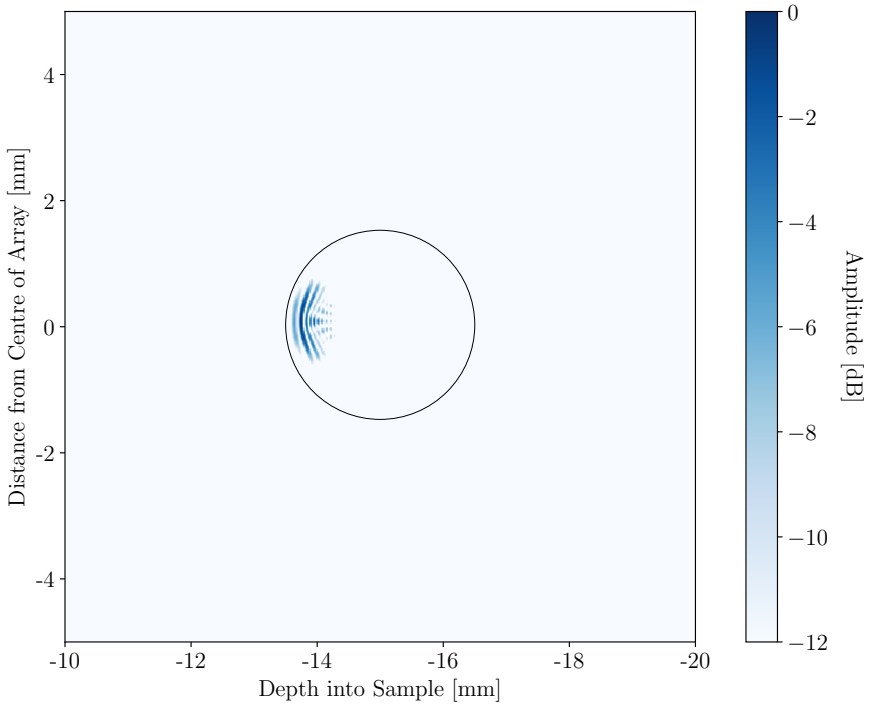

(b) *TFM image of simulated 3 mm diameter void reflector in water without measured peak time error incorporated into TFM algorithm.*

Figure 3.16: *TFM images generated from simulated FMC data set of a 3 mm diameter void reflector in water.*

ferent materials and illustrates that the peak time error is mostly due to hardware variation and not heterogeneity in the sample medium.

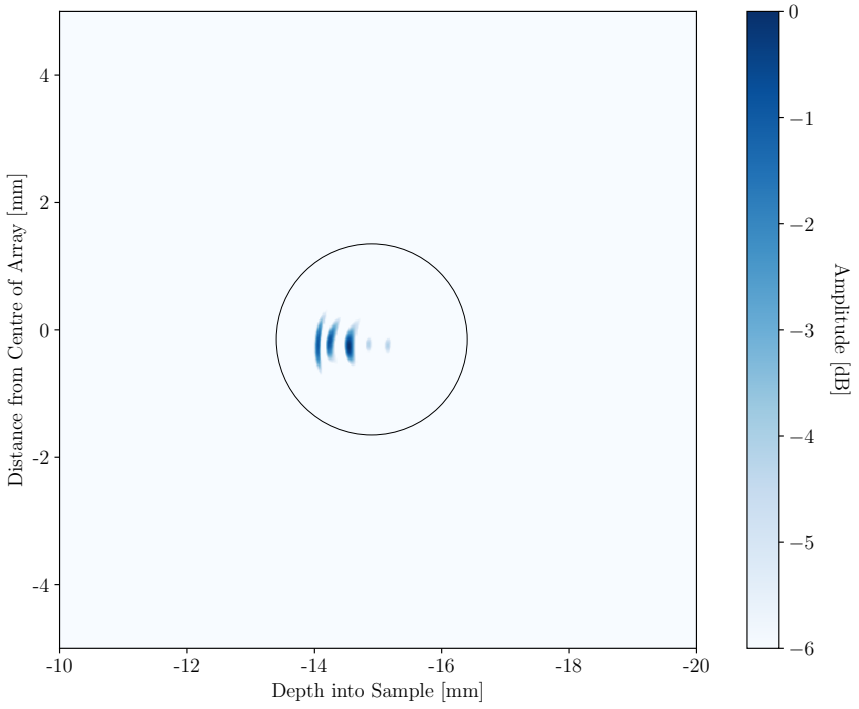

(a) *TFM image of 3 mm SDH in Perspex without TFM calibration.*

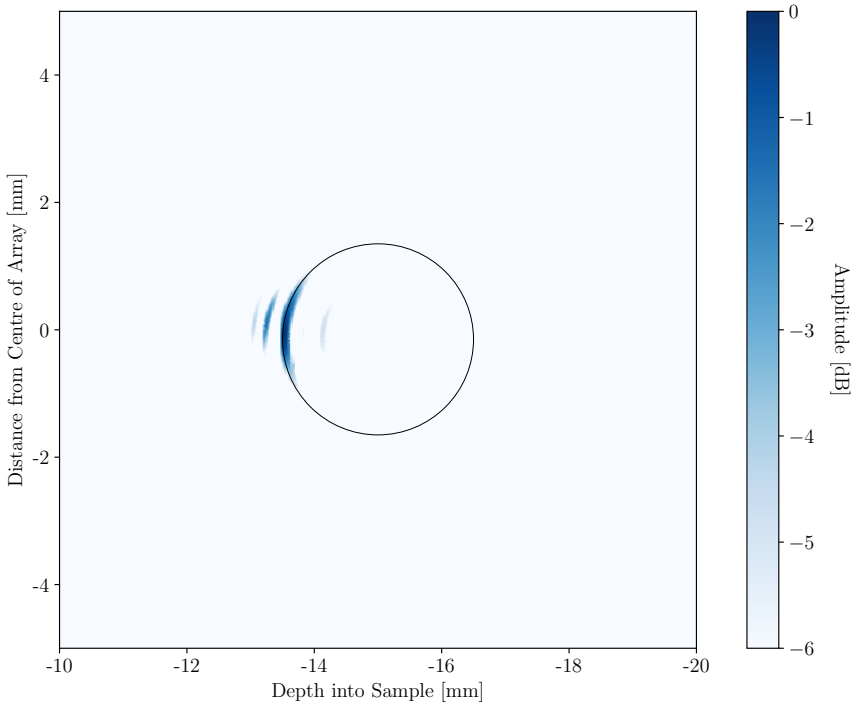

(b) *TFM image of 3 mm SDH in Perspex with TFM calibration.*

Figure 3.17: *TFM images generated from experimental FMC data sets of a 3 mm diameter SDH in Perspex.*

3.4 Summary

The aim of this Chapter was to present a novel calibration methodology for ultrasonic hardware including linear phased arrays and PACs. A quick and robust methodology was presented to detect individual channel or element irregularities on the ultrasonic hardware via a user-friendly GUI. This is the first example of ultrasonic hardware calibration being applied specifically for FMC data sets, where previous attempts have focussed on beam integrity rather than array integrity.

A key output of this work was demonstrating that the A-Scan response observed at a given element location is highly dependent on the PAC used. Therefore, it is vital that calibration procedures pertain to the coupled array-PAC system rather than a single component of the ultrasonic hardware system. The calibration process led to the development of a peak time correction method that was incorporated directly into the TFM imaging algorithm. This enhanced the accuracy of TFM images by offsetting time delays deriving from inconsistencies within the hardware.

In summary, calibration of ultrasonic hardware provides useful insight into the performance of phased arrays and the PACs used to drive them. By gathering experimental data about the accuracy of signal acquisition, the quality of data acquired from these instruments can be increased and the images generated from these data enhanced. This ultimately increases the certainty of ultrasonic measured data that will be used to increase the accuracy of TFM images generated in the remainder of this Thesis.

Chapter 4

Non-Invasive Ultrasonic Imaging

4.1 Introduction

Non-invasive process analysis involves the transmission of process information through the process vessel wall. The fundamental technical challenge for non-invasive ultrasonic measurement is the transmission across the strongly reflecting acoustic boundary at the steel-process interface. At this interface most energy is reflected back towards the transducer, making signals reflected from within the process relatively weak and introducing reverberations into the measured data.

These high amplitude reverberations are aliased with the lower amplitude reflections from within the process stream. Therefore, the amplitude of pixels

corresponding to points in space within the process stream receive pixel value contributions from the reverberations within the steel vessel. This has the impact of masking signals from within the process stream and offsetting the dynamic range of the final TFM image.

In terms of the practical application of phased arrays to non-invasive process imaging, it is advantageous to design a system that is not dependent on the measurement of a background signal. It is not always possible or cost-effective to turn off a process to acquire a background measurement, therefore an aim of this work is to investigate methodologies that required minimal *a priori* knowledge of the ultrasonic system.

In this Chapter, one-based indexing has been used to identify reverberations. This means the first reflection from the steel-fluid interface that arrives at the transducer, the wave that has travelled twice the vessel wall thickness, is referred to as the first reverberation. The reason for using this notation was that due to signal aliasing this initial reflection still impacts on the dynamic range of the image scene. So it was important to include interference from this reflection as a reverberation to be suppressed. The wave that has travelled the distance corresponding to four times the vessel wall thickness is referred to as the second reverberation.

By postulating that signals relating to the process are contained within the bulk ultrasonic data but are just masked due to their lower amplitude, it is reasonable to hypothesise that these signals of interest can be extracted through signal processing of the bulk signal. This Chapter proposes several methodologies relating to the extraction of signals of interest from a bulk FMC data set contain-

ing reverberation interference. In addition, two of the proposed methodologies have been coupled together to enhance the observed reduction in reverberation interference.

4.2 Reverberation Suppression Methodologies

4.2.1 Reverberation Pattern Gain Correction Method

4.2.1.1 Background

A novel methodology has been proposed to identify and minimise the impact of signal aliasing due to ultrasonic reverberations. The methodology is a two-stage process, first the reverberation pattern is identified using ray tracing and the TOF values for each reverberation are stored in a look-up table (LUT). Next, the time samples corresponding to the reverberation pattern are passed through a gain correction window to reduce the amplitude of the time samples corresponding to the reverberations. When the two processes were combined the methodology was called the reverberation pattern gain correction method (RP-GCM).

Previous attempts to identify reverberations within layered media have used the frequency domain power spectra of the raw time domain data to ascertain the likelihood that a reflection is due to a primary reflection or a reverberation pattern [135, 136]. In these examples, the TOF of the reverberations was not empirically estimated but the likelihood that a signal corresponded to a reverberation was determined. In doing so, it was assumed that the incident wave was plane and not spherical so this method could not be applied to FMC data sets.

Non-invasive ultrasonic flow mapping has been developed for monitoring of crystallisation during the photovoltaic cell solidification process [137, 138]. Ultrasonic measurements were acquired through a glass vessel wall that was thick enough to create a large time separation between reverberations. Therefore it was proposed to cancel out the reverberation signals by using a rectangular window with a value of zero for time samples corresponding to reverberations and a value of one elsewhere.

4.2.1.2 Theory

Consider a linear phased array with K elements in the active aperture each positioned precisely the same distance apart, creating a well-defined element pitch, p (mm). This array was coupled directly to the outside wall of a steel layer, where the array was assumed to be perfectly coupled to the steel and no noise was introduced into the system from mis-alignment of the array. The system was simplified further by assuming the steel-fluid interface was parallel to the front face of the array. A schematic of this system is shown in Figure 4.1 for $K = 8$ elements and for the first two reverberations.

Under these conditions, the reverberating system was geometrically similar, independent of the element that was transmitting. This increased the efficiency of the algorithm because only K individual path lengths needed to be determined for n reverberations to construct the LUT. The path length to be extracted from the LUT was then dependent on the integer difference between the transmitting, T_x, and receiving, R_x, element indices rather than their absolute positions in the system.

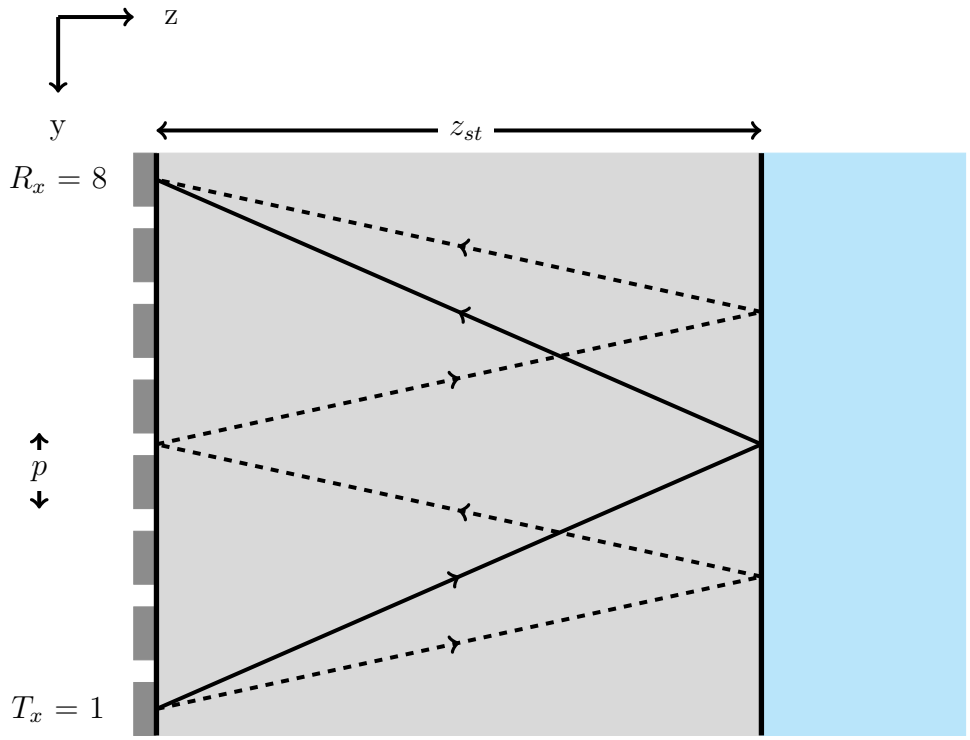

Figure 4.1: *Schematic of reverberation pattern in steel layer for first two reverberations.*

The ray path length, $r(n)$ (mm), for the n^{th} reverberation could then be established using the distance to the steel-fluid interface from the front face of the array, z_{st} (m), using Pythagoras' Theorem

$$r(n) = 2n\sqrt{z_{st}^2 + \left(\frac{p(T_x - R_x)}{2n}\right)^2}. \tag{4.1}$$

The values of $r(n)$ were converted to TOF values in units of samples, TOF_s,

$$TOF_s = \left(\frac{r(n)}{\nu} - t_0\right)\frac{1}{F_s} \tag{4.2}$$

where ν (ms^{-1}) was the speed of sound in the steel layer. These TOF sample

values were then stored in the LUT with K rows and n columns. The number of reverberations to be calculated was determined by the desired image depth into the fluid load.

Once the LUT has been generated the number of time samples corresponding to the pulse length of the transmitted signal was determined. The peak detection methodology employed was that developed by Namas et al [134]. This was the same process used for time domain peak detection in Chapter 3. This generated a clear time domain peak of the first reverberation, where the pulse length was the time difference (samples) between the first and last samples greater than an arbitrary cut-off value. The cut-off value was selected to be -40 dB because this represented the typical amplitude difference between reverberations and the signals of interest and this will be presented in the results below. In addition, it enabled ring-down time to be accounted for in addition to the main reverberation peak.

Finally, the FMC data set was passed through a gain window prior to TFM image construction. The first time sample corresponding to each reverberation was identified from the LUT and the following time samples comprising one pulse length were reduced in value by an arbitrary number of decibels. The gain reduction process will have the impact of attenuating signals corresponding to the reverberations but also signals of interest that were aliased closely with these reverberations. Therefore, it was important to adjust the gain window with respect to the SNR required to generate coherent reflectors in the final image.

4.2.2 Phase Coherence Imaging

4.2.2.1 Background

Phase coherence imaging (PCI) was developed by Camacho et al [139] to improve image quality in samples containing noise from artefacts that do not derive from the main beam. The underlying principle of PCI states that image quality is predominantly determined by the lateral resolution of the ultrasonic beam. That is, the ratio of the intensity of the main beam relative to any side or grating lobe artefacts.

It was their aim to develop a methodology that was easy to implement while working in real time relative to the image generation process. This can be achieved by integrating the PCI process into the TFM process, as there is an intrinsic overlap in how these two processes operate. Consider the regular TFM process, where the value of a pixel is explicitly defined by the amplitude of the time domain A-Scan signals in the FMC data set. In contrast, the PCI process determines the instantaneous phase of the FMC data to map the phase concentration of the image.

The distribution of the instantaneous phase is used to generate a phase coherence factor (PCF). The PCF provides a measure of the variance of the phase through the time domain A-Scan signals at each pixel, which is used to weight the value of pixels in the final image. This is possible because the distribution of the phase from a perfectly focussed scatterer will always be zero, whereas phase artefacts from spatial side lobe activity deviate the phase distribution towards one. Therefore the PCF becomes a matrix with the same dimensions as the TFM

image, although with values ranging from 0 to 1 for each pixel corresponding to the coherence of the focal point with the main beam.

4.2.2.2 Theory

The instantaneous phase, $\psi(t)$, of the signal can be determined from the real and imaginary terms of the Hilbert transform of the time domain signal,

$$H(t) = S_r(t) + jS_i(t), \tag{4.3}$$

where $S_r(t)$ and $S_i(t)$ represent the in-phase and quadrature components of the signal. From this analytical signal representation, the instantaneous phase is calculated

$$\psi(t) = \tan^{-1}\left(\frac{S_i(t)}{S_r(t)}\right). \tag{4.4}$$

For a given pixel, $\psi(t)$ is calculated $M = K^2$ times and the value of the PCF at that pixel location is calculated from

$$PCF_{ij} = \max\left[0, 1 - \frac{\sigma(\psi)}{\sigma_0}\right] \tag{4.5}$$

where $\sigma(\psi)$ is the standard deviation of the instantaneous phases of the A-Scan signals and $\sigma_0 = \pi/\sqrt{3}$ represents the standard deviation of a uniformly distributed random variable. Note, the PCF assumes the phase can be represented by a continuous variable within $[-\pi,\pi]$, so σ_0 can be said to be uniformly distributed.

When this delay and sum approach is implemented via a GPU, it computes the pixel intensity, I_{ij}, and PCF_{ij} in parallel on a pixel-by-pixel basis. The GPU TFM algorithm has been optimised to minimise the total memory allocation required per pixel. This is achieved using an accumulator float that has a fixed memory location for the given pixel being calculated. Each iteration of the TOF calculation simply adds to this accumulator, without storing the data point in memory, therefore reducing the total memory cost required. However, determination of the PCF requires M values of instantaneous phase to be stored in memory, for each pixel, prior to its calculation. Although, this would still be in real time relative to the TFM imaging process, it would slow down the overall process by restricting the device memory available for parallel processing. Camacho et al [139] have also proposed an alternative criterion called the sign coherence factor (SCF), which significantly simplifies the PCI process while maintaining accuracy within 1% of the PCF criterion.

The SCF proposes that the total phase variation can be discretised, where previously it was considered a continuous variable ranging $[-\pi,\pi]$. The SCF proposes that the total phase interval can be represented by a discrete [-1,+1] variable, which is done by representing the time sample by a single signed bit

$$b = \begin{cases} +1, & \text{if } y_m(t) >= 0, \\ -1, & \text{if } y_m(t) < 0, \end{cases} \tag{4.6}$$

where b is the sign bit of the time sample. The variance of b is then represented

as

$$\sigma^2 = \frac{M \sum_{m=1}^{M} b_m^2 - \left(\sum_{m=1}^{M} b_m \right)^2}{M^2}. \tag{4.7}$$

However, since b represents sign bits, $\sum b^2 = M$, the variance can be simplified to

$$\sigma^2 = 1 - \left(\frac{1}{M} \sum_{m=1}^{M} b_m \right)^2 \tag{4.8}$$

The SCF at the pixel location is then defined as

$$SCF_{ij} = 1 - \sigma = 1 - \sqrt{1 - \left(\frac{1}{M} \sum_{m=1}^{M} b_m \right)^2}. \tag{4.9}$$

The key advantage of using the SCF over the PCF is that it is estimated from the average of the sign bit values. Since the total number of sign bits will always be known, it is not necessary to store them in individual memory locations. Therefore a SCF accumulator can be used to sum the sign bits for each TOF calculation. This greatly reduces the processing cost relative to using the PCF, limiting the impact to the imaging algorithm processing speed.

4.2.3 Subspace Analysis

4.2.3.1 Background

Subspace analysis is a clutter filter methodology based on principal component analysis (PCA) proposed by Demirli et al [140]. The methodology was designed specifically to overcome noise introduced into ultrasonic data due to the presence of reverberating layers in NDE samples. It is argued that most techniques, including predictive deconvolution and background subtraction, rely on the repeatability of measured data and on reverberation patterns, and therefore are not robust enough when applied to experimental NDE systems. Given that here the phased array is in direct contact with the steel vessel, it has been argued that there is uncertainty in the FRD resulting from wave speed inhomogeneity, surface roughness and coupling of the probe to the steel. It was argued that these added to the complexity of the reverberation pattern such that it cannot be easily predicted and erased from the FRD.

The methodology uses PCA to rank the latent variables of the FRD in terms of their variation contribution to the bulk FRD. The latent variables corresponding to the reverberations are then identified using an information theoretic criterion. These latent variables can then be actively deselected from the FRD removing contributions from the reverberations prior to construction of the ultrasonic image.

A particular advantage of this approach was that it does not require any *a priori* knowledge of the measurement system. Alternative methodologies typically require metadata associated with the measurement system before they can be

implemented. For example, predictive deconvolution requires the digitisation frequency, F_s, of the ADC to be known. Also, estimation of the reverberation TOF requires knowledge of the layer and device geometry and the speed of sound while also assuming that these are well defined and consistent across different data sets. Subspace analysis is only dependent on the FRD itself, reducing uncertainty in the methodology.

Subspace analysis has been previously applied to FMC data sets for phased array imaging of NDE samples [141]. Here an FMC data set corresponding to a 128 element linear array was processed using PCA to identify the latent variables corresponding to artefacts of the dead zone. However, only the first 200 time samples were analysed, significantly reducing the computational strain on the algorithm. This was not possible in this Thesis because the reverberations to be suppressed were present throughout the entire A-Scan length.

Also, Scharrer et al [9] have proposed the application of a synthetic aperture focusing technique for NDE samples that were pre-processed using subspace analysis. The FRD consisted of A-Scans acquired using a spherically focused single element transducer positioned at precise measurement locations. However, as this was not acquired using a phased array the data set does not represent the full matrix of array measurement data and images were not constructed using the TFM.

4.2.3.2 Theory

Consider a phased array with a K element aperture, that was used to acquire the full matrix of transmit receive signals. If the FMC data set, $Y_e \in \mathbb{R}^{\mathrm{M}\times\mathrm{N}}$,

arose from an array mounted to the outside wall of a steel vessel, there will be wall reverberations intrinsic to all the measured data. These reverberations are in addition to measurement noise and the signals of interest from within the process. Therefore, the time domain signals can be represented by three terms

$$y_m(t) = s_f(t) + r(t) + n(t), \tag{4.10}$$

where $s_f(t)$ is the signal of interest from reflectors within the process stream, $r(t)$ is the clutter due to reverberations within the steel vessel wall and $n(t)$ represents zero-mean white Gaussian noise. This means that both the signals of interest and noise are completely independent of the reverberation signals. Assuming the vessel wall is infinite relative to the size of the aperture on the y-axis, the only variation in $r(t)$ between elements will be local heterogeneity due to surface roughness or speed of sound. This means there is a large degree of coherency between the reverberation signals from any pair of elements. However, for the signals of interest there will be a higher degree of inconsistency across the FMC because the spatial orientation from reflectors within the process is not consistent for all element locations.

The covariance matrix, $C_{Y_e} \in \mathbb{R}^{\mathrm{M}\times\mathrm{M}}$, of the FMC is

$$C_{Y_e} = \frac{1}{M} Y_e Y_e^T \tag{4.11}$$

where $[\cdot]^T$ denotes the transpose operator. The covariance matrix is then decom-

posed into its latent variables using Eigen decomposition

$$C_{Y_e} = \sum_{m=1}^{M} \lambda_m \mathbf{u}_m \mathbf{u}_m^T, \tag{4.12}$$

where λ_m is the m^{th} eigenvalue ordered from largest to smallest and $\mathbf{u}_m$ represents its corresponding eigenvector.

For the purpose of this investigation, the number of eigenvectors corresponding to $r(t)$ was not determined using the Akaike information criterion proposed by Demirli et al [140] because it was too computational intensive for real-time analysis. However, it was reasoned that the eigenvectors corresponding to the largest K eigenvalues, describe the variation in Y_e resulting from the wall reverberations and the remaining $\eta = M - K$ eigenvectors describe the variation in Y_e resulting from the signals of interest *i.e.* the reflections from the voids and noise. This is because the reverberation signals were much larger in amplitude, dominating the response relative to the weaker void reflections and noise.

From the first K eigenvectors in the ordered set, the reverberation subspace, $U_r \in \mathbb{R}^{\mathrm{M}\times\mathrm{K}}$, was constructed

$$U_r = [\mathbf{u}_1 \ \mathbf{u}_2 \ \ldots \ \mathbf{u}_K]. \tag{4.13}$$

When the orthogonal subspace of U_r was projected onto the FMC data, the signals corresponding to the reverberation clutter were weighted relative to the signals of interest, which had the impact of removing them from the FMC data,

$$\hat{s}_f = I - \left(U_r U_r^T\right) Y_e, \tag{4.14}$$

where I is the identity matrix and $\hat{s}_f \in \mathbb{R}^{M \times N}$ was the modified FMC data used to construct the image scene.

4.3 Simulation Model

An FE model was developed in PZFlex [55] to generate an FMC data set of the target image scene. A schematic of the FE model is shown in Figure 4.2, which indicates the key design parameters. Note, the image target was stationary because it was not possible to model a dynamic system, however, relative to the data acquisition rate, this was a reasonable approximation to an experimental system. The transducer itself was modelled as a pressure loaded array, meaning no transducer effects were modelled and it was assumed the device was perfectly coupled to the outside wall of the steel vessel. This simplified design ensured that variations were purely due to the integrity of the methodology rather than noise from the array design. A two-dimensional model was created because there was symmetry along the yz-plane.

This model was designed to replicate an experimental apparatus. As will be discussed in Chapter 6, to maximise the experimental data acquisition rate, a 32 element aperture is used. Therefore the FE model was designed as a 32 element array. The driving conditions of the model were a 5 MHz Blackman-Harris function that was selected to reduce any frequency domain side lobe activity. The element width was set to 0.6 mm, which is approximately half the wavelength of the 5 MHz driving function in steel. The water was modelled at 25 °C with a density of 1000 kgm^{-3} and speed of sound of 1496 ms^{-1}. The steel was mod-

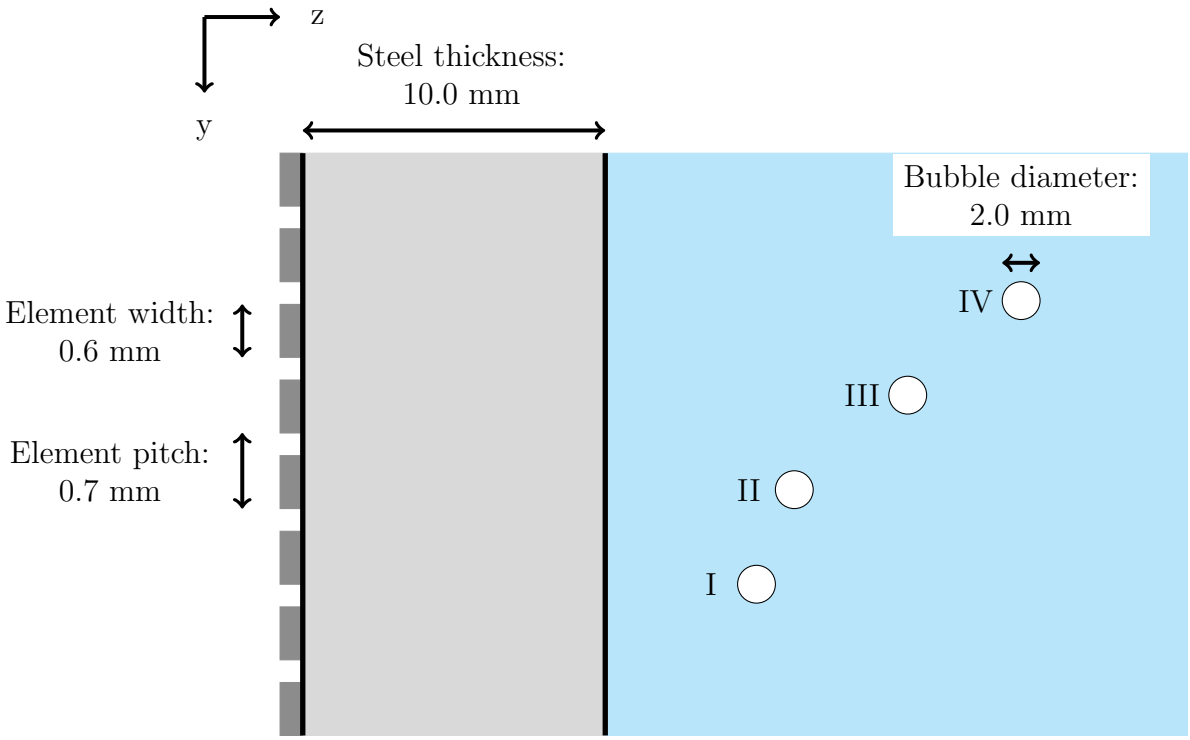

Figure 4.2: *Schematic of PZFlex model used to generate a non-invasive FMC data set.*

elled at 25 °C with a density of 7890 kgm^{-3} and speed of sound equal to 5790 ms^{-1}. The mesh size was set to 15 elements per wavelength relative to a 5 MHz input function and the speed of water. The thickness of the steel vessel wall was set to 10 mm which was approximately eight times the ultrasonic wavelength in steel. This created a time separation between reverberations leading to each being well spatially resolved in the final images. The bubble reflectors were modelled as stationary circular voids that reflected 100% of the ultrasonic energy at their boundaries. The diameter of the bubbles was set to 2 mm, approximately ten times the ultrasonic wavelength in water, providing strong interaction with the ultrasonic wave. The position of the bubble reflectors was designed so that aliasing occurred with the reverberation signals for reflectors I and III but not

reflectors II and IV. The boundary conditions on the model were set to absorbing and the void reflectors were placed in water at 20 °C, with the boundaries infinitely extending relative to the temporal range of the ultrasonic reflections. This generated a system with adequate reverberations but without artefacts from the transducer or elsewhere.

In addition to the model outlined above, an identical model was created except without any void reflectors in the water load. This was used to generate a background FMC data set that when subtracted from the FMC data set containing reflector signals, provided a benchmark for the reverberation removal methodologies proposed. However, in practice this background signal would not be available in a process analysis environment because it requires turning the process off to acquire the data set.

4.4 Quantification of Reverberation Suppression

For classification purposes, in the remainder of this Chapter, the 'regular' image refers to the TFM image when no reverberation suppression has been applied and the 'modified' image refers to the TFM image after application of any of the signal processing methodologies outlined in Section 4.2.

The quantification process was performed on specific regions of interest (ROI) for each of the four reflectors. To establish a benchmark response, the background FMC data set was subtracted from the regular FMC data set and the image scene constructed using the TFM. For each ROI in the modified TFM image generated from the background subtracted data set, the pixel coordinates of the

maximum pixel amplitude were recorded. These same pixel coordinates were used to quantify the image enhancement resulting from the application of each of the reverberation removal methodologies. The value of these pixels were measured in units of decibels relative to the maximum pixel value in the full image scene of the corresponding image. The decibel difference of the pixel coordinates in the regular and modified images represented the image enhancement for that ROI.

4.5 Results and Discussion

4.5.1 Reverberation Response and Benchmark Solution

To provide a visual understanding of how the reverberation pattern clutters the image scene, the FMC data set generated from the FE model with the four reflectors present was constructed into a TFM image in Figure 4.3. In this image the true positions of the void reflectors were shown by the black circles, where reflector I was shown to be strongly aliased with the third reverberation. The reverberations were observed as high-amplitude vertical lines attenuating along the z-axis. The most strongly interfering reverberations were located within the first two millimetres of the z-axis. The dynamic range of the image scene was set by the maximum pixel value such that it was set by these initial reverberations. This was because the dynamic range was a logarithmic scale (decibels) relative to the maximum pixel value in the image scene. This offsets the dynamic range of the ROIs corresponding to the void reflectors, such that they were only observable by setting the dynamic range to be at least 40 dB. Therefore, it was difficult to ex-

tract quantitative information about the position and size of the void reflections from this image. This demonstrates the reasoning for investigating reverberation removal methodologies. In this Section, the quantification of reverberation suppression image enhancement pertains to the degree of enhancement relative to the image scene in Figure 4.3.

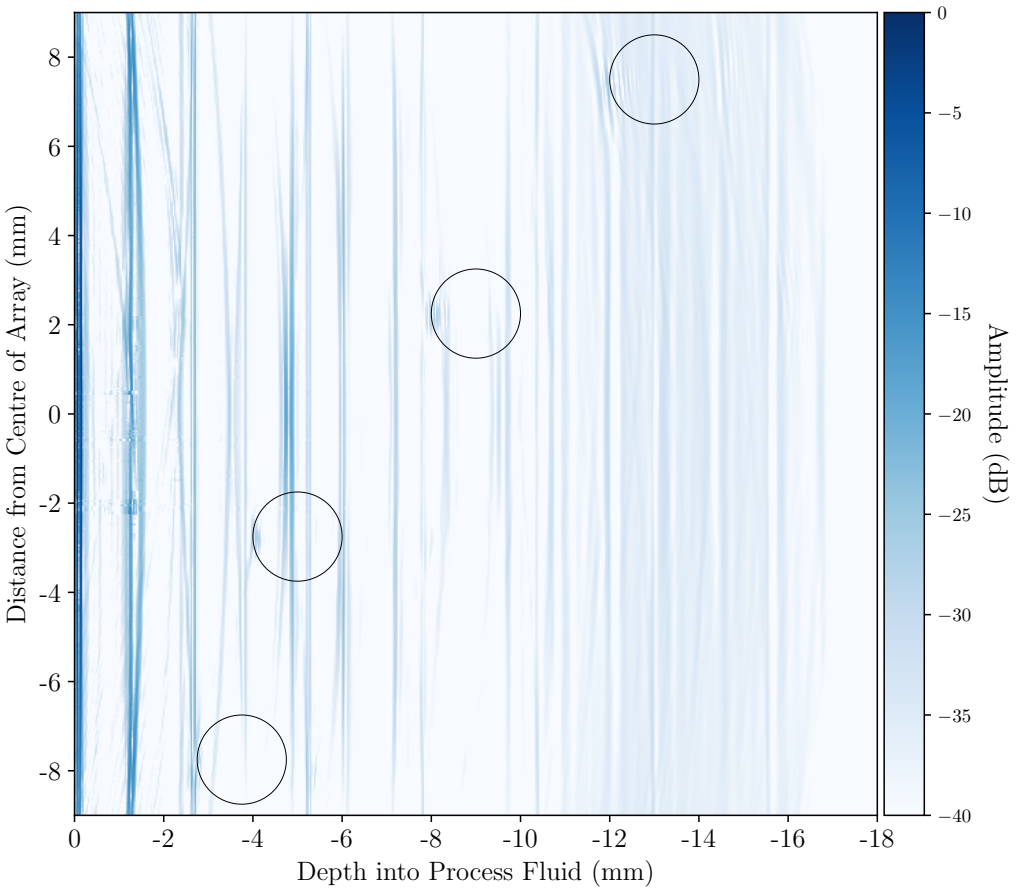

Figure 4.3: *TFM image from simulated FMC data without any reverberation removal prior to image construction. Black circles represent the true location of the reflectors.*

Under ideal conditions, the background response from the image scene is known. The background FMC data set was subtracted from the FMC data set with void reflectors present to obtain the background subtracted FMC data set. The resulting TFM is shown in Figure 4.4. This response represents the benchmark or ideal reverberation suppression response, where all noise from the incident reverberations has been removed prior to image construction. Note, the dynamic range of the benchmark image was set to 20 dB, which illustrates the enhanced SNR. The degree of image enhancement from the background subtraction was recorded alongside each of the different reverberation suppression methodologies to demonstrate the image enhancement relative to this ideal case.

In Figure 4.4, there were additional artefacts observed as low amplitude multiples of the void reflectors. These corresponded to signals reflected from the void reflectors that echoed within the steel vessel wall after the initial wave reaches the transducer. These were observed only when the dynamic range was extended beyond 15 dB, however they generate additional complexity in terms of extraction of quantitative information from the image.

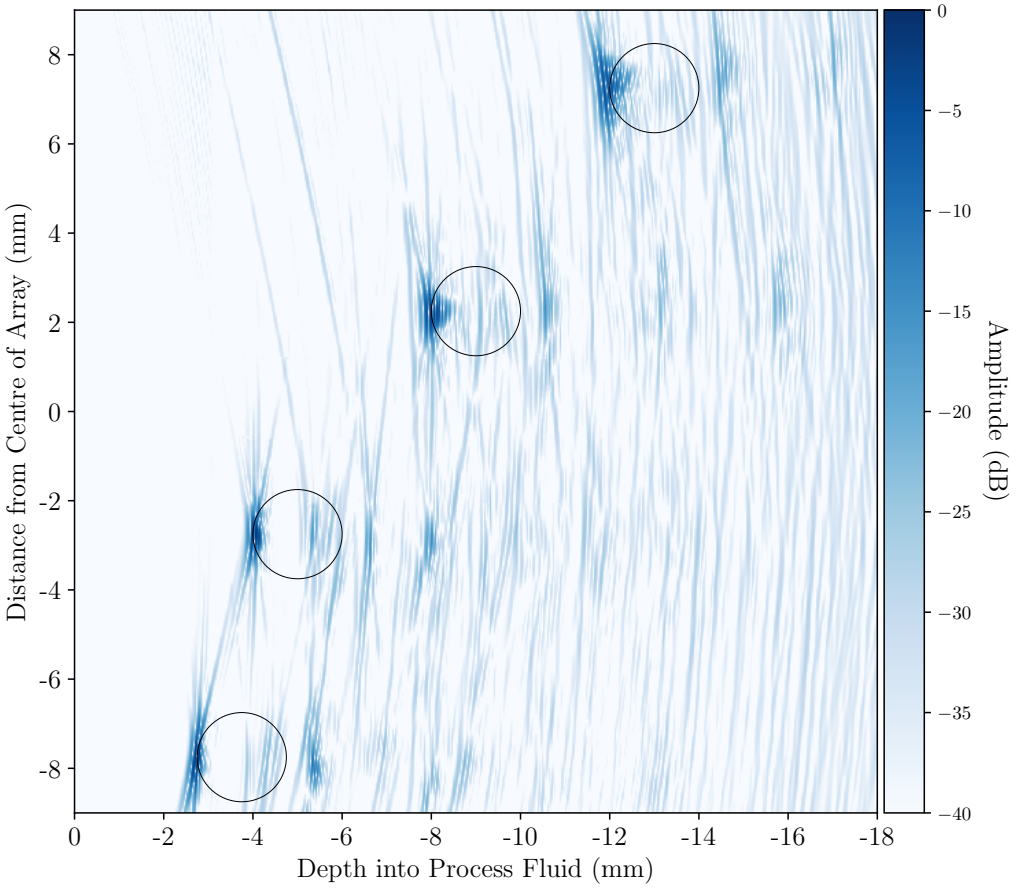

Figure 4.4: *Result from background subtraction of simulated FMC data prior to TFM image construction. Black circles represent the true location of the reflectors.*

4.5.2 Reverberation Pattern Gain Correction Method

The pulse length was estimated from the first reverberation signal, in Figure 4.5, to be 712 time samples at the -40 dB level. Therefore the first 712 time samples after the TOF identified in the LUT were passed through the gain window.

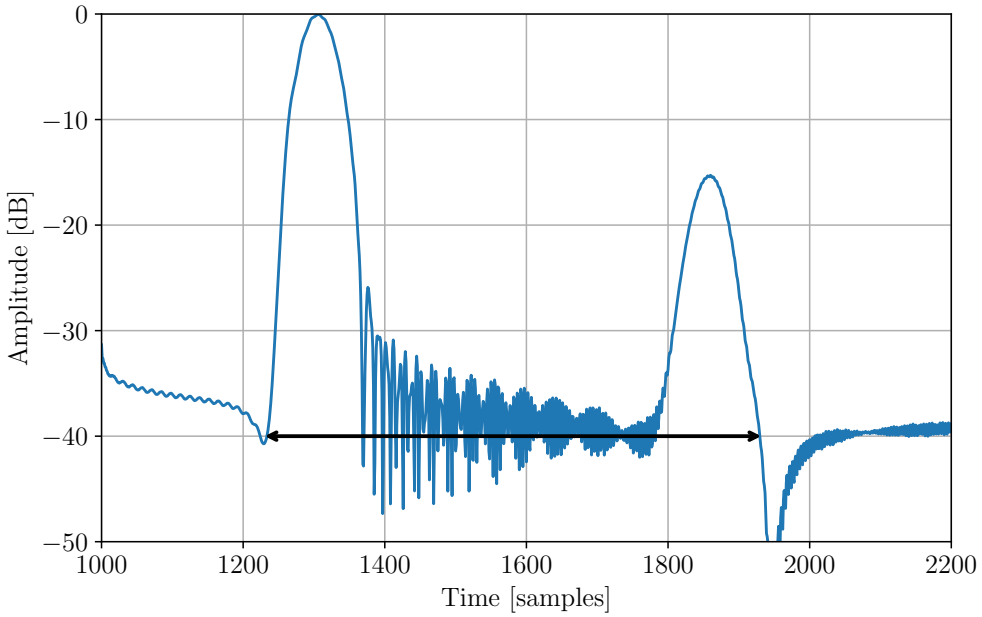

Figure 4.5: *Plot of first reverberation used to estimate the pulse length of the reverberation signal shown by the doubled-headed arrow.*

A LUT was generated for the first 12 reverberations to ensure all reverberations within the image scene were adequately identified. Following this, the FMC data set generated from the FE model with the four reflectors was passed through the gain window, where signals corresponding to reverberations were reduced by 100 dB to provide strong signal suppression. This gain-corrected FMC data set was then used to construct the TFM image shown in Figure 4.6. To adequately image the ROIs the dynamic range in Figure 4.6 was set to 12 dB, which is much less than the 40 dB required in Figure 4.3 to achieve a similar degree of void visualisation. This highlights how the RP-GCM has enhanced the SNR relative to when no post-processing was undertaken.

Upon application of the RP-GCM, the amplitude of the reverberations was

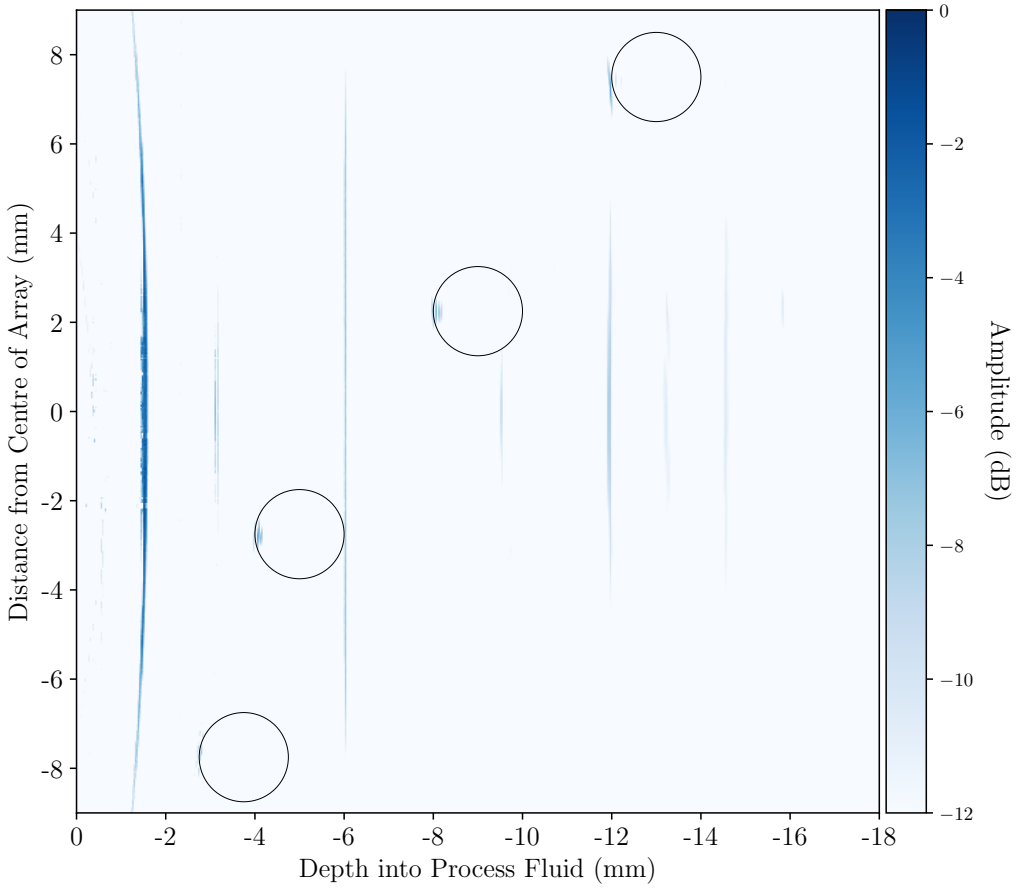

Figure 4.6: *Image scene of void reflectors with the dead zone included and the RP-GCM applied prior to TFM image construction. Black circles represent the true location of the reflectors.*

reduced, however, although the signals from the reverberations were minimised, the estimated pulse length did not capture the full reflection from the steel-fluid surface. This resulted in some signals corresponding to the second reverberation (the second highest amplitude reverberation) not being passed through the gain

window, off-setting the dynamic range of the final image. However, if the pulse length was increased further to remove this artefact, the signals corresponding to the ROIs were also passed through the gain window. Therefore a compromise was required to generate adequate images of the process region. Given that the highest amplitude reverberations always occurred in the region closest to the steel-fluid interface, the first two millimetres were declared a dead zone where signals could not be reasonably resolved.

The TFM image constructed with the z-axis beginning at 2 mm to remove pixels from the dead zone is shown in Figure 4.7. The dynamic range of this image was kept at 12 dB to illustrate the relative enhancement in the brightness of the ROIs. However, it was also observed that subsequent reverberations became amplified. This highlights the compromise required when estimating the pulse length as increasing the number of time samples passing through the gain window resulted in a weaker response from the ROIs. This was seen as a significant drawback to the methodology because it was highly sensitive to the estimation of the pulse length.

The amplitude enhancement for each ROI was recorded in Table 4.1 for the background subtracted image and for the RP-GCM with and without the dead zone included in the image scene. The RP-GCM with the dead zone included represented an enhancement, in the pixel coordinates for each of the ROIs, of at least 9.03 dB relative to the background subtracted response. Upon removal of the dead zone from the image scene, the pixel response from the ROIs was no more than 6.22 dB relative to the benchmark response.

The RP-GCM was somewhat capable of separating reverberation noise from

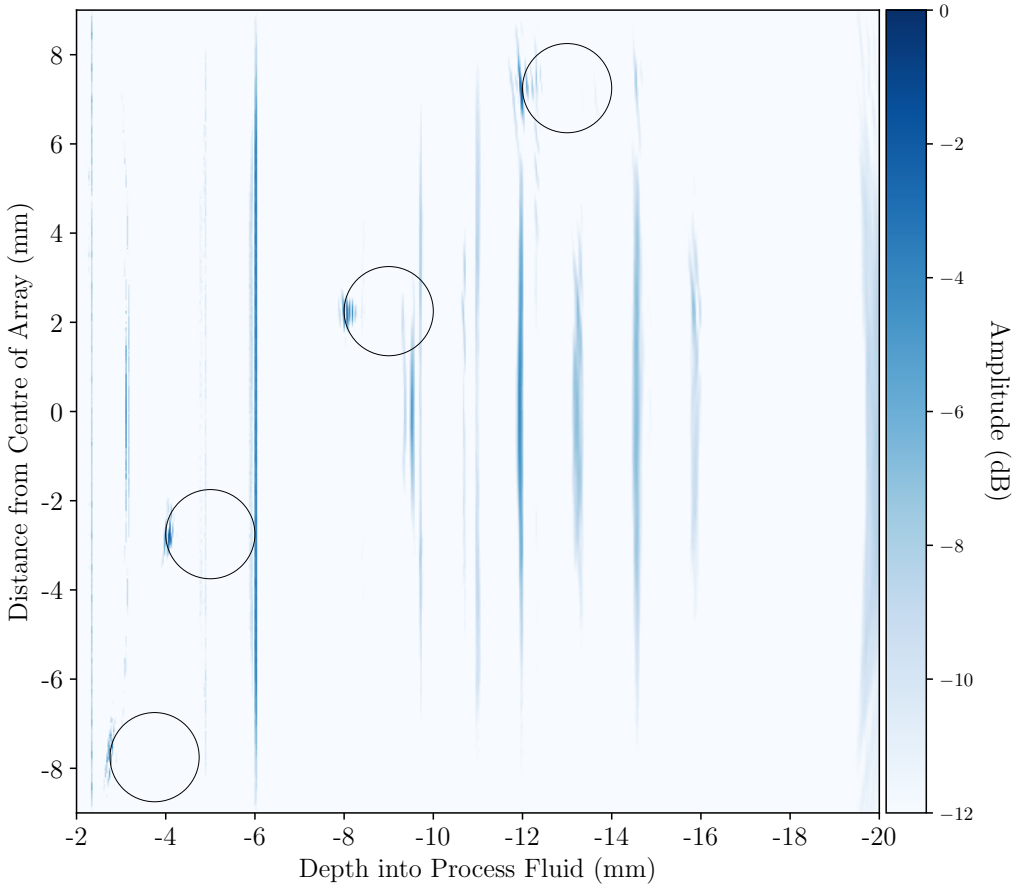

Figure 4.7: *Image scene of void reflectors excluding the dead zone and the RP-GCM applied prior to TFM image construction. Black circles represent the true location of the reflectors.*

the signals of interest. Reflectors I and III were positioned to aliase with the TOF of the third and eighth reverberations respectively. These two ROIs were shown to be enhanced by a similar degree to reflectors II and IV in Table 4.1. However, this was only achieved by reducing the number of time samples passed through

Table 4.1: *Image enhancement using RP-GCM, all values in decibels.*

Reflector	Background Subtraction	RP-GCM with dead zone	RP-GCM without dead zone
I	25.54	18.34	19.32
II	24.30	20.39	22.53
III	24.71	19.06	22.36
IV	27.83	18.90	21.63

the gain window that increased reverberation noise in the final image.

The quantification methodology employed did not fully capture the degree of SNR enhancement. Upon qualitative inspection of Figures 4.6 and 4.7 it was observed that the RP-GCM was not robust enough to completely remove the reverberation signals. The presence of the reverberation noise in the images means that it was still difficult to identify and extract quantitative information about the size and position of the void reflectors from these images.

4.5.3 Sign Coherence Factor Imaging

The SCF matrix was generated in parallel with the linear TFM image matrix using the FMC data output from the FE model. The sensitivity of the SCF matrix was manually adjusted using the exponent, w, where $w = 1.0$ uses the full sensitivity of the SCF and $w = 0.0$ is equivalent to imaging without the SCF. To maximise the SCF sensitivity the $\mathrm{SCF}^{1.0}$ matrix was computed prior to multiplication with the linear TFM matrix. The resulting scaled image is shown in Figure 4.8.

A dynamic range of 40 dB was required to observe the ROIs. This was larger

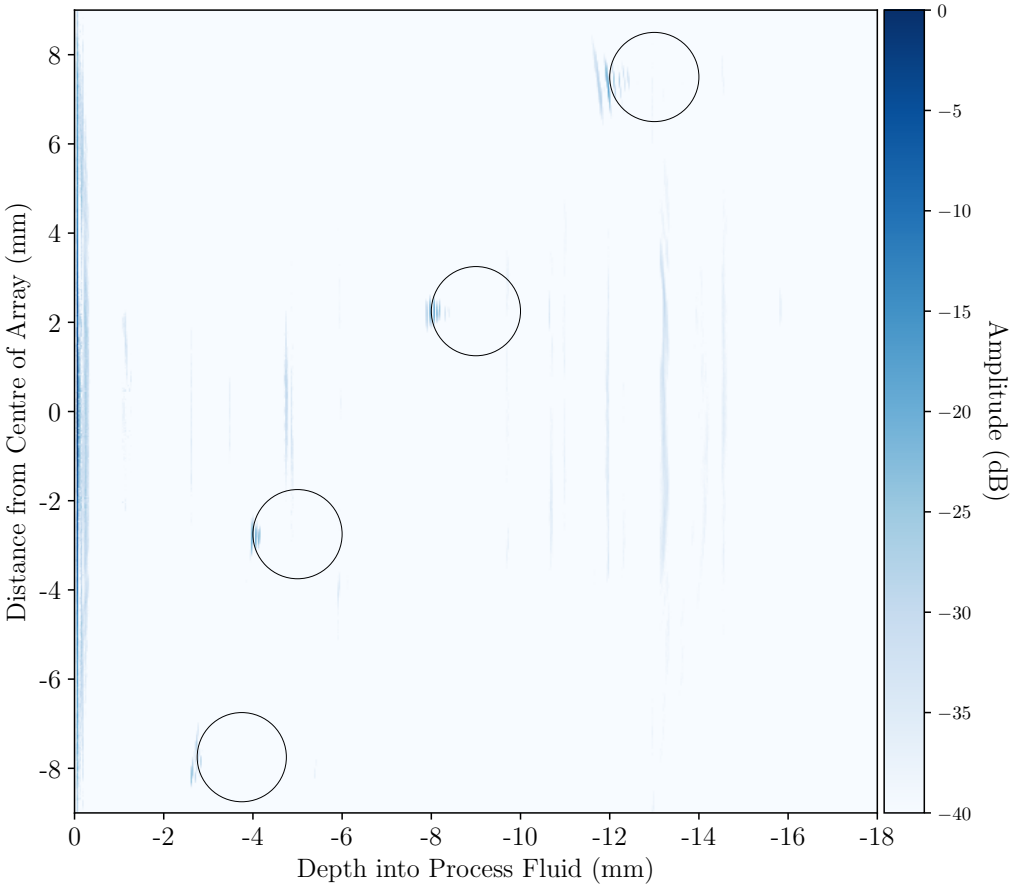

Figure 4.8: *Image scene of void reflectors with the dead zone included and the* $SCF^{1.0}$ *applied to the TFM image construction. Black circles represent the true location of the reflectors.*

than that required to observe the ROIs with the RP-GCM because the SCF has the impact of weighting the linear TFM pixel values by a fraction between zero and one. Therefore, unless a pixel corresponds to a direct reflection from the main beam, it will have a value lower in amplitude relative to when the SCF is

not applied. An additional drawback of the SCF was that signals corresponding to the first reverberation were not suppressed because they were reflected directly from the main beam. Therefore, this high amplitude region set the dynamic range of the image, resulting in the ROIs appearing less bright.

To remove the influence of the first reverberation on the dynamic range of the image, the first two millimetres of the z-axis were again declared a dead zone. When the pixels in the first 2 mm of the z-axis were excluded from the image scene the resulting image showed a significant enhancement in the brightness of the ROIs, shown in Figure 4.9. Removal of the dead zone enhanced the SNR of the image demonstrated by reduction of the dynamic range from 40 dB in Figure 4.8 to 20 dB in Figure 4.9.

The amplitude enhancement for each ROI was recorded in Table 4.2 for the background subtracted image and for the $\text{SCF}^{1.0}$ image with and without the dead zone included in the image scene. A negative enhancement was observed for ROIs I and IV when the dead zone was included in the image scene. This means the values of these pixel coordinates have decreased relative to the maximum pixel value in the image. This is most likely due to the pixel coordinates corresponding to the maximum value in the image changing after application of the SCF. The amplitude of the pixels in each ROI were enhanced by approximately 10 dB upon the exclusion of the dead zone from the image scene, demonstrating the impact of the first reverberation on the response from the ROIs.

Overall, the enhancement of the pixel coordinates for all four ROIs are less than when the RP-GCM was applied. However, qualitative inspection of Figures 4.8 and 4.9 demonstrates that the SCF has significantly reduced the amplitude of

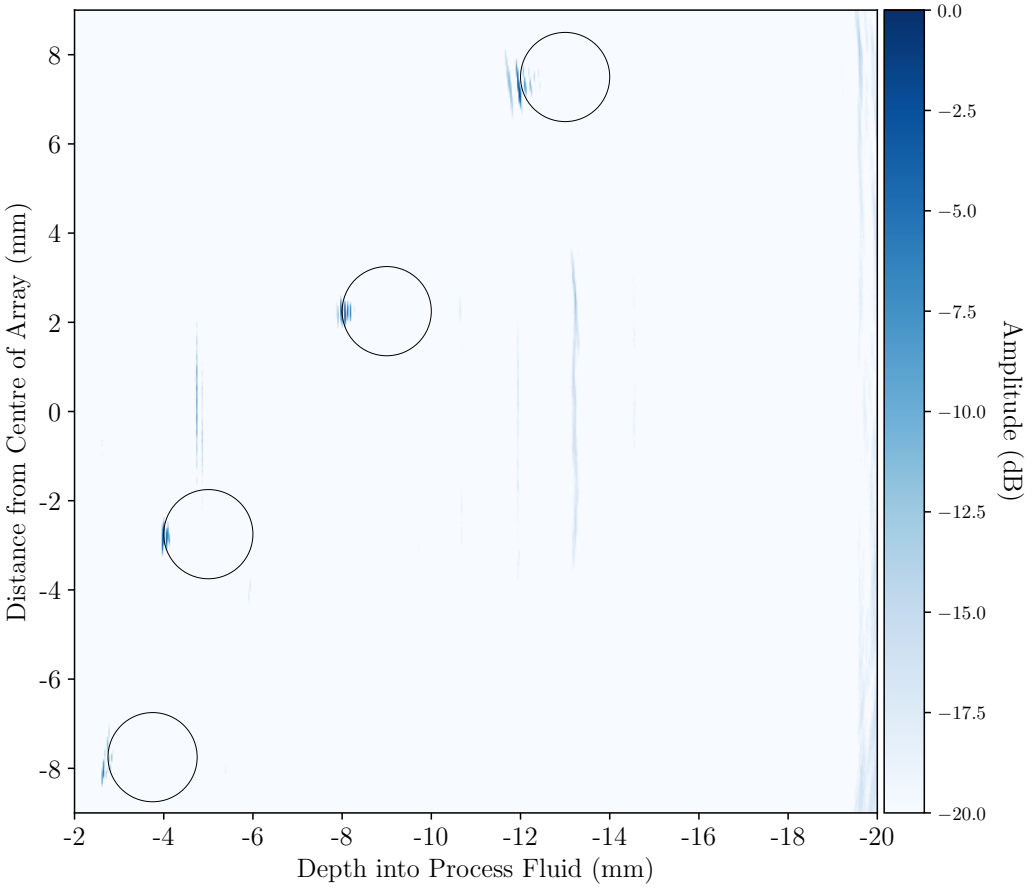

Figure 4.9: *Image scene of void reflectors excluding the dead zone and with the* $SCF^{1.0}$ *applied to the TFM image construction. Black circles represent the true location of the reflectors.*

reverberations in the image scene. This has been at the expense of the pixel amplitudes in the ROIs but enables more accurate detection of the size and positions of the reflectors from the image. This shows that SCF imaging is a more robust methodology than the RP-GCM to separate the reverberation clutter from

the void reflectors.

Table 4.2: *Image enhancement using SCF, all values in decibels.*

Reflector	Background Subtraction	SCF with dead zone	SCF without dead zone
I	25.54	-2.75	9.53
II	24.30	6.13	16.87
III	24.71	7.20	20.15
IV	27.83	-6.47	6.33

4.5.4 Subspace Analysis

Using the FMC data set generated from the FE model with the four void reflectors, Eigen decomposition of the FMC covariance matrix was used to generate the principal components of the FMC data. Upon Eigen decomposition of the FMC covariance matrix, the explained variance captured in the first $K = 32$ eigenvectors was 99.994%. This highlighted the variation described by the reverberations relative to the signals of interest and noise. Therefore, the reverberation subspace was constructed using the first K eigenvectors in the ordered set. The reverberation subspace was then projected on to the FMC data to remove the reverberation clutter prior to application of the regular TFM process. The resulting TFM image is shown in Figure 4.10. From visual inspection it can be seen that the reverberation clutter has been completely removed from the image scene, including the first reverberation parallel to the y-axis. Therefore, no dead zone was associated with the image scene and the ROIs could be resolved in all areas of the image scene. Indeed, subspace analysis has been previously implemented in NDE applications specifically to remove interference present in the dead zone

close to the transducer [141].

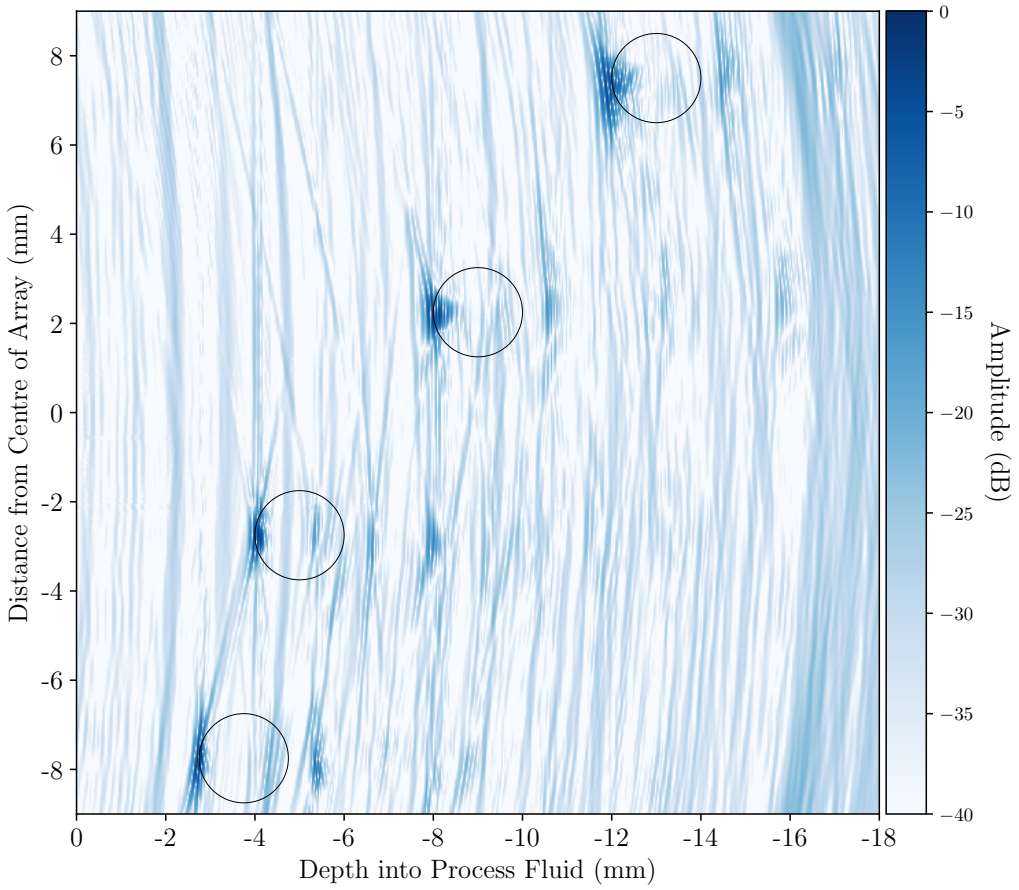

Figure 4.10: *Image scene of void reflectors after application of subspace analysis. Black circles represent the true location of the reflectors.*

Similar to the background subtraction response in Figure 4.4, there were artefacts in Figure 4.10 due to signals from the ROIs reverberating within the steel vessel wall. These were only observed when the dynamic range of the image was extended beyond 15 dB, however, these artefacts led to incorrect interpretation of

the image scene when included. These artefacts did not originate from the main beam, therefore it was proposed to couple the subspace analysis methodology with the sign coherence imaging to remove all the undesired artefacts from the image scene. When $w = 1.0$, the ultrasonic echoes from the ROIs were sufficiently removed from the image scene, as demonstrated in Figure 4.11.

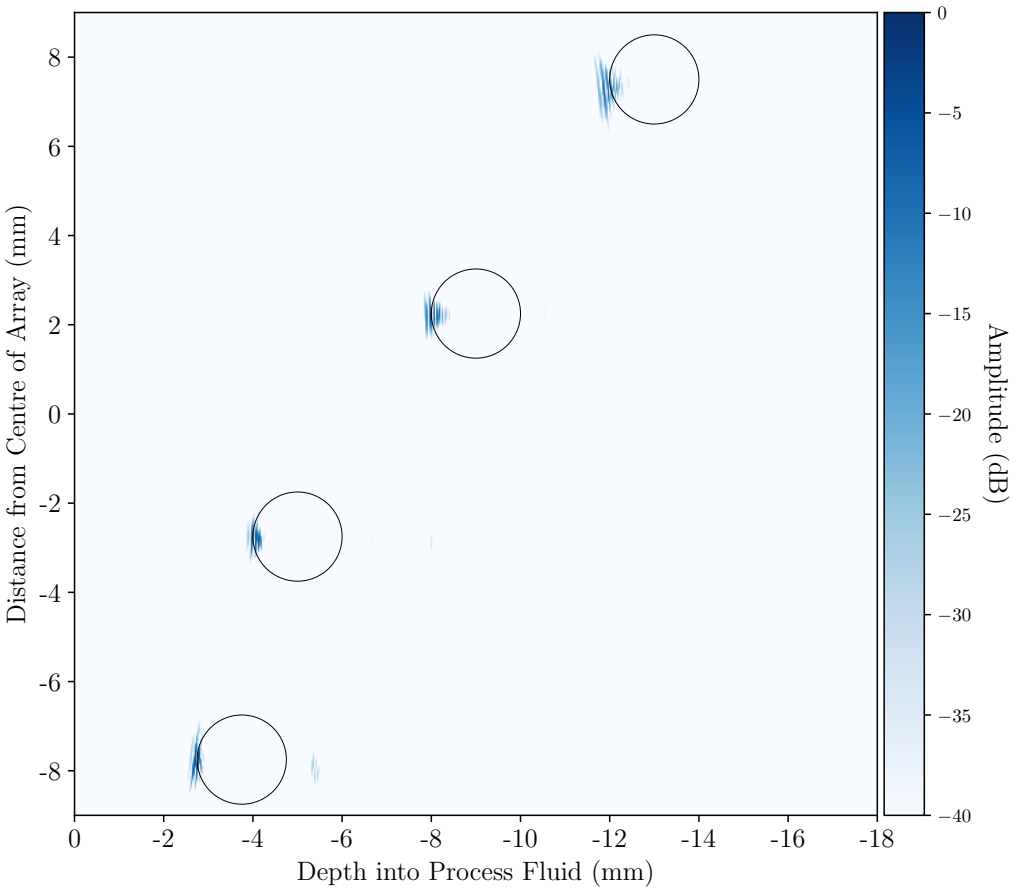

Figure 4.11: *Image scene of void reflectors after application of subspace analysis and with the $SCF^{1.0}$ applied to the TFM image construction. Black circles represent the true location of the reflectors.*

Quantification of the ROI enhancement, recorded in Table 4.3, showed that subspace analysis generated images with comparable results to the ideal case using background subtraction. Indeed, reflectors III and IV exhibited values slightly better than the ideal case, which shows the power of this methodology to separate the reverberation clutter from the signals of interest. In addition, the application of the $SCF^{1.0}$ to this image only reduced the degree of image enhancement by less than 1.4 dB, so it had a minimal impact on the quality of the ROIs while also being able to suppress the additional echo artefacts.

Table 4.3: *Image enhancement using subspace analysis and in combination with the SCF, all values in decibels.*

Reflector	**Background Subtraction**	**Subspace analysis**	**Subspace analysis and $SCF^{1.0}$**
I	25.54	25.45	25.14
II	24.30	24.04	24.02
III	24.71	24.73	24.20
IV	27.83	28.50	27.19

4.6 Summary

The aim of this Chapter was to investigate how signal processing of FRD could be used to generate non-invasive through-steel images of industrial processes. In order to extract accurate quantitative information from these non-invasive images relating to the size and position of reflectors within the process, it was important to minimise interference from steel wall reverberations while maximising the response from reflectors located in the process stream. Three signal processing methodologies were investigated, namely the RP-GCM, sign coherence imaging

and subspace analysis. An FE model of a 32 element phased array was designed to generate FMC data of four void reflectors situated in a water load beyond a 10 mm thick steel layer.

It was found that the RP-GCM was highly sensitive to the size of the gain window, determined by the measured pulse length, applied to reduce reverberation interference. The applicability of the RP-GCM to industrial process analysis was limited because it could not completely remove the reverberation pattern without compromising the reflectors of interest. In contrast, sign coherence imaging was capable of completely removing reverberation interference. However, it also reduced the sensitivity of pixels relating to the reflectors of interest. Both of these approaches were negatively impacted by the presence of a dead zone, comprising the first 2 mm of the z-axis. Therefore, these methodologies could not be used alone to adequately resolve reflectors situated close to the steel-fluid interface.

Subspace analysis proved to be the most effective methodology to separate reverberation interference from the signals of interest. It was able to adequately suppress all reverberation signals while preserving the signals from the void reflectors. Two of the reflectors in the FE model were aliased in time with the reverberations and it was still able to extract these reflectors without any loss of pixel sensitivity. In terms of the image response, subspace analysis was as good as the ideal benchmark response using background subtraction.

Subspace analysis was also coupled with sign coherence imaging. The resulting image was completely free of reverberation interference and did not include any interfering artefacts deriving from the reflectors of interest. In this sense,

when the two methodologies were coupled, the image scene was a more accurate representation than the background subtracted image. These two methodologies present the additional advantage that they do not require any *a priori* knowledge of the image scene. Therefore, it enables the end-user to develop a *clamp-on* style product for non-invasive imaging, which is highly advantageous in a process analysis environment.

Chapter 5

Sizing of Bubble Reflectors

5.1 Introduction

The BSD is a key parameter used to characterise industrial processes [19]. It provides an indication of the total surface area of bubbles in a two-phase flow. To characterise the efficiency of mass transfer between two phases requires a strong understanding of this interfacial area [20]. However, in the context of a typical industrial process environment there are several challenges associated with the quantification of the BSD. Current technologies for the determination of BSD are often intrusive to the process flow or require a clear optical path between the measurement sensor and the process [7, 66]. Ultrasound imaging is not limited in these ways and so is a good candidate technology for imaging of industrial processes to determine the BSD.

The work presented in this Chapter demonstrates a novel methodology for the

determination of BSD in two-phase bubbly flows. An image processing algorithm has been designed to determine the BSD from ultrasonic images of bubble-like reflectors. A detailed outline of how this algorithm extracts quantitative information from the input images is presented. The limitations of this algorithm are then illustrated in terms of the input image quality and the accuracy of the algorithm to extract the diameter of circular reflectors of known size. The findings of this Chapter show that ultrasonic phased array imaging can be deployed to accurately capture information relating to bubble-like reflectors.

5.2 Overview of Image Processing Algorithm

5.2.1 Background

The image processing algorithm was developed in Python 3.6 [142], where the main package dependencies were Numerical Python [143] to perform numerical algebra and scikit-image [144] to perform general image processing such as binary contour measurement. The result of the algorithm is to generate a list of identified objects in the image frame. Each object in this list is an instance of a *BubbleObject* class that has attributes relating to its radius, r (m) and yz pixel coordinates. This can be used to estimate the bubble diameter distribution and the spatial distribution of bubbles in the image respectively. The full program can be found at the University of Strathclyde PURE repository, here, or the full link can be found in Appendix A.

Determination of BSD from optical images typically models the bubble shape

as circular or ellipsoidal [7, 19, 20]. It has been documented that smaller bubbles are more spherical in nature relative to larger bubbles that tend to become more ellipsoidal in shape [19]. Fitting of an ellipse results in a set of solutions from a given number of points on its perimeter, creating uncertainty due to the non-singularity of the solution [145]. On the other hand, fitting of a circle through a set number of points only has one solution, so this greatly simplifies the sizing process. Due to the nature of ultrasonic imaging, where the speed of sound in the load medium relative to the bubble velocity impacts on the resulting image resolution, using an ellipsoidal model for the bubbles could introduce bubble sizing bias due to elongation of bubble objects as they move relative to the data acquisition process, therefore to simplify the bubble sizing algorithm and reduce the introduction of uncertainty, the bubbles were modelled as circular reflectors only.

The image processing algorithm has eight sequential steps, outlined in Figure 5.1. The process begins with the uploading of the linear TFM image matrix, prior to decibel logarithmic scaling, to the kernel. In Step II the image matrix is normalised and binarised prior to object identification in Step III. Steps IV and V, where the diameter and position of each bubble object are determined, are looped for each object in the image before exclusion parameters, Steps VI and VII, are used to mark objects that should not be included in the final output as invalid. These Steps are outlined in further detail in the remainder of this Section.

There are a number of conditions that must be met before this algorithm can be successfully deployed. The ultrasonic wavelength must be much smaller

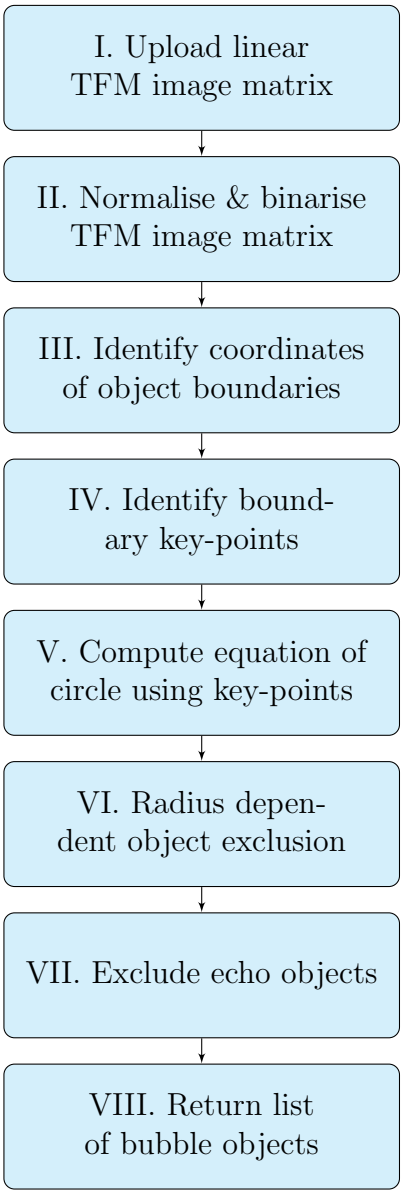

Figure 5.1: *Flow chart illustrating eight steps of the image processing algorithm.*

than the smallest bubble dimension so that Kirchoff reflection is observed at the surface of the bubble. When direct reflection is observed from the bubble surface it is assumed that the curvature of the reflectors is mapped into the TFM image. This means the array aperture must be sufficiently large relative to the size of the reflectors to adequately capture the object curvature.

5.2.2 Image and Data Upload

It was the aim to minimise the number of input parameters required to run the algorithm. The key input was the linear TFM image matrix, this is the raw output generated from the TFM prior to decibel scaling used in typical TFM image displays. An example of this image is shown in Figure 5.2(a). The image processing algorithm makes two assumptions about this image matrix: the pixels are square with equal length in both the y and z dimensions and the linear array is orientated along the y dimension. This means the direction of movement of the bubble objects must be parallel to the y-axis and any other orientation will result in inaccurate bubble sizing. An instance of the *TFM* class, which contains the parameters dP (m), the pixel dimension, ν (ms^{-1}), the speed of sound in the bulk medium and *TFM_lin* the linear TFM image matrix, is passed to the bubble sizing class as an input.

5.2.3 Image Matrix Normalisation and Binarisation

The linear TFM image matrix represents an amplitude or brightness map of the FMC data set. However, there is no frequency content included within the pixel

values such that the image matrix can be considered monochromatic. Although this simplified the dimensionality of the image matrix, the dynamic range of the image was still dependent on the number pixels in the image. For example, in this work, the dynamic range could extend up to 1024^2 individual values, corresponding to the number of pixels in the image, and these values were also dependent on the size of the reflectors present in the image scene. Therefore, to simplify the image matrices and to ensure that all images processed using this algorithm were treated under the same initial conditions, the images were converted to greyscale, shown in Figure 5.2(b). This has the impact of scaling the image matrix between zero and one using 256 individual values, essentially reducing the image size from 32-bit to 8-bit, and enhances the SNR of the image.

The greyscale images were simplified further using image binarisation. This has the impact of separating objects within the image from the background, therefore enhancing the contour detection method in Step III. To reduce the computation time a global binarisation threshold was determined for each image frame. There were six binarisation threshold methods available in the *skimage.filters* package. From visual inspection of the binarised images, three methods, namely Li's [146], Otsu's [101] and Yen's [147] were able to adequately identify the objects from the background. Of these three, Li's method was the most computationally intensive, taking approximately eight times longer per image frame than either Yen's or Otsu's method. Otsu's method was found to be less stable when tested with further ultrasonic images because it assumes that the image scene has been equally illuminated. Therefore Yen's method was selected for the image binarisation threshold determination.

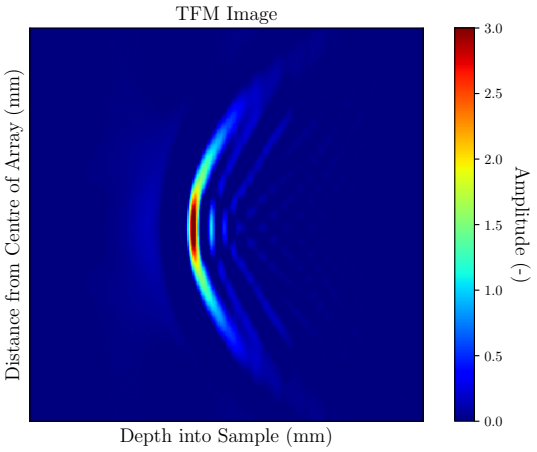

(a) *Linear scale TFM image.*

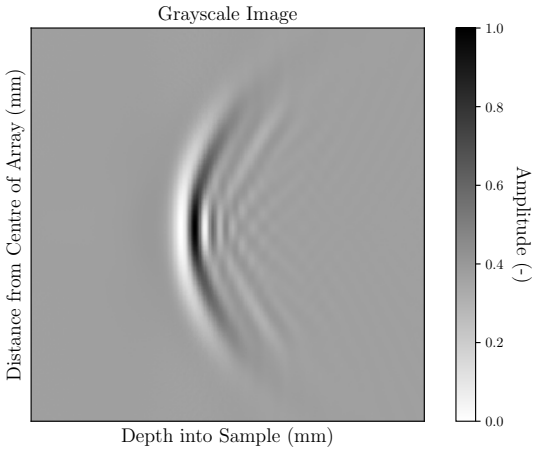

(b) *Greyscale TFM image.*

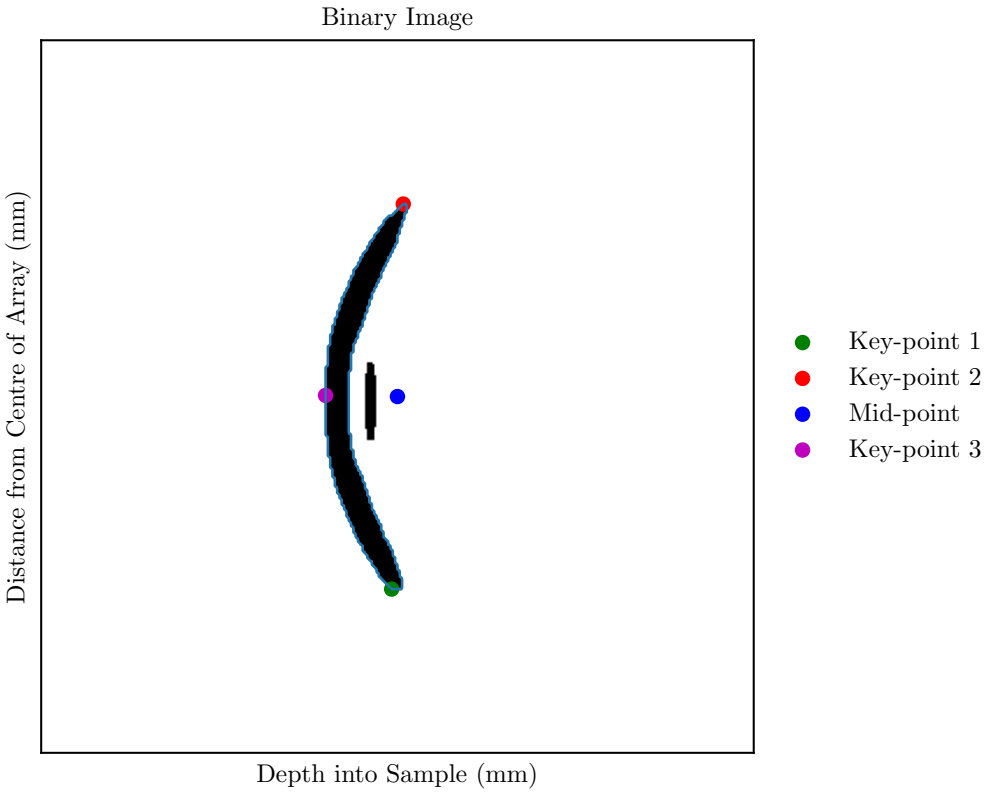

(c) *Binary TFM image showing object boundary identification and four key-point positions.*

Figure 5.2: *Images outling Steps I to IV of the image processing algorithm.*

5.2.4 Measurement of bubble object boundaries

The binary image was passed through the *measure.find_contours* command within the *scikit-image* Python package. This returned a list of arrays each containing the pixel coordinates of each object within the binary image. If no objects were found in the image or the image contained too much noise, the algorithm will *return* and the image frame is marked as invalid. Next, a condition was placed on the objects such that no coordinates along the object boundaries could equal the coordinates of the image frame edges. This meant that objects that were not completely within the image frame were marked as invalid.

5.2.5 Key-point Identification

To model each object as a circle required the identification of two key-points at the outer bounds of the object boundary, the mid-point between these two and finally a third point on the outer circumference between the first two. The proposed approach was to identify these points on the boundary and then to solve for the equation of the circle that fits through the three key-points on the boundary. These key-points are shown in Figure 5.2(c) for a simulated void reflector with a diameter of 3 mm, generated using a 128 element aperture.

The first key-point, shown by the green point in Figure 5.2(c) was determined by iterating through the boundary coordinates in the lower half of the object. Coordinates on the right-most column indices of the object are initially selected, shown as the red candidate coordinates in Figure 5.3(a). Then from this Group 1 Candidate Coordinates, the coordinate with the lower-most row index is selected

and all coordinates in the lower half of the object are iterated again. This process results in the Group 2 Candidate Coordinates shown as the red points (including the green key-point 1) in Figure 5.3(b). From these, the left-most column index is selected as the coordinate position for key-point 1.

To determine key-point 2, the same process is repeated for the coordinates in the upper half of the object to find the upper-most row, left-most column index. The reason for taking this path through the potential coordinates is that objects do not always have an ideal geometry. Therefore, without first finding the Group 1 Candidate Coordinates, the algorithm could generate false positives of the desired key-point. This method essentially avoids this by iterating through all potential coordinates and selecting the correct one. For example, if the object was at the base of the image rather than the ideal position in the centre here, the orientation of the reflector in the binary image would not be perpendicular relative to the transducer surface, so there would be several potential coordinates corresponding to left-most column.

The midpoint between key-point 1 and key-point 2, represented by the blue point in Figure 5.2(c), was then determined from their pixel coordinates. The equation of the line that passes through the three points was determined, where the gradient, m_1, was used to find key-point 3, represented by the magenta point in Figure 5.2(c). If the object was symmetric in relation to key-points 1 and 2, the gradient was not defined, otherwise the gradient was a real number. The gradient, m_2, perpendicular to m_1 was determined from $m_2 = -1/m_1$. Finally to estimate key-point 3, the boundary coordinates were iterated to identify the coordinates that lie on the equation of the line passing through the mid-point with a gradient

of m_2. The algorithm typically identifies two candidate coordinates for key-point 3, where the coordinate with the left-most column index is selected to be key-point 3. If the gradient, m_1 was not defined, then the boundary coordinates were iterated to fit the equation of a line that is parallel to the z-axis and passed through the mid-point.

To reduce pixel bias, the position within each pixel that corresponds to the pixel coordinate was defined as the centre or the interpolated position of the pixel. The reason for this being, where an object is only one pixel wide, which is likely within the localities of the key-points here, the algorithm will yield degenerate contour coordinates [148], this is explored in further detail in Section 5.4.1. This means there is an error associated with each key-point with a value $\pm\ 0.5 \times dP$ in both y and z dimensions. This error is intrinsic to the overall sizing algorithm such that the value of this error depends on the pixel dimension used to construct the TFM image.

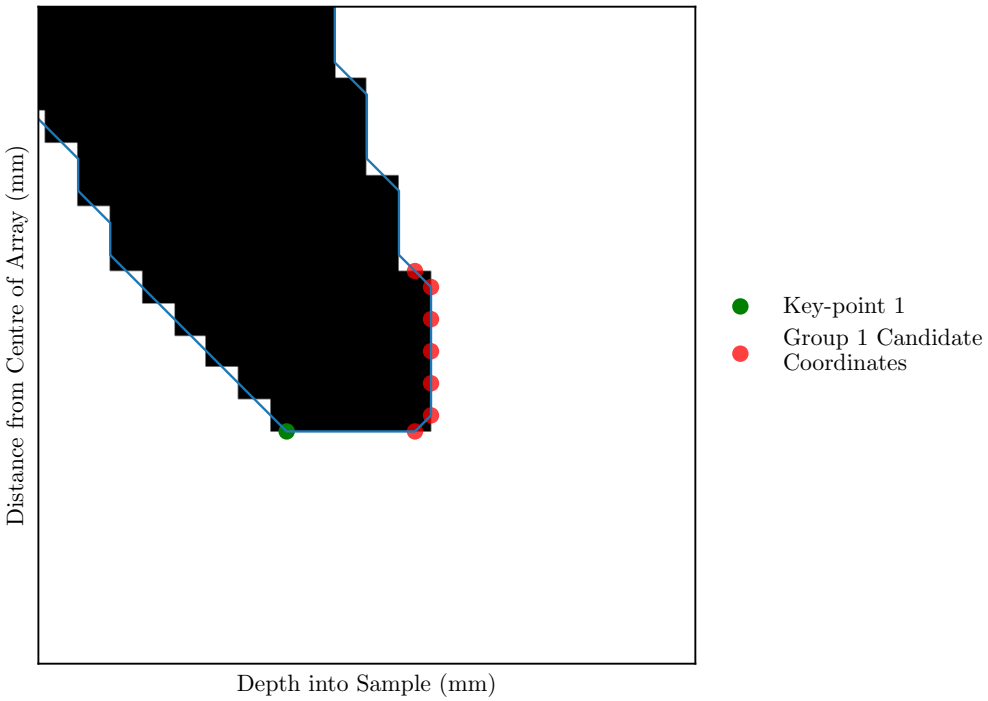

(a) *Binary image showing Group 1 candidate coordinates.*

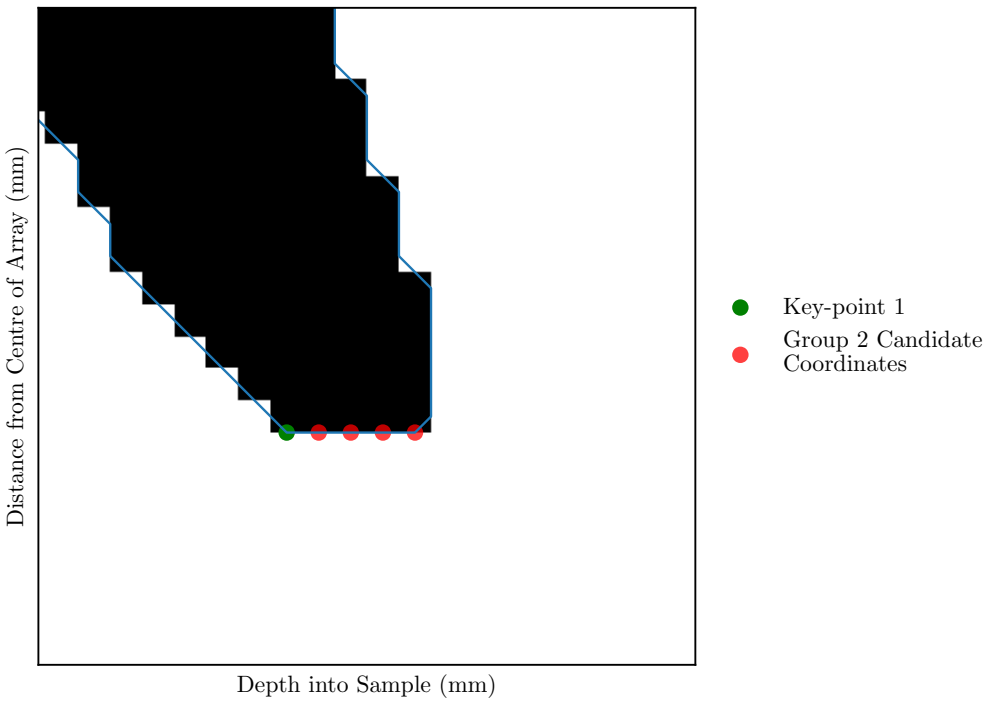

(b) *Binary image showing Group 2 candidate coordinates.*

Figure 5.3: *Binary image showing localisation path for identifying key-point 1.*

5.2.6 Solving for Equation of the Circle

The equation of the circle was solved from the only solution that satisfied having all three key-points on the circumference of a circle. A schematic outlining the key parameters used to identify the centroid and radius of the circle is shown in Figure 5.4. The methodology proposed was to determine the bisector between key-points 1 and 3 and between key-points 2 and 3. Then the centroid of the circle was determined from the intersect of the perpendicular bisectors. The radius was then calculated using the distance between the centroid and any one of the key-points.

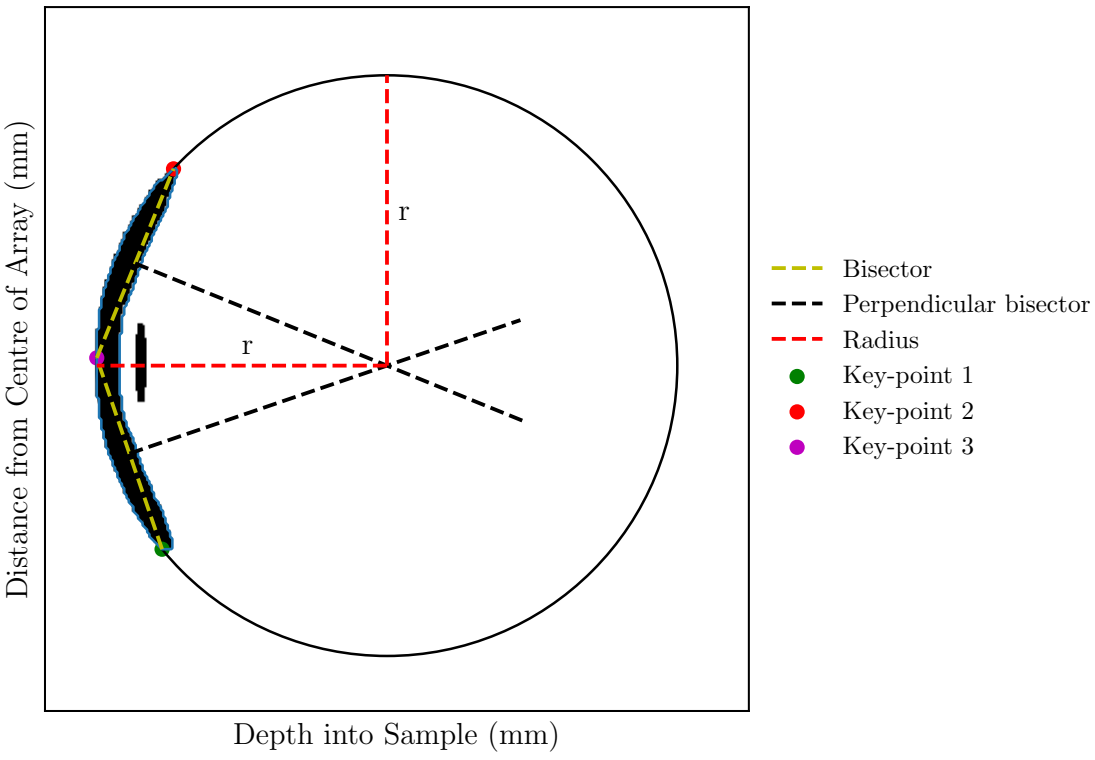

Figure 5.4: *Technical diagram showing properties used to determine centre of circle and radius from three points.*

5.2.7 Object Exclusion Criteria

Step VII of the image processing algorithm was to mark objects as invalid if they have a null radius according to the following exclusion criteria; if the object has a radius of zero, infinity or *nan* they were marked invalid as these do not represent real values of a radius. Finally, user-defined limits were set on the size of the objects, for example, objects with a radii smaller than 1 mm or larger than 5 mm could be marked invalid.

5.2.8 Echo Exclusion Criterion

Step VIII of the image processing algorithm involved the identification of objects corresponding to echo artefacts and marking these as invalid. An example of an echo artefact is shown in Figure 5.5 as the smaller circle, C_1, located inside the larger circle, C_2. The Euclidean difference, d, between the centres, (y, z), of the two circles is

$$d = \sqrt{(y_2 - y_1)^2 + (z_2 - z_1)^2}, \tag{5.1}$$

such that if

$$r_2 > r_1 + d, \tag{5.2}$$

then C_1 will be marked invalid and C_2 is retained. The algorithm iterates through every pair combination of the circles to identify if any objects are positioned within a larger object. Therefore the final result only relates to objects without

any echo objects being quantified.

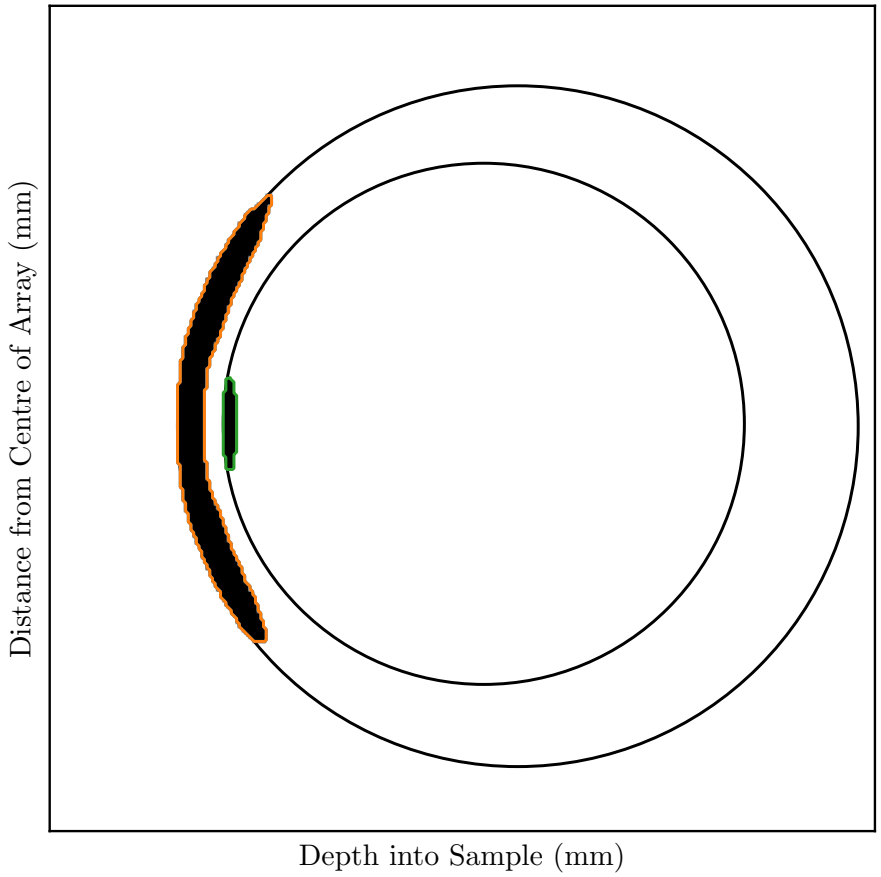

Figure 5.5: *Example of echo object to be excluded represented by the object with the green boundary.*

5.3 Calibration Methodology

5.3.1 Experimental Materials

The hardware available for FMC acquisition consisted of a 128 element, 5 MHz linear phased array and an FIToolbox PAC. The phased array was designed to be coupled to Perspex, therefore the wavelength, λ (m), of the driving function was

0.546 mm in Perspex, where $\nu = 2720\ ms^{-1}$. The element pitch of the array was known to be 0.7 mm but the element width was not cited in its technical description. The PAC consisted of 32 transmit-receive channels such that multiplexing across the channels was required for apertures greater than 32 elements.

Due to the dynamic nature of the target application, it was difficult to control the size and velocity of the moving bubbles for the purpose of calibration. To simplify the imaging system a solid cylindrical Perspex sample was acquired which was approximately 300 mm long with a 15 mm radius. The acoustic impedance of Perspex is 3.5 MRayl, therefore Perspex exhibits similar acoustic properties to water and so can be used to model the acoustic interaction observed in water. The Perspex sample, hereafter named the Perspex Calibration Sample, was a cylindrical block of Perspex where a flat surface was machined into it so the phased array could be directly coupled, illustrated in Figure 5.6. The radius of the sample was 40 mm and the distance from the flat edge to the centre was 15 mm.

The Perspex Calibration Sample was purchased without any defects or bubbles present. Five SDHs were added to this sample where the position of the centre of each SDH was 12 mm from the surface, chosen to prevent interference from the back wall. These circular SDHs ranged from 1 to 5 mm in diameter, with 1 mm increments. They were spaced 75 mm apart to maximise the distance between the SDHs and minimising any interference due to scattering from adjacent SDHs. When the array was mounted to the Perspex Calibration Sample, the SDHs were equivalent to two-dimensional bubbles relative to the image plane.

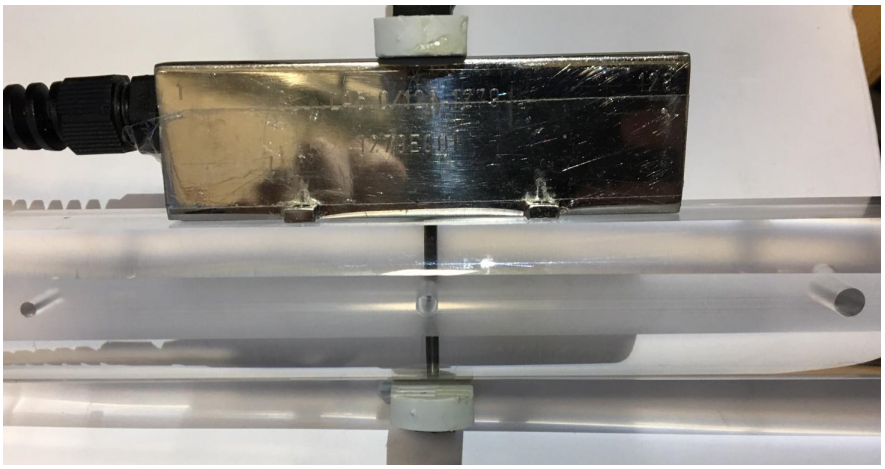

(a) *Photograph of Perspex Calibration Sample.*

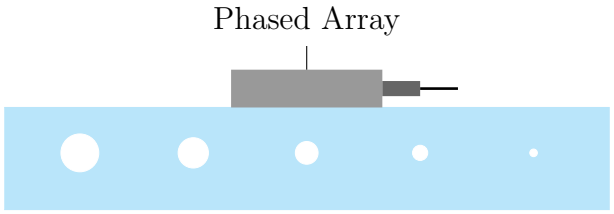

(b) *Schematic of Perspex Calibration Sample containing five SDHs.*

Figure 5.6: *Overview of Perspex Calibration Sample with the phased array coupled to its surface.*

5.3.2 Finite Element Modelling

An FE model was developed in PZFlex [55] to generate FMC data sets of bubble-like reflectors immersed in water. A schematic of the FE model is shown in Figure 5.7 indicating the key design parameters. The water was modelled at 25 °C with a density of 1000 kgm^{-3} and speed of sound of 1496 ms^{-1}. The mesh size was set to 15 elements per wavelength relative to a 5 MHz input function and the speed of water. At the time of the model design, it was the aim to replicate the experiment as closely as possible. For this reason, the element width was set to 0.6 mm with an element pitch of 0.7 mm, corresponding to that of the hardware

in Table 3.1. However, the load medium in the experimental application was water so this corresponds to a two-wavelength element width rather than a half-wavelength element width. This disparity was investigated towards the end of the research project, where a minimal impact was observed and is explained in Appendix C. The impact of element pitch on imaging performance has also been investigated by Wilcox and Zhang [149]. In their work it was found that the Nyquist element spacing ($\lambda/2$) was too conservative and that element pitch can be increased without compromising the image quality. As a result, these models were not repeated using a half-wavelength width. The driving function of the 128 element FE model was a 5 MHz Blackman-Harris function, which was selected to reduce any frequency domain side lobe activity.

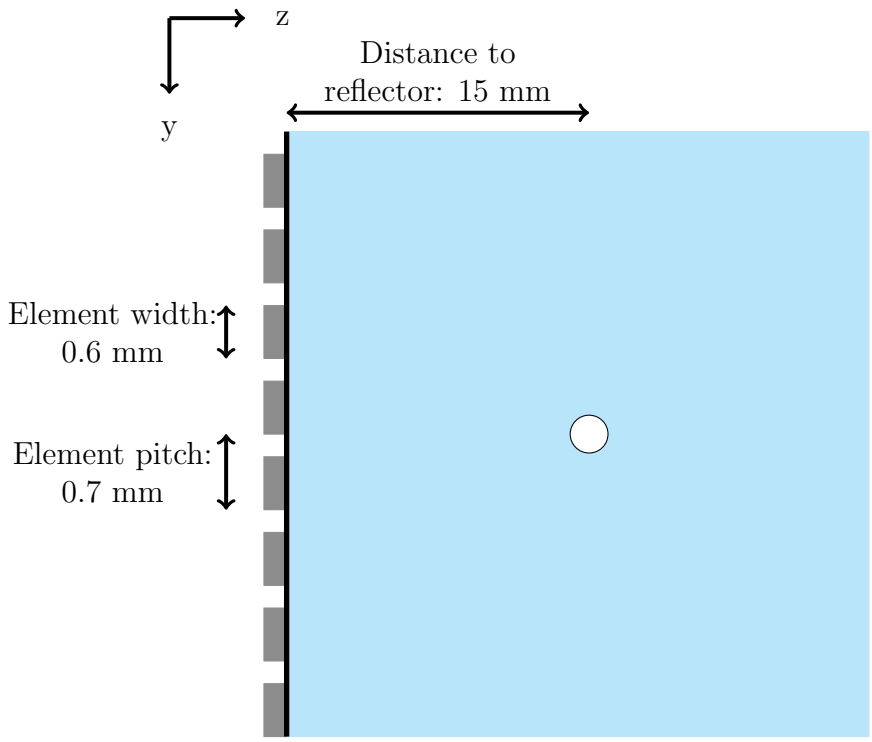

Figure 5.7: *Schematic of FE model of void reflector suspended in water.*

A circular void reflector was suspended in the centre of the water load, at 20 °C, that reflected 100% of the ultrasonic energy at its boundary. The void reflector was stationary as it was not possible to generate FE data of a dynamic system, however, relative to the data acquisition rate of the experimental hardware, this was a reasonable approximation to the experimental system. The distance to the void reflector from the array was set to 15 mm because this was the distance to the SDHs in the Perspex Calibration Sample. The models were constructed for circular void reflectors ranging between 3.3 to 16.7 λ respectively such that all the voids generated strong reflections at their interfaces.

The transducer itself was modelled as a pressure loaded array, meaning no transducer effects were modelled. This simplified design ensured results were purely due to the integrity of the image processing algorithm rather than noise from the array design. A two-dimensional model was created because there was symmetry along the yz-plane, provided that the water load was assumed to be infinitely large relative to the array probe. The boundary conditions on the model were set to absorbing, with the boundaries infinitely extending relative to the temporal range of the ultrasonic reflections. This generated a system without artefacts from the transducer or elsewhere.

Using all 128 elements in the FE model, an FMC data set was generated for each circular void reflector. Then sub-apertures of these data sets were extracted by taking the centre-most elements corresponding to an aperture of 16, 32, 64 and 96 elements. These sub-apertures were used to investigate the impact of the aperture dimension on sizing accuracy using the image process algorithm.

5.3.3 Experimental Data Acquisition

Experimental FMC data of the Perspex Calibration Sample were acquired using the full aperture of 128 elements of the linear phased array. The array was centred over each of the SDHs and three FMC data sets were acquired of each SDH. Then from these data, FMC data sets corresponding to sub-apertures of 16, 32, 64 and 96 elements, were extracted from the centre-most elements. Therefore, for each SDH there were 3×5 individual data sets corresponding to the three sample replicates and five apertures.

5.3.4 Image Structure

Every TFM image generated in this work has been constructed under identical conditions. The extent of the z-axis ranged from -10.0 mm to -20.0 mm and the extent of the y-axis ranged $\pm$ 5.0 mm from the centre of the array. There were 1024 pixels in both the y and z dimensions, corresponding to the maximum number of pixels that could be handled by the GPU. This ensured the maximum resolution possible of the images and ensured that the pixels were perfectly square. The physical dimension of the pixels were identical in all TFM images, however, the pixel size in water corresponded to 0.033 λ, whereas in Perspex it was equivalent to 0.018 λ. Therefore, in both the simulated results, performed with water, and the experimental results, performed with Perspex the pixel dimension was much less than the wavelength, removing uncertainty associated with pixel resolution between the simulated and experimental results.

In all the images generated from experimentally acquired data, the TFM im-

ages were generated with the transmit and receive time delays incorporated, presented in Chapter 3. In addition, for all images generated from both simulated and experimental data sets, the SCF matrix was determined as presented in Chapter 4.

5.4 Results and Discussion

5.4.1 Visualisation of Algorithm Output

For each object identified in the TFM images supplied to the image processing algorithm, the coordinates of the boundary, the key-points and the predicted centroid and radius were recorded as attributes to the *BubbleObject* class. To conceptualise these outputs, the results from a 1 mm diameter simulated void reflector in water have been superimposed onto the input TFM image and the binary output image. This is demonstrated in Figure 5.8 where the TFM image was constructed using a 128 element aperture.

In Figure 5.8 the red circles represent the object size predicted by the algorithm whereas the green circles represent the true size of the void, where the centroid has been adjusted such that key-point 3, in magenta, is the same for both the predicted and true instances. In the TFM image, the key-points appear to be located within the background of the image, however, upon binarisation of the image, the extent of the object is actually much larger. This would have been observed if the envelope (Hilbert transformed) response were plotted in the final image, which would remove amplitude variations from the TFM image, however,

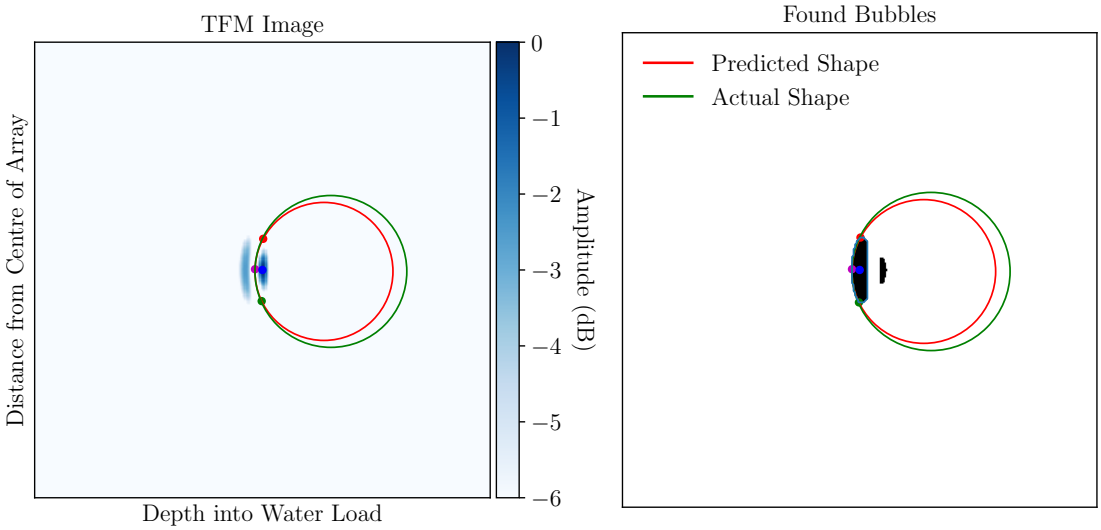

Figure 5.8: *Left: Example of TFM image of a simulated 1 mm diameter void generated using a 128 element aperture. Right: Binary image output from image processing algorithm. In both cases the predicted and actual void size and position have been superimposed onto the image.*

this would compromise the curvature of the objects, preventing the algorithm from accurately sizing them.

In the example shown in Figure 5.8 there is an error between the predicted and true size of the void reflector, shown by the offset between the red and green circles. To highlight where this error arises, the region around key-point 2, in red, has been highlighted in Figure 5.9, where the object boundary coordinates lie on the blue line. In Figure 5.9 the error associated with the object sizing is due to the boundary coordinate definition, such that the error in the definition of key-point 2 corresponds to half of a pixel. This is an example of the potential error introduced by interpolation of the boundary coordinates.

In addition, error in the sizing of objects was largely due to the accuracy of the input TFM image to represent the object of interest. This is highlighted

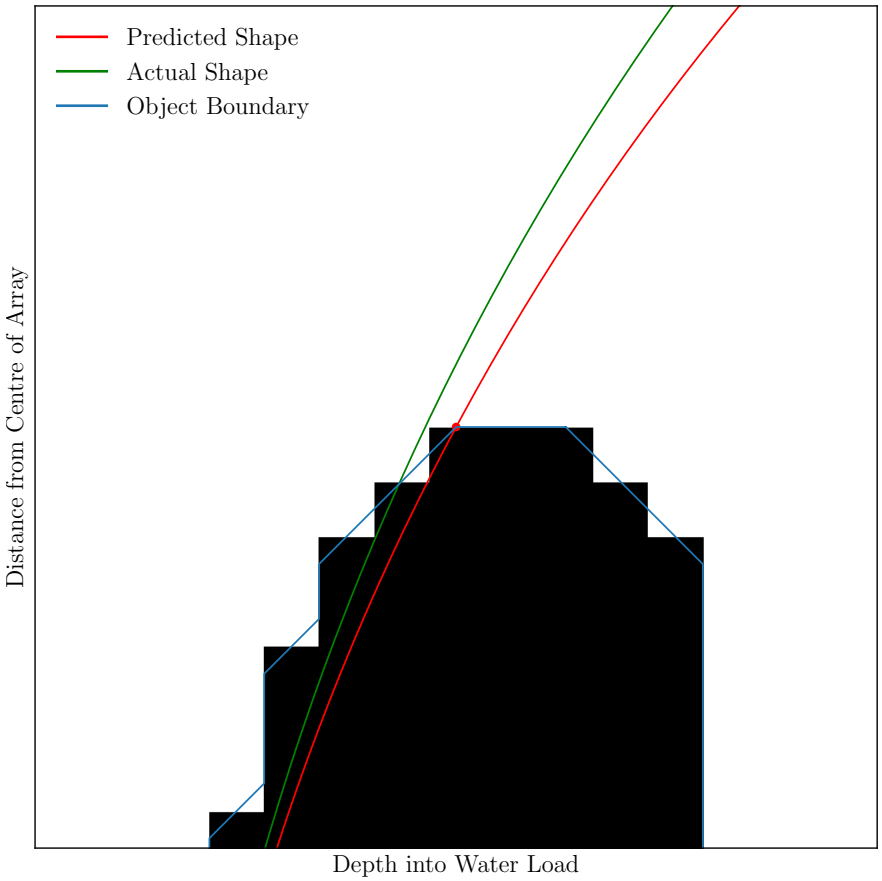

Figure 5.9: *Result from simulated 1 mm diameter void generated using a 128 element aperture zoomed to key-point 2.*

in Figures 5.10 and 5.11 where the image processing algorithm has correctly identified the key-points and fitted a circle through these points. However, in Figure 5.11 the input image was less representative of the object's true shape which resulted in the difference between the green and red circles.

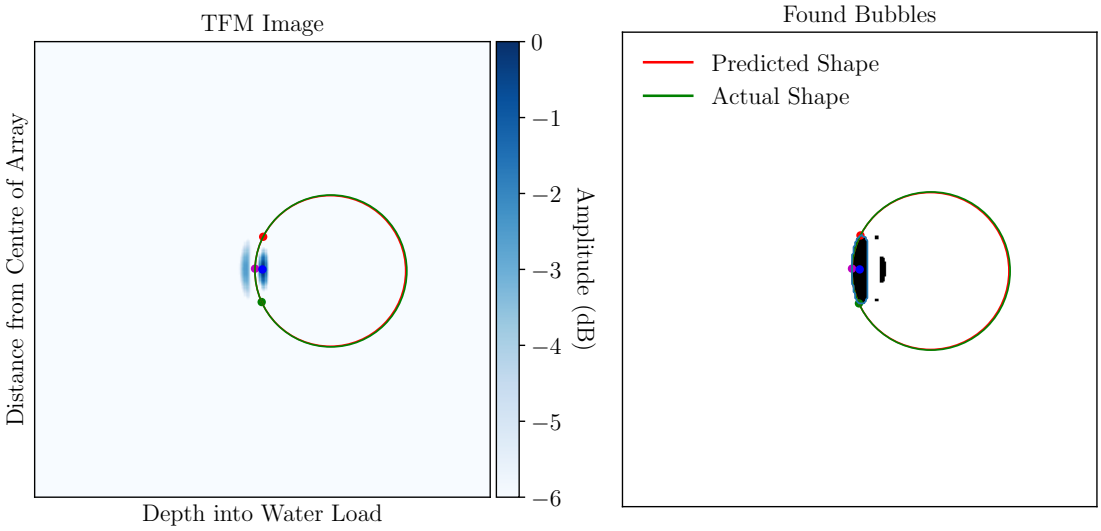

Figure 5.10: *Example of accurate object sizing. Image represents 1 mm diameter simulated void constructed using a 96 element aperture.*

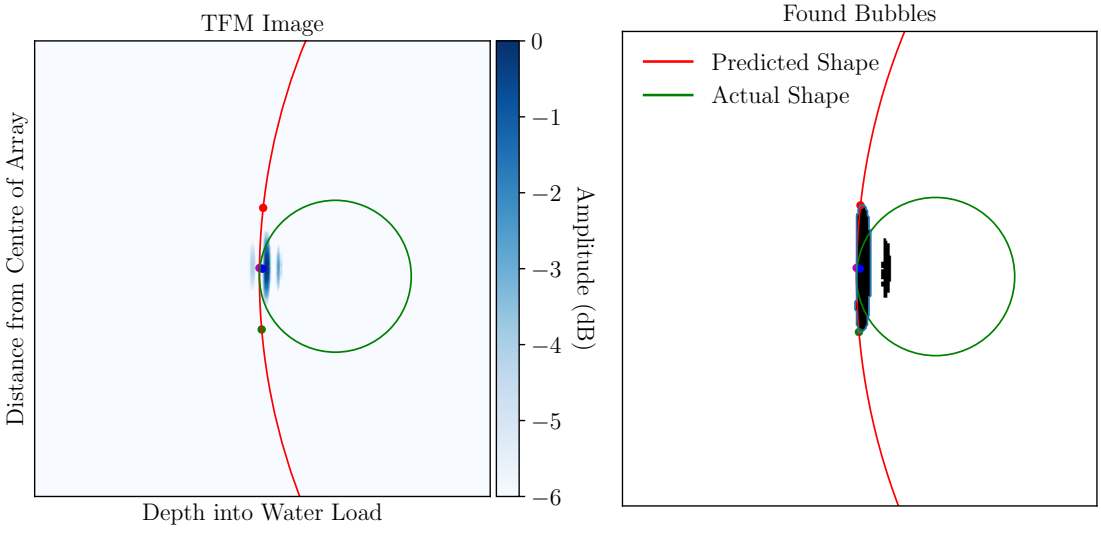

Figure 5.11: *Example of inaccurate object sizing. Image represents 1 mm diameter simulated void constructed using a 16 element aperture.*

5.4.2 Reducing Error due to Object Elongation

The shapes of objects in the input images were dependent on the size of the reflectors being imaged. Smaller reflectors were imaged with a lower degree of curvature than larger reflectors due to the lower amplitude of reflections. When the sizing algorithm was applied to images of the simulated void reflectors constructed using all five aperture sizes, this trend was observed regardless of the aperture used. The sizing algorithm was designed to accept images containing curved objects, however, smaller objects often appeared flat, such that the algorithm began to fail for small flat objects. This demonstrates where the algorithm is sensitive to the quality of the input image and where the algorithm begins to fail for objects lacking curvature. An approach has been developed to compensate for this lack of curvature here, however, the validity of this approach could not be verified, so it is presented here for demonstration purposes.

To measure the curvature of objects in the binary images and to observe the trend in the sizing accuracy as a function of the input object curvature, a curvature ratio, ϕ, was established,

$$\phi = \frac{l_1}{l_2}, \tag{5.3}$$

where l_1 represented the width of the object along the line intersecting key-point 3 and the mid-point and l_2 represented the distance between key-point 3 and the mid-point. An example of these features is illustrated in Figure 5.12 for an object with a low degree of curvature. The lower the value of ϕ the greater the degree of curvature captured in the object whereas the larger the value of ϕ the lower

the degree of curvature.

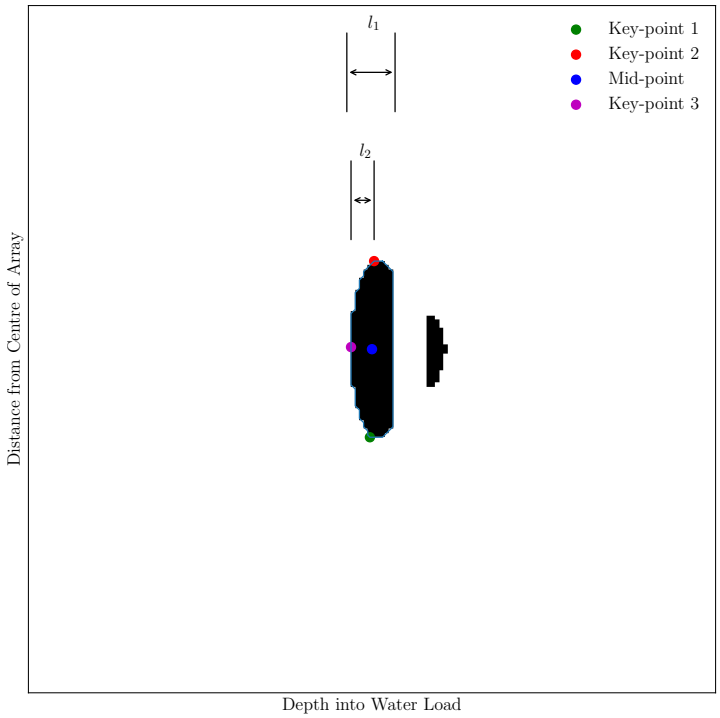

Figure 5.12: *Illustration of curvature parameters: l_1 and l_2 using a binary image of a simulated 5 mm diameter void reflector constructed using a 128 element aperture.*

The sizing algorithm was applied to the TFM images generated from the simulated FMC data sets of the five void reflectors constructed using the five different aperture sizes. The relative accuracy of the predicted void diameters were determined from the known void diameters programmed in the FE models and were expressed as a percentage error. These values were plotted against ϕ in Figure 5.13, where it was observed that for objects with a value of $\phi \geq 0.8$ the sizing algorithm began to fail, exhibiting sizing errors greater than 200%. It was also observed in Figure 5.13 that as the size of the active aperture increased, the relative error tended to decrease. This was expected because increasing the size

of the active aperture increases the quantity of information captured within the image, making it more representative of the reflector.

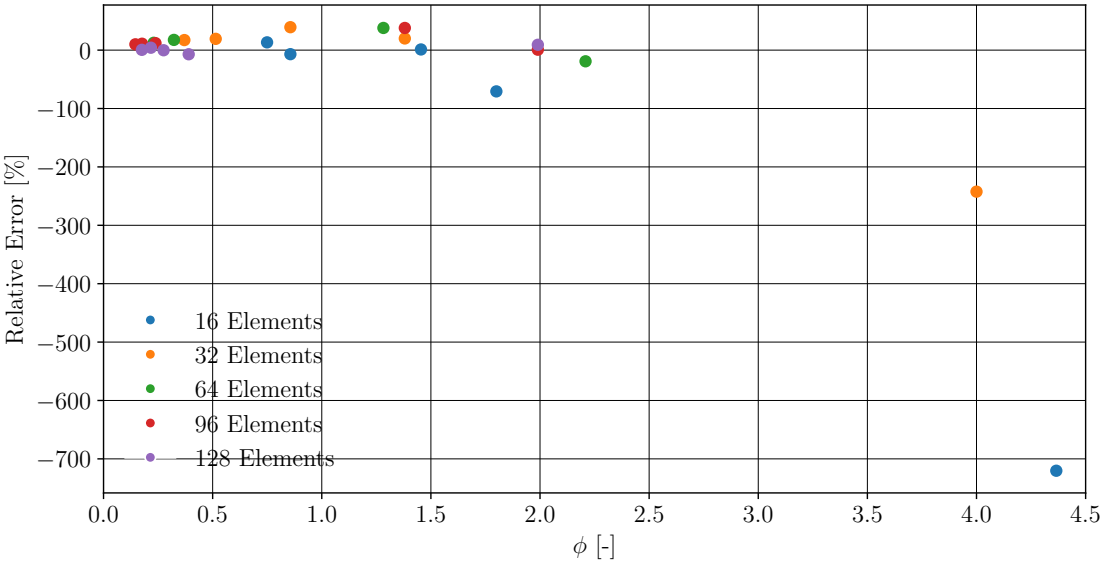

Figure 5.13: *Relative error of simulated voids for each aperture as a function of the object elongation, ϕ.*

To compensate for this error due to object elongation the algorithm was adjusted by altering the coordinates of either key-point 1 and/or key-point 2. Only objects that met the following criteria were considered for this alternative sizing approach. The first criterion was that the object must exhibit a value of $\phi \geq 0.8$. Following this the coordinate of key-point 1 or key-point 3 were altered if the position of the key-point in question, relative to key-point 3, was within one third of the object width. This threshold was set to 0.8, based on these data, however, it could be selected to compensate for other objects based on their relative curvature.

Upon meeting these criteria, the coordinate of the key-point in question was changed. To illustrate this process, the redefinition of key-points 1 and 2 has

been demonstrated for a 1 mm diameter void imaged using a 32 element aperture, which exhibited $\phi = 4.0$. First the coordinates of the boundary on the rear side of the object were identified, shown in cyan in Figure 5.14(a). These represent the coordinates perpendicular to the line intersecting key-point 3 and the mid-point. From these candidate coordinates, the upper-most and lower-most coordinates were selected, as shown by the cyan points in Figure 5.14(b). Then the new position of the key-point was selected to be the boundary coordinate half way between this candidate point and the original key-point position. The half-way point along the boundary was chosen because it was not possible to infer the exact location based on the input image geometry alone. Redefining the key-point coordinates in this way had the impact of bringing the key-points closer together so that when a circle is fitted through these points, the algorithm estimates a smaller diameter than it otherwise would have predicted.

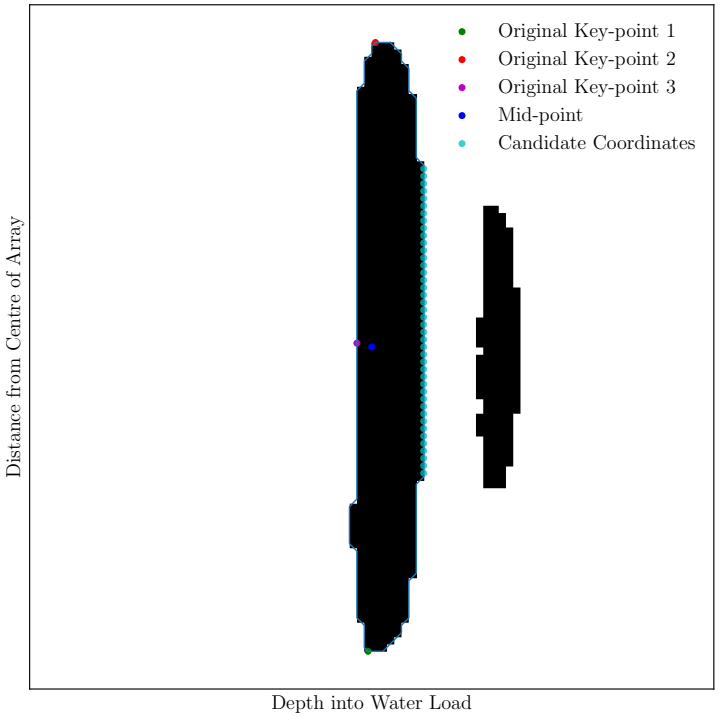

(a) *Candidate coordinates selected in first stage of key-point redefinition process.*

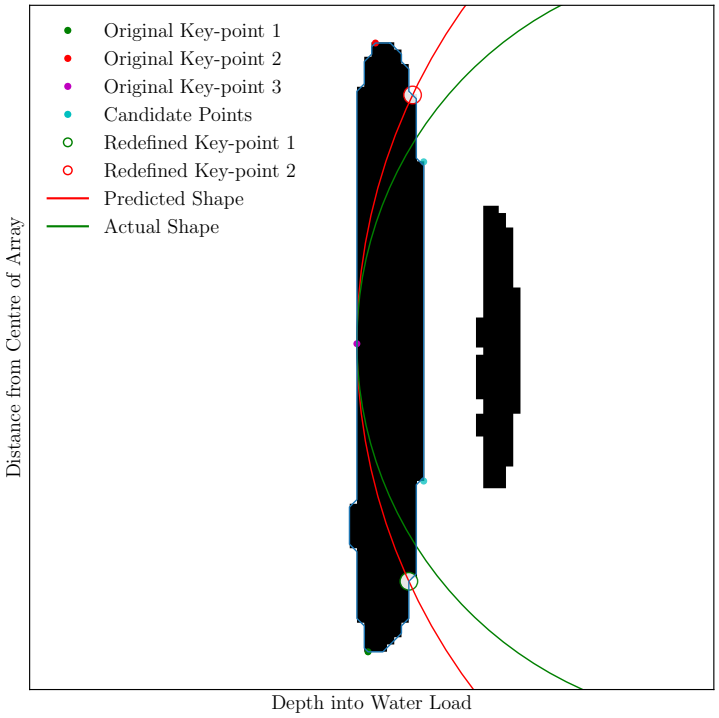

(b) *Selection of new coordinates for key-points 1 and 2 from the mid-coordinate between the original key-point position and the upper and lower most candidate points.*

Figure 5.14: *Procedure for redefining key-points 1 and 2 if the object shape meets the elongation criterion.*

5.4.3 Impact of Active Aperture on Sizing Accuracy

The accuracy of the input image to represent the true shape of a reflector depends on a range of factors. The key controlled variable associated with the image quality was the size of the active aperture, which directly relates to the quantity of information used to construct the image.

The impact of the key-point redefinition process for each active aperture has been illustrated in Figure 5.15. When the relative error was plotted against the known simulated void diameter, it was observed that there was a significant error for smaller objects. However, upon redefinition of the key-points for elongated objects the average enhancement in sizing error was 462%. Indeed, in Figure 5.15(b) it was observed that for apertures greater than 32 elements there was a similar degree of sizing accuracy. This indicated that insufficient information was captured in the images generated using an aperture of 16 elements to make these images representative of the reflector object. Note, the scale of the y-axis in Figure 5.15(a) ranges 800 % whereas in Figure 5.15(b) it ranges only 100%, indicating the degree of enhancement from this alteration. Note, a positive percent error corresponds to an underestimation of the true value and a negative value corresponds to an overestimation.

Upon inspection of the relative errors of prediction recorded in Figure 5.15(b), the overall trend in the simulated results indicated that the larger the void the more accurate the sizing prediction. This was because there was a stronger reflection returned to the array and the array extent was larger relative to the reflector size so the image generated from these reflectors is able to be more representa-

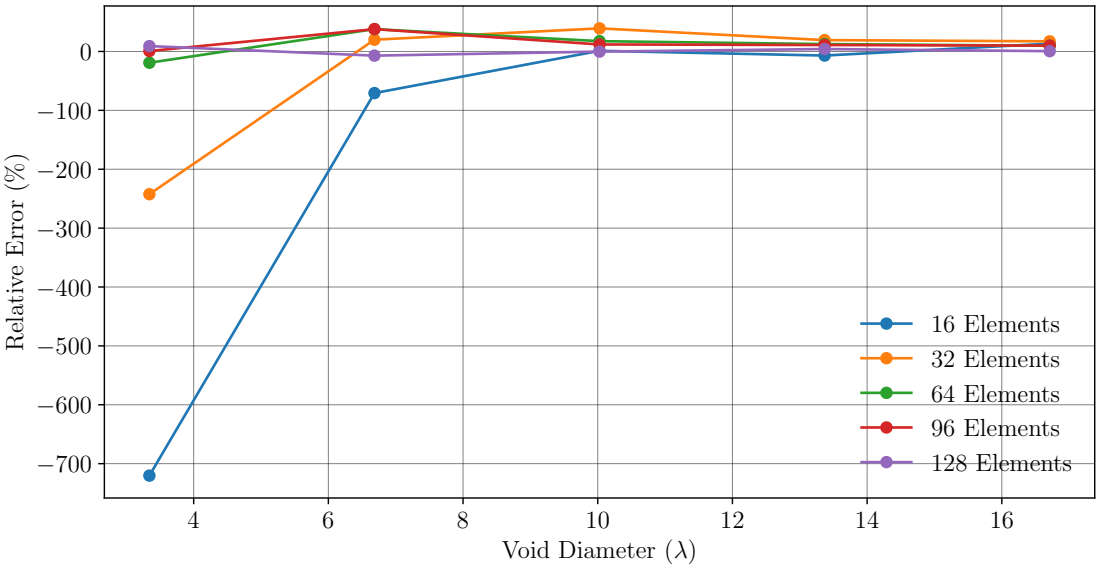

(a) *Sizing accuracy using original key-point definition for all objects.*

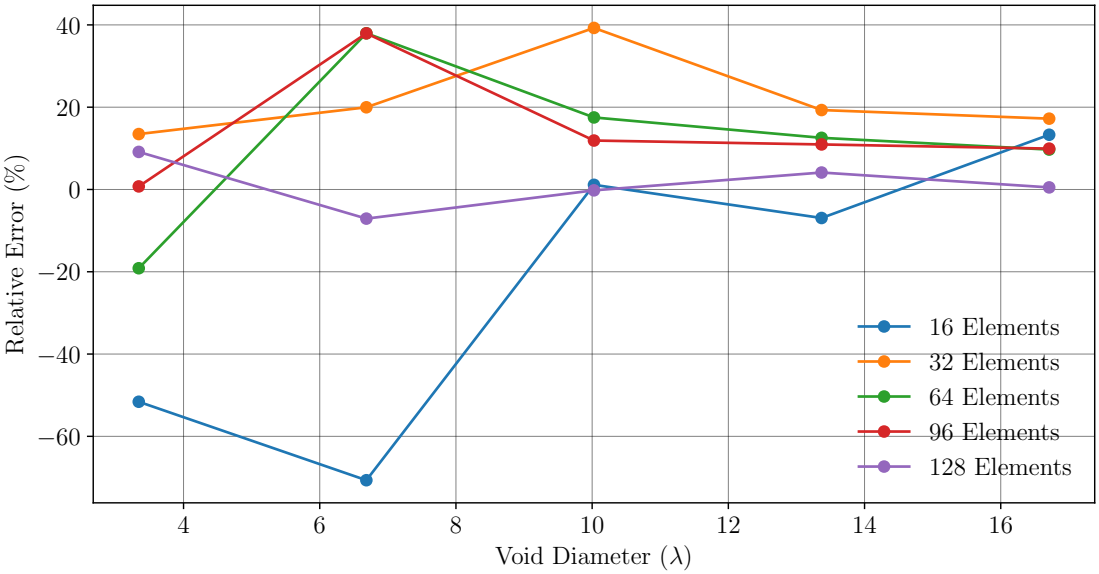

(b) *Sizing accuracy using redefined key-point coordinates for elongated objects.*

Figure 5.15: *Relative sizing error of simulated void reflectors when two different key-point definitions were used to size elongated relfectors.*

tive of the reflector. Also, the greater the number of elements in the aperture the more information captured within the image, therefore increasing the image representativeness and leading to an increase in the sizing accuracy.

5.4.4 Experimental Validation

The TFM images generated from the experimentally acquired FMC data of the Perspex Calibration Sample were passed to the bubble sizing algorithm. The relative error for each SDH was recorded as a mean value across the three sample replicates in Figure 5.16, where the error bars correspond to one standard deviation. Overall, it was observed that the relative error was larger for the experimentally acquired data than in the simulated results. However, it was also observed that the spread in the results was low, indicated by the small size of the error bars, indicating the images were consistent between individual data acquisition events.

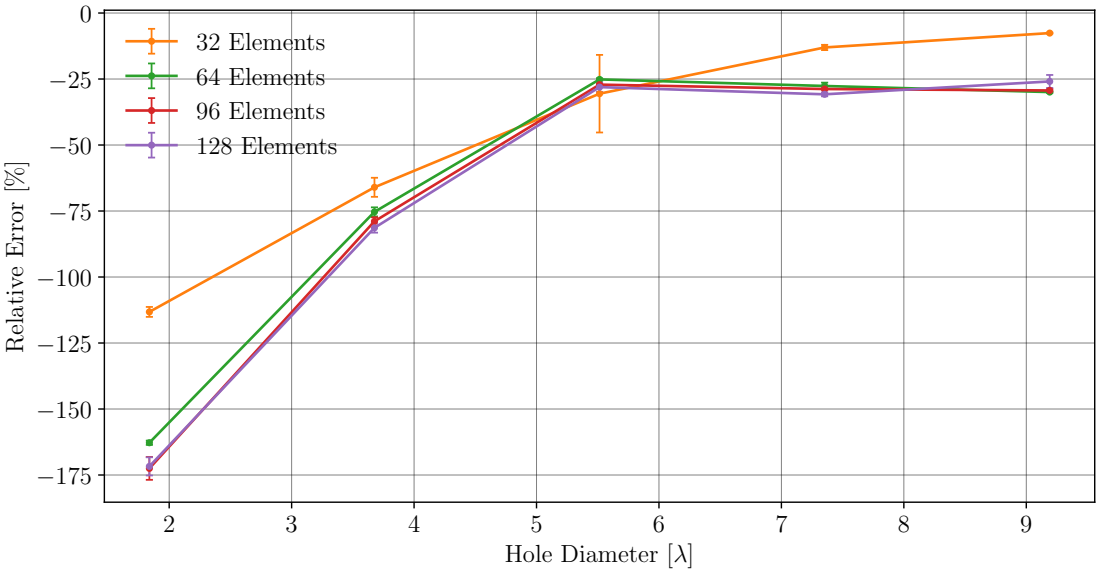

Figure 5.16: *Relative error of experimentally imaged SDHs in Perspex Calibration Sample predicted from images generated using different active apertures.*

It was important to note that due to the difference in the acoustic velocity in water and Perspex, the wavelength in these two media were different for the

same driving function frequency. Therefore the reflectors in the experimentally acquired data sets were smaller relative to the acoustic wavelength than the equivalent void diameters in the simulated data sets. This difference explains why the experimental results were not as accurate, as less ultrasound was reflected.

The predicted SDH diameter was plotted against the actual diameter for the experimentally acquired data in Figure 5.17. In agreement with the simulated results, the experimental results indicated a strong correlation between the predicted SDH diameter and the actual value, demonstrated by the r^2 values in Table 5.1. This suggested that for a highly controlled or stationary experimental imaging system, it would be possible to calibrate the image processing algorithm to correct for the true reflector size. However, given that these results only correspond to stationary reflectors, these regression models cannot be deployed towards dynamic applications. The reason these cannot be applied to a dynamic system is because the bubble movement will elongate and distort the shape of the object in the TFM image and this is demonstrated in Section 6.2.3.

In Figure 5.16 it was observed that using a 32 element aperture resulted in the lowest relative error across the different SDHs. In addition, Table 5.1 indicates that using 32 elements exhibited the greatest degree of correlation between the actual and predicted SHD diameters. Given that sizing accuracy is dependent on the input image quality, this suggests that using a 32 element aperture enhances the TFM image quality. The impact of aperture size on TFM image performance has been investigated by Zhang et al [150] where it was concluded that including elements in the aperture that did not record specular reflections had a detrimental impact to the overall image quality. That is to say, reducing the aperture

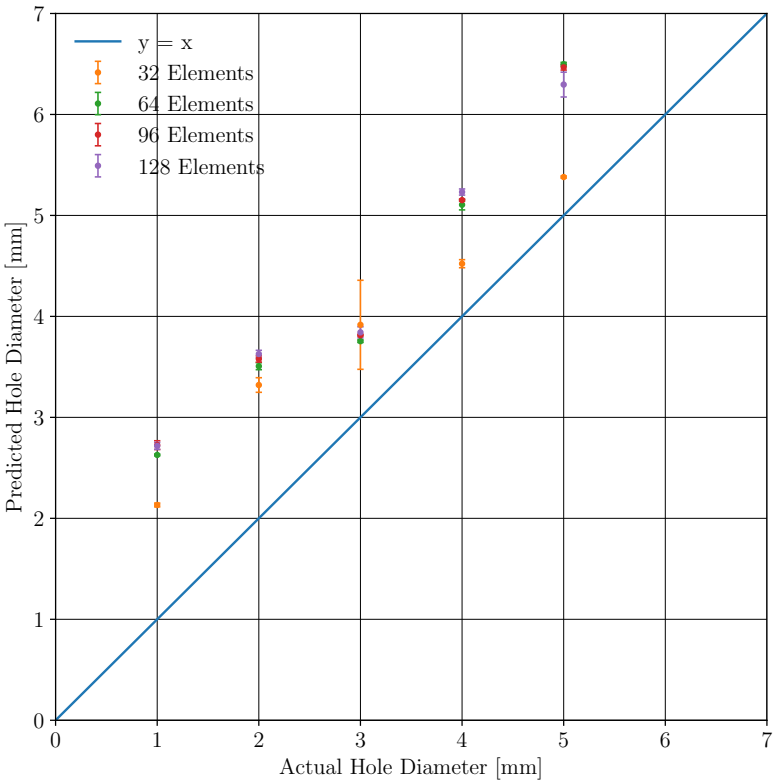

Figure 5.17: *Actual diameter against predicted diameter from experimentally acquired data of SDHs.*

size reduces the likelihood of there not being a reflector in the image scene and therefore enhances the SNR of the final image.

Table 5.1: *Experimental bubble sizing trends for each aperture*

Aperture (elements)	**m - slope**	**c - intercept**	**r^2**
16	0.088	3.949	0.002
32	0.739	1.545	0.983
64	0.909	1.497	0.948
96	0.843	1.630	0.949
128	0.876	1.714	0.958

5.4.5 Impact of Reflector Angle

In the simulated and experimental results presented so far the reflector is positioned with its centroid 15 mm from the surface of the array in the z dimension and centred relative to the aperture length in the y dimension. Having the reflector positioned precisely in the centre of the aperture is the ideal case because it creates a line of symmetry through the aperture such that spatial variations in the data used to construct the image are minimised. However, in a dynamic industrial process environment the bubble reflectors will be positioned randomly throughout the image scene. Therefore, it was important to measure the sizing accuracy as a function of the spatial orientation of the object relative to the array. The angle between the centre of the full array aperture to key-point 3 of the object, θ, illustrated in Figure 5.18 has been used to quantify this variation.

For each simulated void diameter, the FMC data sets corresponding to the full 128 element aperture were sub-sampled to create several FMC data sets each corresponding to a 32 element aperture. This was achieved using signals corresponding to elements 1 - 32, then 2 - 33 and so on resulting in 97 $(128-32+1)$ individual FMC data sets, each representing a discrete reflector angle. This provided the maximum number of possible reflector angles to be investigated using a 32 element aperture. These FMC data sets were then constructed into TFM images using the same pixel dimension previously, however the image scene was shifted along the y-axis to ensure the object was kept within the image. The TFM images were weighted using the SCF before being passed to the bubble sizing algorithm, where the overall results were recorded in Figure 5.19.

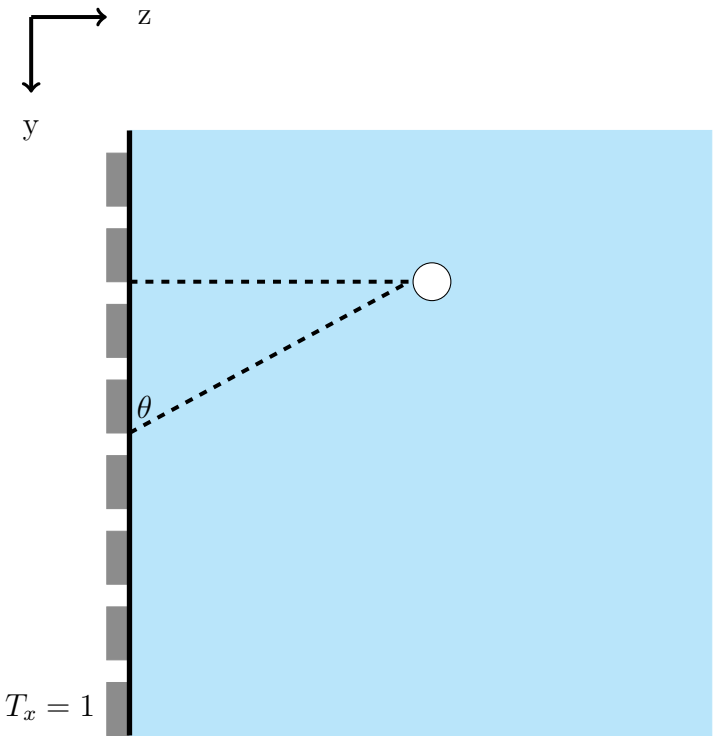

Figure 5.18: *Schematic showing reflector angle, θ.*

The results from this process indicated that when using a 32 element aperture, the sizing accuracy was relatively consistent for values of θ between $\pm 40°$, however, beyond these angles the sizing accuracy decreased significantly for all void reflectors. Also, it was noted that the negative impact of the object angle was dependent on the object size, where smaller objects began to fail at smaller angles than the larger objects. The minimum reflector diameter in the Perspex Bubble Sample was 2 mm, therefore at for the smallest reflectors the relative error was in the range between 50% to 80% across all angles expected. In practice, since the algorithm over-estimates the bubble diameters, as shown in Figure 5.17, this would bias the BSD towards a larger mean value. If there were a greater number of reflectors 2 mm or smaller in diameter, this would compromise the accuracy of

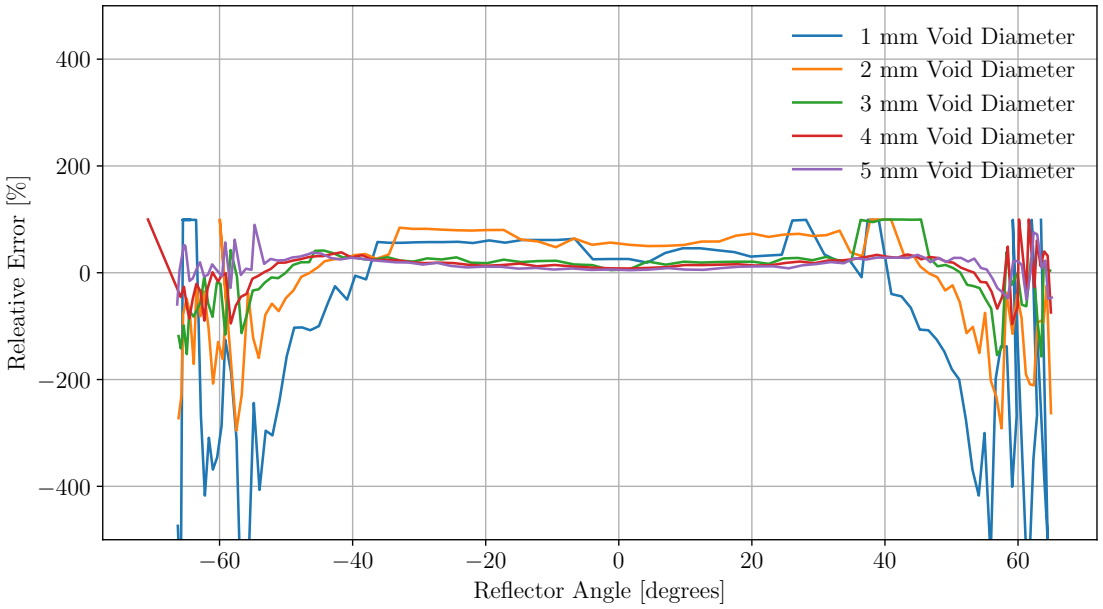

Figure 5.19: *Relative sizing accuracy of images constructed using 32 element aperture at every reflector angle available for each simulated void diameter in a water load.*

the measured BSD, therefore, reducing the algorithm's applicability to systems with bubble diameters larger than 3 mm. On the other hand, for reflector diameters of 3 mm or more the error was within 30% which was deemed acceptable for the purpose of this work.

For the TFM image dimensions used in this work, the minimum and maximum object angles possible were 14.0° and 26.6° respectively. This corresponds to the angle between the centre of the aperture and the nearest and furthest corners of the set image scene. For reflector angles in this range there will not be a significant impact on the sizing accuracy, demonstrated in Figure 5.20 showing the relative error between 14.0° and 26.6°. Therefore, the algorithm was determined to be robust enough for the angular variations expected in this work. If the extent of the y-axis was increased, for example, by increasing the number of elements in the

aperture, such that the maximum possible angle in the image scene was greater than 40.0°, an additional exclusion parameter could be easily incorporated into the image processing algorithm.

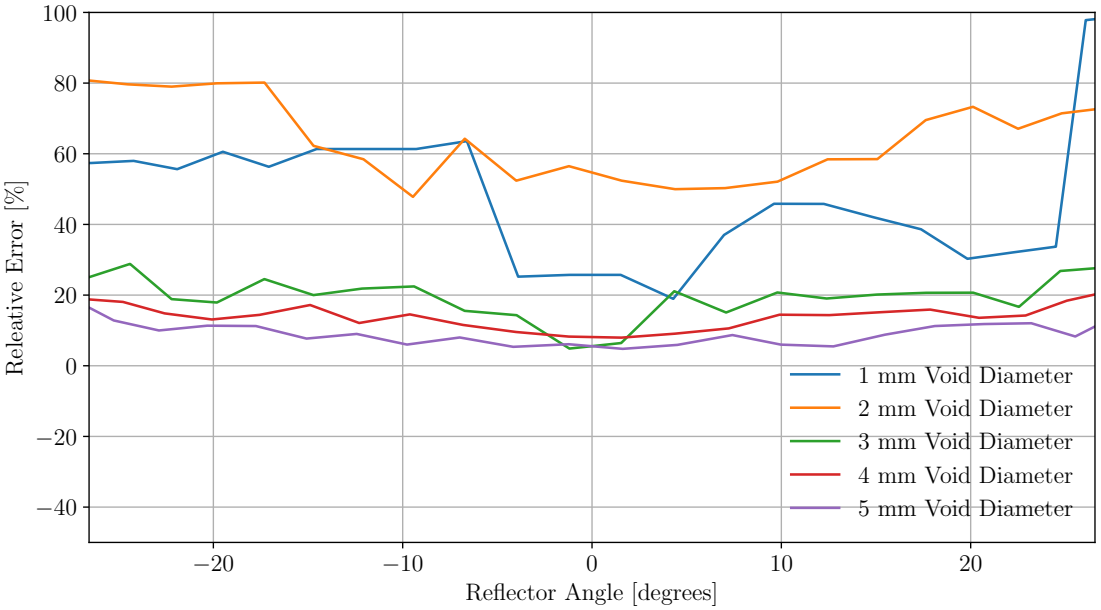

Figure 5.20: *Relative sizing accuracy from images constructed using a 32 element aperture zoomed to angles corresponding to the image scene created using the robotic arm data in a water load.*

5.4.6 Impact of Sign Coherence Factor

Upon visual inspection of the binary images for SDH diameters less than or equal to 2 mm, it was observed that increased spatial side lobe activity in the experimental data led to spurious images being generated for small reflectors. This lead to the curvature of the objects being reduced in the final images, especially for smaller objects. An example was recorded in Figure 5.21, indicating where the algorithm has sized the object correctly based on its design, however, the input image was not representative of the actual object shape. This means the sizing er-

ror was associated with the quality of the input image deriving from experimental data acquisition rather than from the image processing algorithm.

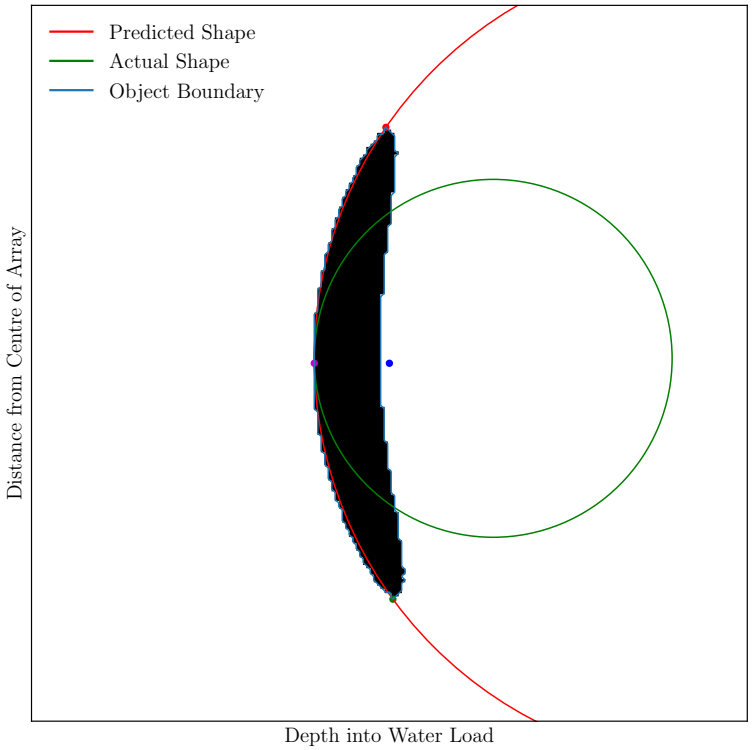

Figure 5.21: *Normalised TFM image of 1 mm SDH generated using 32 element aperture. The predicted size is larger than the actual size due to the shape of the input image.*

In Chapter 4 it was proposed to use the SCF to weight the TFM images when imaging through steel to reduce spatial side lobe activity. Therefore, in order to reduce the impact of spatial side lobes on smaller reflectors and to investigate the feasibility of non-invasive reflector sizing, the impact of the SCF was investigated.

The active aperture with the strongest correlation between the actual and predicted SDH diameters was 32 elements, meaning size predictions could be most accurately corrected. Therefore, TFM images generated from both the simulated

and experimental data sets with a 32 element aperture were investigated. The TFM images weighted using the SCF were passed to the bubble sizing algorithm and the relative error of prediction was recorded against the relative reflector diameter in Figure 5.22. The reflector diameters have been plotted in units of wavelengths to provide a valid comparison between the simulated and experimental results.

Figure 5.22 indicates that the response between experimental samples was consistent, demonstrated by the small error bars. Also, the overall accuracy was higher for all the experimental results than the simulated results. This is the opposite of what was previously found. This indicates that the experimental results were more influenced by spatial side lobe interference than the simulated data.

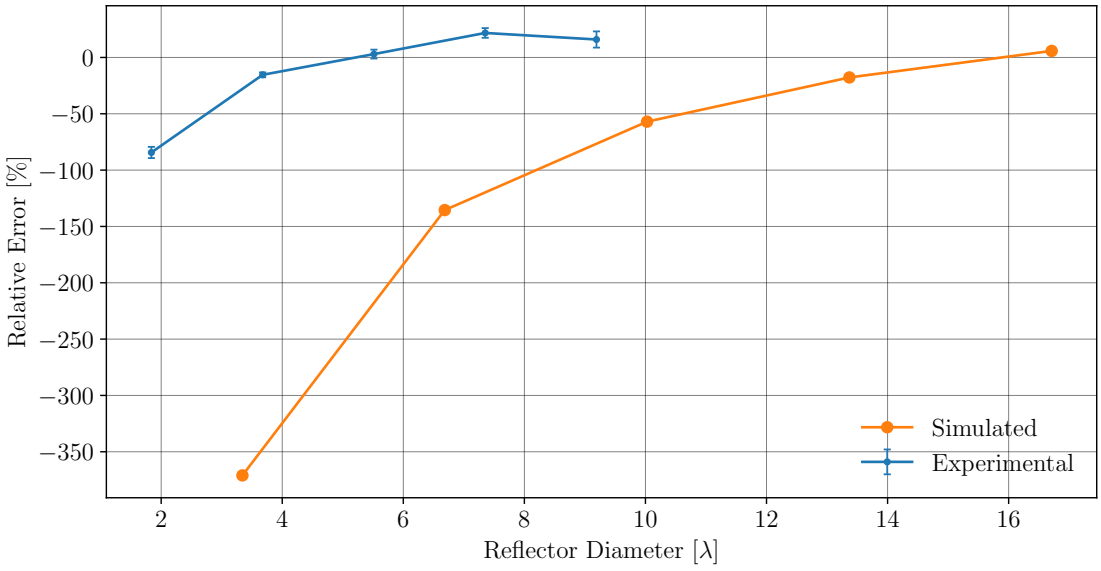

Figure 5.22: *Relative error of diameter prediction for 32 element aperture images after application of the SCF, experimental and simulated results.*

To emphasise the enhancement in the SDH sizing accuracy, the experimental

results have been plotted in Figure 5.23 with and without the application of the SCF to the TFM images. In Figure 5.23 the largest improvement was observed for the smallest reflectors, where the SCF has decreased the prediction error of the smallest SDH from -118% to -84%. A prediction error of -84% is still not ideal, however, it is an improvement. In practice, this demonstrates a limitation of the algorithm when applied to bubble diameters less than 5λ. If the physical size of the bubbles cannot be increased during the final application, an alternative solution could be to increase the inspection frequency leading to a decrease in the wavelength. However, higher frequency signals are more attenuated so this illustrates a compromise when applying this algorithm in practice.

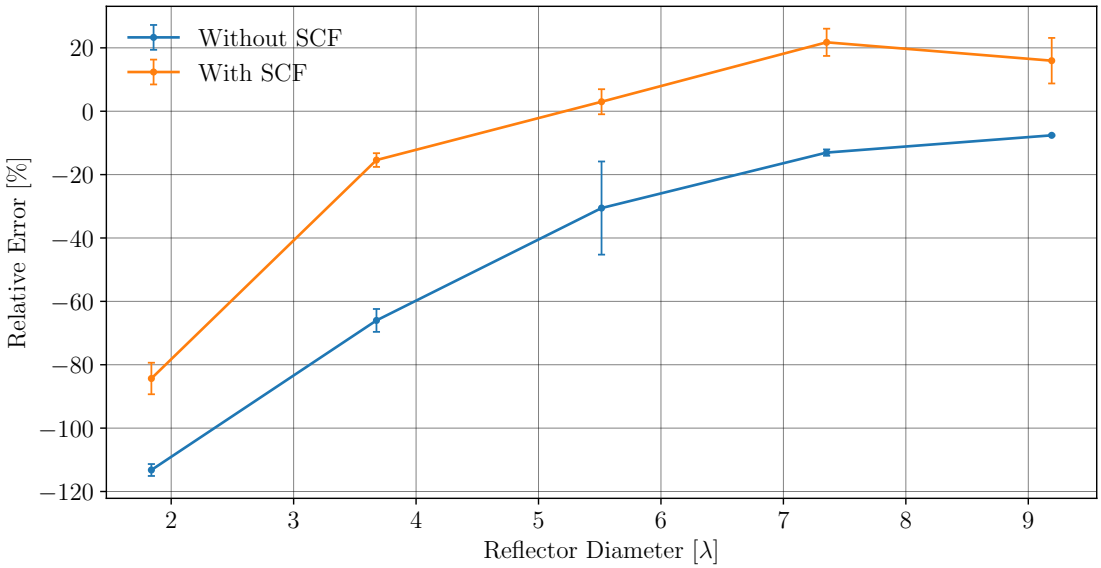

Figure 5.23: *Relative error of prediction of experimentally acquired ultrasonic data of SDHs, imaged using a 32 element aperture with the application of the SCF.*

5.5 Summary

An image processing algorithm has been presented to extract the spatial position and diameter of bubble-like reflectors captured in TFM images. The algorithm has been demonstrated to be robust under certain stationary experimental conditions illustrated in this Chapter. In particular, the sizing error was dependent on the size of the reflectors relative to the ultrasonic wavelength. Under the experimental conditions described in this Chapter, objects less than 5λ in diameter were predicted with an error greater than 60% when the SCF was not applied to the image matrix. Therefore, it is neccessary to deploy this algorithm to large reflectors to observe more accurate size predictions.

A significant factor in the deployment of the algorithm was the quality of the input TFM images to represent the true shape of the reflector objects. To overcome this challenge two solutions were proposed. Firstly, for elongated objects that did not exhibit a large enough degree of curvature the bubble sizing algorithm was modified to account for the object elongation. For the objects this had an impact on, the average improvement in reflector size prediction was 462%. This presents a specific limitation of the algorithm because the dynamic movement of reflectors can introduce this elongation effect into the image. Second, the impact of the SCF was investigated to reduce spatial side lobe interference in the input images, where an average sizing accuracy improvement of 34% was recorded for object diameters greater than or equal to 5λ.

Using simulated FMC data sets of bubble-like void reflectors suspended in water, the impact of the reflector angle relative to the surface of the array was

investigated. It was found that reflector angles greater than $\pm 40^{\circ}$ began to significantly compromise the image representativeness. In particular for the two smallest reflector sizes investigated, the minimum error was 50% for all angles. This provided a further indication that the applicability of the algorithm towards bubbles diameter less than 5λ was limited.

It was observed that the size of the active aperture impacted on the accuracy of diameter prediction. Using a 32-element aperture resulted in the most accurate size predictions. This was reasoned because restricting the aperture size increases the likelihood of a reflector being present in the target region relative to a larger aperture. This means enhances the SNR of the FMC data set and therefore the TFM images generated were more representative of the reflector objects. Also, for all apertures investigated the algorithm began to fail for smaller objects less than 5λ in diameter indicating that the degree of reflection from smaller objects is inadequate for this study.

Chapter 6

Modelling Dynamic Reflectors

6.1 Introduction

This Chapter presents the application of ultrasonic phased arrays to the imaging of dynamic reflectors and moving bubbles. The work presented in this Thesis so far has pertained only to phased array imaging of stationary reflectors. In order to understand the applicability of ultrasonic phased arrays to industrial process analysis it is imperative to model dynamic systems.

The key challenge to imaging of dynamic bubbles is the ability to control the dynamic nature of the image target. In this Chapter it is proposed to overcome this challenge by keeping the reflector stationary and to control the movement of the ultrasonic transducer relative to this image target. In doing so, a motivation for this work has been to characterise the robustness of the image processing algorithm presented in Figure 5.6 under dynamic conditions.

Practical application to dynamic systems requires the algorithm to extract information from moving bubbles, each of which will be travelling at a different velocity and have a different size. In light of this, several practical challenges are discussed, for example, the time difference between data acquisition and the movement of the image target. Following this, an algorithm is presented to track bubble-like reflectors through a sequence of image frames and to extract the bubble velocity while the bubbles are being tracked.

The conclusion of this work will set the scene in terms of the applicability of ultrasonic phased array imaging towards a dynamic industrial process. In particular, by testing the imaging system under controlled dynamic conditions, this work provides confidence in the imaging system prior to the application towards a dynamic system with a higher number of uncontrolled variables.

6.2 Experimental Methodology

6.2.1 Materials

The linear phased array and PAC corresponding to Hardware System 1 in Table 3.1 were deployed to acquire FMC data. In addition to the Perspex Calibration Sample presented in Chapter 5, a second Perspex sample in Figure 6.1 was acquired with the same acoustic properties and dimensions as the first Perspex Calibration Sample but containing an assortment of suspended bubbles throughout, hereafter named the Perspex Bubble Sample. A flat surface was machined onto the sample so that the phased array could be directly coupled to it.

Figure 6.1: *Photograph of Perspex Bubble Sample.*

6.2.2 Data Acquisition

In Chapter 5 an image processing algorithm was presented to extract the BSD from TFM images. It was observed that the quality of the input image to represent the image scene played a significant role in the overall accuracy of the algorithm to size individual stationary reflectors. It was also observed that there was a strong correlation between the actual and predicted diameter of SDHs determined from images created using an aperture size with a minimum of 32 elements.

The FIToolbox PAC had 32 transmit-receive channels available for FMC data acquisition. This meant that to acquire an FMC data set using an aperture larger than 32 elements required multiplexing of the channels. The time associated with multiplexing was expensive relative to the time to switch between individual elements, therefore using more than 32 elements significantly reduced the acquisition rate possible for a given depth range. This has been demonstrated in Table 6.1, where FMC data sets have been recorded at the maximum pulse repetition frequency (PRF) possible and the depth range has been set to 20 mm in water, representing the maximum image depth in this investigation. To maximise the FMC acquisition rate for modelling of the dynamic system, a 32 element aperture was deployed. However, under ideal conditions the PAC would have more transmit-receive channels available enabling a larger aperture to be deployed without the need for multiplexing.

Table 6.1: *FMC acquisition rate when fired 20 mm into water at the maximum PRF.*

Active Aperture (Elements)	**FMC Acquisition Rate (Hz)**
16	250
32	145
64	37
96	17
128	9

Unfortunately, due to a manufacture fault at one extremity of the Perspex Calibration Sample, the first 32 element indices could not be deployed without compromising the image integrity. Instead the aperture consisted of the 32 element indices in the centre of the array corresponding to elements 48 to 79. However,

due to the element-channel combinations being unsynchronised, the order of the A-Scans in the FMC data sets were incorrect, as described in Appendix B. The A-Scan order correction method outlined in Appendix B was therefore deployed prior to image construction from the FMC data sets used in this Chapter.

6.2.3 Dynamic System Modelling

To model the dynamic nature of the target system it was proposed to move the array relative to the position of a stationary reflector. This provided a feasible way to control the dynamic system and to increase the reliability of results in comparison to moving an individual bubble past a stationary transducer. The phased array was mounted to a six-axis programmable robotic arm (KR 6 R900 sixx, Kuka, Germany). The robotic arm was used to scan both the Perspex Calibration Sample and Perspex Bubble Sample, demonstrated in Figure 6.2, at speeds of 50, 100, 200, 300, 400 and 500 mms^{-1}. These speeds were chosen as they represent typical superficial gas velocities corresponding to bubble and slug flow in two-phase gas-liquid flows [151]. The Perspex samples were set level on the robot cell surface and the robotic arm was positioned to minimise any gap between the front face of the array and the surface of the sample. The path of the robotic arm was programmed prior to scanning the Perspex samples to maintain consistency between measurements. The robotic arm was situated within a fixed volume meaning there was an acceleration curve between the robot beginning to move and reaching its set speed and a deceleration curve vice versa. The FMC acquisition was programmed to begin at the same time as when the robot scanned the sample.

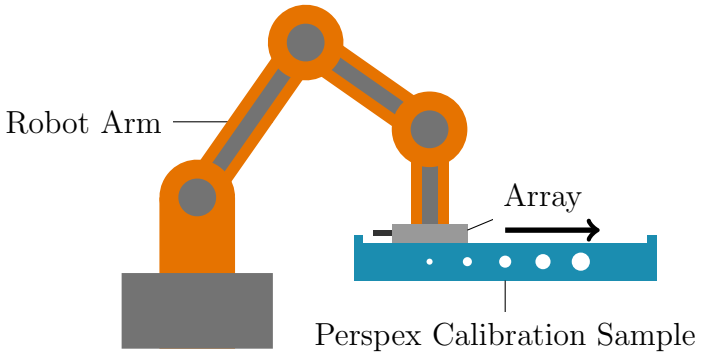

Figure 6.2: *Robotic arm used to scan Perspex samples at set speeds.*

When performing FMC, the elements in the aperture transmit ultrasound into the load medium sequentially. This means that each transmit event occurs from a spatial position adjacent to the previous. When constructing a TFM image, the precise location of each pixel relative to each element in the array is set prior to determination of the TOF between these element and pixel locations. The TFM algorithm assumes that the image scene geometry is constant throughout the image construction process such that the temporal resolution of the FMC data set is aligned with the positions of the elements and the image pixels.

When the robotic arm was used to scan the Perspex samples, the spatial position of the elements were not constant throughout the acquisition time of an FMC data set. This introduced error into the construction of the TFM images from data acquired under these conditions. Note, this source of error was not applicable when the reflector target was dynamic relative to a stationary array because the spatial location of the elements relative to the image pixels does not vary.

If the PAC acquires FMC data at a rate of 145 Hz as described in Table 6.1, the time to acquire a single FMC data set is 6.897 ms. If it is assumed that there

is no time delay between each FMC data set, the time for a single transmit event in the 32 element aperture is approximately 0.216 ms. If the array was moving at 50 mms^{-1}, the position of the array would have moved approximately 0.011 mm for each transmit event. This spatial offset increases to 0.107 mm or 14% of an element pitch per transmit event if the array is moving at 500 mms^{-1}. The value of this spatial offset is dependent on the index of the transmitting element such that the spatial offset between transmission on the first and last elements would be 0.345 mm and 3.448 mm at these two speeds respectively. Given that the element pitch was 0.7 mm, this spatial offset introduced a significant degree of error in the construction of the TFM images.

This error could not be removed from the TFM imaging algorithm without redesigning the imaging algorithm to account for this spatial offset. To incorporate an accurate offset parameter would require an accurate measurement of the FMC acquisition rate for each data set in terms of the precise timing of when the first and last elements transmitted and the value of any time delay between FMC data sets. The expected result of applying this modified TFM algorithm would be to increase the certainty of images relating to when the array was coupled with the robotic arm. However, this was out-with the scope of this investigation as the practical application involved the movement of bubbles relative to a stationary transducer, therefore, this was not undertaken. Alternatively, if the position of the reflector object were known, for example, after the first transmit event in the FMC process an auto-focusing algorithm could be implemented to refocus or delay the time domain A-Scans such that the object is focused at this initial position. Auto-focusing of FMC data has been performed for flexible ar-

ray transducers where the z position of the array elements is unknown and must be determined from the FMC data [152]. A similar approach could be implemented here whereby the y position of the elements is to be found. This could be achieved by correlating the pulse-echo response from each element with the FMC data to find the maximum correlation between the two. This sample point would be declared the time-of-arrival to the point of interest and the A-Scan delayed according to this error with respect to the empirical TOF.

To minimise this error the direction of the transmit events, in terms of the order of elements transmitting to acquire FMC, was aligned with the direction of the movement of the reflectors. This is demonstrated in Figure 6.3, where the first element to transmit could be either $T_{x_1} = 1$ or $T_{x_1} = 8$. If the direction of FMC transmit events is aligned with the direction of the bubble movement, the second element to transmit is $T_{x_2} = 2$, whereas the reverse direction corresponds to $T_{x_2} = 7$. It was observed that images generated from data acquired in the reverse direction to the bubble movement were significantly compromised relative to those generated from data acquired in the same direction as bubble movement. Therefore, all data acquired in this Chapter were performed with the spatial position of the first transmit event at the edge of the image scene where reflectors entered the image scene.

Due to the physics of the ultrasonic wave propagation in the dynamic system of interest, the bubbles will move relative to the acquisition process. For the FRD acquisition rate of 145 Hz, outlined in Table 6.1, and for bubbles moving in a linear path relative to the front face of the transducer at a speed of 50 mms^{-1}, the bubble will have moved approximately 0.34 mm during the acquisition of the

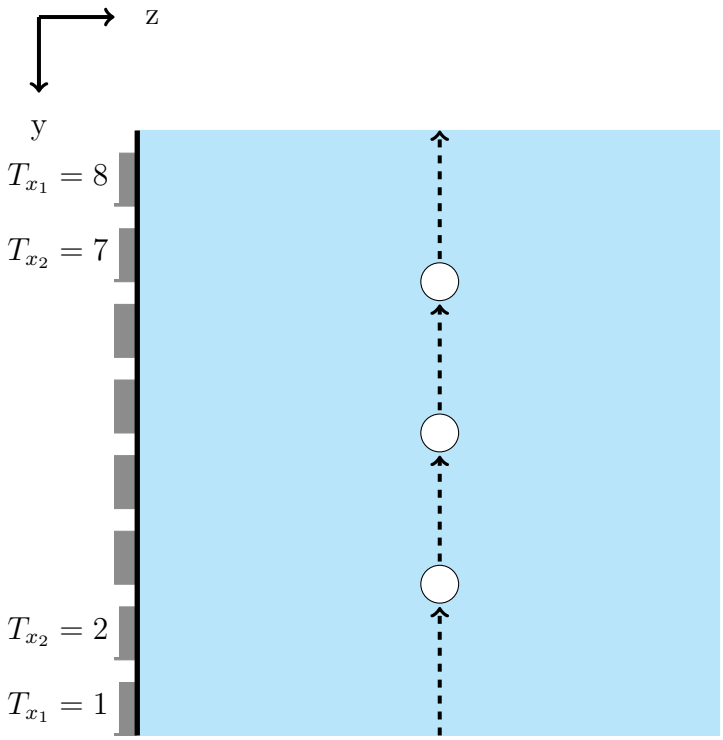

Figure 6.3: *Schematic showing direction of reflector relative to direction of element transmit events.*

FRD. Since this corresponds to a 32 element aperture, the bubble will have moved approximately 0.01 mm per transmit event. This corresponds to approximately half a pixel in the work presented in this Thesis, so will have a minimal impact on the image quality. However, if the bubble moves at 500 mms^{-1} the bubble position will be 3.4 mm from its initial position during the acquisition of the FRD. The impact of this is to elongate the image because the TFM algorithm assumes reflectors are stationary relative to the acquisition process and maps the signals onto the 'wrong' pixels. This is illustrated in Figure 6.4 using a 32 element sub-aperture of the simulated FMC relating to a 3 mm diameter void suspended in water, described in Section 5.3.2. Both binarised TFM images in Figure 6.4 relate to the same reflector, however, in Figure 6.4(b) the pixel values have been

shifted by a value corresponding to 0.1 mm $\approx$ 3.4/32 for each transmit event prior to compounding the pixel values from each transmit event. This has the impact of elongating the shape of the reflector such that it no longer represents the true shape of the reflector. This was repeated for each speed investigated using the robotic arm, where it was found that the speed limit before images were too compromised was 100 mms^{-1}, beyond which the images no longer represented the initial shape or position of the equivalent stationary object. This is a significant limitation of the applicability of ultrasonic phased array to these types of dynamic systems.

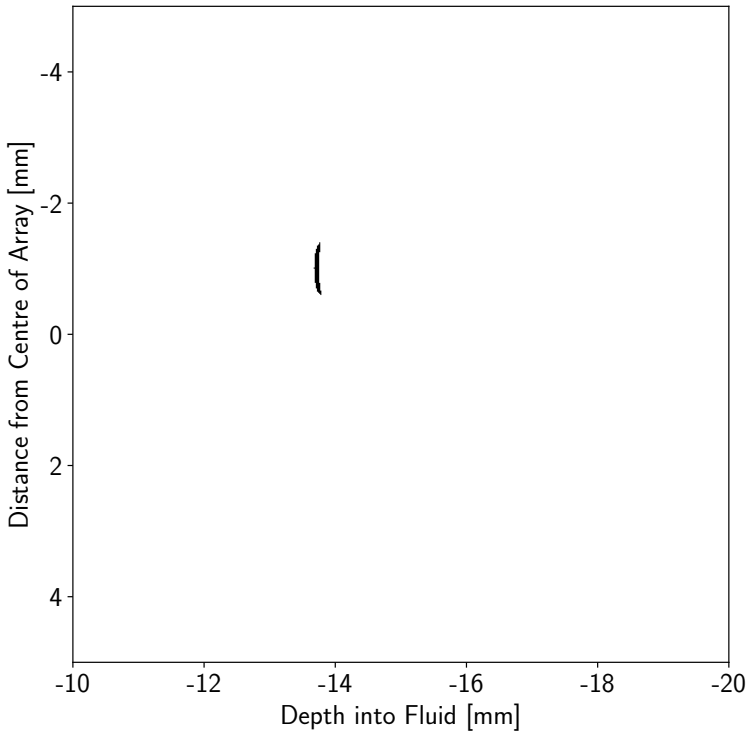

(a) *Simulated stationary bubble.*

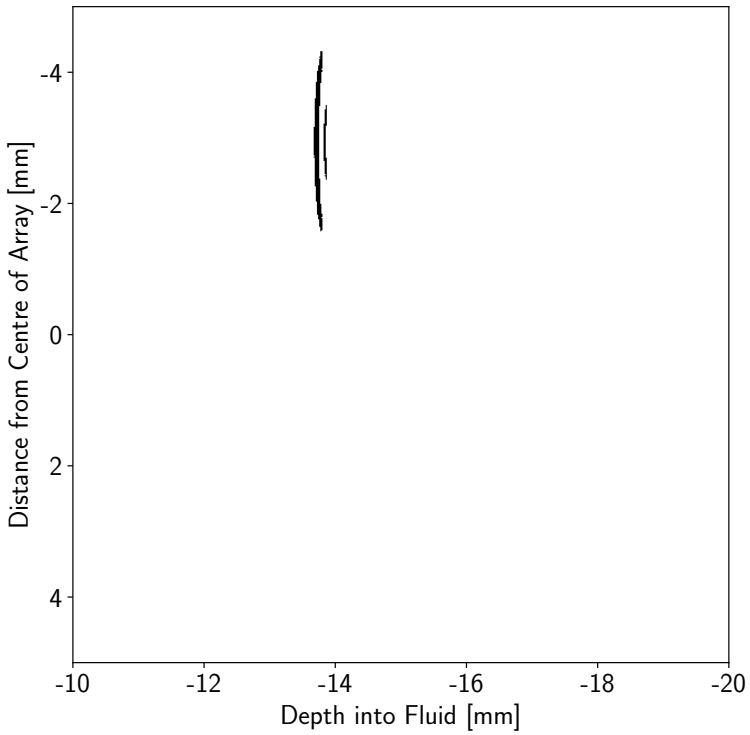

(b) *Simulated bubble velocity of 500 mms^{-1}.*

Figure 6.4: *Impact of bubble velocity on TFM image construction using a 32 element aperture.*

6.3 Object Tracking Algorithm

6.3.1 Background

Determination of BSD from individual image frames is performed by plotting a histogram of the diameter of all objects in the image frame. However, as objects move between individual image frames the same object may be quantified more than once, leading to bias towards individual objects in the overall BSD. Therefore to minimise the risk of object bias, a bubble tracking algorithm was developed, which can be found at the University of Strathclyde PURE repository, here, or the full link can be found in Appendix A.

Object tracking algorithms are designed to take an image frame containing individual objects and to assign an identity (ID) number to each object when it first appears. The algorithm should then track these objects while maintaining the same ID number for the tracked objects throughout subsequent image frames. Due to the uncertainty in noise associated between individual TFM images, the algorithm needed to be robust under conditions such as when a tracked object is lost for a certain number of image frames before reappearing, where upon the algorithm should identify the object ID and continue to track it.

6.3.2 Object Tracking Algorithm Design

The rate determining step in typical object tracking algorithms is the detection of objects within an image frame. Once these objects are detected, the tracking process is much faster, therefore if the objects are already identified then the

tracking process can be performed quickly. This was the case here, where the image processing algorithm presented in Chapter 5 generated an instance of a class containing the position of each object in the image frame to be tracked. Each instance of a bubble object class also had additional attributes, for example, its radius. Therefore, the object tracking algorithm was able to extract the spatial position associated with each occurrence of the tracked object while recording the parameters relating to the object.

The overall process for tracking the bubbles through consecutive TFM image frames has been outlined in Figure 6.5. The process begins by supplying an instance of the bubble sizing class that contains a list of valid objects in the current image frame. If there are currently no objects being tracked then all the objects supplied are registered for tracking. Otherwise, the algorithm must identify if there are any objects in the image frame. If there are none, then this means all currently tracked objects have disappeared in the current frame. To increase the tracking certainty, objects were only permitted to disappear once between consecutive image frames. Upon an object disappearing, for example, due to signal noise, the object is registered as having disappeared but the current object location is not altered. Then in the next frame, the object can reappear and be identified for tracking again. If a currently tracked object does not appear in two consecutive frames, the object ID is de-registered from the list of currently tracked objects.

When there are objects in the current frame, the algorithm determines the Euclidean distance between each combination of the objects' key-point 3 positions. The centroid positions are not used in the tracking algorithm because

these were dependent on the shape of the objects in the image such that using the centroid location introduced uncertainty due to the calculation of the object radius. However, the key-point 3 position was always located precisely on the object boundary. Following this, the distances were ranked from smallest to largest and those closest to the key-point 3 values of currently tracked objects were considered to belong to the same object. In addition, some restrictions were placed on the relative spatial positions of the two objects. Given that the bubble flow was always from the base to the top of the image scene, only when the new object was above the previous object was it considered to belong to the same object ID. Also, if an object was observed to have moved laterally by a distance greater than the larger of the two radii in question, the second object was not considered to have the same object ID as the original. This prevented spurious tracking based on euclidean distance measurements. Finally, if the two objects in question were not within 50% of each other's radius, then they were not considered to have the same object ID. After passing all of these criteria, the key-point 3 value of the tracked object ID is updated with the new value in the current image frame and the list of tracked objects is updated with the new position of the bubble object. However, if the distance between objects is greater than an arbitrary threshold, the object ID is de-registered from the list of tracked objects.

Once the individual objects were identified and tracked, the velocity of each tracked object could be determined. This was done by calculating the distance between the key-point 3 position of each tracked object in the first and last image frames that they were recorded. Given that each image frame has an associated timestamp, acquired using a hardware timer on the PAC via a dynamic link

library (DLL), the time difference between the first and last image frame was determined. Alternatively, the bubble velocity could be determined using cross-correlation of sequential images to determine their optical flow [153]. However, this was more computationally intensive than using object tracking because it considers the differential between corresponding pixels in each image frame rather than using known reference points such as the identified object key-points.

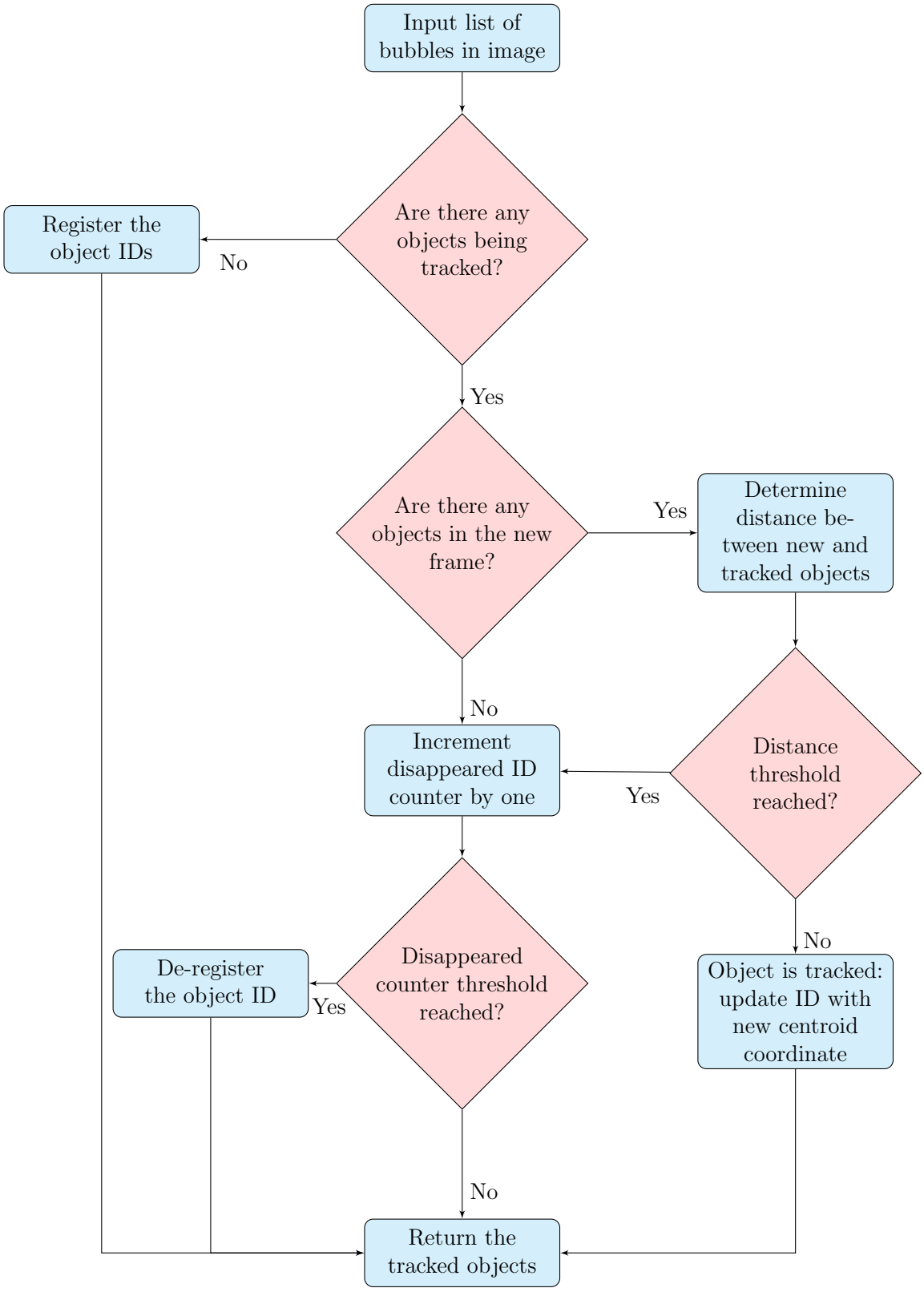

Figure 6.5: *Flow chart illustrating bubble tracking algorithm.*

6.4 Bubble Sizing in Perspex Bubble Sample from Photographs

6.4.1 Background

The Perspex Bubble Sample was used to model a typical industrial process with a range of bubble sizes suspended in Perspex. However, the sample was not bespoke for the purpose of this investigation so the BSD was not known and needed to be determined experimentally. To achieve this an image processing algorithm was developed in Python 3.6 [142] to extract an estimate of the BSD from photographs of the sample. This can be found at the University of Strathclyde PURE repository, here, or the full link can be found in Appendix A.

The methodology was designed to provide a reasonable estimation of the BSD however it was not calibrated using the Perspex Calibration Sample. The image processing algorithm deploys well-established methodologies to extract the equivalent diameter of regions corresponding to bubbles in photographs of the sample, so it was assumed to be a close enough approximation for the purpose of this investigation.

6.4.2 Data Acquisition Methodology

Photographs of the Perspex Bubble Sample were captured using a digital camera (Nikon, Japan) with a 20.7 mega pixel resolution. A ruler with a millimetre length scale was positioned at the base of the transparent Perspex sample to

enable estimation of the pixel dimension. The sample was illuminated using an LED lamp with an illuminated area of 200 × 210 mm^2 and an illumination intensity of 10 klx, positioned behind the sample. Three photographs were captured along the length of the sample to ensure maximum coverage of the reflectors. These were exported in *.jpg* format to a PC to be read into the image processing algorithm.

6.4.3 Image Processing Methodology

The images were uploaded using the Python Imaging Library [154], where the three-channel RGB images were then converted to greyscale images, demonstrated in Figure 6.6(a). The images were cropped to reveal just the bubbles relating to the ROI and to remove interference from the edges of the sample.

Following this, the images were binarised using Otsu's method [101], where it was assumed the illumination was even throughout the sample. Binary dilation, using an arbitrarily chosen structure of 16 × 16 pixels, was applied to expand the extent of objects in the binary image. This had the impact of closing gaps in the image that would otherwise prevent objects from representing closed regions. Finally, binary hole filling was applied to remove interference from overlapping objects located within other objects. The result of this binary image processing was recorded in Figure 6.6(b). Note, in practice binary erosion using a 16 × 16 structure should also be applied following binary hole filling because the binary image was initial dilated using this structure size. In error, this was not performed here, so it should be noted that this image processing algorithm is likely to overestimate the size of the objects in the image as the binary objects were dilated

but not eroded.

Segmentation of the individual objects in the image was performed using the Watershed algorithm [155]. The Watershed algorithm first identifies markers in the binary image corresponding to local maxima relative to the distance to the background of the image. These markers represent the basins to be filled by the Watershed algorithm. The second stage of the algorithm is equivalent to filling the image from these marker positions, where the edge of a region is defined as the position where the Watershed to a neighbouring region is reached. The result of application of the Watershed algorithm was recorded in Figure 6.6(c), where the perimeters of the identified objects have been recorded by the red lines.

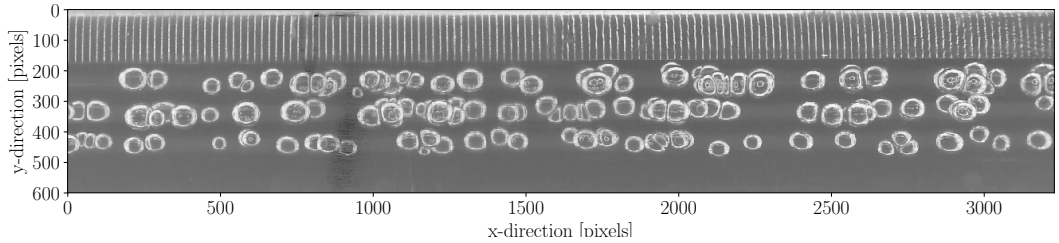

(a) *Greyscale image of Perspex Bubble Sample, including millimetre scale.*

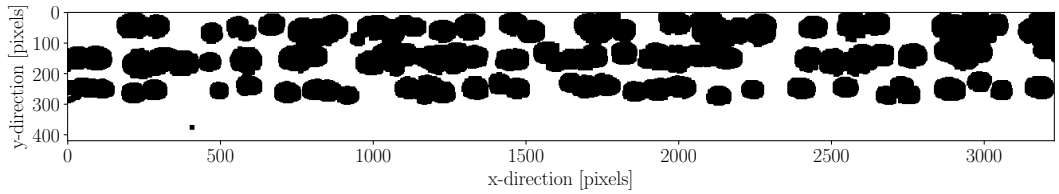

(b) *Binary image of Perspex Bubble Sample, generated using Otsu's threshold method, scale has been cropped from image.*

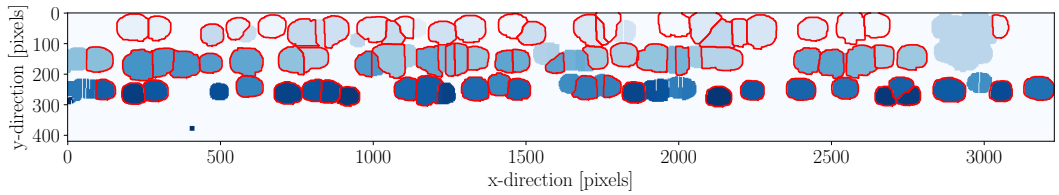

(c) *Image of Perspex Bubble Sample after application of Watershed segmentation algorithm, regions of interest are highlighted by red contours.*

Figure 6.6: *Key stages of image processing algorithm to extract BSD in Perspex Bubble Sample.*

6.4.4 Estimated Bubble Size Distribution

The area of the individual watershed regions were converted to the equivalent diameter (m) of a circle with the same area. However, this assumed that the pixels were square which was not the case. The length of a pixel in the y dimension was approximately five-sixths of the length of a pixel in the x dimension, so this difference was deemed negligible for the purpose of this investigation. Once

the equivalent diameter was determined, object exclusion parameters were set to remove objects that were too small or too large to represent true bubbles.

The value of these exclusion limits were determined from manual inspection of small and large bubbles in the images that were clearly separated from other bubbles. The advantage of manual inspection was that interference was easily identified, so only relevant objects were used. The smallest and largest bubbles in the images were approximately determined to have 2.0 mm and 5.5 mm diameters respectively. Therefore these values were set as the exclusion parameter limits prior to plotting the histogram of the BSD.

The image processing methodology was repeated for all three images acquired of the sample, where it was assumed the overall output was representative of the total sample. The identified equivalent diameters from all images were collated into a single array and recorded as a histogram in Figure 6.7. It was observed from the empircal data that the BSD was described by a logarithmic Normal distribution, where the mean and standard deviation of the distribution were 2.838 ± 1.038 mm respectively and its probability density function (PDF) has been superimposed onto the histogram. This distribution was used as a reference BSD when sizing the bubbles in the Perspex Bubble Sample from the TFM images.

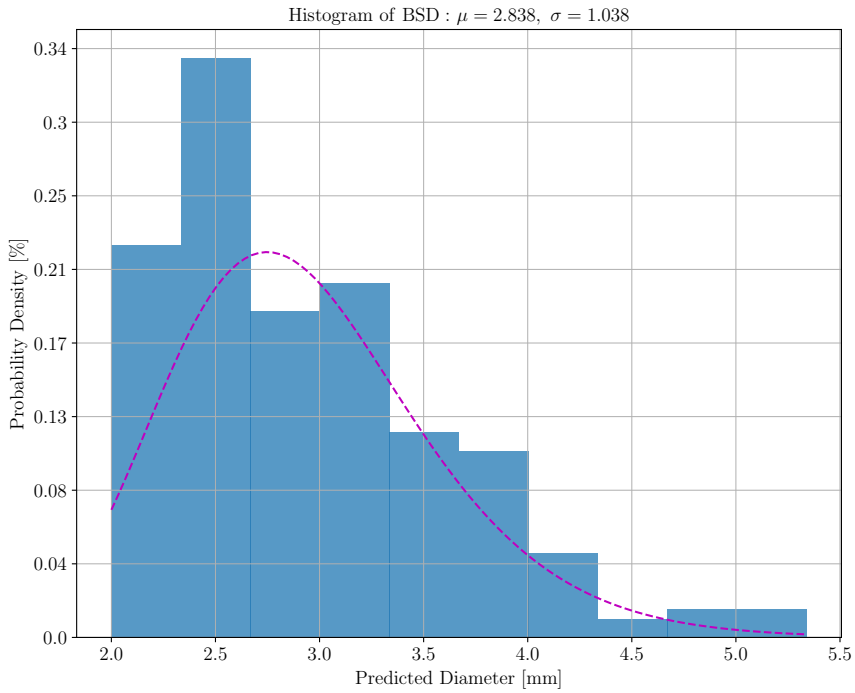

Figure 6.7: *BSD estimated from photographs of Perspex Bubble Sample. Purple line corresponds to the log-Normal PDF fitted to the measured data.*

6.5 Results and Discussion

6.5.1 Visualisation of Robotic Arm Scan

The robotic arm was used to scan the two Perspex samples while acquiring FMC data using a 32 element aperture. The typical output from this experimental procedure is shown as an animation in Figure 6.8 (click ▶). This represents each of the five SDHs in the Perspex Calibration Sample, when the robotic arm scanned the array across the sample at 50 mms^{-1}. Note, Figure 6.8 indicates where objects not completely in the image were excluded from the sizing algorithm and how the

algorithm was robust enough to size reflectors orientated with a range of angles and positions relative to the array surface.

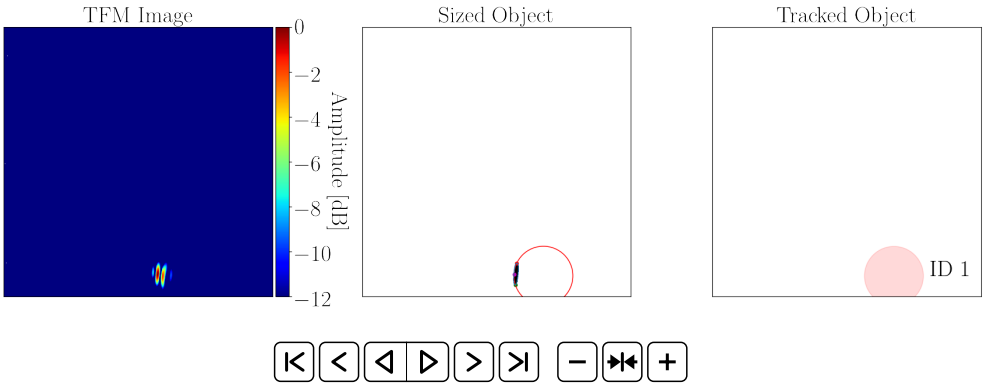

Figure 6.8: *Animation demonstrating dynamic sizing and tracking of SDHs in Perspex Calibration Sample scanned at 50 mms^{-1} - click ▶.*

6.5.2 Velocity Determination using Object Tracking

The key-point 3 positions of the SDHs in each TFM image of the Perspex Calibration Sample were passed to the bubble tracking algorithm in the order that they were acquired. The velocity was determined for each SDH at each speed that the robotic arm was programmed to move. The predicted velocity was plotted against the actual velocity of the robotic arm in Figure 6.9.

It was observed that for SDH diameters of 2, 3 and 4 mm the predicted velocities were close to the actual velocities in all cases except for the 3 mm diameter SDH at 400 mms^{-1}. However, for SDH diameters of 1 and 5 mm, the predicted velocity was underestimated at velocities greater than 200 mms^{-1}. The 1 and 5 mm SDHs were located at either extremity of the Perspex Calibration Sample. Therefore, the error for these SDHs can be explained by the acceleration

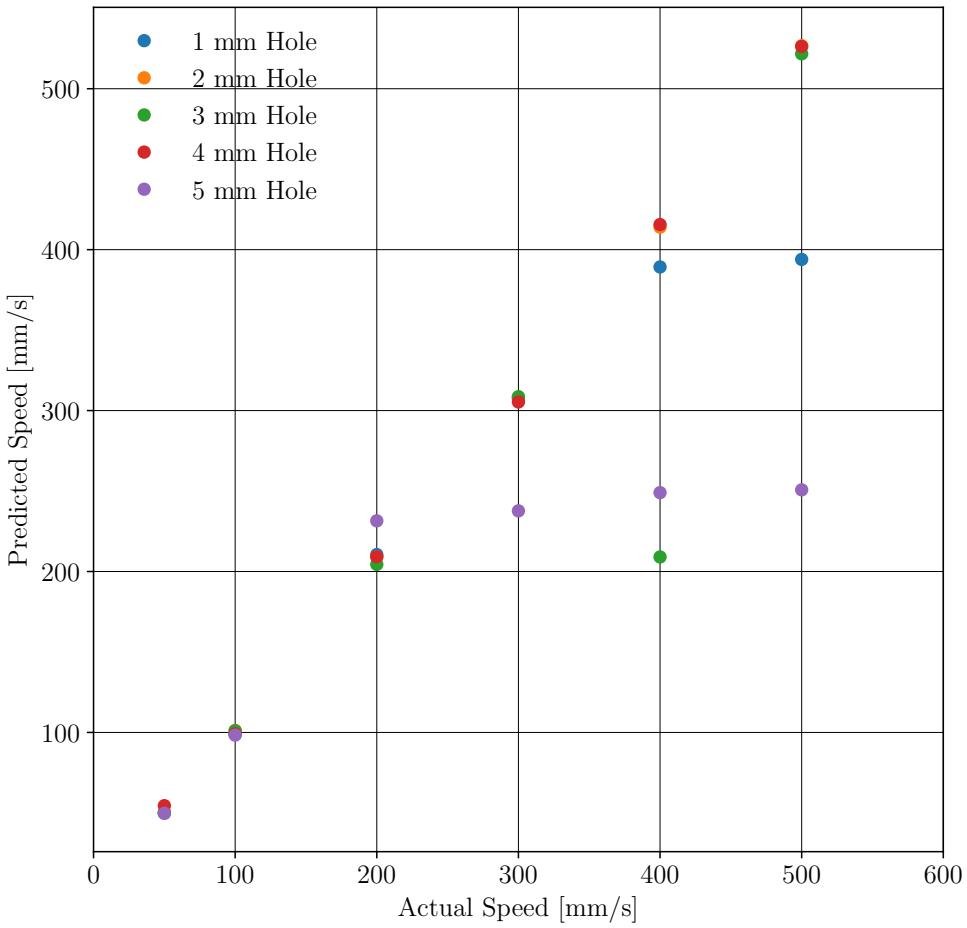

Figure 6.9: *Predicted velocity from bubble tracking algorithm against the actual velocity for each SDH in the Perspex Calibration Sample.*

and deceleration curves associated with the robot to reach its set speed. For the 3 mm diameter SDH at 400 mms^{-1} the error was a result of there only being two images available that represented the SDH. Upon inspection of these images, it appears the object has been imaged and sized correctly, however the difference between the two images was not very significant. Therefore, this result

was deemed an outlier within the context of the bubble velocity estimation.

It was also observed that the prediction error was greater at the higher velocity values. An average error of 2% was observed at 50 mms^{-1} whereas an average error of 17% was observed at 500 mms^{-1}. This was a result of the slower velocities leading to a higher number of individual images being supplied to the bubble tracking algorithm, therefore increasing the reliability of the results.

6.5.3 Impact of Robotic Arm Movement

The images generated from the data recorded using the robotic arm to scan the Perspex Calibration Sample were passed to the bubble sizing algorithm using the SCF to weight the pixels in the TFM images. The identified and sized objects in each image frame were collated for each robotic arm speed and for each SDH diameter, where the empirical mean and standard deviation were recorded. These results were represented in terms of the relative error of SDH diameter prediction in Figure 6.10, where the error bars correspond to one standard deviation. It was observed that the relative error was consistent for speeds of 50, 100 and 200 mms^{-1} but for speeds greater than 200 mms^{-1} the sizing algorithm began to generate spurious results. This trend was characterised by a decrease in the mean sizing accuracy and also an increase in the spread between the results. For the results corresponding to 200 mms^{-1}, the spread between the results began to increase, however, the mean response for each SDH was consistent with the results from 50 and 100 mms^{-1}. This increase in spread can be attributed to the uncertainty associated with the image construction algorithm due to the misalignment of the true spatial position of the elements relative to the programmed positions

of the image pixels. For speeds of 50, 100 and 200 mms^{-1}, the most accurate predictions were of the 1 and 5 mm diameter SDHs. This was due to these SDHs being located at the extremities of the Perspex sample, so the robotic arm would have been moving at slower speeds at the time of data acquisition of these SDHs, leading to more representative image construction. Therefore, in the context of this investigation, it was concluded that accurate sizing of the Perspex Bubble Sample could only be achieved at speeds up to 200 mms^{-1}.

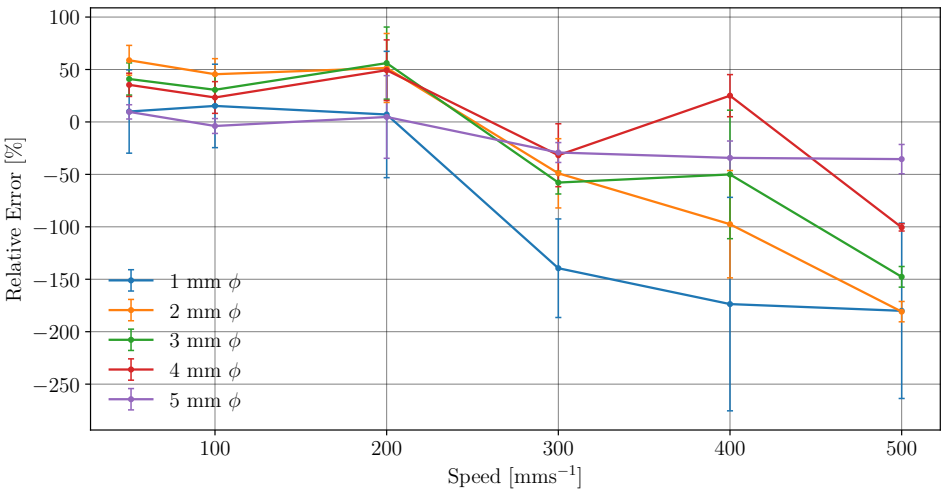

Figure 6.10: *Relative error of SDH diameter prediction against speed of robotic arm for each SDH.*

In light of this, the predicted SDH diameter was plotted against the actual SDH diameter for speeds of 50, 100 and 200 mms^{-1} in Figure 6.11. The uncertainty envelope was determined from the standard deviation at each data point for each velocity. Using these results as a LUT, the predicted diameter can be corrected if the velocity of the sized object has been determined, for example, from deployment of the object tracking algorithm. The wide shape of the uncertainty envelope at 200 mms^{-1} meant that the algorithm was less sensitive to

changes in the true reflector size at this speed, reducing the applicability of the algorithm at this speed. Therefore, it was recommended to deploy this plot only for reflectors moving at 100 mms^{-1} or slower.

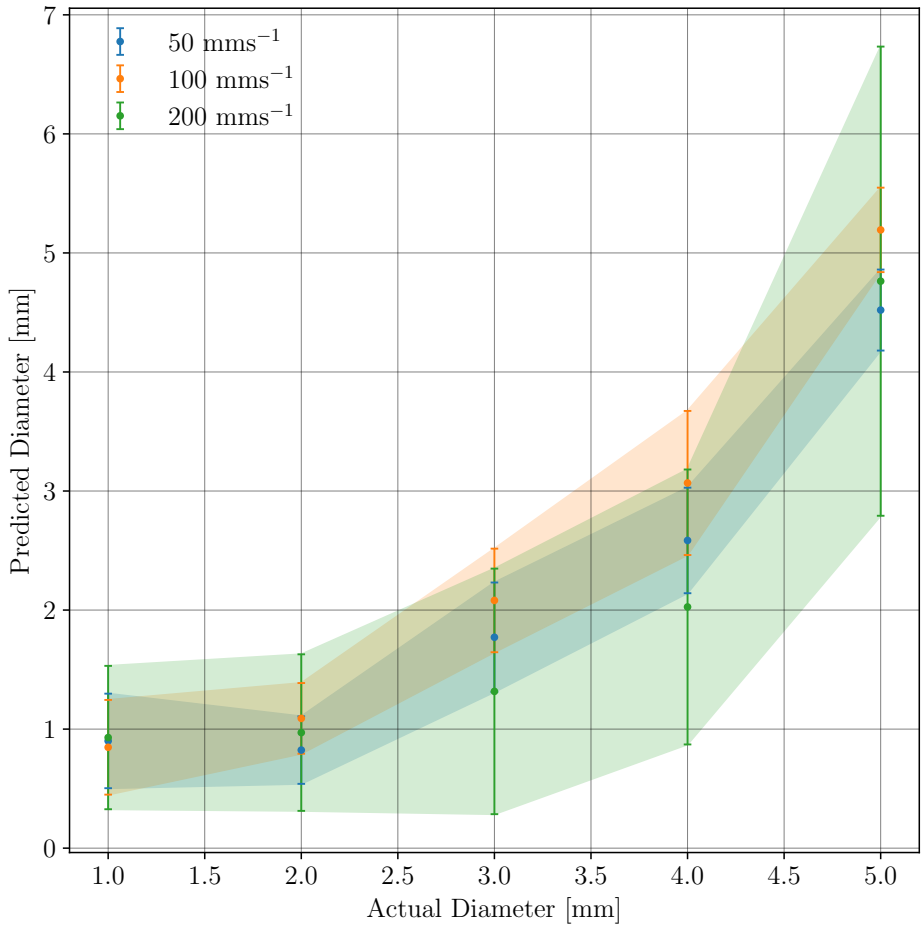

Figure 6.11: *Predicted SDH diameter against actual SDH diameter for arrays speeds up to 200 mms^{-1} and their uncertainty envelopes.*

The application of the uncertainty envelope to correct the size of a tracked reflector moving at 100 mms^{-1} has been demonstrated in Figure 6.12. For exam-

ple, if a reflector was predicted to have a 1.35 mm diameter and a velocity of 100 mms^{-1}, the modified value can be predicted by extrapolating to the midpoint of the uncertainty envelope and projecting this value onto the x-axis. In this case the modified value was 2.13 ± 0.53 mm, however if the input value was 4.0 mm the estimated modified value was 4.41 ± 0.26 mm, indicating the greater sensitivity at higher input diameter values. Given that the bubble sizing algorithm always underestimated the true value for the SDH diameters, this procedure provided a crude but effective method to offset this underestimation. Note, it was concluded in Chapter 5 that smaller reflectors, corresponding to 1 and 2 mm diameter reflectors here, could not be accurately sized because the objects did not reflect enough ultrasound to generate a representative image of the true object shape. Therefore, in practice the bubble sizing algorithm should only be deployed for bubble reflectors larger than 5λ in diameter and at bubble velocities slower than 200 mms^{-1}.

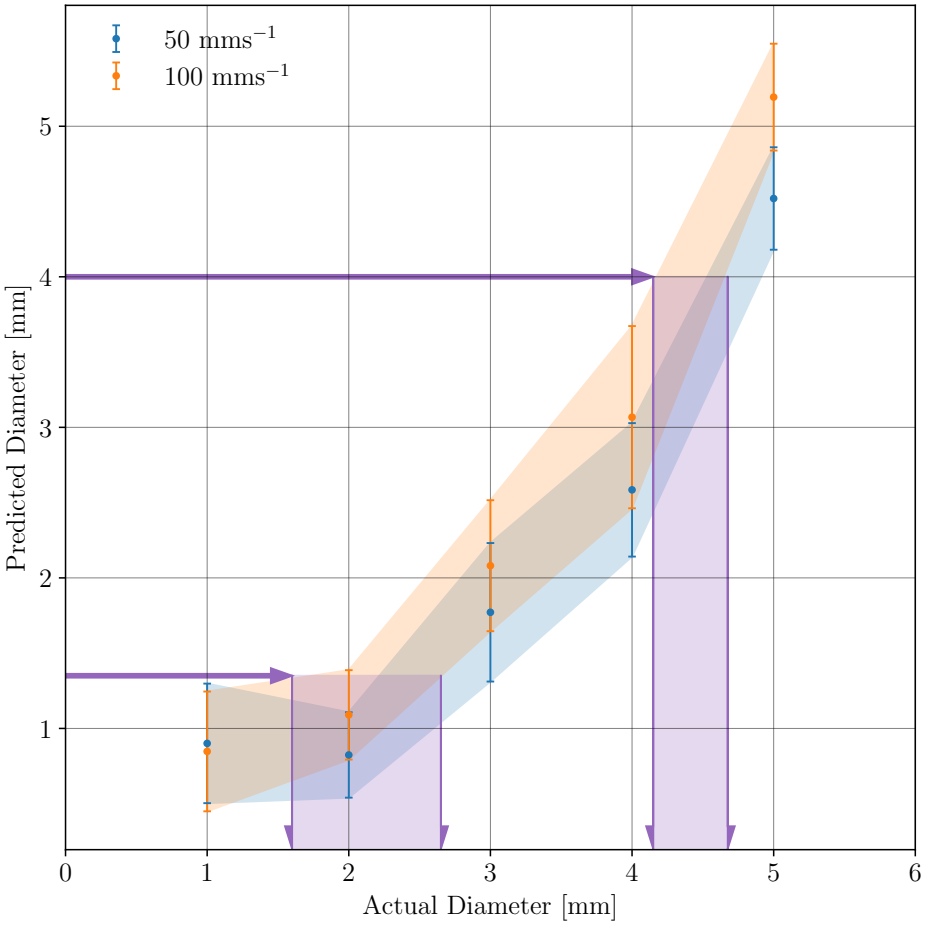

Figure 6.12: *Predicted SDH diameter against actual SDH diameter for arrays speeds of 50 and 100 mms^{-1} and their uncertainty envelopes used to determine the modified size prediction.*

6.5.4 Testing of Perspex Bubble Sample

The Perspex Bubble Sample was scanned using the robotic arm at speeds of 50 and 100 mms^{-1}. The array was deployed using a 32 element aperture and the images were generated using the SCF to weight the pixel values. The sizing algo-

rithm always underestimated the true reflector size at these speeds, demonstrated in Figure 6.10. Also, from manual inspection, the BSD in the Perspex Bubble Sample was determined to range from 2.0 and 5.5 mm. Using these criteria, the diameter thresholds were set to 1.5 and 5.5 mm for objects sized from TFM images of the Perspex Bubble Sample, to account for the underestimation. Given that the smallest bubble diameter in the Perspex Bubble Sample was approximately 2 mm, this met the conditions for application of the sizing algorithm outlined in Chapter 5. Following this, the BSDs were recorded in Figures 6.13(a) and 6.13(b), where a log-Normal distribution was also observed to fit the measured data and superimposed onto the histograms.

It was observed that the mean response slightly increased as the speed of the robotic arm increased. This indicated that the objects in the images were becoming more elongated as the speed increased but could also be attributed to the misalignment between the true element positions and the pixel coordinates as discussed previously.

The velocity of the robot arm was predicted from the movement of the tracked bubble objects in the sequence of images relating to the Perspex Bubble Column. The predicted velocities were 41 ± 20 and 72 ± 26 mms^{-1} for when the robot was programmed to move at 50 and 100 mms^{-1} respectively. This corresponded to velocity prediction errors of approximately 20% and 30% respectively. These errors were higher than those observed for the Perspex Calibration Sample, which were within 10% at these robotic arm speeds. Since the data acquisition was identical for the two Perspex sample, the accuracy difference in velocity determination suggests that the bubble tracking algorithm incorrectly tracks some objects or

that noise has been introduced when multiple objects are present in the TFM images.

Given that the predicted BSD from the photographic image processing methodology was described by the mean and standard deviation of 2.8 ± 1.0 mm, the TFM image processing algorithm has generated a result consistent with this methodology at both speeds presented here. However, it was expected that the image processing algorithm using photographs would overestimate the true size because binary dilation had not been performed following binary hole filling. Where the mean value of the BSD was within 18% and 10% for the 50 and 100 mms^{-1} velocities respectively. Also, given that the extracted velocities were within 30% it was concluded that the ultrasonic image processing algorithm was effective at extracting the BSD and bubble velocity to a reasonable accuracy at these bubble velocities. Note, in the practical application, although the bubbles exhibit a distribution of sizes they would also exhibit a distribution of velocities and would not all be consistent as in this experiment.

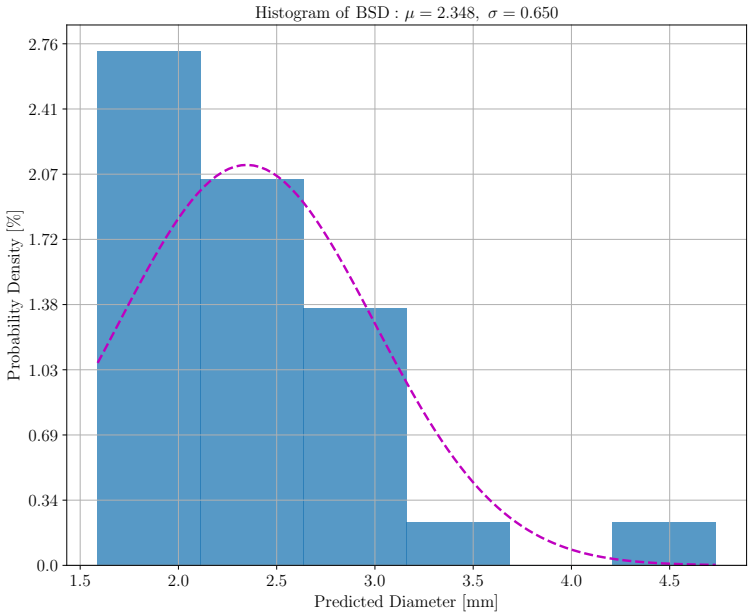

(a) *Bubble size distribution with robotic arm scanning the Perspex Bubble Sample at 50 mms^{-1}.*

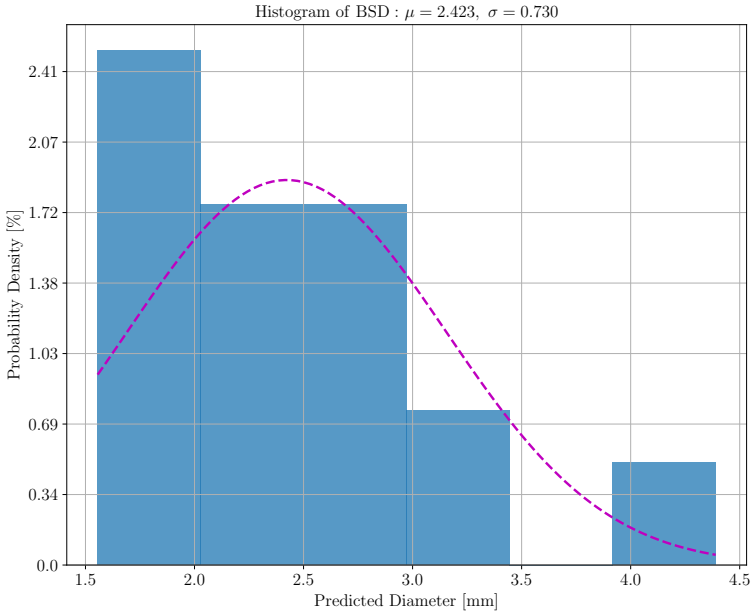

(b) *Bubble size distribution with robotic arm scanning the Perspex Bubble Sample at 100 mms^{-1}.*

Figure 6.13: *Estimated BSDs in Perspex Bubble Sample and log-Normal distributions fitted to the measured data.*

6.6 Summary

In this Chapter, challenges associated with the extraction of quantitative information from TFM images of dynamic bubble-like reflectors have been investigated. To model the dynamic nature of the target industrial process, the phased array was coupled with a six-axis robotic arm to scan Perspex samples containing stationary reflectors. This provided ground truth under controlled imaging conditions prior to extending the imaging system to dynamic systems containing more uncontrolled variables. Using an object tracking algorithm it was found that there was a very strong correlation between the predicted and actual velocities of the robotic arm, which was accurate within 30% at the investigated velocities, specifically 50 and 100 mms^{-1}.

In terms of reflector sizing, it was found that the controlled dynamic imaging system began to fail at robotic arm speeds greater than 200 mms^{-1}, however, this was partly attributed to the design of the imaging algorithm that failed to account for the movement of element positions between individual transmission events. Upon investigation of the impact of bubble movement on image quality, it was observed that velocities greater than 100 mms^{-1} compromised the TFM image such that the TFM images no longer represented the initial shape of an equivalent stationary object. This limits the applicability of this algorithm to slow moving dynamic systems with large bubble diameters.

The ability to extract the BSD at speeds up to 100 mms^{-1} was tested using a Perspex Bubble Sample containing a distribution of bubbles between 2.0 to 5.5 mm in diameter. The BSD in this sample was estimated using a photographic

image processing algorithm alongside the TFM image processing algorithm. The mean bubble diameter predicted from the TFM images was within 18% and 10% of the photographic result for robotic arm speeds of 50 and 100 mms^{-1} respectively. However, due to an error during development of the photographic image processing algorithm, BSD estimates were overestimated using this methodology. This means the significance of this result cannot be validated.

Chapter 7

Experimental Validation

7.1 Introduction

This Chapter brings together the concepts presented throughout the previous four Chapters into the experimental domain. The motivation for this work is to demonstrate the potential for ultrasonic phased arrays to be deployed for imaging of a bubble column in an industrial process stream. In doing so, it is the aim to demonstrate how these images can be used to extract meaningful quantitative information about the process stream without prior knowledge of the system.

The Chapter begins by describing the experimental methodology used to acquire ultrasonic data of a bubble column intrusively and non-invasively. Following this, a photographic representation of the image scene is provided and analysis of this image is used as a benchmark for the ultrasonic image analysis. Next,

the results are presented in terms of the BSD and bubble velocity extracted from the ultrasonic images. Finally, a discussion is opened on the optimisation of the overall imaging system towards real-time process analysis.

7.2 Methodology

7.2.1 Materials

The linear phased array and PAC corresponding to Hardware System 1 in Table 3.1 were deployed to acquire FMC data. A detailed schematic of the experimental apparatus is shown in Figure 7.1, where non-invasive data acquisition was achieved by using cable ties to secure the solid non-invasive medium to the front face of the phased array. For both intrusive and non-invasive measurements the phased array was submerged in water ensuring the array was acoustically coupled to the load medium. If the array were to be positioned on the outside wall of the tank, this risked introducing error from the coupling medium between the transducer and the tank wall. Note, the water was supplied directly from the tap, it did not undergo degassing or any other treatment process prior to be used in these experiments.

The BSD was highly dependent on the flow rate of gas being supplied to the bubble diffuser module. To maintain a relatively constant BSD throughout all measurements, a flow meter was positioned between the air pump and bubble diffuser. The flow meter had a measurement range of 0.00 to 0.85 $dm^3 min^{-1}$. The flow meter was a rotameter that consisted of a graduated tubing containing a ball

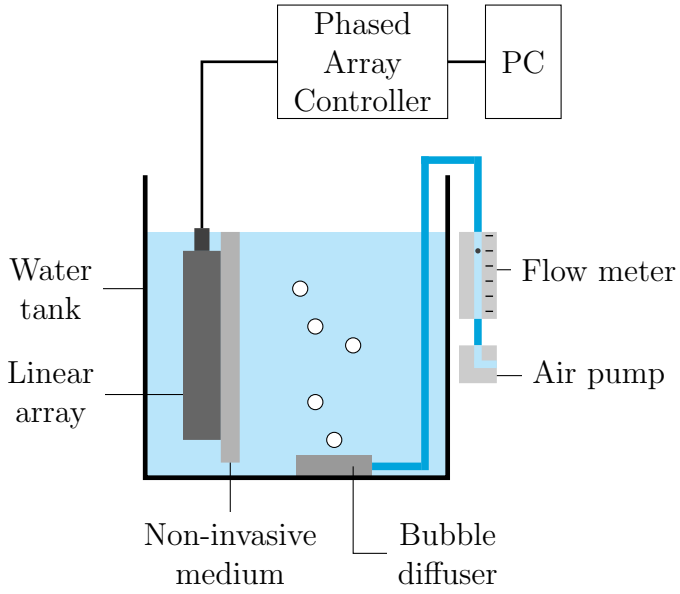

Figure 7.1: *Schematic representing experimental apparatus to acquire in-situ ultrasonic data of dynamic bubble column.*

bearing that had been calibrated with respect to the force of gravity. This meant the flow meter needed to be positioned vertically and flow rate measurements were taken from visual inspection of the ball bearing position within the tubing. This created a degree of uncertainty in terms of the flow rate measurement values, however, this uncertainty was minimised as there was only one analyst recording the flow rate values.

Non-invasive data acquisition was performed using materials with increasing values of reflection coefficient, described in Equation (2.4), relative to water, as recorded in Table 7.1. The greater the reflection coefficient the less ultrasonic energy that is transmitted into the water load, resulting in weaker signals being reflected from the bubbles. Also, the greater the reflection coefficient the greater the interference from reverberations within the non-invasive medium. It should also be noted that the transducer/non-invasive medium boundary presents an

acoustic boundary, which was not previously present in the FE models. Moreover, the transducer has been designed to operate most efficiently into Perspex.

Due to sample availability, the Perspex and crown glass samples were 10 mm thick whereas the steel sample was 5 mm thick, however, this still modelled typical vessel wall thicknesses in a process analysis environment. The non-invasive materials were all flat and were coupled to the phased array underwater to ensure no air gaps existed between the two. The speed of sound in each medium was determined using the methodology outlined in Section 3.2.4.2.

Table 7.1: *Acoustic impedance, reflection coefficient (relative to water) and acoustic velocity for each material under investigation.*

Material	**Acoustic Impedance [MRayl]**	**Reflection Coefficient [%]**	**Acoustic Velocity [ms^{-1}]**
Water	1.5	0.0	1496
Perspex	3.5	16.0	2720
Crown glass	14.5	66.0	5814
Steel	45.0	93.75	5940

7.2.2 Photographic Experimental Validation

Using the same camera and illumination conditions as described in Section 6.4, photographs of the bubble column were captured to provide an indication of the true BSD. The water tank had transparent Perspex walls, approximately 2 mm thick enabling clear visualisation of the bubble column. The illumination source was positioned outside the tank, directing the light beam through the bubble column towards the camera lens.

The pixel dimension was determined using a laminated sheet of grid paper

with a 4 mm^2 grid dimension positioned flat against the inside wall of the tank. A single image of the grid paper was captured without the bubble column present where the illumination source was able to penetrate through the paper. From this image, the pixel dimension was determined to be approximately 66.67 μm per pixel. The pixel size in the x-dimension was within $\pm$ 11 μm of the y-dimension so this difference was considered negligible on the scale of the bubble diameters to be estimated.

A greyscale image showing the bubble column is shown in Figure 7.2. The bubble column exhibited a higher bubble density close to the bubble diffuser, reducing the ability to distinguish between individual bubble objects in the image. Also, at the top of the image there is a large group of bubbles corresponding to the surface of the water. To prevent bias towards larger objects in the BSD estimation, the photos were cropped to the region shown in red.

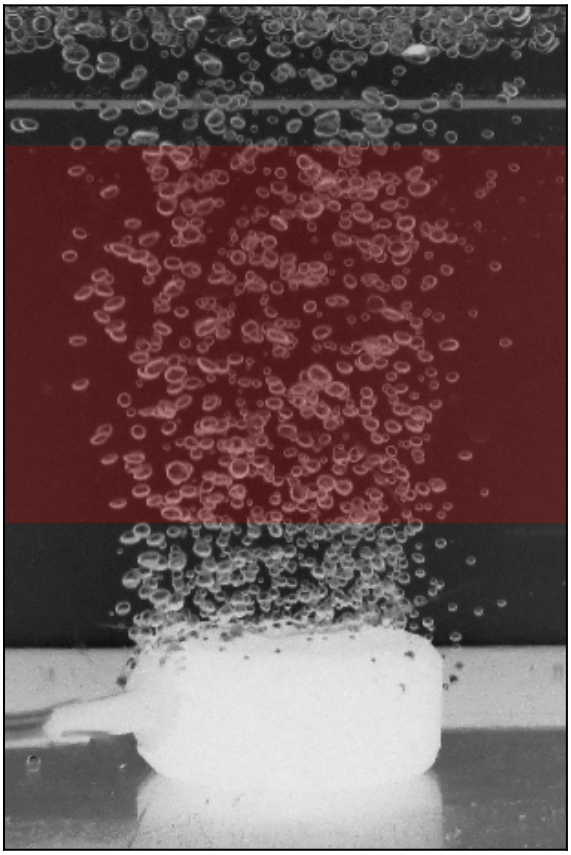

Figure 7.2: *Greyscale photograph of bubble column with region of interest highlighted in red.*

7.2.3 Data Acquisition and Imaging

The aperture was set to 32 elements, namely elements 65 to 96 in order to capture information relating to the red region in Figure 7.2. This ensured the bubbles were more spread out when passing through the image scene, reducing interference

from neighbouring bubbles in the ultrasonic images. The number of FMC data sets consisting of a single experimental acquisition was set to one hundred in order to reduce the size of the data sets while still capturing enough frames to track the bubbles and variation between image frames. The data acquisition rate was approximately 145 Hz, corresponding to a total acquisition time of approximately 0.7 s.

The extent of the z-axis was set to begin at 5 mm from the front face of the phased array when performed intrusively in the water load or at the interface between the non-invasive layer and the water load. For the non-invasive image investigation, subspace analysis was applied to all FMC data sets prior to image construction, as outlined in Section 4.2.3.

When tracking the bubble objects, the maximum distance between objects in consecutive frames was set to 10 mm as this represented just under half the axial dimension of the image scene. When the tracked objects were collated, only those that appeared in at least two image frames were considered. This had the impact of reducing uncertainty from spurious reflectors or noise contained within the images. This is in agreement with Section 6.2.3, where it was discussed that at 500 mms^{-1} the bubble would move approximately 3.4 mm between image frames. Therefore, if the image width is 10 mm, the maximum number of consecutive image frames that bubbles could appear in is three.

7.3 Results and Discussion

7.3.1 Optimisation of Air Flow Rate

The impact of the air flow rate was investigated by acquiring images at a range of different flow rates. The array was intrusively positioned in the water with the front face positioned within 10 mm from the centre of the bubble column. The air flow rate was set to values between 0.1 to 0.8 dm^3min^{-1}, with increasing steps of 0.1 dm^3min^{-1}. Twenty images were generated at each flow rate and these were passed to the bubble sizing and tracking algorithms to extract the bubble velocity corresponding to each flow rate.

There was no trend observed between the flow rate set on the flow meter and the estimated bubble velocities. The mean and spread bubble velocity across all the air flow rates was 189 $\pm$ 97 mms^{-1}. This suggested that the flow rates were just within the limit outlined in Section 6.2.3, however, some objects would appear above the speed limit and introduce inaccuracies in the measurement of faster objects. Since these estimated bubble velocities were not far above the speed limit, no further treatment of the liquid fluid was performed to increase its viscosity to slow the bubbles down.

It was observed that the number of tracked bubble objects increased as the flow rate increased which means the higher flow rates led to more objects being captured in the images. This increased the validity of the results corresponding to images acquired at higher air flow rates. Therefore the flow rate was set to 0.8 dm^3min^{-1} throughout the remainder of this investigation.

7.3.2 Estimation of BSD from Photographs

Five photographs were captured of the bubble column with the camera held in the same position as when the photo of the grid paper was taken. For these images, the grid paper was removed enabling more light to pass through the bubbles. The image processing algorithm, presented in Chapter 6, was deployed to extract the BSD from all five image frames. The diameter thresholds were set between 1 and 5 mm to capture the size range that the ultrasonic image processing algorithm was calibrated to in Section 5.3.1. The resulting histogram was recorded in Figure 7.3 where a Normal distribution has been fitted to the recorded data and its PDF has been superimposed onto the histogram. The mean and spread of the BSD were recorded as 2.6 ± 0.8 mm respectively, which was within the range that the ultrasonic image processing algorithm could be accurately deployed.

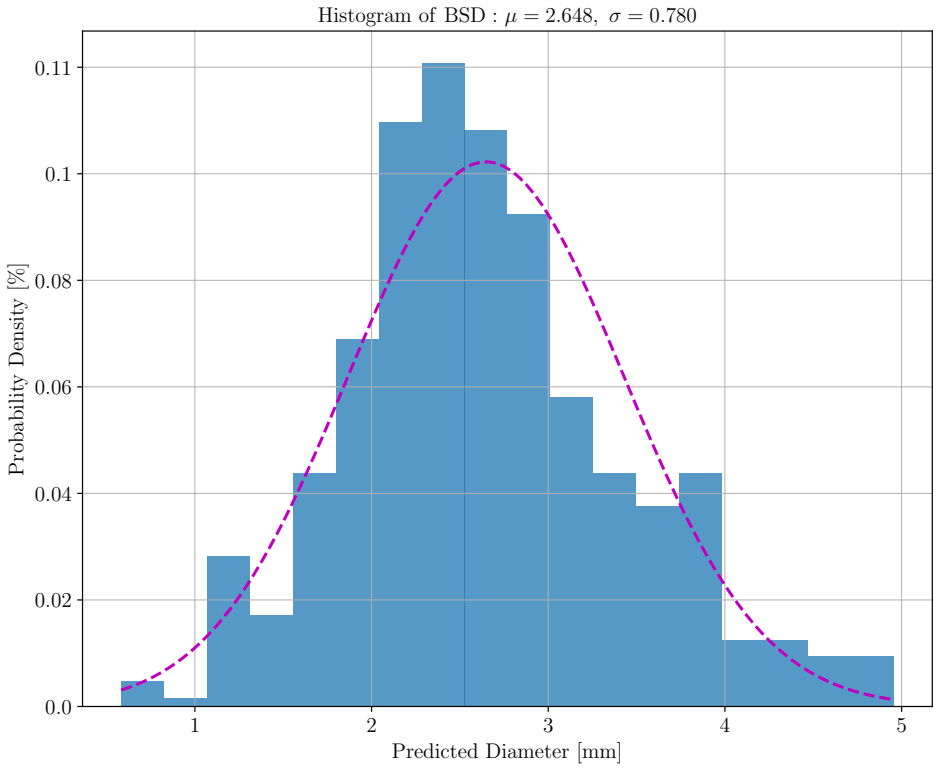

Figure 7.3: *BSD of bubble column estimated using image processing of photographs.*

7.3.3 Intrusive Data Acquisition

The phased array was immersed in the water and positioned within 10 mm from the centre of the bubble column without any material between the array and the bubble column. The one hundred TFM images were passed to the bubble sizing algorithm both with and without the SCF being applied to weight the values of the pixels in the images. In addition, the time delay errors determined in Chapter 3 were incorporated into the image construction process. The lower and upper diameter thresholds applied to the sizing algorithm were 1 and 5 mm

respectively. These values were selected to constrain the algorithm within the size limits of the SDH diameters investigated in Chapter 5. An example of the typical output from the intrusive imaging system without application of the SCF and after sizing of bubble objects has been recorded in Figure 7.4.

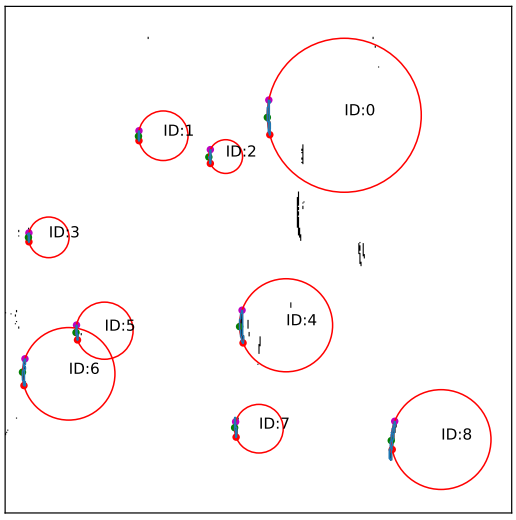

Figure 7.4: *Example of processed TFM image acquired under intrusive acquisition conditions.*

The resulting BSDs were recorded in Figure 7.5 where the PDF recorded from the photographic image processing has been superimposed onto both histograms. The mean and spread of the BSD when the SCF was not applied to the TFM images were 2.66 ± 0.98 mm respectively. Whereas, when the SCF was used to weight the pixel values in the TFM images the mean and spread were 1.97 ± 0.95 mm respectively. From these results it was observed that not using the SCF led to an estimated BSD within 0.5% to that recorded using the photographic methodology, whereas this error increased to 25.0% when using the SCF.

Given that application of the SCF had the impact of reducing pixel amplitudes, this has led to fewer individual objects being contained within the images. Indeed, there were 123 tracked objects without application of the SCF compared to 61 when it was applied. This means application of the SCF reduced the representativeness of the overall BSD. In addition, as a result of application of the SCF, there was a bias towards smaller objects because it had the impact of reducing the number of pixels in the individual objects in the input image. This is in agreement with the results presented in Chapter 5, where application of the SCF reduced the size of individual objects in the TFM images resulting in a more accurate measurement of the true reflector size.

When the tracked objects were used to extract the bubble velocity, the mean values were 115 $\pm$ 87 and 118 $\pm$ 74 mms^{-1}, with and without application of the SCF respectively. However, the large spread in values was set by a small number of outliers that had velocities greater than 350 mms^{-1}, in practice limits could be set on the velocity estimation within known constraints of the industrial process. However, given that the mean velocity value determined under both conditions were very close, it was concluded that the application of the SCF did not have a significant impact on the velocity estimation. Therefore, this imaging technique could still be deployed towards velocimetry of an industrial process.

It was observed when the phased array was positioned intrusively that application of the SCF created a strong bias for bubbles less than 2 mm in diameter. It was also observed in Figure 5.23 that the bubble sizing algorithm had a reduced degree of sensitivity for diameters between 1 and 1.5 mm when the SCF was applied. Therefore, it was recommended to restrict the size distribution between 1.5

to 5 mm diameter bubbles only when performing non-invasive analysis because the SCF was required under these conditions.

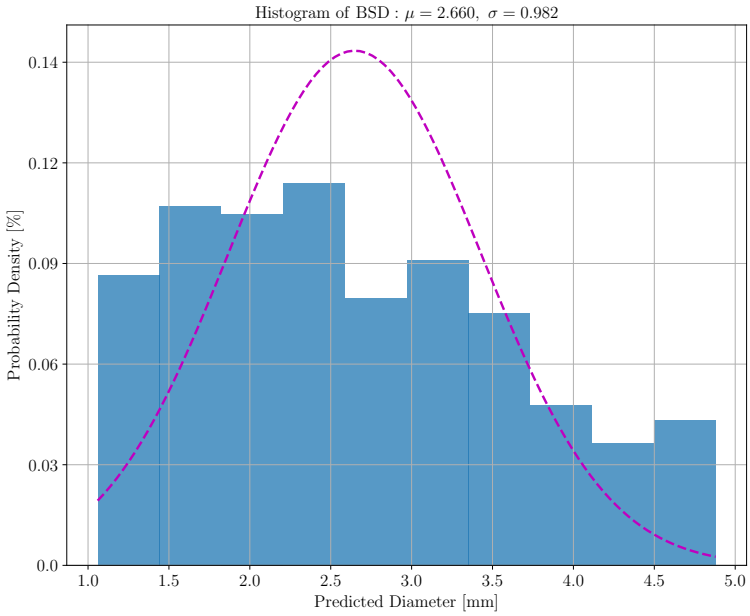

(a) *BSD of tracked bubble objects without application of the SCF. Normal distribution corresponding to BSD estimated from photographic investigation represented by purple dashed line.*

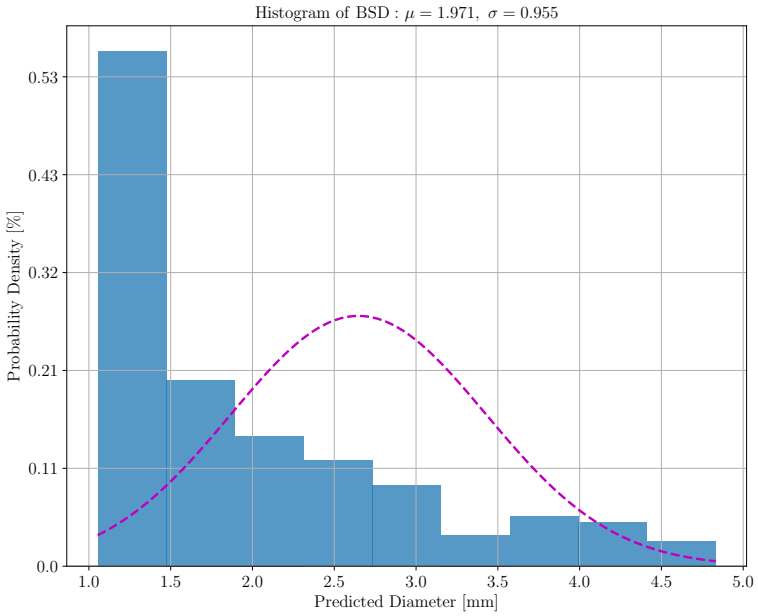

(b) *BSD of tracked bubble objects with application of the SCF. Normal distribution corresponding to BSD estimated from photographic investigation represented by purple dashed line.*

Figure 7.5: *BSD recorded when phased array was immersed in the water load without a non-invasive material present.*

7.3.4 Non-Invasive Imaging

One hundred FMC data sets were acquired of the bubble column under the same conditions as before except with each of the non-invasive materials coupled to the front face of the transducer. The bubble diffuser was positioned as close as possible to the non-invasive materials to ensure the bubble reflectors could be exposed to the highest ultrasonic energy level possible. Subspace analysis was performed on the FMC data prior to TFM image construction. Images were generated both with and without the SCF being applied to weight the values of the pixels in the images. In addition, the time delay errors determined in Chapter 3 were incorporated into the image construction process.

7.3.4.1 Through Perspex

An example of the typical output from the non-invasive through-Perspex imaging system after sizing of bubble objects has been recorded in Figure 7.6. The BSD observed when Perspex was used as the non-invasive layer was recorded in Figure 7.7, where the PDF recorded from the photographic image processing has been superimposed onto the histogram. The histogram in Figure 7.7 only represents 14 tracked objects, where the criterion was for an object to appear in at least two image frames. Given that there were 100 image frames generated from this overall experiment, this suggests the true distribution has been under-represented.

Depending on the overall dynamics of the process stream under observation, it may be necessary to acquire a much larger sample size to capture the variations

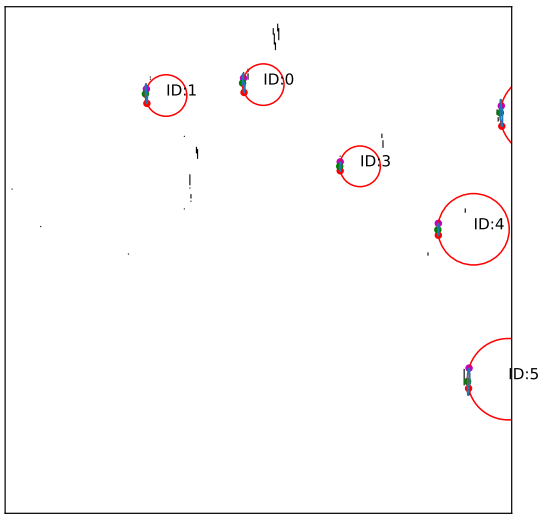

Figure 7.6: *Example of processed TFM image acquired non-invasively through Perspex after application of subspace analysis and the SCF.*

and distribution within the process. However, for these tracked objects available here the mean and spread values were 2.81 ± 0.83 mm respectively which is within 6.1% error relative to the photographic investigation.

When the tracked objects were used to extract the bubble velocity, the mean and spread values were 115.68 ± 51.70 mms^{-1} respectively. This was consistent with the results observed when the array was deployed intrusively within the water. Although, given that this value corresponds to only 14 tracked bubbles it is less representative than the result recorded from intrusive measurement.

Overall, this successfully demonstrates the applicability of ultrasonic phased arrays for non-invasive process analysis on an experimental level. The results were in close agreement with those acquired using a photographic measurement

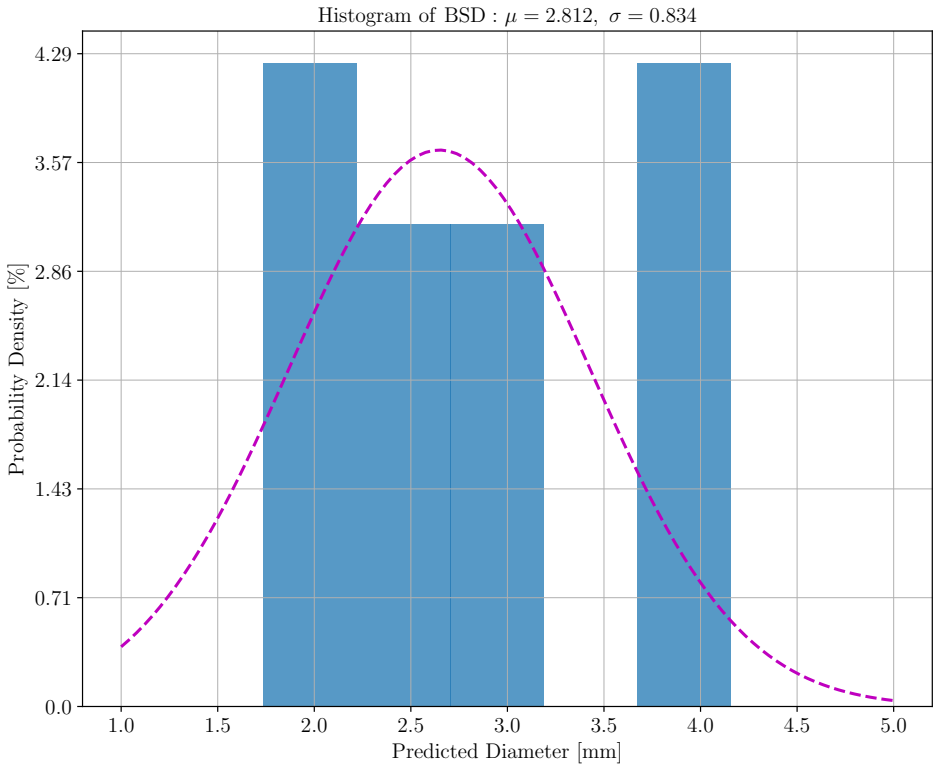

Figure 7.7: *Non-invasive through-Perspex BSD of bubble column estimated and PDF from photographic image processing after application of subspace analysis and the SCF.*

technique and when the phased array was positioned intrusively within the process. However, to increase the representativeness of the non-invasive result would require a larger sample size in terms of the number of image frames acquired and processed. To achieve this would require a greater computational capacity to process the increased quantity of data. This was not performed in this Thesis due to time constraints at the time the work was carried out.

7.3.4.2 Through Glass and Steel

An identical experimental set-up and data processing procedure was performed using crown glass and steel as the non-invasive material. Unfortunately, it was not possible to track any objects in the images generated under these conditions. Upon inspection of the input images, where examples have been shown in Figure 7.8, it was observed that they did not contain any coherent reflections from the bubble column.

In Figure 7.8(a), which corresponds to an image of the bubble column through glass, there was a region in the lower left hand side in the image that contained a consistent level of noise throughout all the images available. This has been shown here to illustrate the how the bubble sizing algorithm can detect noise as a coherent signal, generating spurious results. In Figure 7.8(b), which corresponds to an image of the bubble column through steel, there were no coherent signals in the image at all.

The transducer used in this investigation was designed to be acoustically matched to Perspex. Therefore when coupled to Perspex as the non-invasive material or directly in water, the acoustic path between the transducer and the load facilitated an efficient transmission of ultrasound, as illustrated by the low reflection coefficients in Table 7.1. However, if crown glass or steel are coupled to the phased array, this generates a large acoustic impedance mismatch between the front face of the transducer and the non-invasive material. Therefore, only a small fraction of ultrasonic energy is transmitted from the transducer into the non-invasive material. Under these conditions, most of the ultrasonic energy is

trapped within the transducer. This means the fraction of energy that is theoretically transmitted into the water load via the transducer-steel and steel-water interfaces is only 3.12% of the incident energy. This energy is then scattered within the load medium prior to returning to the transducer via these same acoustic boundaries, resulting in approximately 0.10% of the incident energy returning to be detected. This explains why this experimental apparatus has not been successful.

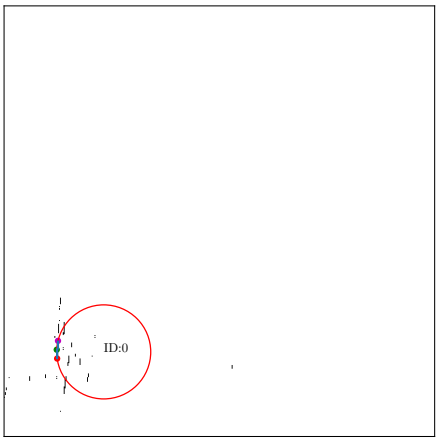

(a) *Through-glass input image example.*

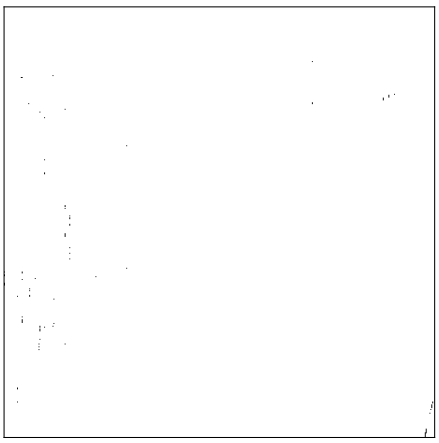

(b) *Through-steel input image example.*

Figure 7.8: *Example input images for bubble sizing algorithm from non-invasive data sets.*

7.3.5 Optimisation of Data Throughput

This Section discusses a key aspect of the practical deployment of this process analysis tool; the ability to deliver real-time information to the end-user. During the coal liquefaction process the throughput of coal can exceed 150 ton day^{-1} [16] and the production capacity for the Fischer-Tropsch process can be thousands of cubic metres per day [15]. Therefore, feedback to the analyst should be on a time scale of minutes or seconds to retain its validity with respect to the variability of the process. However, fermentation processes can last for several days [12], so a time delay of several minutes will be less detrimental to the process control.

In Chapter 5 the data acquisition rate was maximised by setting the size of the aperture to a value less than or equal to the number of channels available on the PAC. In order to maximise the quantity of information contained within each image under these conditions, the aperture was set to 32 elements. When acquiring a data stream corresponding to a depth of 20 mm in water under these conditions, the throughput was approximately 145 FMC data sets per second.

For non-invasive imaging the proposed approach was to use subspace analysis on the FMC data prior to passing the modified FMC data to the TFM imaging algorithm. The key computational processes involved are two transpose operations, three inner matrix products and Eigen decomposition. The overall subspace analysis, including projection onto the original FMC data set, when performed using a quad core CPU took approximately 2.42 s, corresponding to a rate of 0.41 Hz. This is much slower than the data acquisition rate, creating a back-log of data to process even before the images had been constructed. Therefore, the subspace

analysis was implemented on a GPU (GeForce GTX 750 Ti, NVIDIA, USA) enabling faster processing. This resulted in the processing time being reduced by 58% to 1.00 s, corresponding to a throughput of 1 Hz. However, relative to the acquisition rate of 145 Hz, this was still too slow to deliver instant feedback. Note, subspace analysis was only used for non-invasive imaging so this would not contribute to the overall processing time if the measurement was performed intrusively within the process stream. Also, the processing time for subspace analysis was dependent on the size of the input FMC matrix. If the aperture is increased beyond 32 elements, the data throughput is further compromised.

The image construction process was also performed using the same GPU for enhanced processing rates. The TFM image construction rate was dependent on the number of computations required to construct the overall image scene. For a given pixel in the image the number of computations required was equal to the number of transmit-receive combinations. This is only performed once by generating a time map as a LUT. Therefore, reducing the number of elements in the aperture reduced the total image construction time. For a given aperture the computation time then becomes a function of only the number of pixels in the image scene. Using FMC data corresponding to a 32 element aperture, the computation times to construct the TFM image matrix and both the TFM and SCF image matrices have been recorded in Table 7.2. Note, these computation rates only pertain to the image construction process and do not include any preprocessing steps.

It was found that construction of the SCF matrix had a negligible impact on the overall image construction time. This was because the computationally

Table 7.2: *Total Focusing Method image construction rates.*

Number of Pixels	Computation Rate [Hz]	
	With SCF calculation	Without SCF calculation
256^2	12.82	13.33
512^2	4.35	4.42
1024^2	1.21	1.22

intensive process was the extraction of the correct sample in the FMC data to add to the pixel of interest, rather than the accumulation of the time samples or sign bit values.

As expected, as the number of pixels in the image scene increased, the computation time increased. In this Thesis, images have been constructed using 1024 pixels in each dimension that is the maximum number that could be processed by the GPU. For the image dimensions used here, this corresponded to square pixels with an axial length of 0.28 λ or 14 pixels per λ in water. This is much more than the 6 pixels per λ recommended within the NDE community [156]. Using 512 pixels in each dimension corresponds to 7 pixels per wavelength in water and increases the image construction rate by a factor of 3.6 relative to using 1024 pixels in each dimension. Therefore, this can be used to increase the data throughput without compromising the integrity of the image. However, as computer processing power increases over time, this will become less of a hindrance to data throughput.

Following image construction the bubble sizing and bubble tracking algorithms were tested for their throughput. This was performed using the data corresponding to intrusive data acquisition of the bubble column in Section 7.3.3. For

the purpose of this investigation, the SCF was not applied to the image in order to increase the number of tracked objects under investigation. The results corresponding to the bubble sizing algorithm were recorded in Table 7.3. This demonstrates that the data throughput of the bubble sizing algorithm was also dependent on the number of pixels in the image. When these processed images were passed to the bubble tracking algorithm, the processing time was less than 0.2 μs per frame. This means the bubble tracking algorithm was the fastest step in the full ultrasonic image processing system.

Table 7.3: *Bubble sizing algorithm processing computation rates.*

Number of Pixels	Computation Rate [Hz]
256^2	29.4
512^2	20.4
1024^2	6.8

Overall, the rate determining step in the ultrasonic image processing system was the image construction, even with the application of a GPU for this step. Therefore, it has been recommended that to deploy ultrasonic phased array imaging on site, data acquisition should be completed prior to image construction and processing that can be performed off-line. If the array is deployed non-invasively, using a 32 element aperture, with 512 pixels in each image dimension and including application of the SCF, the throughput is approximately 0.78 Hz or 1.28 seconds per image. Under these ideal conditions, if the end-user were to acquire 500 consecutive image frames to generate a representative data set of the process stream, they could expect a time delay of approximately 10 minutes between data acquisition and result output. This is on the same time scale as GC measurement [25], so is a good starting point for its introduction into the field of

industrial process analysis. However, as GPU technology advances, the overall ultrasonic image processing system will approach a throughput closer to instant feedback. In terms of the petrochemical processes identified above, this current technology would be able to provide real-time feedback for fermentation, however, its application may be limited towards coal liquefaction or the Fischer-Tropsch processes.

7.4 Summary

The results presented in this Chapter have demonstrated the successful application of ultrasonic phased arrays to generate images of a dynamic process stream through Perspex. In particular, non-invasive through-Perspex imaging was achieved where the BSD output from these images was in good agreement with the result obtained from intrusive measurement and from photographic analysis of the process stream. This means the BSD could be determined non-invasively for processes such as coal liquefaction, Fischer-Tropsch synthesis or fermentation, where the process medium contains slurries that are not optically transparent.

When the non-invasive imaging approach was extended to crown glass and steel, representing the same acoustic properties of typical vessel wall materials in industrial process environments, the imaging technique was not successful. This was due to the acoustic impedance mismatch between the transducer and the non-invasive material in addition to that between the non-invasive material and the water load. This reduced the total energy that was transmitted from the transducer to the process stream, such that only approximately 0.10% of the

incident energy returns to the transducer. This means received signals were too weak to generate coherent images.

Using GPU technology the throughput of the data preprocessing and image construction was maximised, however, relative to the data acquisition rate available, real-time analysis could not be performed. The work presented here provides ground truth in the feasibility of the technology to perform quantitative non-invasive process imaging, but a key goal of its future development should be to deploy GPUs with a greater processing power and to develop phased array transducers with a greater transduction efficiency into steel.

Chapter 8

Conclusions

8.1 Overview of the Thesis

This Thesis aims to explore the application of ultrasonic phased arrays for industrial process analysis. In doing so, several research questions were proposed at the outset of this Thesis:

i. Can ultrasonic phased arrays be deployed to image dynamic processes?

ii. If so, how can these images provide novel information about the process?

iii. Which data acquisition methodologies and image construction algorithms should be deployed?

iv. How can acoustic imaging overcome challenges in process analysis specifically associated with optical imaging techniques?

v. What challenges exist to deploy this technology towards real-time process

analysis and how can these be overcome?

In particular, the aims of this research were to deploy phased arrays for imaging of a dynamic process and to determine quantitative information about such a process from these ultrasonic images. From the outset, it was the aim to investigate ultrasonic imaging whereby the phased array is positioned both intrusively and non-invasively to the process. The determination of BSD and bubble velocity from TFM images of bubbles rising to the surface of a fluid was identified as the specific target process.

Following this investigation, it can be concluded that ultrasonic phased arrays can be deployed to image dynamic processes containing bubbles, although there were several practical limitations associated with their deployment. The novel information that could be determined from these images is the BSD within opaque processes. This cannot be determined using optical imaging techniques nor pressure gauge measurements without perturbing the flow. Recent technological advances in ultrasound phased array instrumentation and GPU technology has enabled highly focussed images to be generated, which could not previously be created. This has led to the generation of ultrasonic images containing more information about the process and with a higher spatial and temporal resolution. It has been shown that ultrasonic imaging can be deployed to image through optically opaque non-invasive materials, which is not possible using digital image capture. Also, this was only demonstrated theoretically using a data set simulated using FE analysis and was not successful on an experimental level. It was reasoned that this was due to insufficient transmission of ultrasound from the phased array to the process via the steel material. Two key limiting factors have

been identified in terms of the overall ultrasonic phased array imaging system; the transduction efficiency into steel is too low with the current phased array transducers available and greater data throughput is required to provide faster feedback.

It is the aim of this Chapter to consider each of these aims within the context of the practical limitations of the ultrasonic phased array hardware and the implications of these findings on current practice of industrial process analysis are presented. Limitations to the research have led to the identification of further questions to be considered by future investigative research and these are also presented here.

8.2 Summary of Findings

The characterisation and calibration of ultrasonic hardware presented in Chapter 3 provided a novel methodology to understand the typical experimental variation encountered between individual ultrasonic data sets. This was relevant when acquiring sequences of image frames for tracking of bubbles objects, presented in Chapter 6. It was found that there was good consistency between ultrasonic data sets. The maximum variation across array element indices was 35% when using either of the FIToolbox PACs, however, there was a significant difference between results generated from the FIToolbox and the Dynaray PACs, shown in Figures 3.11 and 3.12 in the frequency and time domains respectively. The methodology also detected individual channel and/or element irregularities and was designed to be quick and robust to use via a user-friendly GUI. This is

the first example of ultrasonic hardware calibration being applied specifically for FMC data sets, where previous attempts have focused on beam integrity rather than probe integrity.

A key output of this work was demonstrating that the A-Scan response observed at a given element location is highly dependent on the PAC used, as shown in Figure 3.12. Therefore, it is vital that calibration procedures pertain to the coupled array-PAC system rather than a single component of the ultrasonic hardware system. The calibration process led to the development of a peak time correction method that could be incorporated directly into the TFM imaging algorithm. The main assumptions of this methodology are that the measured speed of sound in the calibration sample is accurate and that the path length from the array front face to the back wall of the calibration sample is well-defined. In addition, it was required that the total time delay only derive from inconsistencies on the ultrasonic hardware and are independent of heterogeneity within the calibration sample. This enhanced the spatial accuracy of TFM images by offsetting time delays deriving from inconsistencies within the ultrasonic hardware. This is demonstrated in Figure 3.17 for a 3 mm diameter SDH in Perspex where the position of the SDH surface has been realigned with its true shape, marked by the black circle.

A significant advantage of acoustic imaging over optical-based imaging techniques is the ability to transmit information across an optically opaque interface. This was investigated through steel in Chapter 4 using a simulated phased array FE model representing a typical industrial process. The challenge, to create coherent images through such an interface, is the ability to suppress interference

from reverberation echoes within the steel interface. Several methodologies were investigated to overcome this reverberation interference, where the most effective was subspace analysis [140].

Using Eigen decomposition, the signals corresponding to the reverberation from the main beam could be explicitly identified and removed from the acquired data prior to image construction. When this was coupled with sign coherence factor imaging, spurious artefacts deriving from the reflectors of interest were also successfully suppressed, however, at the cost of reduced sensitivity for pixels relating to the reflectors of interest. A specific advantage of this coupled approach is that it does not require any *a priori* knowledge of the target image scene to be implemented. Therefore, it enables the end-user to develop a *clamp-on* style product for non-invasive imaging. This is highly advantageous in a process analysis environment as it provides access to valuable quantitative information about the process without the need to modify the process vessel.

When this non-invasive imaging methodology was extended to an experimental apparatus, using a 32 element aperture, it was found to be ineffective at imaging bubble reflectors through glass or steel. This was believed to be due to the acoustic impedance mismatch between the transducer and the non-invasive material in addition to that between the non-invasive material and the water load. This reduced the total energy that was transmitted from the transducer to the process stream, meaning received signals were too weak to generate coherent images. However, non-invasive imaging was successfully demonstrated using a Perspex vessel wall material. This was closely matched to the acoustic impedance of the transducer resulting in a high degree of acoustic transmission from the transducer

to the process stream.

To extract quantitative information from the ultrasonic images an image processing algorithm was developed. This was evaluated under stationary conditions in Chapter 5 and under dynamic conditions in Chapter 6. Using simulated data sets it was found that for reflector diameters ranging between 3.6 and 17.2 λ the algorithm could extract the diameter within 40% for apertures greater than or equal to 32 elements, shown in Figure 5.15. However, when the algorithm was tested under experimental conditions, it was found that the accuracy of prediction decreased below 100% error for the smallest diameter reflectors, shown in Figure 5.16. From visual inspection of the experimentally generated images, spatial side lobes impacted on the shape of the reflectors leading to the algorithm to overestimate the true reflector diameters.

Given that there were 32 channels available on the PAC, using a 32 element aperture resulted in the best value for accuracy relative to the data acquisition rate. Using a 32 element aperture also resulted in the most accurate sizing predictions when performed on experimental data. This was due to the enhanced SNR resulting from the increased likelihood of a reflector being in the aperture region for a given transmitting element. However, a limitation of using a 32 element aperture, over larger apertures, is the reduced image width available meaning fewer reflectors are contained within a single image.

To model the dynamic nature of the target industrial process, the phased array was coupled with a six-axis robotic arm to scan Perspex samples containing stationary reflectors. When the Perspex sample was scanned at speeds up to 100 mms^{-1} it was found that the image processing algorithm could extract the di-

ameter of circular reflectors within 50% when applied to the Perspex Calibration Sample in Figure 6.10. However, for speeds greater than or equal to 200 mms^{-1}, the sizing algorithm began to break down. This was partly attributed to the design of the image construction algorithm that failed to represent the true nature of the image scene rather than directly resulting from the image processing algorithm. In addition, a drawback to using the programmable robotic arm was that it exhibited an acceleration and deceleration curve while scanning the samples. This means the actual robotic arm speed was less accurate at the extremities of the samples.

The impact of bubble velocity on TFM image quality was investigated by generating TFM images with the pixel positions shifted prior to image compounding by a value corresponding to the velocities investigated. The result of this was to elongate the shape of the objects, for example in Figure 6.4. This demonstrated that speeds greater than 200 mms^{-1} resulted in images that were compromised such that they no longer represented the equivalent stationary reflector. This indicates a significant limitation to the application of FMC for ultrasonic imaging of dynamic processes moving faster than 200 mms^{-1}.

Following this, an object tracking algorithm was presented in Chapter 6 to extract the bubble velocity and BSD of tracked objects. This reduced the bias in the BSD towards smaller bubbles by ensuring each tracked object only contributed to one value in the overall BSD. When tested to extract the object velocity there was a strong correlation between the predicted bubble velocity and the velocity of the robotic arm movement under these conditions, where the error of prediction was within 30% $\pm$ 25% at 100 mms^{-1}.

CHAPTER 8: CONCLUSIONS

The ultrasonic imaging and image processing system was tested under experimental conditions in Chapter 7. Using a bubble diffuser with a controlled air flow rate, the BSD and bubble velocity were extracted from 100 image frames acquired in quick succession. The estimated mean bubble diameter was within 0.5% of that extracted from image processing of high resolution photographs of the bubble column generated under identical experimental conditions. However, this algorithm erroneously omitted binary erosion as a final step resulting in overestimation of the BSD using this methodology.

The image processing algorithm was deployed on an experimental system containing bubbles rising to the surface of a water tank. Although this was successfully able to generate TFM images representing the bubbles and the BSD could be extracted from these images, there were not enough tracked objects available to provide a confident measure of the size distribution. Due to the small image width and short acquisition time, approximately 0.7 s, 100 image frames only included 123 individual tracked objects when the SCF was not applied. This was not enough tracked objects to observe a representative distribution of the bubble size. Unfortunately to acquire more images would require much more computer processing power, so this highlights another limitation of the work for deployment towards dynamic industrial processes. However, to maximise the data throughput for this ultrasonic imaging system, GPU technology has been employed wherever possible. Real-time processing was not possible, where the image construction process was the rate determining step. However, the work presented in this Thesis provides ground truth for ultrasonic phased array imaging to perform quantitative non-invasive process analysis.

8.3 Implication of the Research

These findings have significant implications for the advancement of industrial process analysis, particularly within the chemical processing industry. There are several challenges associated with process measurement technologies currently used in industry, for example, process interference, bulk representativeness and the cost of measurement. The potential for ultrasonic phased array imaging to overcome these challenges is discussed here in the context of current industry practice.

Imaging of industrial processes has been typically performed using digital cameras to capture optical images of process streams [7, 19]. Although these images provide high resolution images with high pixel densities, the pixel dimension must be determined using experimental calibration [99]. On the other hand, with ultrasound imaging, the image construction process is user-defined meaning this uncertainty is removed from ultrasound images [8]. The implication of using ultrasound imaging over optical imaging for the process analyst is greater flexibility in the measurement process and increased measurement certainty. Indeed, using the TFM imaging algorithm generates images that are focused at every pixel in the image, therefore removing uncertainty due to out-of-focus objects typically encountered using optical imaging techniques [10]. This will ultimately lead to greater confidence in decision-making about the process as there is a greater degree of control over the spatial resolution of the images.

The benefits of this new non-invasive measurement technique have several novel implications toward industrial process analysis itself. In addition to provid-

ing an in-situ measurement tool, without extractive sampling or interference of the process, this technique is not dependent on having an optical path between the sensor and the process. This means spatial quantitative information about a process can be extracted from optically opaque processes [157]. For example, the coal liquefaction, Fischer-Tropsch and fermentation processes involve the movement of bubbles with similar size distributions and velocities to those investigated here.

Ultrasonic tomography is currently the only established ultrasonic imaging methodology for industrial process analysis [126]. The development of ultrasonic phased array imaging will have wider implications for extending this field of research. The benefits of ultrasonic tomography, including non-invasive imaging, are limited due to the path length the ultrasound must traverse to reach each of the receiving transducers. Due to this increased path length, low frequency signals are used because they are less attenuated than higher frequency signals. However, using lower frequencies results in images with poorer spatial resolution. A significant implication of using phased array imaging is that much higher frequency input signals can be easily deployed [8]. This means the ultrasonic signal can interact with smaller reflectors more effectively and so images contain more detail about the process [130]. In addition, using multiple-channel PACs enables faster data acquisition rates to be achieved, increasing the temporal resolution of phased array images and pushing the measurement system much closer to real-time measurement. However, the ultrasonic path length still ultimately determines the data acquisition rate, such that if the array is positioned far from the image target, the benefit of higher frequency ultrasound would be compromised

as the signals would be more attenuated relative to a lower frequency signal.

Finally, the most significant implication of this research towards industrial process analysis is the development of an algorithm for through-steel imaging. Although this could not be successfully deployed experimentally, it was theoretically shown using a simulated data set generated using FE analysis. Current optical imaging techniques rely on an optical path between the camera and the process. Installation of a sampling window requires modification of the process vessel material, increasing the overall measurement cost [5]. For acoustic measurements, the vessel material is typically modified to promote the transmission of ultrasound across the vessel wall [119]. This can be achieved by installing an acoustic waveguide, essentially making the measurement in-line to the process, or using Perspex [119]. The implication of being able to imaging directly through steel is increased measurement flexibility as the phased array can be directly coupled to the bulk process stream as a *clamp-on* device. In addition, since modification of the process vessel is not required this technology will provide a more cost-effective measurement tool. However, although the algorithms for this are ready, the transduction efficiency into steel remains a challenge to be overcome. Given the fundamental laws of physics associated with this challenge, the solution will require a degree of technological innovation to be achieved.

8.4 Recommendations for Future Research

Throughout this Thesis, a number of practical or theoretical limitations to the research were encountered. These are discussed here in order to provide insight

into how these limitations could be overcome. In doing so, the potential for future research is elucidated.

One of the key limitations of the imaging system was the total area that could be imaged. The image dimension in the y-dimension was determined by the number of elements in the aperture. Therefore, if the size of aperture was increased the area of the image could be increased. However, as was discussed in Chapter 5, the number of channels available on the PAC limited the data acquisition rate. It has been recommended that future work should investigate the application of a PAC with more than 32 channels. This would lead to an increase in the quantity of information captured within the images and therefore the overall TFM imaging accuracy along with the area that can be imaged.

One drawback of using FMC as the data acquisition process was that the total energy input into the system was reduced relative to multi-element B-Scan apertures. This presents a problem when performing through-steel imaging because the total energy that is transmitted across the steel-fluid interface is already low. Therefore, it was proposed that alternative data acquisition modes should be investigated to increase the ultrasonic energy input into the system. For example, a plane wave could be generated by transmitting on all available elements in the aperture at the same time and receiving on all elements. However, in order to perform this non-invasively through a refracting interface would require the GPU TFM imaging code to be modified. This could be achieved by setting the outbound wave path to be identical for a given image depth and setting the TOF calculation to search for just the in-bound TOF. Given that only one transmit event takes place and only the in-bound TOF would need to be determined for

each pixel, this would greatly reduce the computation time required to generate each image frame. Alternatively, FMC could be performed using pairs of adjacent elements instead of individual elements to increase the ultrasonic energy. This would require redefining the element location to the centre of the two elements in the TFM imaging algorithm to generate representative images.

During conception of the calibration methodology presented in Chapter 3, a key criterion was that it needed to be quick and easy to use in order to encourage uptake by other users. This was achieved by limiting the data acquisition process to a single experimental apparatus but led to fewer data being gathered about the hardware performance. For further understanding of the individual element performance it is suggested that impedance analysis is undertaken, which will provide information about the transduction efficiency of each element. Indeed, the impedance analyser requires the array to be decoupled from the PAC so this would provide good understanding of which artefacts derive from the array rather than the PAC. This analysis could not be performed for the phased array used in Hardware System 1, in Table 3.1, because the pins on the phased array were not individually accessible.

Analysis of the literature identified a gap related to the relationship between the quality of the TFM images to variations in the received signal strength. In other words, it would be useful to have a criterion for the number of inactive elements permitted on an array before TFM image quality is compromised beyond a certain threshold. This could be achieved by simulating an FMC data set of a single point reflector and reducing the gain on specific A-Scans in the FMC data set. The array performance indicator [10] could be used to quantify the

deterioration of the TFM image until a specific threshold has been reached. Once this has been completed, the appropriate number of defective elements could then be incorporated into the calibration methodology described in Chapter 3 to determine whether a Hardware System had 'passed' or 'failed'.

In Chapter 5, ultrasonic data were simulated with bubbles immersed in water whereas experimental data were acquired of reflectors in Perspex. Although the simulated results represented the acoustic properties of the target application more closely, the difference in acoustic impedance and wavelength between the simulated and experimental results means there was uncertainty when comparing these results. Therefore, it was recommended to perform these simulations again, but with Perspex as the propagating medium to facilitate more valid comparisons between the simulated and experimental results.

The bubble sizing algorithm presented in Chapter 5 used three key points to fit a circle through each of the identified objects in the binary TFM images. This was used to fit a circle to the outside edge of the image objects, however, this was sensitive to the definition of the three key points. An alternative approach could be to skeletonise the binary input images followed by a least squares fit of a circle through this skeleton. The skeletonisation process has the impact of representing a binary object by its basic internal structure as a one-dimensional line. The coordinates of this line could then be used to fit a circle. Including a greater number of coordinates in the circle fitting process could lead to a more representative estimation of the object shape. However, it is expected that this would be at the cost of increased processing time, reducing its applicability to real-time industrial process analysis.

There was a significant hindrance in the experimental investigation using the phased array coupled to the robotic arm in Chapter 6. The misalignment between the true element spatial locations relative to the pixel locations in the image scene resulted in spurious images being generated. To correct for this misalignment it is necessary to adjust the TFM imaging algorithm, whereby the extent of the image scene is increased prior to calculation of the TOF values. In addition, an temporal offset parameter would need to be determined from a known time associated with each individual transmit event in order to account for distortion in the TOF values corresponding to each pixel. This would also need to assume that the precise time that each element transmits is known. This would be a large body of work, so was not considered here and has not been previously done within the NDE community. However, it is expected to validate the results demonstrated in Chapter 6 further and enable the imaging system to be more easily extended to robotic arm speeds greater than 200 mms^{-1}. Note, this is not required in practice when the reflector moves relative to a stationary transducer as the array element positions are fixed relative to the pixels in the image scene.

In Chapter 6 an algorithm was presented to extract the BSD from photographs. The diameter that was extracted for each region identified by the watershed algorithm corresponded to the equivalent diameter of a circle with the same area. This was contained within the *regionprops* command that also includes several other regional property functions. For example, the equivalent diameter could have been determined from the area of each region corresponding to the convex hull or bounding box area. This would have the effect of smoothing the object perimeter and increasing the total area, however, it could also lead to a more

accurate diameter if the algorithm was found to typically under size the objects from photographs. Therefore, it is recommended that future work should include an investigation into the impact of the sizing method for this algorithm. Also, any future work using this algorithm to extract BSD from photographs should be adapted to include binary erosion following binary dilation and binary hole filling. This was omitted in error here and would lead to overestimation of the object sizes.

A key challenge encountered during practical deployment of non-invasive through-steel imaging was the weak signal response from the process stream. Therefore, a bespoke transducer design should be developed to facilitate the transmission of ultrasound from the active element into steel. The acoustic impedance of PZT-5H ceramic is 34 MRayl whereas steel is 45 MRayl. Therefore a matching layer would need to be designed that increases in acoustic impedance relative to the PZT-5H ceramic. Typically, piezo-composite materials are developed to reduce element cross-talk and to reduce the acoustic impedance of the active element to match closer to water or Perspex. So, it might be appropriate not to design a composite material but an array of single crystals.

The method to quantify the degree of reverberation suppression in Chapter 4 relied on the identification of specific pixels. However, due to signal aliasing it was not possible to identify quantitatively if the value of these pixels was due to contributions from the reflectors of interest or the reverberations. An alternative approach could be to use the image normalisation and binarisation, as presented in Chapter 5. This would pool together the work presented in the remainder of the Thesis while also enabling identification of the effectiveness of the reverberation

suppression technique. It is suggested that this approach is used when writing this research into a journal paper.

In Chapter 7 the bubble flow rate was optimised to increase the representativeness of the overall experimental results. During this process it was observed that increasing the flow rate only had an impact on the number of objects detected in the image scene. Therefore it was recommended that a potential application of this imaging methodology could be to determine gas volume fraction in two-phase bubbly flows. By controlling the flow rate of air supplied to the bubble diffuser and estimating the total volume of tracked bubbles per second; the observed flow rate could be related to the actual flow rate. From this a correction factor could be established, leading to a new technique for flow rate determination. This was not performed here due to limited time available towards the end of the PhD programme.

Another potential application of this measurement technique could be a viscometer. Given that the object tracking algorithm output a size and velocity for each tracked object. The velocity distribution could be plotted against the size distribution of the tracked objects, where the correlation between these two variables could be used to infer the viscosity of the bulk medium.

Overall, ultrasonic phased arrays have demonstrated huge potential for imaging of dynamic industrial process streams. Using this technology enables the process analyst to overcome significant challenges associated with typical industrial process analysis. This technology also presents the potential to acquire spatial information about a process while reducing the cost of process measurement. There still exists a body of work to be completed before this technology

will become established in an industrial process environment. However, a suggested research path has been elucidated here after consideration of the physical and technological constraints of this research.

Bibliography

[1] UK Robotics and Autonomous Systems Network. Manufacturing Robotics: The Next Robotic Industrial Revolution (White Paper), 2016. [Online; accessed 19$^{\text{th}}$ May, 2019].

[2] House of Commons Library. Manufacturing: Statistics and Policy, 2017. [Online; accessed 19$^{\text{th}}$ May, 2019].

[3] Government Office for Science. Technology and Innovation Futures, 2017. [Online; accessed 19$^{\text{th}}$ May, 2019].

[4] F McLennan. Process analytical chemistry in perspective. In *Process Analytical Chemistry*, pages 1–13. Springer, 1995.

[5] James B Callis, Deborah L Illman, and Bruce R Kowalski. Process analytical chemistry. *Analytical Chemistry*, 59(9):624A–637A, 1987.

[6] F Alba, GM Crawley, J Fatkin, DMJ Higgs, and PG Kippax. Acoustic spectroscopy as a technique for the particle sizing of high concentration colloids, emulsions and suspensions. *Colloids and Surfaces A: Physicochemical and Engineering Aspects*, 153(1-3):495–502, 1999.

[7] RA Grau and Kari Heiskanen. Visual technique for measuring bubble size in flotation machines. *Minerals Engineering*, 15(7):507–513, 2002.

[8] B. Drinkwater and P. Wilcox. Ultrasonic arrays for non-destructive evaluation: A review. *NDT & E International*, 39(7):525 – 541, 2006.

[9] Thomas Scharrer, Michael Schrapp, Stefan J Rupitsch, Alexander Sutor, and Reinhard Lerch. Ultrasonic imaging of complex specimens by processing multiple incident angles in full-angle synthetic aperture focusing technique. *IEEE transactions on ultrasonics, ferroelectrics, and frequency control*, 61(5):830–839, 2014.

[10] C. Holmes, B. Drinkwater, and P. Wilcox. Post-processing of the full matrix of ultrasonic transmit-receive array data for non-destructive evaluation. *NDT & E International*, 38(8):701 – 711, 2005.

[11] Alison Nordon, Anthony Gachagan, and Anthony Mulholland. Development of acoustic techniques for the monitoring of petrochemical processes, 2014.

[12] Pradeep Chaminda Munasinghe and Samir Kumar Khanal. Biomass-derived syngas fermentation into biofuels: opportunities and challenges. *Bioresource technology*, 101(13):5013–5022, 2010.

[13] Malcolm JW Povey. Ultrasound particle sizing: A review. *Particuology*, 11(2):135–147, 2013.

[14] Jeffrey S Smith, Louis F Burns, Kalliat T Valsaraj, and Louis J Thibodeaux. Bubble column reactors for wastewater treatment. 2. the effect

of sparger design on sublation column hydrodynamics in the homogeneous flow regime. *Industrial & engineering chemistry research*, 35(5):1700–1710, 1996.

[15] ST Sie and R Krishna. Fundamentals and selection of advanced fischer–tropsch reactors. *Applied Catalysis A: General*, 186(1-2):55–70, 1999.

[16] H Ishibashi, M Onozaki, M Kobayashi, J-i Hayashi, H Itoh, and T Chiba. Gas holdup in slurry bubble column reactors of a 150 t/d coal liquefaction pilot plant process. *Fuel*, 80(5):655–664, 2001.

[17] N Mehrshad and M Massinaei. New image-processing algorithm for measurement of bubble size distribution from flotation froth images. *Minerals & Metallurgical Processing*, 28(3), 2011.

[18] N Sadr-Kazemi and JJ Cilliers. An image processing algorithm for measurement of flotation froth bubble size and shape distributions. *Minerals Engineering*, 10(10):1075–1083, 1997.

[19] Ashish Karn, Christopher Ellis, Roger Arndt, and Jiarong Hong. An integrative image measurement technique for dense bubbly flows with a wide size distribution. *Chemical Engineering Science*, 122:240–249, 2015.

[20] Jussi Tamminen, Esko Lahdenperä, Tuomas Koiranen, Toni Kuronen, Tuomas Eerola, Lasse Lensu, and Heikki Kälviäinen. Determination of single droplet sizes, velocities and concentrations with image analysis for reactive extraction of copper. *Chemical Engineering Science*, 167:54–65, 2017.

[21] RE Challis, MJW Povey, ML Mather, and AK Holmes. Ultrasound techniques for characterizing colloidal dispersions. *Reports on progress in physics*, 68(7):1541, 2005.

[22] MH Bharati and JF MacGregor. Multivariate image analysis for real-time process monitoring and control. *Industrial & Engineering Chemistry Research*, 37(12):4715–4724, 1998.

[23] F Lehr, M Millies, and D Mewes. Bubble size distributions and flow fields in bubble columns. *AIChE Journal*, 48(11):2426–2443, 2002.

[24] S Cochran. Piezoelectricity and basic configurations for piezoelectric ultrasonic transducers. In *Ultrasonic transducers*, pages 3–35. Elsevier, 2012.

[25] Anita Peters, Mark Klemp, Lourdes Puig, Christine Rankin, and Richard Sacks. Instrumentation and strategies for high-speed gas chromatography. *Analyst*, 116(12):1313–1320, 1991.

[26] EB Overton and KR Carney. New horizons in gas chromatography: field applications of microminiaturized gas chromatographic techniques. *TrAC Trends in Analytical Chemistry*, 1994.

[27] Mark A LaPack, James C Tou, and Christie G Enke. Membrane extraction mass spectrometry for the on-line analysis of gas and liquid process streams. *Analytical Chemistry*, 63(15):1631–1637, 1991.

[28] MA DesJardin, SJ Doherty, JR Gilbert, MA LaPack, and J Shao. Better understanding of plant and pilot plant operations using on-line mass spectrometry. *Process Control and Quality*, 6(4):219–228, 1994.

[29] KPJ Williams. Remote sampling using a fibre-optic probe in fourier transform raman spectroscopy. *Journal of Raman spectroscopy*, 21(2):147–151, 1990.

[30] Hoeil Chung. Applications of near-infrared spectroscopy in refineries and important issues to address. *Applied Spectroscopy Reviews*, 42(3):251–285, 2007.

[31] ND Lourenço, JA Lopes, CF Almeida, MC Sarraguça, and HM Pinheiro. Bioreactor monitoring with spectroscopy and chemometrics: a review. *Analytical and bioanalytical chemistry*, 404(4):1211–1237, 2012.

[32] Thomas De Beer, Anneleen Burggraeve, Margot Fonteyne, Lien Saerens, Jean Paul Remon, and Chris Vervaet. Near infrared and raman spectroscopy for the in-process monitoring of pharmaceutical production processes. *International journal of pharmaceutics*, 417(1-2):32–47, 2011.

[33] Graeme McNay, David Eustace, W Ewen Smith, Karen Faulds, and Duncan Graham. Surface-enhanced Raman scattering (SERS) and surface-enhanced resonance Raman scattering (SERRS): a review of applications. *Applied spectroscopy*, 65(8):825–837, 2011.

[34] TJ Mason, L Paniwnyk, and JP Lorimer. The uses of ultrasound in food technology. *Ultrasonics sonochemistry*, 3(3):S253–S260, 1996.

[35] R Chanamai and DJ McClements. Depletion flocculation of beverage emulsions by gum arabic and modified starch. *Journal of Food Science*, 66(3):457–463, 2001.

[36] Vijay Kumar, Michael K Taylor, Amit Mehrotra, and William C Stagner. Real-time particle size analysis using focused beam reflectance measurement as a process analytical technology tool for a continuous granulation–drying–milling process. *AAPS PharmSciTech*, 14(2):523–530, 2013.

[37] Alex R Heath, Phillip D Fawell, Parisa A Bahri, and Jean D Swift. Estimating average particle size by focused beam reflectance measurement (FBRM). *Particle & Particle Systems Characterization*, 19(2):84–95, 2002.

[38] HANS JAFFE. Piezoelectric ceramics. *Journal of the American Ceramic Society*, 41(11):494–498, 1958.

[39] Lester W Schmerr. An ultrasonic system. In *Fundamentals of Ultrasonic Nondestructive Evaluation*, pages 1–13. Springer, 2016.

[40] A. Nordon, R. Waddell, L. Bellamy, A. Gachagan, D. McNab, D. Littlejohn, and G. Hayward. Monitoring of a heterogeneous reaction by acoustic emission. *The Analyst*, 129(5):463 – 467, 2004.

[41] Mark Whitaker, Guy R Baker, Julian Westrup, Paul A Goulding, David R Rudd, Ron M Belchamber, and Michael P Collins. Application of acoustic emission to the monitoring and end point determination of a high shear granulation process. *International journal of pharmaceutics*, 205(1-2):79–91, 2000.

[42] Manuel Tramontana. *The application of passive and active acoustic techniques in process monitoring*. PhD thesis, University of Strathclyde, 2011.

[43] John William Strutt Baron Rayleigh. *The theory of sound*, volume 2. Macmillan, 1896.

[44] Paul S Epstein and Richard R Carhart. The absorption of sound in suspensions and emulsions. i. water fog in air. *The Journal of the Acoustical Society of America*, 25(3):553–565, 1953.

[45] JR Allegra and SA Hawley. Attenuation of sound in suspensions and emulsions: theory and experiments. *The Journal of the Acoustical Society of America*, 51(5B):1545–1564, 1972.

[46] Valerie J Pinfield. Acoustic scattering in dispersions: Improvements in the calculation of single particle scattering coefficients. *The Journal of the Acoustical Society of America*, 122(1):205–221, 2007.

[47] Valerie J Pinfield and Malcolm JW Povey. A perturbation approach to acoustic scattering in dispersions. *The Journal of the Acoustical Society of America*, 120(2):719–732, 2006.

[48] W. Mason. *Electromechanical transducers and wave filters*, chapter VI. Electromechanical Converting Systems, pages 187 – 193. D. Van Nostrand Co., 1948.

[49] S. Sherrit, S. Leary, B. Dolgin, and Y. Bar-Cohen. Comparison of the mason and klm equivalent circuits for piezoelectric resonators in the thickness mode. In *Proceedings of the 1999 IEEE Ultrasonics Symposium.*, volume 2, pages 921 – 926. IEEE, 1999.

[50] G. Hayward. A systems feedback representation of piezoelectric transducer operational impedance. *Ultrasonics*, 22(4):153 – 162, 1984.

[51] R. Krimholtz, D. Leedom, and G. Matthaei. New equivalent circuits for elementary piezoelectric transducers. *Electronics Letters*, 6(13):398 – 399, 1970.

[52] S. Cochran, C. Dmor, and C. Courtney. *6 - Modelling ultrasonic-transducer performance: one-dimensional models*. Woodhead Publishing Series in Electronic and Optical Materials. Woodhead Publishing, 2012.

[53] W. Smith and B. Auld. Modeling 1-3 composite piezoelectrics: thickness-mode oscillations. *IEEE Transactions on Ultrasonics, Ferroelectrics, and Frequency Control*, 38(1):40 – 47, 1991.

[54] Philip M Morse. Ku ingard, theoretical acoustics. *Princeton University Press, 949p*, 4:150, 1968.

[55] PZFlex, OnScale, USA. https://onscale.com.

[56] PZFlex, OnScale, USA. Introduction to FEA and PZFlex. Downloaded February 2016.

[57] Olympus. Introduction to Phased Array Ultrasonic Technology Applications, 2004. [Online; accessed 19$^{\text{th}}$ May, 2019].

[58] T. Szabo. *Diagnostic ultrasound imaging: Inside out*. Academic Press, 2004.

[59] Kai E Thomenius. Evolution of ultrasound beamformers. In *Ultrasonics Symposium, 1996. Proceedings., 1996 IEEE*, volume 2, pages 1615–1622. IEEE, 1996.

[60] Alan J Hunter, Bruce W Drinkwater, and Paul D Wilcox. The wavenumber algorithm for full-matrix imaging using an ultrasonic array. *IEEE transactions on ultrasonics, ferroelectrics, and frequency control*, 55(11):2450–2462, 2008.

[61] David Romero-Laorden, Javier Villazón-Terrazas, Oscar Martinez-Graullera, Alberto Ibanez, Montserrat Parrilla, and M Santos Penas. Analysis of parallel computing strategies to accelerate ultrasound imaging processes. *IEEE Transactions on Parallel and Distributed Systems*, 27(12):3429–3440, 2016.

[62] J. Dziewierz, T. Lardner, and A. Gachagan. A design methodology for 2D sparse NDE arrays using an efficient implementation of refracted-ray TFM. In *2013 IEEE International Ultrasonics Symposium (IUS)*, pages 136–138, July 2013.

[63] LA Glasgow, LE Erickson, CH Lee, and Sneha1 A Patel. Wall pressure fluctuations and bubble size distributions at several positions in an airlift fermentor. *Chemical engineering communications*, 29(1-6):311–336, 1984.

[64] DJ Lee, X Luo, and L-S Fan. Gas disengagement technique in a slurry bubble column operated in the coalesced bubble regime. *Chemical Engineering Science*, 54(13-14):2227–2236, 1999.

[65] H-M Prasser, D Scholz, and C Zippe. Bubble size measurement using wire-mesh sensors. *Flow measurement and Instrumentation*, 12(4):299–312, 2001.

[66] Casey Tompkins, Horst-Michael Prasser, and Michael Corradini. Wire-mesh sensors: A review of methods and uncertainty in multiphase flows relative to other measurement techniques. *Nuclear Engineering and Design*, 337:205–220, 2018.

[67] Manuel Banowski, Matthias Beyer, Lutz Szalinski, Dirk Lucas, and Uwe Hampel. Comparative study of ultrafast x-ray tomography and wire-mesh sensors for vertical gas–liquid pipe flows. *Flow Measurement and Instrumentation*, 53:95–106, 2017.

[68] D Ito, H-M Prasser, H Kikura, and M Aritomi. Uncertainty and intrusiveness of three-layer wire-mesh sensor. *Flow Measurement and Instrumentation*, 22(4):249–256, 2011.

[69] Giorgio Besagni, Fabio Inzoli, and Thomas Ziegenhein. Two-phase bubble columns: A comprehensive review. *ChemEngineering*, 2(2):13, 2018.

[70] Jan G Drenthen and Geeuwke de Boer. The manufacturing of ultrasonic gas flow meters. *Flow Measurement and Instrumentation*, 12(2):89–99, 2001.

[71] Yasushi Takeda. Velocity profile measurement by ultrasound doppler shift method. *International journal of heat and fluid flow*, 7(4):313–318, 1986.

[72] L. Sandrin, S. Manneville, and M. Fink. Ultrafast two-dimensional ultra-

sonic speckle velocimetry: A tool in flow imaging. *Applied Physics Letters*, 78(8):1155 – 1157, 2001.

[73] Sanehiro Wada, Hiroshige Kikura, Masanori Aritomi, Yasushi Takeda, and Michitsugu Mori. Multiline flow rate measurement using ultrasonic doppler method. In *Papers of the Third International Symposium on Ultrasonic Doppler Methods for Fluid Mechanics and Fluid Engineering Co-organized by EPFL and PSI*, 2002.

[74] Feng Dong, Huan Gao, Weiling Liu, and Chao Tan. Horizontal oil-water two-phase dispersed flow velocity profile study by ultrasonic doppler method. *Experimental Thermal and Fluid Science*, 2018.

[75] Sounding Out the Flow: How Ultrasonic Flowmeters Work. https://www.omega.com/. Accessed January 10th 2019.

[76] Christian Poelma. Ultrasound imaging velocimetry: a review. *Experiments in Fluids*, 58(1):3, 2017.

[77] S. Rodriguez, X. Jacob, and V. Gibiat. Plane wave echo particle image velocimetry. In *Proceedings of Meetings on Acoustics*, volume 19. Acoustical Society of America, 2013.

[78] H. Kim, J. Hertzberg, and R. Shandas. Development and validation of echo PIV. *Experiments in Fluids*, 36(3):455 – 462, 2004.

[79] Hairong Zheng, Lingli Liu, Logan Williams, Jean R Hertzberg, Craig Lanning, and Robin Shandas. Real time multicomponent echo particle image

velocimetry technique for opaque flow imaging. *Applied physics letters*, 88(26):261915, 2006.

[80] D. Duxbury, J. Russell, and M. Lowe. The effect of variation in phased array element performance for non-destructive evaluation (nde). *Ultrasonics*, 53(6):1065 – 1078, 2013.

[81] S. Mosey, M. Sutcliffe, M. Weston, B. Knight-Gregson, and D. Liaptsis. Development and implementation of calibration process for full matrix capture. In *Proceedings of the 53rd Annual Conference of The British Institute of Non-Destructive Testing. Manchester: BINDT*, 2014.

[82] C.T. Lancée, J.M. Vissers, S. Mientki, C.M. Ligtvoet, and N. Bom. Influence of phase errors on beam-steered phased arrays. *Ultrasonics*, 25(3):154–159, 1987.

[83] C.T. Lancée, J.M. Vissers, S. Mientki, C.M. Ligtvoet, and N. Bom. Influence of amplitude errors on beam-steered phased arrays. *Ultrasonics*, 25(3):147–153, 1987.

[84] C. Nageswaran. Coping with failed elements on an array: a modelling approach to the technical justification. *Insight-Non-Destructive Testing and Condition Monitoring*, 52(7):372–379, 2010.

[85] J. Zhang, B. Drinkwater, and P. Wilcox. Effects of array transducer inconsistencies on total focusing method imaging performance. *NDT & E International*, 44(4):361–368, 2011.

[86] International Organization for Standardization. Non-destructive testing:

Characterization and verification of ultrasonic phased array equipment - Part 2: Probes. Standard, International Organization for Standardization, Geneva, CH, July 2017.

[87] Kang Zou, Tao Liu, Yan Huo, Fangkun Zhang, and Xiongwei Ni. Image analysis for in-situ detection of agglomeration for needle-like crystals. In *Control Conference (CCC), 2017 36th Chinese*, pages 11515–11520. IEEE, 2017.

[88] Jan Eggers, Michel Kempkes, and Marco Mazzotti. Measurement of size and shape distributions of particles through image analysis. *Chemical Engineering Science*, 63(22):5513–5521, 2008.

[89] Amir Sheikhi, Rahmat Sotudeh-Gharebagh, Reza Zarghami, Navid Mostoufi, and Mehrdad Alfi. Understanding bubble hydrodynamics in bubble columns. *Experimental Thermal and Fluid Science*, 45:63–74, 2013.

[90] Puneet Mishra, Alison Nordon, Julius Tschannerl, Guoping Lian, Sally Redfern, and Stephen Marshall. Near-infrared hyperspectral imaging for non-destructive classification of commercial tea products. *Journal of Food Engineering*, 2018.

[91] AA Gowen, CPo O'Donnell, PJ Cullen, G Downey, and JM Frias. Hyperspectral imaging–an emerging process analytical tool for food quality and safety control. *Trends in Food Science & Technology*, 18(12):590–598, 2007.

[92] Bjørn K Alsberg. Is sensing spatially distributed chemical information using sensory substitution with hyperspectral imaging possible? *Chemometrics and Intelligent Laboratory Systems*, 114:24–29, 2012.

[93] Kumar Patchigolla and Derek Wilkinson. Crystal shape characterisation of dry samples using microscopic and dynamic image analysis. *Particle & Particle Systems Characterization*, 26(4):171–178, 2009.

[94] PJ Cullen. Monitoring fluid-bed granulation and milling processes in-line with real-time imaging. *Pharmaceutical Technology*, 39(3), 2015.

[95] RT Rodrigues and Ja Rubio. New basis for measuring the size distribution of bubbles. *Minerals Engineering*, 16(8):757–765, 2003.

[96] Antonio Busciglio, Alberto Brucato, Francesca Scargiali, and Franco Grisafi. A novel technique for measuring local bubble size distribution. In *8th world congress of chemical engineering*, pages 1–6. CA, 2009.

[97] Eric S Winkel, Steven L Ceccio, David R Dowling, and Marc Perlin. Bubble-size distributions produced by wall injection of air into flowing freshwater, saltwater and surfactant solutions. *Experiments in Fluids*, 37(6):802–810, 2004.

[98] Chong Xu and Thomas Shepard. Digital image processing algorithm for determination and measurement of in-focus spherical bubbles. In *ASME 2014 4th Joint US-European Fluids Engineering Division Summer Meeting*. American Society of Mechanical Engineers, 2014.

[99] Zhengyou Zhang. A flexible new technique for camera calibration. *IEEE Transactions on pattern analysis and machine intelligence*, 22, 2000.

[100] Duhgoon Lee, Yong Sun Kim, and Jong Beom Ra. Automatic time gain

compensation and dynamic range control in ultrasound imaging systems. In *Proc. of SPIE Vol*, volume 6147, pages 614708–1, 2006.

[101] Nobuyuki Otsu. A threshold selection method from gray-level histograms. *IEEE transactions on systems, man, and cybernetics*, 9(1):62–66, 1979.

[102] M Hassan Najafi, Anirudh Murali, David J Lilja, and John Sartori. Gpu-accelerated nick local image thresholding algorithm. In *2015 IEEE 21st International Conference on Parallel and Distributed Systems (ICPADS)*, pages 576–584. IEEE, 2015.

[103] E Stride and N Saffari. Microbubble ultrasound contrast agents: a review. *Proceedings of the Institution of Mechanical Engineers, Part H: Journal of Engineering in Medicine*, 217(6):429–447, 2003.

[104] Bastien Denarie, Thor Andreas Tangen, Ingvild Kinn Ekroll, Natale Rolim, Hans Torp, Tore Bjåstad, and Lasse Lovstakken. Coherent plane wave compounding for very high frame rate ultrasonography of rapidly moving targets. *IEEE transactions on medical imaging*, 32(7):1265–1276, 2013.

[105] Lukas B Uittenbogaard, Monique C Haak, Marieke D Spreeuwenberg, and John MG van Vugt. Fetal cardiac function assessed with four-dimensional ultrasound imaging using spatiotemporal image correlation. *Ultrasound in Obstetrics and Gynecology*, 33(3):272–281, 2009.

[106] Leonard J Bond and Hans Matthiesen. Ultrasonic methods for the on-line real-time characterization of mixing in multiphase systems. *The Journal of the Acoustical Society of America*, 103(5):2880–2880, 1998.

[107] Lei Kang, Andrew Feeney, Riliang Su, David Lines, Axel Jäger, Han Wang, Yavor Arnaudov, Sivaram Nishal Ramadas, Mario Kupnik, and Steve Dixon. Two-dimensional flexural ultrasonic phased array for flow measurement. In *Ultrasonics Symposium (IUS), 2017 IEEE International*, pages 1–4. IEEE, 2017.

[108] Dimitri Ackermann and Georg Schmitz. Detection and tracking of multiple microbubbles in ultrasound B-mode images. *IEEE transactions on ultrasonics, ferroelectrics, and frequency control*, 63(1):72–82, 2016.

[109] D Ito, H Kikura, M Aritomi, and M Mori. Application of an ultrasonic array sensor to air-water bubbly flow measurement. In *Journal of Physics: Conference Series*, volume 147, page 012005. IOP Publishing, 2009.

[110] Mantvydas Kalibatas, Richard Nauber, Christian Kupsch, and Jürgen Czarske. Flow field imaging with ultrasonic guided waves for exploring metallic melts. *IEEE transactions on ultrasonics, ferroelectrics, and frequency control*, 65(1):112–119, 2018.

[111] Peng Li, Yulei Cai, Xiaolong Shen, Sharon Nabuzaale, Jie Yin, and Jiaqiang Li. An accurate detection for dynamic liquid level based on mimo ultrasonic transducer array. *IEEE Trans. Instrumentation and Measurement*, 64(3):582–595, 2015.

[112] Naïm Samet, Pierre Maréchal, and Hugues Duflo. Ultrasound monitoring of bubble size and velocity in a fluid model using phased array transducer. *NDT & E International*, 44(7):621–627, 2011.

[113] Naïm Samet, Pierre Maréchal, and Hugues Duflo. Ultrasonic imaging of bubble motion in a fiber preform. In *Acoustics 2012*, 2012.

[114] Naïm Samet, Pierre Maréchal, and Hugues Duflo. Monitoring of an ascending air bubble in a viscous fluid/fiber matrix medium using a phased array transducer. *European Journal of Mechanics-B/Fluids*, 54:45–52, 2015.

[115] Pulsar Process Measurement, Malvern, UK. https://www.pulsar-pm.com. Accessed August 8th 2018.

[116] J. Bamberger and M. Greenwood. Non-invasive characterization of fluid foodstuffs based on ultrasonic measurements. *Food Research International*, 37(6):621 – 625, 2004.

[117] Manuel Tramontana, Anthony Gachagan, Alison Nordon, David Littlejohn, Richard OLeary, and Anthony J Mulholland. System modelling and device development for passive acoustic monitoring of a particulate-liquid process. *Sensors and Actuators A: Physical*, 228:159–169, 2015.

[118] GT Clement, PJ White, and K Hynynen. Enhanced ultrasound transmission through the human skull using shear mode conversion. *The Journal of the Acoustical Society of America*, 115(3):1356–1364, 2004.

[119] J. Bouchard, M. Beesley, and D. Farrington. Acoustic diagnostics in process plant: application of pattern recognition techniques. In *International Conference on Acoustic Sensing and Imaging.*, pages 189 – 194. IET, 1993.

[120] R. Carvalho, O. Venturini, E. Tanahashi, F. Neves, and F. Frana. Application of the ultrasonic technique and high-speed filming for the study of

the structure of air-water bubbly flows. *Experimental Thermal and Fluid Science*, 33(7):1065 – 1086, 2009.

[121] S. Cunha, F. Jurandyr, M. Farias, J. Faccini, C. Lamy, and J. Su. High speed ultrasonic system to measure bubbles velocities in a horizontal two-phase flow. In *International Nuclear Atlantic Conference-INAC*, volume 2009, 2009.

[122] J. Sikorska and J. Pan. The effect of waveguide material and shape on acoustic emission transmission characteristics part 1: traditional features. *Journal of Acoustic Emission*, 22:264 – 274, 2004.

[123] J. Sikorska and J. Pan. The effect of waveguide material and shape on acoustic emission transmission characteristics part 2: Frequency and joint-time frequency characteristics. *Journal of Acoustic Emission*, 22:274 – 287, 2004.

[124] S. Wada, H. Kikura, and M. Aritomi. Pattern recognition and signal processing of ultrasonic echo signal on two-phase flow. *Flow Measurement and Instrumentation*, 17(4):207 – 224, 2006.

[125] Chen Shen, Jun Xu, Nicholas X. Fang, and Yun Jing. Anisotropic complementary acoustic metamaterial for canceling out aberrating layers. *Phys. Rev. X*, 4:041033, Nov 2014.

[126] L. Xu and L. Xu. Gas/liquid two-phase flow regime identification by ultrasonic tomography. *Flow Measurement and Instrumentation*, 8(3):145 – 155, 1997.

[127] B. Hoyle. Process tomography using ultrasonic sensors. *Measurement Science and Technology*, 7(3):272 – 280, 1996.

[128] R. Rahim, M. Rahiman, K. Chan, and S. Nawawi. Non-invasive imaging of liquid/gas flow using ultrasonic transmission-mode tomography. *Sensors and Actuators A: Physical*, 135(2):337 – 345, 2007.

[129] Z. Zakaria, F. Rahiman, A. Rahim, M. Ali, M. Baharuddin, and A. Jahidin. Small scale imaging using ultrasonic tomography. *Journal of Nuclear and and Related Technologies*, 6(1):266 – 281, 2009.

[130] J. Abbaszadeh, H. Rahim, R. Rahim, S. Sarafi, M. Ayob, and M. Faramarzi. Design procedure of ultrasonic tomography system with steel pipe conveyor. *Sensors and Actuators A: Physical*, 203:215 – 224, 2013.

[131] CR Hill. Calibration of ultrasonic beams for bio-medical applications. *Physics in Medicine & Biology*, 15(2):241, 1970.

[132] J. Kerr and B. Warsaw. Pickle, 2017.

[133] Python Software Foundation. https://www.python.org/. Downloaded April 2017.

[134] T. Namas and M. Dogruel. A feasible and accurate technique for determining the time-of-flight in ultrasonic distance measurements. In *ELMAR, 2008. 50th International Symposium*, volume 1, pages 337–340. IEEE, 2008.

[135] Marcelo A Duarte, João C Machado, and Wagner CA Pereira. A method to identify acoustic reverberation in multilayered homogeneous media. *Ultrasonics*, 41(9):683–698, 2004.

[136] Kay K Win, Jing Wang, Cishen Zhang, and Ran Yang. Identification and removal of reverberation in ultrasound imaging. In *Industrial Electronics and Applications (ICIEA), 2010 the 5th IEEE Conference on*, pages 1675–1680. IEEE, 2010.

[137] Norman Thieme, Paul Bönisch, Dagmar Meier, Richard Nauber, Lars Büttner, Kaspars Dadzis, Olf Pätzold, Lamine Sylla, and Jürgen Czarske. Ultrasound flow mapping for the investigation of crystal growth. *IEEE transactions on ultrasonics, ferroelectrics, and frequency control*, 64(4):725–735, 2017.

[138] Norman Thieme, R Nauber, L Büttner, J Czarske, K Büchner, and O Pätzold. Ultrasound flow mapping for 3D turbulent liquid metal flows. In *Ultrasonics Symposium (IUS), 2017 IEEE International*, pages 1–4. IEEE, 2017.

[139] Jorge Camacho, Montserrat Parrilla, and Carlos Fritsch. Phase coherence imaging. *IEEE transactions on ultrasonics, ferroelectrics, and frequency control*, 56(5), 2009.

[140] Ramazan Demirli, Moeness G Amin, Xizhong Shen, and Yimin D Zhang. Ultrasonic flaw detection and imaging through reverberant layers via subspace analysis and projection. *Advances in Acoustics and Vibration*, 2012, 2012.

[141] J.E. Carlson, S. Ranefjard, and F. Trulsson. A subspace based method for near transducer interference suppression. In *International Ultrasonics Symposium (IUS)*. IEEE, 2018.

[142] G. van Rossum. Python tutorial. Technical Report CS-R9526, Centrum voor Wiskunde en Informatica (CWI), Amsterdam, May 1995.

[143] David Ascher, Paul F Dubois, Konrad Hinsen, Jim Hugunin, Travis Oliphant, et al. NumPy: Open source numerical tools for Python, 2001–2018. [Online; accessed 19$^{\text{th}}$ May, 2019].

[144] Stefan Van der Walt, Johannes L Schönberger, Juan Nunez-Iglesias, François Boulogne, Joshua D Warner, Neil Yager, Emmanuelle Gouillart, and Tony Yu. scikit-image: image processing in python. *PeerJ*, 2:e453, 2014.

[145] Zygmunt L Szpak, Wojciech Chojnacki, and Anton Van Den Hengel. A comparison of ellipse fitting methods and implications for multiple-view geometry estimation. In *Digital Image Computing Techniques and Applications (DICTA), 2012 International Conference on*, pages 1–8. IEEE, 2012.

[146] Chun Hung Li and CK Lee. Minimum cross entropy thresholding. *Pattern recognition*, 26(4):617–625, 1993.

[147] Jui-Cheng Yen, Fu-Juay Chang, and Shyang Chang. A new criterion for automatic multilevel thresholding. *IEEE Transactions on Image Processing*, 4(3):370–378, 1995.

[148] William E Lorensen and Harvey E Cline. Marching cubes: A high resolution 3D surface construction algorithm. In *ACM siggraph computer graphics*, volume 21, pages 163–169. ACM, 1987.

[149] Paul D Wilcox and Jie Zhang. Quantification of the effect of array element pitch on imaging performance. *IEEE transactions on ultrasonics, ferroelectrics, and frequency control*, 65(4):600–616, 2018.

[150] Jie Zhang, Bruce W Drinkwater, Paul D Wilcox, and Alan J Hunter. Defect detection using ultrasonic arrays: The multi-mode total focusing method. *NDT & e International*, 43(2):123–133, 2010.

[151] K Mishima and T Hibiki. Some characteristics of air-water two-phase flow in small diameter vertical tubes. *International journal of multiphase flow*, 22(4):703–712, 1996.

[152] Alan J Hunter, Bruce W Drinkwater, and Paul D Wilcox. Autofocusing ultrasonic imagery for non-destructive testing and evaluation of specimens with complicated geometries. *NDT & E International*, 43(2):78–85, 2010.

[153] John L Barron, David J Fleet, and Steven S Beauchemin. Performance of optical flow techniques. *International journal of computer vision*, 12(1):43–77, 1994.

[154] Fredrik Lundh, Alex Clark, and Contributors. Python Imaging Library, 1995–2018. [Online; accessed 19$^{\text{th}}$ May, 2019].

[155] Fernand Meyer. Topographic distance and watershed lines. *Signal processing*, 38(1):113–125, 1994.

[156] Zetec Inc. Fundamental Principles of FMC and TFM Technologies, 2017. [Online; accessed 19$^{\text{th}}$ May, 2019].

[157] Daniel B Patience and James B Rawlings. Particle-shape monitoring and control in crystallization processes. *AIChE Journal*, 47(9):2125–2130, 2001.

Appendices

A Links to Data and Software Repositories

i. Link appears on page ii:

http://dx.doi.org/10.15129/5998d554-5c08-48d3-90d7-d1db6bcc6da0

ii. Link appears in Section 3.2.5:

http://dx.doi.org/10.15129/de42e45a-ec54-4c22-bbef-3f08d9f0eb01

iii. Link appears in Section 3.2.4.1:

http://dx.doi.org/10.15129/de42e45a-ec54-4c22-bbef-3f08d9f0eb01

iv. Link appears in Section 5.2:

http://dx.doi.org/10.15129/2b3687d1-cca7-412e-a1b1-f4899c06569c

v. Link appears in Section 6.3:

http://dx.doi.org/10.15129/56bc676b-4ad2-4e87-8094-575d3f1cd1a7

vi. Link appears in Section 6.4:

http://dx.doi.org/10.15129/56bc676b-4ad2-4e87-8094-575d3f1cd1a7

B Full Raw Data Acquisition and Correction

Introduction to the Data Set

Full raw data (FRD) is the term used to describe any ultrasonic data set containing multiple A-Scans acquired using an ultrasonic phased array. The data set is a matrix with dimensions $M \times N$ corresponding to M transmit-receive A-Scans and N time samples. The indices of the A-Scan order is used to program the spatial position of received signals, which is then used to generate ultrasonic images. It is therefore vital that the indices of the A-Scans correspond to the correct transmit-receive combination.

FIToolbox Phased Array Controller

The FIToolbox phased array controller (Diagnostic Sonar Ltd., Livingston, UK.) has 32 channels that can be used in transmission and reception. There are two software routes that can be deployed to acquire a single FRD data set, these are either directly via the *FITStreamFRD* LabVIEW based tool developed by Diagnostic Sonar Ltd or indirectly via a Dynamic-Link Library (DLL) that was also established by Diagnostic Sonar Ltd. The former route generates a two files: a *.png* that contains the FRD data set represented as an unsigned 64-bit scaled image and a *.cfg* configuration file that records the metadata associated with the FRD. The latter route provides a data stream of the FRD and requires the user to generate a look-up table (LUT) to reorder the data stream into a coherent FRD data set. The LUT is generated using the function *GetU64StreamIndexAndStep*,

which was developed by Diagnostic Sonar Ltd.

FRD Acquisition via the DLL

When the DLL is used to acquire the FRD stream there is an error associated with the determination of the LUT. The indices of every four A-Scans is mirrored throughout the FRD. To represent this anomaly, an FRD acquired via the DLL is shown as an decibel scaled image relative to the maximum sample amplitude in Figure B.1. In this image, the y-axis represents the A-Scan number and the x-axis represents the time sample number. The FRD was acquired using a 32 element aperture, so there are $M = 32^2$ A-Scans in the FRD, however, only the first 32 A-Scans are included in the image as this is the minimum number able to represent the anomaly. The code in Listing 1 demonstrates how the A-Scan indices are corrected by flipping the order of every four A-Scans. The corrected FRD, which should be used to generate any ultrasonic images, is shown in Figure B.1(b).

Listing 1: *FRD acquisition via DLL, code representing correction methodology.*

```
1 import numpy as np
2 nIndices = 4
3 [nScans, nSamples] = np.shape(FRD)
4
5 for rx in range(0,nScans,nIndices):
6     FRD[rx:rx+nIndices,:] = np.flipud(FRD[rx:rx+nIndices
      ,:])
```

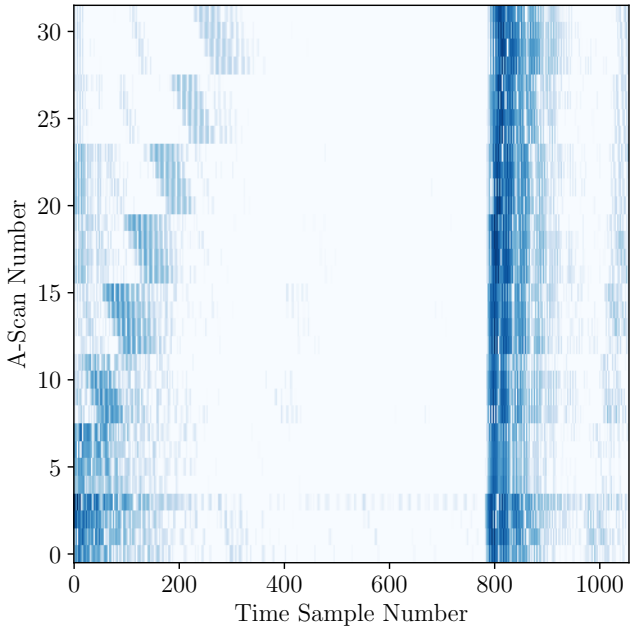

(a) *Incorrect A-Scan order.*

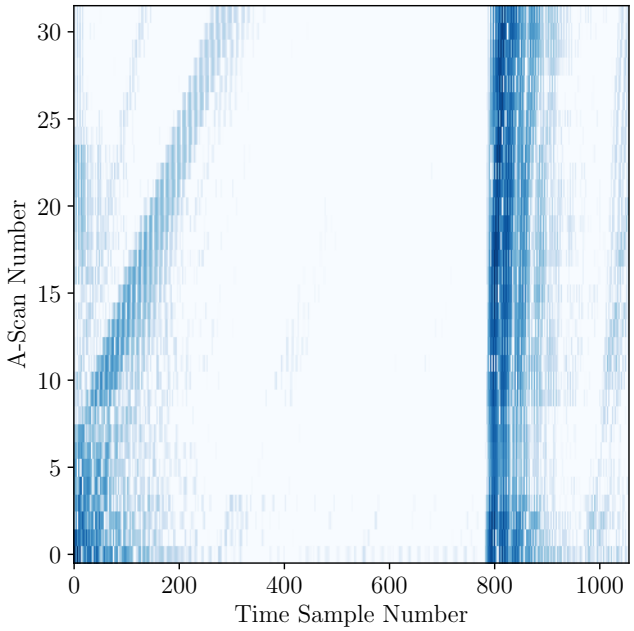

(b) *Corrected A-Scan order.*

Figure B.1: *A-Scan order anomaly for FRD acquired via DLL.*

Unsynchronised Element-Channel Combinations

This problem occurs when the first transmitting element in an aperture does not correspond to transmission on the first channel on the PAC. This offsets the indices of the A-Scans in each group of 32 A-Scans by the difference between the transmitting element and the total number of channels. To demonstrate this effect, an FRD was acquired using a 32 element aperture, where the elements used were 48 to 79. The first 96 A-Scans are shown as a decibel scaled image in Figure B.2, where the A-Scan number that corresponds to the transmitting element has been highlighted with a red line. For example, the indices of the first three transmitting elements are 0, 33 and 66. In Figure B.2(a) it can be seen that the first transmitting element is not in row zero of the y-axis. The code in Listing 2 demonstrates how the index of the first transmitting element relates to the correction of the order of all the A-Scan indices. This trend is repeated for every group of 32 A-Scans, and this is shown by the *for loop*. For example, if the first element to fire on the array is element 48 then the first A-Scan would be offset by $48 - 32 + 1 = 17$ A-Scans. Therefore, the order of each block of 32 A-Scans has been circularly shifted by 17. Upon application of this correction method, the A-Scan indices corresponding to the transmitting elements now match those with the red lines in Figure B.2(b).

Listing 2: *Element-channel synchronisation, code for correction methodology.*

```
1 import numpy as np
2 tx_begin = 48
3 nChannels = 32
4 [nScans, nSamples] = np.shape(FRD)
```

```
5
6 for tx in range(0,nScans,nChannels):
7         FRD[tx:tx+nChannels,:] = np.roll(FRD[tx:tx+
              nChannels,:],tx_begin-nChannels+1,axis=0)
```

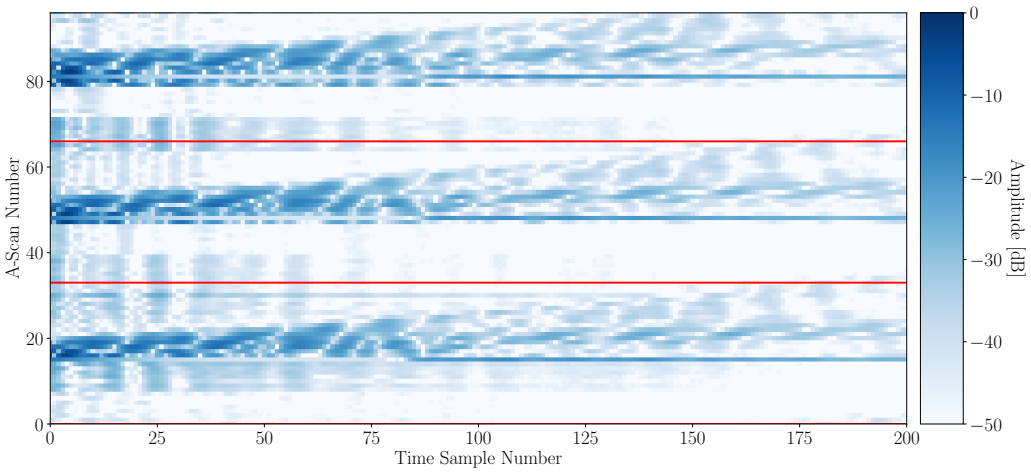

(a) *Incorrect A-Scan order.*

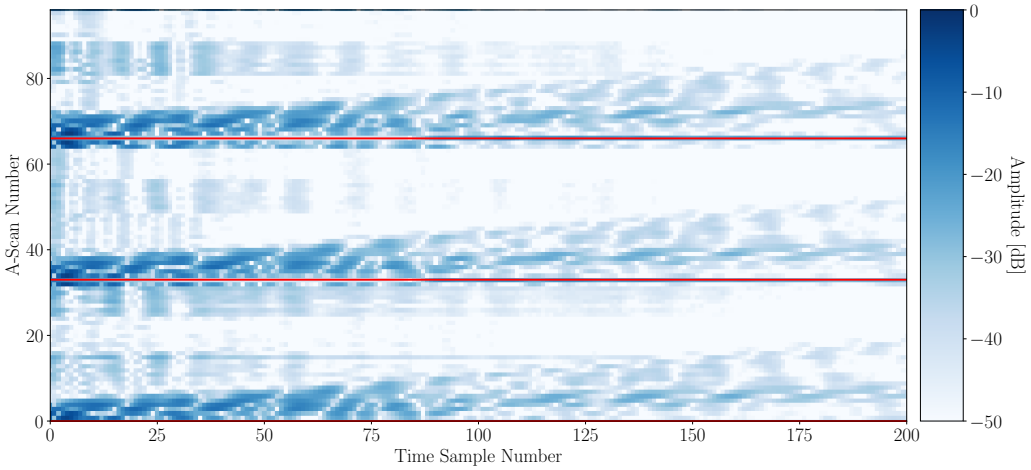

(b) *Corrected A-Scan order.*

Figure B.2: *A-Scan order anomaly for unsynchronised element-channel combinations.*

C Finite Element Model Design Correction

To enhance the directivity of the transmitted beam from an individual element location, the element width should be designed to be half of a wavelength relative to the load medium. The 5 MHz phased arrays used in the experimental work for this Thesis are designed to be acoustically coupled to Perspex. The wavelength of a 5 MHz signal in Perspex is 0.544 mm. These arrays were designed with a pitch of 0.7 mm, however, the precise element width was not quoted in the design specification.

During this PhD, the FE models in Chapters 3 and 4 were designed to have a half-wavelength element width. However, the FE models used in Chapters 5 and 6 were designed and run beforehand, with an element width and pitch approximating that of the physical probes available for experimental research. This means, the element width of 0.6 mm in Chapters 5 and 6 corresponds to approximately two wavelengths in water.

Unfortunately, the total time to run and interpret the results from all of the FE models discussed in Chapters 5 and 6 was approximately two months. So it was not possible to repeat all of the simulations. However, the 128 element FE model presented in Chapter 3 represented the same system as one of the models used in Chapters 5 and 6, namely the 3 mm diameter void suspended in water. The TFm images resulting from both models were passed to the bubble sizing algorithm and are presented in Figure C.1.

The correct element width, shown in Figure C.1(a) has resulted in lower size prediction accuracy than when the larger element width has been used. The

relative error has increased from 4% to 9% when the element width changes from 0.6 to 0.15 mm. The reason for this being the reduction in sensitivity, as less area exists to detect reflected signals. The impact of decreasing the element width has increased spatial side lobe activity, shown by the echoes in Figure C.1(a). The difference between the two results is small and since the 0.6 mm element width is more representative of the physical arrays available for the experimental analysis, this difference was not regarded as a hindrance to interpretation of the data. However, these models would need to be repeated though if the work is published in a journal paper.

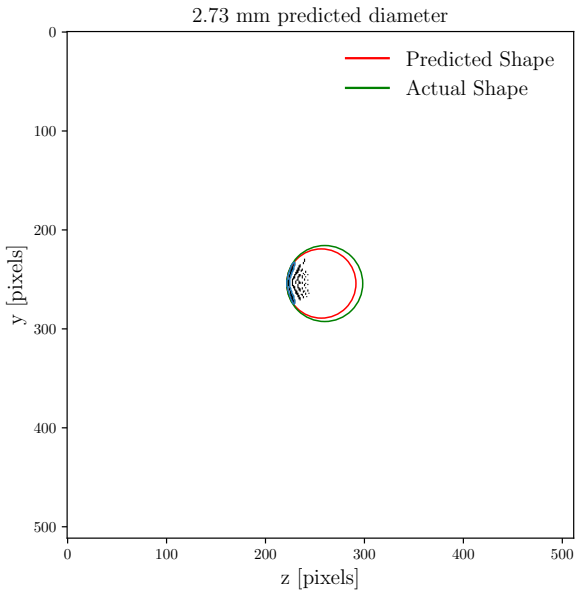

(a) *Element width = 0.15 mm (λ/2).*

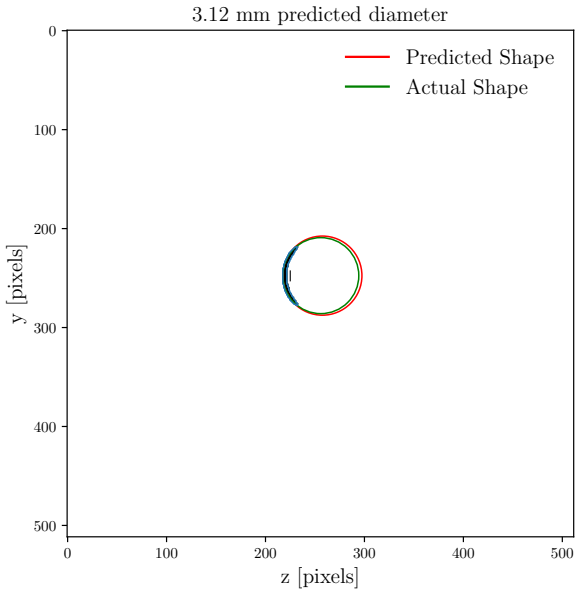

(b) *Element width = 0.6 mm (2λ).*

Figure C.1: *Processed TFM images of 3 mm diameter void suspended in water using a 5 MHz input signal with different element widths.*